

DOCTORAL THESIS

Development of ZnO Nanorod and NiO Thin Film Based Materials for Photocatalytic Applications

Zengjun Chen

TALLINN UNIVERSITY OF TECHNOLOGY
DOCTORAL THESIS
67/2022

**Development of ZnO Nanorod and NiO
Thin Film Based Materials for
Photocatalytic Applications**

ZENGJUN CHEN



TALLINN UNIVERSITY OF TECHNOLOGY

School of Engineering

Department of Materials and Environmental Technology

This dissertation was accepted for the defence of the degree 02/11/2022

Supervisor:

Prof. Malle Krunk
School of Engineering
Tallinn University of Technology
Tallinn, Estonia

Co-supervisor:

Dr. Tatjana Dedova
School of Engineering
Tallinn University of Technology
Tallinn, Estonia

Opponents:

Prof Aivaras Kareiva
Institute of Chemistry
Department of Inorganic Chemistry
Vilnius University
Vilnius, Lithuania

Prof Deniss Klauson
Institute of Engineering and Circular Economy
Tallinn University of Applied Sciences
Tallinn, Estonia

Defence of the thesis: 09/12/2022, Tallinn

Declaration:

Hereby I declare that this doctoral thesis, my original investigation and achievement, submitted for the doctoral degree at Tallinn University of Technology has not been submitted for doctoral or equivalent academic degree.

Zengjun Chen

signature



European Union
European Regional
Development Fund



Investing
in your future

Copyright: Zengjun Chen, 2022

ISSN 2585-6898 (publication)

ISBN 978-9949-83-925-4 (publication)

ISSN 2585-6901 (PDF)

ISBN 978-9949-83-926-1 (PDF)

Printed by Koopia Niini & Rauam

TALLINNA TEHNIKAÜLIKOOL
DOKTORITÖÖ
67/2022

**ZnO nanovarrastel ja NiO õhukestel kiledel
baseeruvate fotokatalüütiliste materjalide
arendus**

ZENGJUN CHEN



Contents

List of publications	7
Author's contribution to the publications	8
Introduction	9
Abbreviations, terms, symbols.....	12
1 Literature overview.....	14
1.1 Photocatalysis	14
1.1.1 Mechanism of photocatalysis	14
1.1.2 Main semiconductor photocatalysts.....	15
1.2 Overview of ZnO photocatalysts.....	16
1.2.1 Main properties and applications of ZnO	16
1.2.2 ZnO as a photocatalyst.....	17
1.2.3 ZnO/noble metal composite photocatalysts.....	18
1.2.4 ZnO heterostructures based photocatalysts.....	20
1.2.5 Methods for synthesis of ZnO nanorods.....	22
1.2.6 ZnO nanorods by hydrothermal method	24
1.3 Overview of NiO photocatalysts	25
1.3.1 Main properties and applications of NiO	25
1.3.2 NiO as a photocatalyst	25
1.3.3 Methods for synthesis of NiO films.....	26
1.3.4 NiO films by chemical spray pyrolysis	27
1.4 Summary of literature overview and aim of study	30
2 Experimental	32
2.1 Deposition of ZnO _{NR} layers, ZnO _{NR} /Au composites, NiO films, ZnO/NiO heterostructures	32
2.1.1 Deposition of ZnO _{NR} layers by hydrothermal method	32
2.1.2 Deposition of Au nanoparticles on ZnO _{NR} layers.....	32
2.1.3 Deposition of NiO and ZnO films by pneumatic spray method.....	33
2.1.4 Deposition of NiO film by ultrasonic spray method and preparation of ZnO/NiO bilayers and ZnO _{NR} /NiO core-shell heterostructures.	33
2.2 Characterization of ZnO _{NR} layers, ZnO _{NR} /Au composites, NiO films, ZnO/NiO heterostructures	34
2.3 Characterization for the photocatalytic properties of ZnO _{NR} layers, ZnO _{NR} /Au composites, NiO films, ZnO/NiO heterostructures	34
3 Results and discussion.....	36
3.1 Effect of surface treatment by HAuCl ₄ on photocatalytic activity of ZnO _{NR} layers ...	36
3.1.1 Structural, morphological, and optical properties of bare ZnO _{NR} layers and ZnO _{NR} /Au composites	36
3.1.2 Photocatalytic activity of ZnO _{NR} layer and ZnO _{NR} /Au composites	38
3.1.3 Surface chemical composition and wettability of ZnO _{NR} layer and ZnO _{NR} /Au composites.....	39
3.2 NiO films deposited by pneumatic spray pyrolysis method.....	40
3.2.1 Structural, morphological, and optical properties of NiO films	40
3.2.2 Photocatalytic activity of NiO films.....	42
3.2.3 Surface chemical composition and wettability of NiO films	43

3.3 ZnO/NiO heterostructures by ultrasonic spray of NiO films on ZnO films and ZnO _{NR}	46
3.3.1 Effect of deposition temperature on structural, morphological, and optical properties of NiO films.....	46
3.3.2 ZnO/NiO bilayer heterostructures: effect of NiO growth temperature.....	47
3.3.3 ZnO _{NR} /NiO core-shell heterostructures: effect of NiO shell thickness.....	49
Conclusions	54
References	56
Acknowledgements.....	75
Abstract.....	76
Lühikokkuvõte.....	79
Appendix 1	83
Appendix 2	119
Curriculum vitae.....	128
Elulookirjeldus.....	130

List of publications

The list of author's publications, on the basis of which the thesis has been prepared:

- I T. Dedova, I. Oja Acik, **Z. Chen**, A. Katerski, K. Balmassov, I. Gromyko, T. Nagyné-Kovács, I.M. Szilágyi, and M. Krunks. Enhanced photocatalytic activity of ZnO nanorods by surface treatment with H₂AuCl₄: Synergic effects through an electron scavenging, plasmon resonance and surface hydroxylation. *Materials Chemistry and Physics*, 245, 122767, 2020, <https://doi.org/10.1016/j.matchemphys.2020.122767>.
- II **Z. Chen**, T. Dedova, I. Oja Acik, M. Danilson, and M. Krunks. Nickel oxide films by chemical spray: Effect of deposition temperature and solvent type on structural, optical, and surface properties. *Applied Surface Science*, 548, 149118, 2021, <https://doi.org/10.1016/j.apsusc.2021.149118>.
- III **Z. Chen**, T. Dedova, N. Spalatu, N. Maticiuc, M. Rusu, A. Katerski, I. Oja Acik, T. Unold, and M. Krunks. ZnO/NiO heterostructure with enhanced photocatalytic activity obtained by ultrasonic spray of a NiO shell onto ZnO nanorods. *Colloids and Surfaces A: Physicochemical and Engineering Aspects*, 648, 129366, 2022, <https://doi.org/10.1016/j.colsurfa.2022.129366>.

Author's contribution to the publications

Contribution to the papers in this thesis are:

- I Deposition of ZnO nanorods by hydrothermal method, characterization of structural and optical properties of ZnO nanorods and ZnO nanorod/Au composites by X-ray diffraction (XRD) and UV-Vis spectroscopy, surface wettability by water contact angle measurements, measurement of photodegradation of methyl orange in aqueous solution by ZnO nanorods and ZnO nanorod/Au composites, data analysis, visuals, minor role in writing.
- II Deposition of NiO films by pneumatic spray method; characterization of structural and vibrational properties of sprayed films by XRD, Raman spectroscopy, and Fourier transform infrared (FTIR) spectroscopy methods; optical properties of NiO films by UV-Vis spectroscopy; surface wettability by water contact angle measurements; measurement of photodegradation of methyl orange in aqueous solution by NiO films; data analysis; visuals; major role in writing.
- III Deposition of NiO films by ultrasonic spray method, deposition of NiO films onto ZnO films grown by chemical spray and ZnO nanorods grown by hydrothermal method to form ZnO/NiO bilayer and ZnO nanorod/NiO core-shell heterostructures, post-deposition thermal treatment of NiO films and ZnO/NiO heterostructures, characterization of structural and optical properties of NiO films, surface chemical composition of NiO films and ZnO nanorod/NiO core-shell heterostructures, electrical properties of ZnO/NiO bilayers, measurement of photodegradation of methylene blue in aqueous solution by NiO films and ZnO/NiO heterostructures, data analysis, visuals, major role in writing.

Introduction

Energy depletion and environmental pollution are the urgent issues that humanity is facing nowadays due to the economic growth and rapid increase of population. In particular, water pollution has caused severe impact on the quality of human's life and ecosystem. Numerous physicochemical and biological methods such as adsorption, filtration, and precipitation have been employed for water and wastewater treatment. However, these techniques cannot sufficiently remove effluents from wastewater, still leaving behind the residues of contaminants in the water streams from ppb to ppm concentrations. For this reason, advanced oxidation processes (AOPs), based on the generation of strong oxidants such as hydroxyl radicals and superoxide radicals, have been proposed as an additional step to mineralize organic pollutants [1]. Photocatalysis, as one of the most promising AOPs, has been widely studied for water and wastewater treatment owing to its ability to degrade organic pollutants to CO₂ and H₂O under light irradiation [2]. To date, semiconductors such as TiO₂, ZnO, NiO, CdS, and ZnS have been used as photocatalysts in photocatalysis process for water and wastewater treatment. Among these semiconductors, TiO₂ is the mostly studied photocatalyst due to its excellent photocatalytic activity (PA), nontoxicity, and chemical stability. Another photocatalyst, ZnO is also considered as an efficient and alternative to TiO₂. Nevertheless, the main drawbacks of TiO₂ and ZnO photocatalysts are the fast recombination of photogenerated electron-hole pairs and weak absorption of visible light [3]. However, compared to TiO₂, ZnO is easy to synthesize in various morphologies. To overcome the drawbacks of ZnO as photocatalyst, several modification methods have been employed to improve the PA of ZnO, such as metal/non-metal doping, and coupling with a metal or semiconductors [4]. NiO has also been used as a photocatalyst to degrade organic pollutants in water owing to its tunable bandgap, chemical stability and low cost [5]. As a p-type semiconductor, NiO is a suitable candidate for coupling with ZnO to form p-n heterostructure and enhancing the PA by such approach.

To date, ZnO and NiO photocatalysts are mostly studied in their powdery form due to their high surface area [6]. However, photocatalyst in its powdery form has drawbacks such as particle agglomeration and difficulty of separation of the photocatalyst from aqueous medium. Hence, immobilizing a photocatalyst on a substrate is a more proper approach due to its easy separation from aqueous medium. The development of photocatalytically efficient ZnO nanorod and NiO film based photocatalysts on substrates by simple and low-cost fabrication methods is of vital importance for further large-scale applications.

The aim of this dissertation was development of strategies for the synthesis of ZnO and NiO based layers as photocatalytic coatings on glass substrates by low-cost chemical solution methods such as hydrothermal growth and chemical spray pyrolysis. ZnO in the form of nanorod layers (ZnO_{NR}) that possess much higher surface area compared to thin films, and NiO thin films with high chemical stability and p-type conductivity were chosen as materials to study. The methodology applied includes the experimental investigation of the relationship between the technological parameters of synthesis and physico-chemical properties of ZnO and NiO in order to find out the technological routes for preparation of materials with enhanced photocatalytic activity.

The first objective of the thesis was the synthesis of photocatalytically efficient ZnO_{NR}/Au composites. The effect of ZnO_{NR} treatment with HAuCl₄ on ZnO_{NR}/Au

composite formation and its optical properties, surface chemical composition and photocatalytic performance was studied.

The second objective was focused on synthesis of photocatalytically active NiO films by cost-effective chemical spray method. Herein, the effect of deposition temperature and solvent type on structural, optical, and surface properties, including photocatalytic activity of NiO films produced by pneumatic spray pyrolysis method using nickel acetate as source material was studied.

The third objective was development of ZnO_{NR}/NiO n-p core-shell heterostructures with improved photocatalytic performance. To obtain this goal, the technology for deposition of uniform NiO thin films by ultrasonic spray method was elaborated using nickel acetylacetonate as a precursor material. Ultrasonically sprayed NiO films were applied to form ZnO/NiO heterostructures. The impact of NiO deposition temperature on NiO film properties, ZnO/NiO bilayer heterostructure formation and photocatalytic activity was studied. Based on those results, the most suitable process parameters were selected for ZnO_{NR}/NiO core-shell heterostructure fabrication.

This dissertation is based on three published papers and consists of three chapters. The first chapter contains a literature overview on the photocatalysis mechanism, main semiconductor photocatalysts, and current status of investigations on ZnO and NiO photocatalysts. At the end of the first chapter, a summary of literature overview and the aim of the study are presented. Applied experimental procedures and characterization methods are summarized in the second chapter.

The third chapter is composed of three sections presenting the main results of the thesis. The first section of this chapter summarizes the results of paper I on synthesis and properties of ZnO_{NR}/Au composite. The second section summarizes the results of paper II on deposition and properties of NiO films grown by pneumatic spray. The third section summarizes the results of paper III on deposition of NiO thin films by ultrasonic spray, and formation and characterization of ZnO/NiO heterostructures with enhanced photocatalytic performance.

The novelty of this study lies within the new strategies for synthesis of photocatalytically active ZnO nanorod and NiO thin film based materials by simple and cost-effective chemical methods. Novelties of the study could be listed as follows. In paper I, for the first time Au NPs were produced by spin-coating of HAuCl₄ solution onto ZnO_{NR} layers followed by thermal treatment to form ZnO_{NR}/Au composite with enhanced PA. In paper II, by systematic study the effect of deposition conditions on surface properties of pneumatically sprayed NiO films we showed that the deposition temperature is the main technological parameter controlling the content of surface hydroxyl groups on the film surface, and consequently, the film photocatalytic performance. In paper III, we demonstrated for the first time that homogeneous crystalline films of NiO with cubic structure can be successfully grown on different substrates by employing a robust ultrasonic spray technique and nickel acetylacetonate as a source material. For the first time ultrasonically sprayed NiO film has been applied to ZnO_{NR} layer to form ZnO_{NR}/NiO core-shell heterostructure demonstrating significantly enhanced photocatalytic performance compared to pristine ZnO_{NR}.

Current research is a continuation of previous studies on the growth and properties of ZnO nanostructures [7-9] performed at the Laboratory of Thin Film Chemical Technologies, Tallinn University of Technology, Estonia. The thesis is directly related to the research topics on the development of semiconductor materials and devices by the Laboratory. The study has been financially supported by Estonian Research Council

projects IUT 19-4 “Thin films and nanomaterials by wet-chemical methods for next-generation photovoltaics”, PRG627 “Antimony-chalcogenide thin films for the next generation of semi-transparent solar cells for use in power-producing windows”, the Estonian Centre of Excellence project TK141 (TAR16016EK) “Advanced materials and high-technology devices for energy recuperation systems”, the European Commission’s H2020 programme under the ERA Chair project 5GSOLAR grant agreement No 952509, and ASTRA “TUT Institutional Development Programme for 2016-2022” Graduate School of Functional Materials and Technologies (2014-2020.4.01.16-0032).

Abbreviations, terms, symbols

AO II	Acid orange II
AOPs	Advanced oxidation processes
at%	Atomic percent
BE	Binding energy
C_0	Initial concentration
CB	Conduction band
D	Crystallite size
d	Thickness
DC	Direct current
e^-/h^+	Electron/hole pairs
E_{CBM}	Energy level of conduction band minimum
E_F	Fermi level
E_g	Bandgap
E_i	Ionization energy
E_{VBM}	Energy level of valence band maximum
FTIR	Fourier transform infrared
FTO	Fluorine doped tin oxide
FWHM	Full width at half maximum
HMT	Hexamethylenetetramine
HT	Hydrothermal
h ν	Photon energy
IC	Indigo carmine
ITO	Indium tin oxide
I-V	Current-voltage
k	Degradation rate constant
KE	Kinetic energy
KP	Kelvin probe
MB	Methylene blue
MeO	Metal oxide
MG	Methyl green
MO	Methyl orange
NA	Not available
NPs	Nanoparticles
OH _{ads}	Adsorbed hydroxyl groups
PA	Photocatalytic activity
ppm	Particle per million
PSP	Pneumatic spray pyrolysis
PYS	Photoelectron yield spectroscopy

RhB	Rhodamine B
RT	Room temperature
SC	Spin coating
SCE	Saturated calomel electrode
SEM	Scanning electron microscopy
SPR	Surface plasmon resonance
t	Irradiation time
T _{an}	Annealing temperature
TCO	Transparent conducting oxide
T _s	Substrate temperature
USP	Ultrasonic spray pyrolysis
UV-Vis	Ultraviolet-visible
V	Volume of pollutant solution
VB	Valence band
V _o	Oxygen vacancy
XPS	X-ray photoelectron spectroscopy
XRD	X-ray diffraction
α'	Auger parameter
η	Degradation efficiency
Φ	Work function
1D	One-dimensional
2D	Two-dimensional
3D	Three-dimensional

1 Literature overview

1.1 Photocatalysis

Photocatalysis is a process of decomposition of organic pollutants based on the generation of hydroxyl radicals under light irradiation [4, 10-12]. Photocatalysis has the advantages over other water purification methods due to its cost-effectiveness, environmental benignity, and the ability to mineralize organic pollutants into CO_2 and H_2O [4, 10-12]. In particular, it is an effective way to remove persistent organic pollutants such as pharmaceuticals, pesticides, and endocrine-disrupting chemicals in a low concentration (such as ppm) [4, 10-12].

Photocatalysis processes are divided into homogeneous and heterogeneous classes [4]. In homogeneous photocatalysis pollutants and photocatalysts are in the same phase, whereas in heterogeneous photocatalysis pollutants and photocatalysts are in different phases [4]. Heterogeneous photocatalysis favoring its advantage of easy separation of photocatalysts from aqueous medium is more widely accepted [4]. Semiconductors are usually used as photocatalysts in heterogeneous photocatalysis [4]. Semiconductor photocatalysts have found numerous applications in environmental and energy fields such as water and wastewater treatment, air purification, photocatalytic hydrogen production, also in the development in self-cleaning, antifogging, antibacterial coatings, and even in cancer treatment [13].

In water and wastewater treatment, semiconductor photocatalysts are used to degrade various organic pollutants including textile dyes, antibiotics, analgesics, herbicides, and pesticides [14].

Thus, heterogeneous photocatalysis is a promising approach to be widely applied for environmental applications [15].

1.1.1 Mechanism of photocatalysis

The photocatalytic process may happen when the photocatalytic material is irradiated by light. The photocatalytic process is illustrated in Figure 1.1.

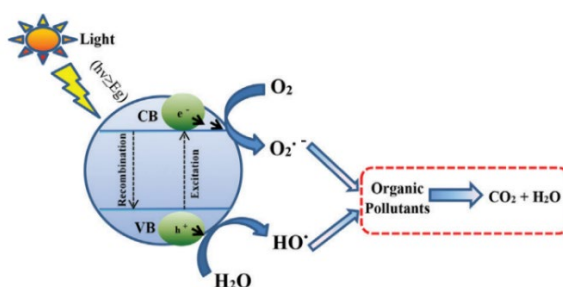
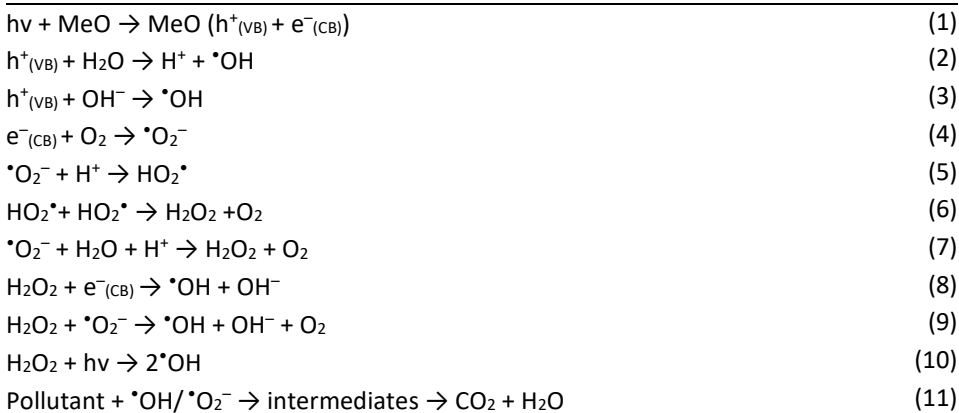


Figure 1.1. Basic mechanism of photocatalysis based on semiconductors [16].

When the semiconductor photocatalyst is photo-induced by light with the photon energy equal to or larger than its bandgap energy (E_g), electron/hole pairs are formed (Eq. (1)) [4]. The photogenerated e^-/h^+ pairs then move to the surface of photocatalysts to participate in redox reactions with adsorbed pollutants. In oxidation reactions, holes, $h^+_{(VB)}$, react with H_2O or hydroxide ion (OH^-) to generate hydroxyl radicals ($^\bullet\text{OH}$) (Eq. (2), (3)). In reduction reaction, electrons, $e^-_{(CB)}$, react with oxygen to generate superoxide radicals ($^\bullet\text{O}_2^-$) (Eq. (4)) [17]. In addition, $^\bullet\text{O}_2^-$, can react with H_2O or H^+ to form hydrogen

peroxide (H₂O₂), which subsequently produces [•]OH (Eq. (5-10)) [4, 17-19]. The resulting [•]OH and [•]O₂⁻ species are powerful oxidizing and reducing agents, respectively, to decompose organic pollutants to CO₂ and H₂O (Eq. (11)) [18]. The basic principles behind the photocatalytic reactions can be summarized as follows [4, 17-19]:



The separation of photogenerated e⁻/h⁺ pairs is the most important step in the photocatalytic reaction process since a large number of e⁻/h⁺ pairs recombine while migrating to the surface. The recombination of e⁻/h⁺ pairs will result in a decrease of PA. Thus, the key for enhancing PA is to prolong the lifetime of photogenerated charge carriers.

1.1.2 Main semiconductor photocatalysts

Semiconductor photocatalysts have the ability to fully degrade organic pollutants to CO₂ and H₂O. In particular, the remarkable mineralization ability to low concentrations (in ppm) of non-biodegradable organic pollutants makes photocatalysts ideal materials for water and wastewater treatment.

In general, an ideal photocatalyst should be photoactive under UV, visible, or solar light; nontoxic; inexpensive; abundant in nature; stable during photocatalytic reactions; and must have high redox potential to produce sufficient amount of hydroxyl radicals [20]. All these features are key factors for efficient photocatalysts. To date, a large number of semiconductors have been used to study their PA such as metal oxides (TiO₂ [21], ZnO [4], SnO₂ [22], WO₃ [23], Fe₂O₃ [24], Cu₂O [25], NiO [26]), metal sulfides (CdS [27], ZnS [28]), and nonmetal semiconductors (g-C₃N₄ [29], SiC [30]).

Among the various semiconductor materials, metal-oxide based photocatalysts are commonly used. TiO₂ is the mostly studied photocatalyst due to its excellent photocatalytic activity, low cost, chemical and photo stability, and nontoxicity [24]. It has been extensively investigated for numerous applications such as water and air purification, hydrogen evolution, self-cleaning, anti-bacterial surfaces and cancer therapy [31]. However, its large bandgap energy of 3.2 eV and fast recombination of the photogenerated electron-hole pairs are the main drawbacks limiting its PA [24].

The PA of TiO₂ has also been investigated at the Department of Materials and Environmental Technology, Tallinn University of Technology. Namely, photocatalytic properties of TiO₂ powders [32-35] and TiO₂ coatings on a substrate prepared by sol-gel method [36] have been studied in Laboratory of Environmental Technology. Photocatalytic

performance of TiO₂ thin film deposited by spray method [37, 38] has been studied in Laboratory of Thin Film Chemical Technologies.

ZnO ($E_g=3.37$ eV) is also widely studied photocatalytic material because ZnO shows excellent photocatalytic activity with advantages of good thermal stability at room temperature and nontoxicity [4]. Similar to TiO₂, ZnO also suffer from fast recombination of electron-hole pairs [4].

SnO₂ ($E_g=3.5$ eV) [22] photocatalyst is active under UV light irradiation, while WO₃ ($E_g=2.7-2.8$ eV) [23], Cu₂O ($E_g=2.2$ eV) [25], and Fe₂O₃ ($E_g=2.0-2.2$ eV) [27] photocatalysts are able to harness visible light. Although these photocatalysts have the advantages of low cost and low-toxicity, however, fast recombination of photogenerated electron-hole pairs is their drawback [22, 23, 25, 27].

NiO ($E_g=3.0-4.3$ eV) is also considered as a photocatalyst due to its low material cost, high stability, and ability to degrade organic pollutants [26]. Fast recombination rate of electron-hole pairs is also its main drawback [26]. Although NiO has lower PA than TiO₂ and ZnO, NiO can be used as a cocatalyst to improve the PA of TiO₂ and ZnO by forming TiO₂/NiO [21] and ZnO/NiO heterojunctions [39].

CdS and ZnS are the most widely used metal sulfide photocatalysts. CdS photocatalyst has high photosensitivity owing to its narrow bandgap of 2.4 eV [27]. The drawback of CdS is insufficient stability and photocorrosion, especially in an aqueous medium [27]. ZnS has a large bandgap of 3.7 eV, and because of this being an UV light active photocatalyst [28]. Compared to metal oxide-based photocatalysts, metal sulfides have poor stability in aqueous solutions that limits their employment as a photocatalyst.

To summarize, most semiconductor photocatalysts suffer from fast recombination rate of photogenerated electron-hole pairs, thus suppressing their PA. For this reason, numerous modification methods including metal/nonmetal doping and coupling with metal or semiconductors have been proposed and employed to suppress the recombination of photogenerated electron-hole pairs [6]. The details of modification on the semiconductor photocatalysts will be discussed on the example of ZnO photocatalyst in the next sections.

1.2 Overview of ZnO photocatalysts

1.2.1 Main properties and applications of ZnO

Zinc oxide is an inorganic compound with the chemical formula of ZnO. ZnO can crystalize in three different forms: hexagonal wurtzite, cubic zincblende and rocksalt (Figure 1.2). Hexagonal wurtzite is the most stable structure of ZnO under ambient conditions [4]. Cubic zincblende can be obtained by growing ZnO on cubic substrates [4]. Rock salt structure can only exist at relatively high pressures [4].

Stoichiometric ZnO naturally appears in the form of rare mineral zincite [40]. Non-stoichiometric ZnO is an n-type semiconductor due to oxygen vacancies or zinc interstitials [41]. It has a direct bandgap of 3.37 eV and a large exciton binding energy of 60 meV [4].

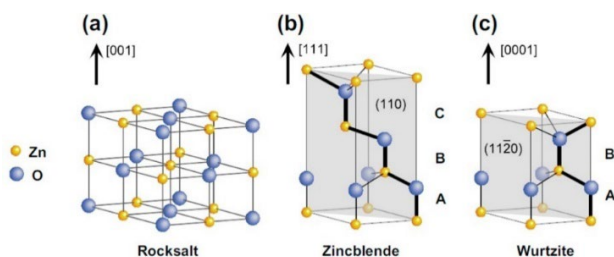


Figure 1.2. ZnO crystal structures: (a) cubic rocksalt, (b) cubic zincblende, and (c) hexagonal wurtzite [4].

ZnO can be easily synthesized in various morphologies. ZnO is mainly used in the form of powders, films, and different nanostructures. Numerous morphologies of ZnO nanostructures from one-dimensional (1D) to three-dimensional (3D) have been developed including nanorods, nanofibers, nanowires, nanotubes, nanoneedles (1D); nanosheets, nanoplates (2D); and nanoflowers (3D) [4].

ZnO has been widely used in many applications such as pharmaceutical, cosmetic, food, rubber, commodity chemical, painting, ceramic, and glass industries [42]. ZnO is an attractive material for electronic and optoelectronic devices such as light-emitting diodes, laser, photodetector, solar cells, transistors [42]. Besides, ZnO has been used in piezoelectric devices, sensors, and also as a photocatalyst [4, 42].

1.2.2 ZnO as a photocatalyst

ZnO with E_g of 3.37 eV is nontoxic, inexpensive material that exhibits excellent photocatalytic activity, which makes it an attractive photocatalyst in water and wastewater treatment. It has also been extensively investigated for water splitting and antibacterial treatment applications [43, 44]. In water and wastewater treatment, the PA of ZnO is mainly studied in the form of nanoparticles (NPs) [45-52], films on substrates [53-57], and nanorods on substrates [8, 58-62]. The results of the PA of ZnO in different forms are summarized in Table 1.1, Appendix 2.

It is well known that surface area of photocatalysts plays an important role in PA, as higher surface area leads to more active generation of hydroxyl radicals and higher adsorption rate of pollutants on the surface of photocatalysts, thereby accelerating the photodegradation efficiency of pollutants [45]. Thus, ZnO nanoparticles [45-52] have shown excellent PA owing to their high surface area. To date, ZnO NPs with different morphologies including rod-like [45-48], wire-like [49], plate-like [50], flower-like [51], and sponge-like [52] have been studied for their PA.

For instance, rod-like [45-47] and flower-like [51] ZnO NPs exhibited ca. 99% MO degradation efficiency under UV light in 50-100 min irrespective of synthesis methods.

Although ZnO NPs showed excellent PA, their powdery form makes it difficult to separate from the aqueous medium, causing secondary pollution of water. For this reason, immobilizing photocatalysts on substrates is a more suitable form due to its ease of separation from polluted water and ease of reuse. To date, the PA of ZnO immobilized on substrates has been studied mainly in the form of ZnO thin film [53-56], and ZnO nanorods [8, 58-62] (Table 1.1, Appendix 2).

ZnO in the form of film usually possesses lower degradation efficiency compared to ZnO NPs due to its lower surface area. For the degradation of MO by ZnO prepared by sol-gel method, 18% MO degradation efficiency was achieved by ZnO film under sunlight

in 150 min [53], being more than five times lower than that from rod-like ZnO NPs (99%, 100 min) [45]. For the degradation of MB, ZnO film prepared by atomic layer deposition showed 40% degradation efficiency under UV light in 240 min [56], being more than twice lower than that from plate-like ZnO NPs (90%, 14 min) [50]. Sprayed ZnO film possessed 88% MB degradation efficiency under UV light in 240 min [57].

However, ZnO_{NR} on substrates demonstrated comparable or even higher degradation efficiency than ZnO NPs. For the degradation of MO by hydrothermally grown ZnO under UV light, ZnO_{NR} on a substrate degraded 87% in 60 min [58] and 95% in 160 min [59], comparable or even higher than that from rod-like ZnO NPs (89%, 180 min) [48], respectively. For the degradation of RhB by hydrothermally grown ZnO under UV light, ZnO_{NR} on substrates owned 70% degradation efficiency in 120 min [60] in comparison to 80% from wire-like ZnO NPs in 500 min [49]. While 98% RhB degradation efficiency was achieved by ZnO_{NR} on a substrate prepared by chemical bath deposition [62], being even higher than that from ZnO NPs (88%, 500 min) [49].

In summary, the form of ZnO nanorods immobilized on the substrate showed a relatively high degradation efficiency, which was only slightly lower compared to nanopowders, but significantly higher than that of thin films. Considering high PA, ease of synthesis and separation from pollutant solution, ZnO nanorods on substrates have great potential for wastewater treatment applications.

1.2.3 ZnO/noble metal composite photocatalysts

ZnO photocatalysts suffer from fast recombination of photogenerated electron-hole pairs and poor absorption of visible light [45]. In order to overcome these drawbacks ZnO/noble metal composites approach has been developed [63-84].

To date, noble metals such as Au [63-67, 74, 76-80], Ag [68, 69, 73, 75, 81, 82], Pt [70, 73, 83, 84], Pd [71-73], and Rh [73] have been used to form ZnO/noble metal composites. Since noble metals can form a Schottky barrier with ZnO and the Fermi levels of noble metals are lower than the conduction band minimum of ZnO, electrons from conduction band of ZnO will migrate to metal side under UV irradiation (Figure 1.3 a) [66, 85]. Thus, noble metals act as effective traps of photogenerated electrons to suppress the recombination of electron-hole pairs generated in ZnO due to the formation of Schottky barrier with ZnO [66, 85]. Besides, noble metal nanoparticles (Au, Ag, and Pt) can strongly absorb visible light owing to their localized surface plasmon resonance (SPR) from the collective oscillation of the surface electrons and they exhibit a great potential to extend the light-absorption range of semiconductors [86]. Under visible light irradiation, electrons from noble metals can transfer to the conduction band of ZnO due to the surface plasmon resonance effect, increasing the number of reactive electrons in the conduction band of ZnO which participate in the generation of superoxide radical anions to decompose pollutants (Figure 1.3 b) [66]. Hence, ZnO coupling with noble metal is an effective strategy to increase PA of a photocatalyst.

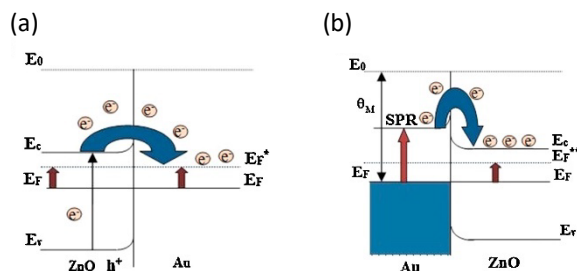


Figure 1.3. Band alignment of electron transfer mechanism of ZnO/Au composite under (a) UV light irradiation and (b) Visible light irradiation [66].

To date, the PA of ZnO/noble metal composites have been studied in the form of powder [63-73] and nanostructures fixed on a substrate [74-84]. The results on PA of ZnO coupling with different noble metals are shown in Table 1.2, Appendix 2.

The powdery form of ZnO/noble metal composites, which is a mixture of ZnO NPs and noble metal NPs, has been fabricated by either one-step [63-70, 72] or two-step [71, 73] solution-based deposition methods. In one-step approach, the precursors for preparing ZnO and noble metal are mixed in one solution for the deposition of ZnO/noble metal NPs by using chemical deposition methods such as spray pyrolysis [64, 70], hydrothermal [65], solvothermal [69, 72], combustion [63], and precipitation in solution [66-68]. In two-step approach, ZnO is firstly prepared by solution-based chemical deposition methods such as hydrothermal growth [71, 73], followed by a deposition of noble metals on their surfaces. Noble metal NPs onto ZnO NPs are mostly prepared by precipitation in solution [73] and photodeposition methods [71].

ZnO/noble metal composites in powdery form including ZnO/Au, ZnO/Ag, ZnO/Pd, ZnO/Pt, and ZnO/Rh have been studied for their PA by degrading various pollutants such as MO, MB, RhB, phenol, IC, AO II [63-73]. All studies revealed that the incorporation of noble metal such as Au, Ag, Pd, and Pt enhances the PA of ZnO NPs [63-73].

For hydrothermally grown ZnO NPs with Ag, Pd, and Pt, 96% AO II degradation efficiency was achieved by ZnO/Pd NPs under UV light in 300 min, compared to 92% from ZnO/Ag NPs, 78% from ZnO/Pt NPs, and 70% from pristine ZnO NPs [73]. For ZnO/Au NPs prepared by precipitation in solution, the MO degradation efficiency was 96% under UV light in 160 min [67] and 75% under visible light in 200 min [66], being 20% and 60% higher than pristine ZnO NPs, respectively. For the MB degradation under UV light, sprayed ZnO/Pt NPs degraded 55% in 60 min in comparison to 54% from ZnO NPs [70]; ZnO/Ag NPs prepared by precipitation in solution degraded 97% in 15 min compared to 65% from ZnO NPs [68]; hydrothermally grown ZnO/Au NPs degraded 96% in 140 min in comparison to 15% from ZnO NPs [65].

ZnO/noble metal NPs possessed higher PA than ZnO NPs. However, its severe drawbacks such as particle aggregation, difficulty of separation of photocatalyst from aqueous medium, and poor reusability limit its development and wide range usage [87]. In particular, particle aggregation not only decreases its surface area but also reduces visible-light response, resulting in poor photocatalytic performance [87]. For this reason, photocatalysts immobilized on substrates is an alternative way to overcome those drawbacks.

To date, the ZnO/noble metal composites fixed on substrates have been mainly studied in two forms which are ZnO thin film composites with noble metals such as Ag

[75] and Au [74], and ZnO_{NR} decorated by noble metal NPs such as Ag [81, 82], Pt [83, 84], and Au [76-80, 88].

For the deposition of ZnO/noble metal thin film composites, sol-gel spin coating was the mostly used method [74, 75]. For the deposition of ZnO_{NR} decorated by noble metal NPs, ZnO nanorods were firstly deposited by chemical deposition methods such as chemical bath deposition [81], hydrothermal growth [76-78, 82-84], electrodeposition [79], and chemical vapor deposition [80]. In the second step, the noble metal nanoparticles are deposited on the surface of ZnO_{NR} by chemical solution methods such as photodeposition [81], hydrothermal growth [83], precipitation in solution [76-78, 82, 84], and physical deposition method such as magnetron sputtering [79].

In the form of thin film composites, Ag and Au have mainly been used to improve the PA of ZnO (Table 1.2, Appendix 2). For example, ZnO/Ag thin film composites prepared by sol-gel spin coating possessed 30% IC degradation efficiency under UV-Vis irradiation in 300 min in comparison to 18% from ZnO film [75]. While ZnO/Au film exhibited 94% MO degradation efficiency under sunlight in 150 min compared to 61% from ZnO film [74].

Majority of the studies were mainly focused on the form of ZnO_{NR} decorated by noble metal NPs due to the higher surface area of ZnO_{NR}. Under UV light, ZnO_{NR}/Pt on Zn foil degraded 62% RhB in 12 min in comparison to 37% from bare ZnO_{NR} [83], ZnO_{NR}/Au on Si substrate degraded 91% RhB in 90 min compared to 27% from bare ZnO_{NR} [76]. For the degradation of MB by ZnO_{NR}/Ag on glass, 49% degradation efficiency was achieved under UV light in 100 min compared to 36% from bare ZnO_{NR} and 65% degradation efficiency was achieved under visible light in 43 min, being 5% higher than ZnO_{NR} [82]. However, ZnO_{NR}/Au possessed MO degradation efficiency of ca. 90-100% under UV light in 180-240 min, compared to ca. 15-70% from bare ZnO_{NR} [77-80].

Among noble metals, Ag [68, 69, 73, 75, 81, 82] and Au [63-67, 74, 76-80] are the mostly used for ZnO to improve its photocatalytic activity. Although Ag is cheaper, Au has a work function of 5.1 eV, which is higher than the work function of Ag (4.3 eV), resulting in a higher Schottky barrier height of ZnO/Au. A higher Schottky barrier is more beneficial for the separation of photogenerated electrons and holes. In addition, the surface plasmon effect of Au and Ag usually occurs in the spectral range of 500-600 nm and 400-500 nm, respectively [89, 90]. Therefore, Au is a more effective coupling metal for enhancing the PA of ZnO under visible light. To date, the reported techniques for the deposition of Au NPs on ZnO_{NR} are including precipitation in solution [76-78], magnetron sputtering [79], and photodeposition [80]. HAuCl₄ is the mostly used precursor for the synthesis of Au NPs on ZnO_{NR} [76-78, 80]. Spin coating method, being a simple and low-cost technique, has not been used to synthesize Au NPs from HAuCl₄ solution upon heat treatment on the surface of ZnO_{NR} up to now.

1.2.4 ZnO heterostructures based photocatalysts

In general, a heterojunction is defined as the interface between two different semiconductors with unequal bandgaps [91].

The formation of p-n heterojunction between p-type and n-type semiconductors is an effective way to separate photogenerated electron-hole pairs in order to increase the PA of photocatalysts [92-107]. In general, when the p- and n-type semiconductors are in contact, they form a p-n heterojunction with a space-charge region at the interfaces due to the diffusion of electrons and holes, and thus create a built-in electrical potential (Figure 1.4) [108]. When the p-n heterojunction is irradiated by photons with energy

higher or equal to the bandgaps of the photocatalysts, the photogenerated electron-hole pairs can be quickly separated by the built-in electric field within the space charge region [108]. Driven by the electric field, the electrons are transferred to the conduction band of the n-type semiconductors and the holes to the valence band of the p-type semiconductors [108]. Thus, the effective charge separation by p-n junction will enhance the photocatalytic performance of heterojunction photocatalyst.

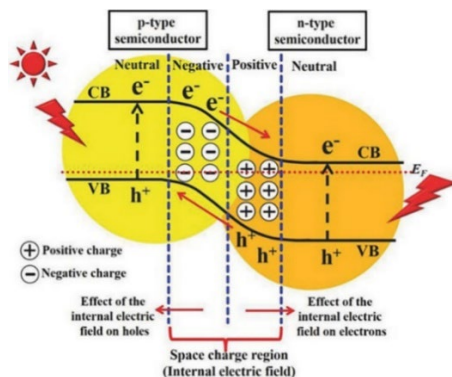


Figure 1.4. Schematic illustration of electron-hole pairs separation in p-n heterojunction under light irradiation [91].

The most widely used p-type metal oxide semiconductors coupling with ZnO are Cu₂O [92, 102, 103], CuO [93, 104-106], and NiO [94-100, 107]. The results on the PA by ZnO heterostructures based photocatalysts are presented in Table 1.3, Appendix 2.

ZnO heterostructures are mainly studied in powdery form [92-97]. For example, hydrothermally grown ZnO/Cu₂O NPs degraded 99% MO under visible light in 120 min, compared to 30% from Cu₂O NPs [92]. ZnO/CuO NPs possessed 78% phenol degradation efficiency under visible light in 180 min in comparison to 40% from ZnO NPs and 20% from CuO NPs [93]. For ZnO/NiO NPs prepared by precipitation in solution, 90% RhB was degraded under UV light in 200 min in comparison to 20% from NiO NPs and 80% from ZnO NPs [95], 100% MO was decomposed by ZnO/NiO NPs in comparison to 10% from NiO NPs and 40% from ZnO NPs [96], 72% MB was degraded by ZnO/NiO NPs under UV light in 80 min compared to 54% for ZnO NPs [97].

In addition to ZnO/NiO nanoparticles, it has been reported that ZnO/NiO nanofibers prepared by electrospinning exhibited 100% degradation efficiency toward MB under visible light in 180 min [99] and 100% degradation efficiency towards RhB under UV light in 50 min [100], being 2.5 times higher than that from NiO nanofibers.

Although ZnO heterostructures in the form of nanoparticle and nanofiber showed high degradation efficiencies compared to their individual components, it is difficult to separate powders from water medium, as already discussed hereinabove. For this reason, fixing ZnO heterostructures on substrates would be a way for fabrication of an efficient photocatalyst. ZnO heterostructures immobilized on substrates such as ZnO/Cu₂O, ZnO/CuO and ZnO/NiO heterostructures have been mainly studied in the form of nanorod layers [102-107]. It has been reported that 90% MO degradation efficiency was achieved by ZnO_{NR}/Cu₂O [102] and ZnO_{NR}/CuO [104] heterostructures under visible light, being more than 70% higher than that from ZnO_{NR}. ZnO_{NR}/CuO heterostructure degraded 78% MB under UV light [105] and 72% under visible light [106] in 180 min, being ca. 30% higher than that from ZnO_{NR}.

The PA of ZnO_{NR}/NiO heterostructures on substrates has been investigated only in one article so far [107]. In this study, the NiO shell was sputtered onto hydrothermally grown ZnO_{NR} and the degradation efficiency towards RhB was 67% by ZnO_{NR}/NiO core-shell heterostructure in comparison to 65% by bare ZnO_{NR} under UV light in 180 min [107]. Nonetheless, studies on optimization of NiO shell properties to improve the PA of ZnO_{NR}/NiO core-shell heterostructure are missing in the literature. For instance, the effect of deposition temperature and thickness of NiO shell on the PA of ZnO_{NR}/NiO core-shell heterostructure has not been studied yet.

To summarize, ZnO coupling with other semiconductors to form a heterojunction is an effective way to suppress the recombination of photogenerated electron-hole pairs, thereby increasing its PA.

1.2.5 Methods for synthesis of ZnO nanorods

Chemical deposition methods

Chemical bath deposition

The growth of ZnO nanorods by chemical bath deposition is usually conducted by immersing a substrate into an aqueous solution with zinc precursor and pH buffer at relatively low temperatures (≤ 100 °C) [62, 109, 110]. Prior to the nanorods growth, ZnO seed layer is usually prepared on the substrates to initiate the growth of well-aligned ZnO nanorods [111]. The most frequently used precursors to grow ZnO nanorods by CBD are Zn(NO₃)₂ and Zn(CH₃COO)₂ [111-116]. Precursor concentration [112], reaction time [111-116], and pH of the solution [115] have been reported to affect the growth and final properties of ZnO nanorods. The parameters listed above should be carefully optimized to obtain ZnO nanorods with possibly high aspect ratio for efficient degradation of pollutants. For example, decrease in ZnO aspect ratio from 13.0 to 8.3 decreases the MO degradation efficiency from 94 to 54% in 3h under UV irradiation [111]. The disadvantage of this method for the production of ZnO nanorods on substrates is a relatively long reaction time (≥ 4 h) [111, 112].

Hydrothermal method

ZnO nanorods growth by hydrothermal method is usually carried out in a sealed vessel containing an aqueous solution of zinc salt and pH buffer, the process temperatures are varied in the range of 100-250 °C, vapor pressures are between 0.3 and 3 MPa [59-61, 117]. The need of autoclave is mentioned to be a disadvantages of this method compared to CBD [118], although shorter process time is a clear advantage. The literature summary on hydrothermally grown ZnO nanorods will be introduced in subsection- "1.2.6 ZnO nanorods by hydrothermal method".

Electrodeposition

Electrodeposition of ZnO nanorods is based on the generation of OH⁻ ions at the surface of working electrode by electrochemical reduction of O₂, NO₃⁻, or H₂O₂ in aqueous solution with zinc salt, followed by precipitation of Zn(OH)₂ and its dehydration to ZnO [119-122]. ZnCl₂ and Zn(NO₃)₂ are the most frequently used precursors to grow ZnO nanorods by electrodeposition [119-122]. The O₂ gas is usually bubbled in the precursor solution to provide oxygen [119-122]. Precise control of the deposition parameters such as voltage [121], current [123], bath temperature [121], precursor concentration [121], and deposition time [122] are critical to get ZnO nanorod structures. For instance, by

changing the deposition voltage from 1.5 to 4V, the rods have a regular rod structure at 2.5V, then collapsed at 3V [121]. The disadvantage of this method is the need of using conducting substrates [119-122].

Chemical spray pyrolysis

Sprayed ZnO nanorods on substrates were firstly fabricated at Laboratory of Thin Films Chemical Technologies, TalTech, in 2006 [124]. ZnCl₂ is the mostly used precursor to deposit sprayed ZnO_{NR} [8, 124-126]. To get elongated rod-like ZnO crystals, zinc precursor solution is usually sprayed at elevated temperature (above 500 °C) [8, 124-126]. Both the deposition temperature and precursor concentration have been reported to influence the growth of ZnO_{NR} [124]. For instance, increasing the deposition temperature from 400 to 560 °C while fixing the ZnCl₂ precursor concentration to 0.1 M, the morphology of deposited ZnO changed from plate-like to rod-like structure [124]. By increasing the ZnCl₂ precursor concentration from 0.05 to 0.2 M while keeping the deposition temperature at 560 °C, the aspect ratio decreased from ca. 15 to ca. 5 [124]. It has been also reported that the sprayed ZnO nanorods prepared by using 0.05 M ZnCl₂ aqueous solution at 550 °C degraded 50% doxycycline under UV light in 4h [8]. The disadvantage of this method for synthesis of ZnO nanorods is the relatively high deposition temperature above 500 °C [8, 124-126].

Physical deposition methods

Vapor-liquid-solid growth

ZnO nanorods deposition by vapor-liquid-solid growth usually takes place via the vaporized mixture of ZnO powders and graphite on an Au-coated Si substrate at growth temperatures of 800-900 °C [127-129]. It has been reported that the ZnO nanorods can be very well vertically aligned if grown on ZnO seed layer along with Au catalyst layer [128]. However, no PA of ZnO nanorods prepared by vapor-liquid-solid growth has been reported yet. The reason behind this might be the high temperature for growing ZnO nanorods, which is not cost-effective and inappropriate surface properties for PA.

Magnetron sputtering

The deposition of ZnO nanorods has been achieved by sputtering metallic zinc target under oxygen atmosphere at high temperature (300-700 °C) [130-132]. It has been reported that the growth temperature controls the morphology of deposited ZnO nanostructures [130]. The deposited ZnO nanostructures exhibited vertically aligned nanorods only when the growth temperature is above 700 °C, below this temperature a film forms [130]. It has also been reported that the sputtered ZnO nanorods degraded 60% MB under solar light in 60 min [133]. The disadvantage of this method for synthesis of ZnO nanorods is the high cost of apparatus and high deposition temperature.

Pulsed laser deposition

The deposition of ZnO nanorods has also been obtained by pulsed laser deposition method, in which a high-power pulsed laser beam bombards ZnO target to generate plasma plume to the heated substrate at high temperature and under vacuum pressure [134, 135]. ZnO nanorods with diameter of 500-700 nm and the length of ca. 1 μm have been fabricated at substrate temperature of 500 °C and background pressure of 10⁻⁶ Pa [135]. The disadvantage of this method for synthesis of ZnO nanorods is also the high cost due to the expensive vacuum equipment and relatively high deposition temperature.

To summarize, the photocatalytic materials should be produced by low-cost technologies, otherwise semiconductor photocatalysts are not competitive in this field. Compared to physical methods, wet chemical routes are more simple with lower cost, the morphology of ZnO could be easily controlled by manipulating the experimental parameters such as precursor, type of solvent, and reaction conditions [4]. Hence, ZnO nanorods on substrates for photocatalysis are usually fabricated by wet chemical routes such as hydrothermal growth [117], chemical bath deposition [109], electrodeposition [119], and chemical spray pyrolysis [124]. Among these methods, hydrothermal growth is the mostly used preparation technique to grow ZnO nanorods due to its simplicity, cost-effectiveness and ability to produce hydroxyl-group rich ZnO nanorods enabling high degradation efficiencies [117].

1.2.6 ZnO nanorods by hydrothermal method

The general setup of hydrothermal processing is shown in Figure 1.5. It consists of an autoclave (1) and a regulator (2) for controlling the temperature.

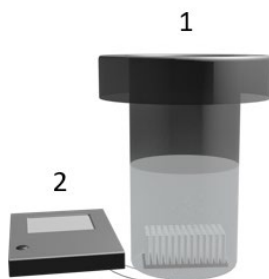
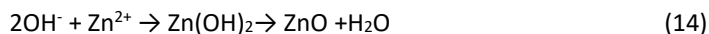
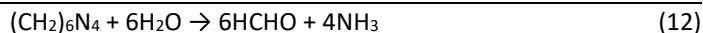


Figure 1.5 Sketch of hydrothermal deposition set-up.

ZnO with various morphologies such as nanoplates, nanoneedles, nanorods, and nanoflowers has been successfully fabricated by hydrothermal method [117].

Zinc nitrate is the most frequently used precursor for hydrothermally grown ZnO nanorods and hexamethylenetetramine (HMT, $(\text{CH}_2)_6\text{N}_4$) is typically used as a pH buffer, also to release hydroxyl ions that react with Zn^{2+} ions to form $\text{Zn}(\text{OH})_2$, ZnO forms thereupon [117]. The formation of ZnO can be summarized by the following equations [117]:



To align ZnO nanorods, ZnO seed layer with good uniformity and homogeneity is usually used prior to the deposition of ZnO nanorods in order to grow ZnO nanorods elongated, vertically standing on a substrate [136]. In addition, factors such as precursor concentration [137], deposition temperature [138], and deposition time [61, 139, 140] influence the growth of ZnO nanorods by hydrothermal method. Precise control of these factors is critical to prepare ZnO nanorods with desired properties [141, 142].

1.3 Overview of NiO photocatalysts

1.3.1 Main properties and applications of NiO

Nickel (II) oxide with the formula of NiO is the principle oxide of nickel. It possesses cubic structure (Figure 1.6) and wide direct bandgap of 3.0-4.3 eV depending on the preparation techniques [143-146]. It also has a good thermal and chemical stability [146]. Non-stoichiometric NiO is an intrinsic p-type semiconductor due to Ni vacancies or oxygen interstitials [146]. Although stoichiometric NiO is an insulator with the resistivity in the order of $10^{13} \Omega \cdot \text{cm}$, the resistivity of NiO can be lowered by increasing the concentration of Ni^{3+} ions or doping with monovalent atoms such as Li, Na, K [147, 148]. Stoichiometric NiO appears in a pale green color, while non-stoichiometric NiO can be gray or dark color determined by the ratio of $\text{Ni}^{3+}/\text{Ni}^{2+}$ [149].

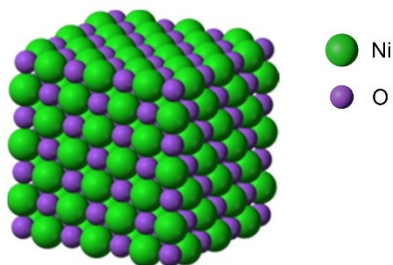


Figure 1.6. Face-centered cubic structure of NiO [146].

NiO has a range of applications such as hole transporting layers in thin film solar cells [150], electrodes in optoelectronic devices [151], a component in nickel-iron battery [152], smart windows [153], sensors [154], UV-photodetector [155], supercapacitors [156], and photocatalysts [157].

1.3.2 NiO as a photocatalyst

NiO has also been used as a photocatalyst for water and wastewater treatment due to its low cost, high chemical stability, and ability to degrade organic pollutants such as methyl orange [158-161], methylene blue [162, 163], rhodamine B [164, 165], methyl green [166], and phenol [167, 168] under UV or visible light irradiation. The results on studies focused on PA of NiO are summarized in Table 1.4. NiO has been mainly studied in the form of nanoparticles [158-164, 167] and thin-film on substrates [165, 166, 168-170].

Hydrothermal method [162], combustion [158], precipitation in solution [159] are the main methods used to deposit NiO NPs, whereas thermal decomposition [169], DC magnetron sputtering [166], pulsed laser deposition [165], electrodeposition [168] and pneumatic spray pyrolysis [170] are used for NiO films deposition.

NiO nanoparticles possess high PA because of their high surface area. For the degradation of MO, rod-like NiO NPs prepared by combustion method degraded 80% under visible light in 50 min [158]; plate-like and flower-like NiO NPs prepared by precipitation in solution degraded 38% under visible light in 110 min [159] and 49% under UV light in 120 min [161], respectively; hydrothermally grown plate-like NiO NPs decomposed 53% under UV light in 120 min [160]. For the degradation of MB, hydrothermally grown sphere-like [162] and plate-like [163] NiO NPs degraded 64% under UV-Vis light in 180 min and 99% under visible light in 20 min, respectively.

NiO films usually possess lower PA than NPs. For instance, NiO film prepared by pulsed laser deposition exhibited 30% RhB degradation efficiency under UV light in 60 min [165], compared to 70% from plate-like NiO NPs [164]. Electrodeposited NiO film degraded 45% phenol under UV light in 60 min [168], compared to 97% from sphere-like NiO NPs [167]. Sprayed NiO film possessed 90% MB degradation efficiency under UV light in 90 min [170] in comparison to 99% from hydrothermally grown NiO NPs under visible light in 20 min [163].

Although the degradation efficiency of the NiO films on substrates is lower than that in powdery form, the film is beneficial for separation of the catalyst from polluted water as already discussed in previous paragraphs.

Besides, NiO could be used to form n-p heterostructure based photocatalysts such as ZnO/NiO [94-100, 107] and TiO₂/NiO [171-174]. For instance, ZnO/NiO NPs degraded under sunlight 90% MB in 60 min, compared to 50% from bare ZnO NPs. TiO₂/NiO hybrid exhibited nearly 100% MB degradation efficiency under visible light in 100 min, being 4 times higher than bare TiO₂ nanosheet [171].

To summarize, NiO as a photocatalyst has shown potential to mineralize various pollutants in water. Its low material cost, high chemical stability and photostability, as well as tunable bandgap make NiO an attractive material in photocatalytic applications.

1.3.3 Methods for synthesis of NiO films

Chemical deposition methods

Sol-gel spin coating

NiO film can be prepared by sol-gel spin coating method via dropping an inorganic colloidal suspension of nickel precursor [175] onto a substrate and spinning to obtain a thin layer, followed by annealing at elevated temperature (≥ 300 °C) [176-179]. Nickel acetate is the mostly used precursor to deposit NiO film [176-179]. The use of sol-gel spin coated NiO film for photocatalytic applications is a single case [179]. In this study, NiO film degraded 100% KMnO₄ in aqueous solution under UV irradiation in 1h [179].

Electrodeposition

NiO film is usually electrodeposited on transparent conducting oxide (such as ITO, FTO) coated glass substrates by the redox reaction taking place in nickel salt aqueous solution for the generation of Ni(OH)₂ and followed by the formation of NiO [180-183]. Nickel nitrate [180], nickel sulfate [181, 182], nickel chloride [183] are the mostly used precursors for the deposition of NiO film. It has been reported that uniform NiO film with fine grained structure was electrodeposited on ITO/glass substrate by using nickel sulfate precursor and applied potential at -1.1 V/SCE [181]. However, the surface of NiO film is covered with big grains with diameter of 300-500 nm and may contain cracks when the film was electrodeposited on FTO/glass using NiCl₂ precursor and applied potential at 4.2 V/SCE [183]. Porous NiO films have also been deposited by pulsed electrodeposition using nickel sulfate precursor [181, 182]. No PA study of electrodeposited NiO films has been reported yet.

Chemical spray pyrolysis

NiO film on a substrate prepared by chemical spray pyrolysis has been deposited via spraying of an aqueous or alcoholic solution containing a nickel salt onto a preheated substrate (300-500 °C) [146]. It has been reported that sprayed NiO film possess 90% MB degradation efficiency under UV light in 180 min [170]. More detailed description of

properties of sprayed NiO films is presented in subsection “1.3.4 NiO films by chemical spray pyrolysis”.

Physical deposition methods

Magnetron sputtering

NiO film can be deposited by DC or RF magnetron sputtering via sputtering Ni or NiO target under vacuum atmosphere [166, 184, 185]. The sputtered NiO film is usually dense and uniform [166, 184, 185]. Wang et al. [185] reported that the crystallite size of sputtered NiO film increased from 7 to 89 nm by increasing the deposition temperature from 30 to 450 °C. Al-Ghamdi et al. [166] sputtered NiO film with 30-80 nm thickness by increasing deposition time and the 30 nm-thick film exhibited 70% MG degradation efficiency under UV-B irradiation in 2h.

Pulsed laser deposition

NiO film on a substrate has been fabricated by pulsed laser deposition technique via irradiating a nickel target by using a pulsed laser beam in a vacuum chamber at elevated temperature (100-400 °C) [186]. It has been reported that the crystallite size along (200) orientation of NiO film prepared by pulsed laser deposition is in a range of 19-32 nm when increasing the deposition temperature from RT to 400 °C. It has also been reported that NiO film prepared by pulsed laser deposition exhibited 30% RhB degradation efficiency under UV-Vis light in 60 min [165].

It is generally accepted that photocatalysts produced by wet chemical deposition methods have higher PA compared to those fabricated by physical deposition methods due to the fact that photocatalysts synthesized by wet chemical deposition methods contain more hydroxyl groups on the film surface [165, 170].

1.3.4 NiO films by chemical spray pyrolysis

Spray pyrolysis is a process in which a thin film is deposited by spraying a precursor solution on a heated surface, where the precursor thermally decomposes to form thermally more stable compound [187]. Depending on the atomization type, spray pyrolysis techniques have been mainly divided into pneumatic, ultrasonic, and electrostatic spray pyrolysis [188].

NiO films by pneumatic spray pyrolysis

A typical pneumatic spray pyrolysis (PSP) set-up is shown in Figure 1.7 and consists of a precursor solution container (1), pneumatic nebulizer (2) that generates fine droplets, substrate heater (3), temperature controller (4), air compressor (5) to deliver carrier gas to the system and rotameter (6) [188].

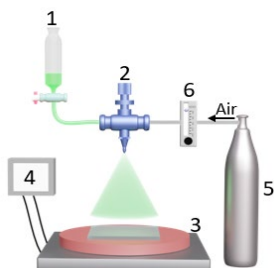


Figure 1.7. Set-up of pneumatic spray pyrolysis [188].

Pneumatic nebulizers produce droplets by expanding a pressurized liquid, these nebulizers have a high droplet output of large sizes around 50 μm , and the droplet sizes and size distribution are difficult to control [189].

The properties of the NiO films synthesized by pneumatic spray pyrolysis methods are highly influenced by the precursor and deposition parameters such as substrate temperature, solution concentration, solvent, also substrate type, solution spray rate, carrier gas flow rate, and distance between the nozzle and substrate [188, 190].

Most commonly used precursors for NiO films by pneumatic spray are nickel chloride [191, 192], nickel nitrate [192, 193], nickel acetate [147, 192, 194] and nickel acetylacetonate [145, 195]. The precursor type largely affects the crystallinity and homogeneity of the films. NiO in films deposited at substrate temperature (T_s) of 450 $^{\circ}\text{C}$ from chloride precursor possessed larger crystallite size ($D_{(111)}=57$ nm) than in case of using acetate ($D_{(111)}=10$ nm) and nitrate precursors ($D_{(111)}=45$ nm) [192]. Meanwhile, the RMS roughness of the film produced from chloride precursor was 90 nm compared to 31 nm and 16 nm for the film produced from acetate and nitrate precursors, respectively. It has been reported that NiO films deposited at $T_s=450$ $^{\circ}\text{C}$ from nickel acetylacetonate in alcoholic solution (ethanol:water=9:1, vol. ratio) possessed NiO crystallite size of 19 nm ($D_{(111)}$) and film RMS roughness of 7 nm [145]. It has also been reported that NiO films deposited from chloride precursor were porous and contained chlorine residues [191].

The deposition temperature is one of the most important parameters controlling the film structural, optical and electrical properties [146]. To date, only few studies have focused on the effect of deposition temperature on NiO film properties [147, 191-193]. NiO films by spray pyrolysis are usually deposited at $T_s=300-500$ $^{\circ}\text{C}$ [147, 191-193]. In general, the crystallite size of NiO increases with increasing the deposition temperature independent of used precursor. For instance, the crystallite size of NiO in films deposited from chloride precursor increased from 30 nm to 35 nm by increasing the T_s from 300 $^{\circ}\text{C}$ to 375 $^{\circ}\text{C}$ [191]. While the NiO crystallite size in film produced from acetate precursor increased from 6 nm to 10 nm with increasing the T_s from 400 $^{\circ}\text{C}$ to 500 $^{\circ}\text{C}$ [147].

Deposition temperature also influences the bandgap of NiO films. For the films produced from aqueous solution, the bandgap of NiO film produced from nitrate precursor increased from 3.1 eV to 4.0 eV with increasing the T_s from 350 $^{\circ}\text{C}$ to 390 $^{\circ}\text{C}$ [193]. The bandgap of NiO films prepared from chloride precursor was found to be in the range of 3.04-3.28 eV when the film deposited in the temperature range of $T_s=425-500$ $^{\circ}\text{C}$ [196]. However, the bandgap of NiO films prepared from acetate precursor decreased from 3.46 eV to 3.17 eV with increasing the T_s from 275 $^{\circ}\text{C}$ to 350 $^{\circ}\text{C}$ [194].

The solvent type also influences the properties of NiO films. The films prepared by spraying alcoholic solutions are usually thinner and smoother compared to those obtained by spraying aqueous solutions [147]. Up to now, only one study has shortly compared NiO films properties obtained from aqueous and alcoholic solution [147].

Little effort has been devoted to study the surface chemical composition of sprayed NiO films. To date, the surface chemical composition has been studied for sprayed NiO films deposited at one fixed temperature of 350 [195] and 450 $^{\circ}\text{C}$ [192, 197]. Goma et al. [192] compared the surface chemical composition of sprayed NiO films prepared from different precursors while fixing the deposition temperature at 450 $^{\circ}\text{C}$. It was found that NiO film prepared from acetate precursor has higher amount of surface carbon species and lower ratio of Ni/O compared to the films deposited from nitrate and chloride

precursors. Chan et al. [197] sprayed NiO film at $T_s=450\text{ }^\circ\text{C}$ from acetylacetonate precursor and discovered that the surface of NiO film contains not only NiO as a main phase, but also Ni_2O_3 phases. Reguig et al. [195] sprayed NiO film by using chloride precursor at $T_s=350\text{ }^\circ\text{C}$ and showed that in addition to NiO and Ni_2O_3 phases the surface of NiO film also contains $\text{Ni}(\text{OH})_2$ phase. There are no studies published on the effect of deposition temperature on the surface chemical composition or photocatalytic activity of NiO films fabricated by spray pyrolysis.

NiO films by ultrasonic spray pyrolysis

Ultrasonic spray pyrolysis (USP) is a more powerful spray technique for deposition of thin films with controlled thickness and lower surface roughness compared to PSP. A typical USP set-up is shown in Figure 1.8 and consists of an air compressor (1) to deliver carrier gas, ultrasonic nebulizer (2) to generate the droplets, temperature controller (3), pipe (4) to transport the droplets to the hot plate, substrate heater (5) to transport droplets to hot place. USP employs an ultrasonic nebulizer that generates ultrasound to break the liquid into droplets. The sizes of the droplets depend on the ultrasound frequency [198]. It has been reported that droplets in a size distribution from 1 to 15 μm are created with a high-frequency ultrasound (0.5-3 MHz) [199]. Hence, ultrasonic nebulizer is able to generate smaller, more stable and uniform in size droplets compared to pneumatic nebulizer. USP can be used for deposition of thinner coatings with better homogeneity, uniformity, and film purity compared to PSP.

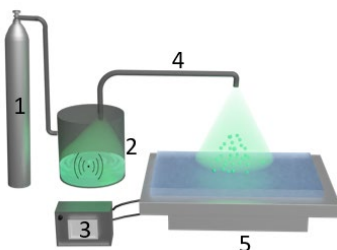


Figure 1.8. Set-up of ultrasonic spray pyrolysis.

There are very few studies related to NiO films deposition by USP up to now [197, 200-203]. Ultrasonically sprayed NiO films have been used as a hole transporting layer in solar cell [201], electrochromic devices [202, 203], and as p-type photocathode [197]. For the deposition of NiO films, the deposition temperature was varied from 300 $^\circ\text{C}$ to 450 $^\circ\text{C}$ [197, 200-203], and nickel nitrate [200-203] and nickel acetylacetonate [197] were used as precursor materials. It has been reported that crystalline NiO film was deposited at 360 $^\circ\text{C}$ on a Si substrate by using a nitrate precursor in solution (water: ethanol= 1:1) [200]. Scheideler et al. [201] deposited NiO_x film at 300 $^\circ\text{C}$ on a ITO/glass substrate by spraying a nitrate precursor in aqueous solution and used it as a hole transporting layer for perovskite solar cell to improve its power conversion efficiency [201]. Tenent et al. [202] and Denayer et al. [203] prepared Li doped NiO film by spraying nickel nitrate with 5 wt% lithium nitrate in aqueous solution at 330 $^\circ\text{C}$ and 350 $^\circ\text{C}$, respectively, for electrochromic applications.

However, ultrasonically sprayed NiO film produced from nickel acetylacetonate precursor has been rarely reported [197]. Chan et al. [197] deposited homogeneous and uniform NiO films by spraying nickel acetylacetonate in acetonitrile at 450 $^\circ\text{C}$, films were used for CdS-sensitized photocathodes. Nonetheless, no study has been found on the

investigation of deposition temperature on properties of ultrasonically sprayed NiO films using nickel acetylacetonate as a precursor material. Furthermore, no study has reported the PA of ultrasonically sprayed NiO nor on its application in heterostructured photocatalyst.

1.4 Summary of literature overview and aim of study

Photocatalysts are promising materials to deal with environmental pollution. Ideal photocatalytic materials must be photoactive, abundant, cheap, nontoxic, and easy to synthesize. So far, semiconductors such as TiO₂, ZnO, NiO, CdS, and ZnS have been used as photocatalysts for water and wastewater treatment. Among these semiconductors, TiO₂ is the mostly studied photocatalyst due to its excellent PA, nontoxicity, and chemical stability.

In addition to TiO₂, ZnO is also considered as a promising photocatalyst due to its high PA, nontoxicity, and various morphologies. So far, ZnO nanoparticles are the mostly studied photocatalysts due to their high surface area. However, photocatalysts in powder form have drawbacks such as particle agglomeration and difficulty of photocatalyst separation from aqueous medium, which in turn, may cause secondary pollution. For this reason, a more suitable approach is to immobilize photocatalysts on substrates enabling easy separation from aqueous medium. ZnO nanorod layers grown on a substrate may be one possible solution and therefore are intensely studied. ZnO nanorods could be grown by variety of physical and chemical methods, but wet chemical technique of hydrothermal growth that is a simple and low-cost method, carried out at relatively low temperatures within acceptable time frame, is proper and widely used technique to fabricate ZnO nanorod photocatalyst [58-60, 117]. ZnO based photocatalysts suffer from poor absorption of visible light and fast recombination of photoinduced electron-hole pairs, limiting their PA. To overcome these drawbacks, ZnO has been coupled with noble metals (Au, Ag, Pt) or p-type semiconductors (NiO, CuO_x) to enhance its PA.

Among noble metals coupling with ZnO, Au is the most frequently used because it is the most effective one which could potentially form the Schottky barrier with ZnO to reduce the recombination of photoinduced carriers and enhance the absorption of visible light due to the surface plasmon resonance effect [89, 90]. To date, the methods for the deposition of Au nanoparticles on the surface of ZnO_{NR} consist of precipitation in solution, magnetron sputtering, and photodeposition. HAuCl₄ is the mostly used precursor for the generation of Au nanoparticles. Spin-coating is a simple and low-cost method and has not been used to synthesize Au nanoparticles from HAuCl₄ solution upon heat treatment on the surface of ZnO_{NR} up to now.

NiO is another promising photocatalyst due to its tunable bandgap, low-cost, and high chemical stability. The PA of NiO is mostly studied in its powdery form. However, the PA of NiO films immobilized on substrate has been rarely studied. To date, the methods used for the deposition of NiO films as photocatalytic coatings include thermal decomposition, DC magnetron sputtering, pulsed laser deposition, electrodeposition, and PSP. Among these methods, PSP is a simple, low-cost method with the potential for mass production. In particular, only one study has been focused on the PA of NiO thin film deposited by PSP up to now [170]. Deposition temperature is one of the most important parameters in PSP. Nevertheless, no study has been focused on the influence of deposition temperature on the PA of NiO film deposited by PSP up to now. In addition to the deposition temperature, the influence of solvent type on the properties of NiO film has only been roughly reported in one publication [147]. The correlation of surface chemical composition and PA of NiO films grown by PSP has not been reported yet.

NiO as a p-type semiconductor is also an appropriate candidate for coupling with ZnO to form a p-n heterojunction to suppress the recombination of electron-hole pairs. To date, the PA of ZnO/NiO heterostructure has been mainly studied in the form of nanopowders and nanofibers. ZnO/NiO heterostructures immobilized on a substrate are rarely studied. Deposition of NiO on ZnO nanorods to form the ZnO_{NR}/NiO core-shell heterostructure could potentially enhance the PA of ZnO_{NR}/NiO core-shell heterostructure and protect the corrosive ZnO_{NR}. However, the PA of ZnO_{NR}/NiO core-shell heterostructure has been investigated only in one study [107]. Sputtering is the only method used to deposit NiO shell on ZnO_{NR} [107]. Ultrasonic spray pyrolysis is a simple and reliable method to deposit thin coatings with controlled thickness and uniformity. To date, USP has not been used for the deposition of NiO shell onto ZnO_{NR} to form ZnO_{NR}/NiO core-shell heterostructure. Although metal acetylacetonates have been found the most suitable precursors for the deposition of smooth and conformal coatings of different metal oxides by USP then nickel acetylacetonate has been used as a precursor for NiO film deposition only in one study [197]. It could be assumed that NiO film deposition temperature and thickness in ZnO_{NR}/NiO core-shell heterostructure are of great significance in development of photocatalytically highly active ZnO_{NR}/NiO core-shell heterostructures. According to literature survey, there are no investigations published on this topic yet.

The formation of n-p junction of ZnO/NiO heterostructures is reported only relying on the PA measurement results rather than actual energy parameters measured by physical characterization methods [94, 96, 204-206]. Therefore, the ZnO/NiO n-p heterojunction formation is required to be confirmed directly applying necessary physical characterization methods.

The aim of this dissertation is to develop the strategies for the synthesis of ZnO nanorod and NiO film based materials as efficient photocatalytic coatings on glass substrates by low-cost chemical solution methods such as hydrothermal growth and chemical spray pyrolysis. To reach the aim of the thesis, the following tasks are outlined:

1. To synthesize ZnO_{NR}/Au composite via spin coating of HAuCl₄ solutions on the surface of hydrothermally grown ZnO_{NR} to form Au nanoparticles upon heat treatment and to study the surface treatment effect on the structural, optical properties, surface chemical composition of ZnO_{NR}, and to study the photocatalytic activity to degrade MO by both ZnO_{NR} and ZnO_{NR}/Au composite under UV and visible light irradiation.

2. To synthesize NiO films by PSP method using nickel acetate as precursor material and to study the effect of film growth temperature and solution type (aqueous or alcohol based) on the structural, optical, morphological properties and surface chemical composition of NiO film. To define the correlation between the surface chemical composition, wettability, and PA towards photocatalytic degradation of MO by sprayed NiO films.

3. To develop the strategy for synthesis of ZnO_{NR}/NiO n-p core-shell heterostructures with improved photocatalytic activity. Firstly, to synthesize NiO films by USP method using nickel acetylacetonate as precursor material and to study the effect of the deposition temperature on the structural, optical, and morphological properties of NiO films. Secondly, to determine the optimal NiO layer deposition temperature on example of ZnO/NiO n-p bilayer structure. Thirdly, to determine the optimal NiO shell thickness in ZnO_{NR}/NiO n-p heterostructure to enhance MB degradation efficiency. To characterize the n-p junction formation and the band structure with the help of advanced physical characterization techniques.

2 Experimental

2.1 Deposition of ZnO_{NR} layers, ZnO_{NR}/Au composites, NiO films, ZnO/NiO heterostructures

All the substrates were thoroughly cleaned by detergent, ethanol, and deionized water in ultrasonic bath before deposition [I-III].

2.1.1 Deposition of ZnO_{NR} layers by hydrothermal method

ZnO_{NR} layers were grown by hydrothermal method [I, III]. Soda-lime glasses covered with ZnO film as a seed layer were used as substrates for ZnO_{NR} layer growth in paper [I], whereas borosilicate glasses covered with ZnO film were used for this purpose in paper [III] (Table 2.1). ZnO films were grown by pneumatic spray pyrolysis method using 0.05 mol/L zinc acetate dihydrate (Zn(CH₃COO)₂·2H₂O, 99.9%, Sigma-Aldrich) solution, and tin bath temperature of 500 °C. To grow ZnO_{NR} layer, zinc nitrate hexahydrate (Zn(NO₃)₂·6H₂O, 99.9%, Sigma-Aldrich) and hexamethylenetetramine ((CH₂)₆N₄, 99%, Sigma-Aldrich) with a molar ratio of 1:1 were dissolved in deionized water to prepare 0.1 mol/L solution. Glass/ZnO substrate was placed into a reactor beaker that contains 40 mL of the ZnO_{NR} precursor solution. The reactor beaker was mounted into a steel autoclave and the reaction was carried out at 120 °C for 2 h (Table 2.1).

Table 2.1. Technological parameters for ZnO and NiO nanostructures deposition.

Sample	Substrate	Precursor	Method	T _s (°C) / time (h)	T _{an} (°C) / time (h)	Ref.
ZnO film	SLG BSG	Zn(CH ₃ COO) ₂ ·2H ₂ O,	PSP	500	-	[I] [III]
ZnO _{NR} layer	SLG/ZnO BSG/ZnO	Zn(NO ₃) ₂ ·6H ₂ O	HT	120/2	- 600/1	[I] [III]
ZnO _{NR} /Au composite	SLG/ZnO/ ZnO _{NR}	HAuCl ₄	SC	RT	100/0.5, 400/1	[I]
NiO film	SLG	Ni(CH ₃ COO) ₂ ·4H ₂ O	PSP	300-420	-	[II]
NiO film	BSG	Ni(C ₅ H ₇ O ₂) ₂	USP	350-500	600/1	[III]
ZnO/NiO bilayer	BSG/ZnO	Ni(C ₅ H ₇ O ₂) ₂	USP	350-500	600/1	[III]
ZnO _{NR} /NiO core-shell	BSG/ZnO/ZnO _{NR}	Ni(C ₅ H ₇ O ₂) ₂	USP	500	600/1	[III]

The detail of the technological procedures can be found in paper [I-III].

2.1.2 Deposition of Au nanoparticles on ZnO_{NR} layers

Au nanoparticles (NPs) were fabricated on ZnO_{NR} layer by spin-coating chloroauric acid (HAuCl₄, 99.9%, Sigma-Aldrich) solution in ethanol followed by drying at 100 °C for 30 min and heat treatment at 400 °C for 1h [I]. The concentrations of precursor solution were set as 0.005 mol/L, 0.01 mol/L, and 0.03 mol/L and the prepared samples were named as ZnO_{NR}/Au: 0.005, ZnO_{NR}/Au: 0.01, and ZnO_{NR}/Au: 0.03, respectively. For comparison, one additional ZnO_{NR} layer [I] was surface treated with 0.01 mol/L HCl solution. This sample was named as ZnO_{NR}/HCl: 0.01 [I].

2.1.3 Deposition of NiO and ZnO films by pneumatic spray method

NiO film was deposited on soda-lime glass by pneumatic spray method. Nickel acetate tetrahydrate ($\text{Ni}(\text{CH}_3\text{COO})_2 \cdot 4\text{H}_2\text{O}$, 99%, Sigma-Aldrich) was dissolved in deionized water and in a mixture of water and isopropanol ($\text{H}_2\text{O}:\text{isopropanol}=2:3$, vol%) to prepare 0.5 mol/L aqueous solution and alcoholic solution, respectively [II]. The pH of the prepared nickel acetate ($\text{Ni}(\text{ac})_2$) solutions was adjusted to 5 to prevent hydrolysis of precursor. The volume of spray solution was fixed to 50 mL for aqueous solution and 150 mL for alcoholic solution. The substrate temperatures were set in the range of 300 °C to 420 °C with an interval of 40 °C for both aqueous and alcoholic solutions. The distance between the nozzle and the substrate was 25 cm. The carrier gas flow rate was 8 L/min and solution spray rate was 2 mL/min.

The deposition of ZnO film for ZnO/NiO bilayer heterostructure [III] is similar to that described for ZnO film [I] on borosilicate glass in section 2.1.1.

2.1.4 Deposition of NiO film by ultrasonic spray method and preparation of ZnO/NiO bilayers and $\text{ZnO}_{\text{NR}}/\text{NiO}$ core-shell heterostructures

Nickel acetylacetonate ($\text{Ni}(\text{C}_5\text{H}_7\text{O}_2)_2$, 96%, Sigma-Aldrich) in ethanol was used as the precursor solution for the deposition of NiO films by ultrasonic spray pyrolysis (USP) method [III] (Table 2.1). The air flow to transport precursor droplets from nebulizer to hot plate was set to 8 L/min. The frequency of nebulizer was 1.7 MHz and the spray rate was 4 mL/min.

To prepare NiO film [III] on borosilicate glass, the concentration of nickel acetylacetonate ($\text{Ni}(\text{acac})_2$) solution was set to 10 mM and number of spray cycles was fixed at 12 cycles. The substrate temperatures were set as 350 °C, 400 °C, 450 °C, and 500 °C.

To make ZnO/NiO bilayer heterostructure [III], NiO film was deposited onto ZnO layer at temperatures of 350 °C, 400 °C, 450 °C, and 500 °C using 10 mM $\text{Ni}(\text{acac})_2$ solution. The number of spray cycles were 6, 4, 3, and 3 for NiO grown at 350 °C, 400 °C, 450 °C, and 500 °C, respectively, to obtain NiO film with closely similar thickness (ca. 15 nm) at each temperature. The deposited ZnO/NiO bilayer heterostructures were labeled as ZnO/NiO(350), ZnO/NiO(400), ZnO/NiO(450), and ZnO/NiO(500), accordingly.

To fabricate $\text{ZnO}_{\text{NR}}/\text{NiO}$ core-shell heterostructure, NiO film was deposited onto hydrothermally grown ZnO_{NR} at 500 °C using 5 mM $\text{Ni}(\text{acac})_2$ solution [III]. The thickness of NiO film was varied by using 1, 2 and 4 spray cycles and the deposited $\text{ZnO}_{\text{NR}}/\text{NiO}$ core-shell heterostructures [III] were labeled as $\text{ZnO}_{\text{NR}}/\text{NiO}(1)$, $\text{ZnO}_{\text{NR}}/\text{NiO}(2)$, and $\text{ZnO}_{\text{NR}}/\text{NiO}(4)$, respectively.

The fabricated NiO films, ZnO_{NR} layers, ZnO/NiO bilayer and $\text{ZnO}_{\text{NR}}/\text{NiO}$ core-shell heterostructures were annealed at 600 °C in air for 1h. The annealed samples of ZnO_{NR} , $\text{ZnO}_{\text{NR}}/\text{NiO}(2)$, and $\text{ZnO}_{\text{NR}}/\text{NiO}(4)$ were named as $\text{ZnO}_{\text{NR}}\text{-600}$, $\text{ZnO}_{\text{NR}}/\text{NiO}(2)\text{-600}$, and $\text{ZnO}_{\text{NR}}/\text{NiO}(4)\text{-600}$, respectively [III].

2.2 Characterization of ZnO_{NR} layers, ZnO_{NR}/Au composites, NiO films, ZnO/NiO heterostructures

The characterization methods for ZnO_{NR}, ZnO_{NR}/Au composites, NiO films, ZnO/NiO heterostructures are summarized in Table 2.2. Detailed descriptions of different characterization methods are given in papers [I-III].

Table 2.2. Methods used for characterization of ZnO_{NR} layers, ZnO_{NR}/Au composites, NiO films, and ZnO/NiO heterostructures.

Properties	Characterization method	Apparatus	Ref.
Crystal structure, crystallite size	XRD	Rigaku Ultima IV	[I-III]
Phase composition	Raman	Horiba's LabRam HR800	[II]
Phase composition	FTIR	Perkin Elmer GX 2000	[II]
Optical transmittance, reflectance, absorbance	UV-Vis	Jasco V-670	[I-III]
Morphology, film thickness	SEM	Zeiss EVO-MA15, Zeiss HR FESEM Ultra 55	[I-III]
Wettability	Water contact angle measurement	DSA 25 (KRÜSS Instrument)	[I, II]
Surface chemical composition	XPS	Kratos Analytical AXIS Ultra DLD	[I, II]
		XPS laboratory system with nonmonochromatic X-ray source from SPECS	[III]
I-V curve	I-V measurement	AutoLab PGSTAT-30	[III]
Work function (ϕ)	KP	Ambient-pressure KP Technology SKP5050-APS02 instrument	[III]
Ionization energy (E_i)	PYS		

2.3 Characterization for the photocatalytic properties of ZnO_{NR} layers, ZnO_{NR}/Au composites, NiO films, ZnO/NiO heterostructures

The PA of ZnO_{NR} layers [I], ZnO_{NR}/Au composites [I], NiO films [III], NiO films [III], ZnO films [III], ZnO_{NR} layers [III], ZnO/NiO bilayer heterostructures [III], ZnO_{NR}/NiO core-shell heterostructures [III] was estimated by photodegradation of MO and MB in aqueous solution under UV and/or visible light irradiation. The detail of the parameters for photodegradation tests is listed in Table 2.3. The description and molecule structures of methyl orange and methylene blue are presented in Table 2.4 in Appendix 2.

Table 2.3. Parameters of photodegradation tests of samples.

Samples	Pollutant type	C ₀ (ppm)	Pollutant volume (mL)	Light source	Reaction time (min)	Ref
ZnO _{NR} layer and ZnO _{NR} /Au composite	MO	15	3	UV-A, Vis	180	[I]
NiO film		10		UV-A		[II]
NiO film, ZnO film, ZnO _{NR} layer, ZnO/NiO bilayer heterostructure, and ZnO _{NR} /NiO core-shell heterostructure	MB	10	2	UV-B		[III]

Philips mercury lamp (15 W, TL-D model, $\lambda_{\max}=365$ nm) with light intensity of 60 W/m² (270-380 nm) was used as UV-A light source, Philips Master TL-D Super 80 (15 W, $\lambda_{\max}=550$ nm) with light intensity of 160 W/m² (400-650 nm) was used as visible light source and Philips mercury lamp (36W, PL-L, $\lambda_{\max}=315$ nm) with 150 W/m² (270-380 nm) was used as UV-B light source. The concentrations of MO and MB aqueous solution were determined every 30 min in 180 min by measuring the highest absorbance intensity of MO and MB aqueous solutions at 464 nm and 660 nm, respectively, from Jasco V-670 UV-VIS-NIR spectrophotometer to compare with the recorded calibration curve of absorbance intensity vs. known dye concentrations.

The photodegradation efficiency of MO or MB was calculated from Eq. (16):

$$\eta = (C_0 - C)/C_0 \times 100\% \quad (16)$$

where η is the photodegradation efficiency (%), C₀ (ppm) is the initial concentration of the MO or MB solution before light irradiation, and C (ppm) is the concentration of the MO or MB solution after the irradiation time.

The photodegradation kinetics of MO and MB dye were estimated using Langmuir-Hinshelwood model, the first order reaction rate constant (k) was calculated from Eq. (17) [207]:

$$\ln(C_0/C) = kt \quad (17)$$

where t is the irradiation time.

3 Results and discussion

3.1 Effect of surface treatment by HAuCl_4 on photocatalytic activity of ZnO_{NR} layers

In this section, the structural, morphological, optical properties, surface chemical composition and PA of ZnO_{NR} layer and $\text{ZnO}_{\text{NR}}/\text{Au}$ composites have been investigated. The results have been published in paper [I].

3.1.1 Structural, morphological, and optical properties of bare ZnO_{NR} layers and $\text{ZnO}_{\text{NR}}/\text{Au}$ composites

XRD was used to study the crystal structure of deposited samples and to confirm the formation of Au nanoparticles (NP) on the surface of ZnO_{NR} layer. XRD patterns of ZnO_{NR} and $\text{ZnO}_{\text{NR}}/\text{Au}$: 0.03 layers are shown in Figure 3.1. The reflections at 2θ of 31.77° , 34.42° , 36.25° , 47.54° , 56.6° correspond to the (100), (002), (101), (102) and (110) planes of hexagonal wurtzite ZnO (PDF-2, 01-084-6784). The sharp and strong reflection from the (002) plane indicates the formation of highly crystalline c-axis oriented ZnO crystals on a substrate. The reflection at 2θ of 38.10° from $\text{ZnO}_{\text{NR}}/\text{Au}$: 0.03 layer belongs to the (111) plane of metallic Au with cubic structure (PDF-2, 00-066-0091), confirming the formation of Au on ZnO_{NR} . However, no reflections belonging to Au were detected by XRD from $\text{ZnO}_{\text{NR}}/\text{Au}$: 0.005 and $\text{ZnO}_{\text{NR}}/\text{Au}$: 0.01 composites.

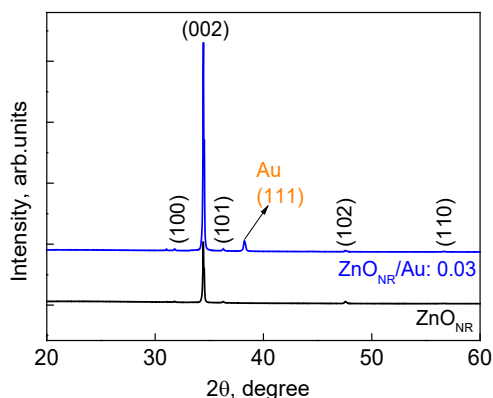


Figure 3.1. XRD patterns of ZnO_{NR} layer and $\text{ZnO}_{\text{NR}}/\text{Au}$: 0.03 composite.

Surface and cross-sectional SEM images of the ZnO_{NR} layer and $\text{ZnO}_{\text{NR}}/\text{Au}$ composite, presented in Figure 3.2, clearly showed a uniform and dense coverage of ZnO nanorods on the glass substrate. The average length of ZnO nanorods is ca. $1 \mu\text{m}$ and diameter of the nanorods varies from 50 nm to 150 nm. Au NPs on the surface of ZnO_{NR} could be clearly seen from back-scattered electron SEM images (Figure 3.2 d left) after surface treatment with 0.01 mol/L HAuCl_4 solution. The diameter of Au NPs increases from 20 nm to 60 nm when increasing the concentration of HAuCl_4 solution from 0.005 mol/L to 0.03 mol/L (Fig. 1 in [I]).

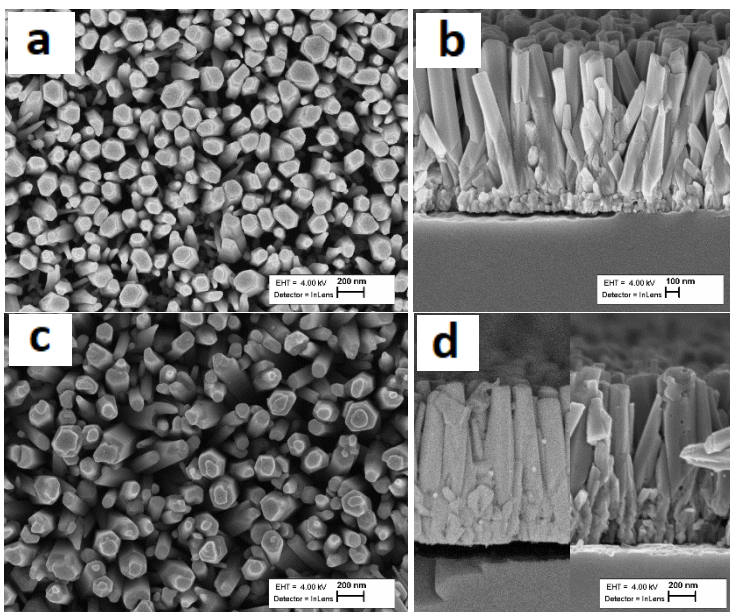


Figure 3.2. SEM images of ZnO_{NR} layer and ZnO_{NR}/Au composite: (a) surface of ZnO_{NR} , (b) cross-section of ZnO_{NR} ; (c) surface of $ZnO_{NR}/Au: 0.01$, (d) cross-section of $ZnO_{NR}/Au: 0.01$.

The absorption spectra of the ZnO_{NR} layer and ZnO_{NR}/Au composites, presented in Figure 3.3, clearly showed a difference in absorption in the spectral region of 500-600 nm. The stronger absorbance in the region of 500-600 nm from ZnO_{NR}/Au composites compared to ZnO_{NR} layer is attributed to plasmonic effect caused by Au NPs [77, 78, 85]. In addition, $ZnO_{NR}/Au: 0.03$ composites demonstrated a higher absorbance in the visible light range in comparison to $ZnO_{NR}/Au: 0.01$ and $ZnO_{NR}/Au: 0.005$ composites probably due to the larger size of Au NPs produced from a solution with higher $HAuCl_4$ concentration.

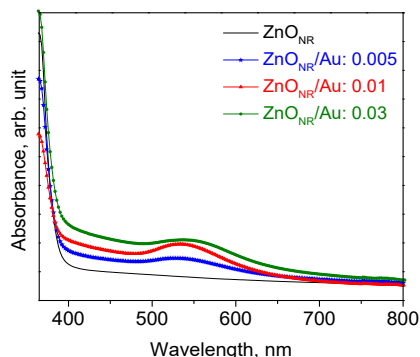


Figure 3.3. Absorption spectra of ZnO_{NR} layer and ZnO_{NR}/Au composites.

To conclude, XRD, SEM, and optical study confirmed the formation of Au NPs on ZnO_{NR} . The increased absorbance in the visible light range (500-600 nm) from ZnO_{NR}/Au composites is due to the plasmonic effect caused by Au NPs.

3.1.2 Photocatalytic activity of ZnO_{NR} layer and ZnO_{NR}/Au composites

The photocatalytic activity of ZnO_{NR} layer and ZnO_{NR}/Au composites was estimated by photodegradation of MO in an aqueous solution. The degradation curves of MO by ZnO_{NR} layer and ZnO_{NR}/Au composites under UV-A and visible light irradiation are presented in Figure 3.4 (a) and (b). The degradation efficiency values and rate constants of ZnO_{NR} layer and ZnO_{NR}/Au composites are summarized in Table 3.1.

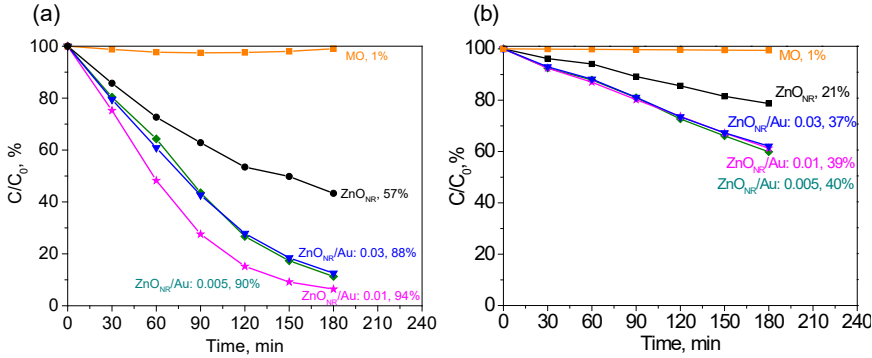


Figure 3.4. Degradation curves of MO by ZnO_{NR} layer and ZnO_{NR}/Au composites under (a) UV-A light and (b) visible light illumination.

As can be seen from Table 3.1, ZnO_{NR} and ZnO_{NR}/Au layers exhibited higher MO degradation efficiency under UV-A light compared to visible light irradiation because the energy from visible light cannot excite ZnO_{NR} due to its large bandgap (3.25-3.27 eV). Moreover, all the ZnO_{NR}/Au composites possessed higher MO degradation efficiency than ZnO_{NR} layer independent of irradiation sources. For instance, ZnO_{NR}/Au: 0.01 composite possessed 94% MO degradation efficiency under UV irradiation in 180 min, being 37% higher than bare ZnO_{NR} layer. Under visible light, ZnO_{NR}/Au: 0.01 composite demonstrated 39% MO degradation efficiency in comparison to 21% from ZnO_{NR} layer.

The degradation rate constant (*k*) of ZnO_{NR}/Au: 0.01 composite is 0.016 min⁻¹ under UV light and 0.0028 min⁻¹ under visible light, compared to 0.006 and 0.0014 min⁻¹ by bare ZnO_{NR} layer under UV and Vis light, respectively.

Table 3.1. Degradation efficiency (*η*) and rate constant (*k*) of ZnO_{NR} layer and ZnO_{NR}/Au composites under UV light and visible light irradiation.

Sample name	UV light illumination		Visible light illumination	
	<i>η</i> (%)	<i>k</i> (min ⁻¹)	<i>η</i> (%)	<i>k</i> (min ⁻¹)
ZnO _{NR}	57	0.006	21	0.0014
ZnO _{NR} /Au: 0.005	90	0.013	40	0.0028
ZnO _{NR} /Au: 0.01	94	0.016	39	0.0028
ZnO _{NR} /Au: 0.03	88	0.010	37	0.0027

This observation indicates that the Au NPs formed on the surface of ZnO_{NR} layer upon thermal degradation of HAuCl₄ [208] largely enhances the photocatalytic activity of ZnO_{NR} layer. In particular, the nearly twice higher MO degradation efficiency under visible light by ZnO_{NR}/Au composites compared to ZnO_{NR} could be assigned to the surface plasmonic effect that increases the light absorption in the visible light spectral region (Figure 3.3) [66]. Notably, the PA of the ZnO_{NR}/Au composite almost doubled under UV

light irradiation (Figure 3.4, Table 3.1). To obtain better understanding of causes responsible for the increased PA of ZnO_{NR}/Au under UV light irradiation, XPS analysis was performed to investigate the surface chemical composition of ZnO_{NR} layer and ZnO_{NR}/Au composites.

3.1.3 Surface chemical composition and wettability of ZnO_{NR} layer and ZnO_{NR}/Au composites

O 1s core-level spectra of ZnO_{NR} layer and ZnO_{NR}/Au composites are presented in Figure 3.5. Three main peaks were deconvoluted at binding energies (BE) of 530.2±0.2 eV, 531.1±0.3 eV, and 532 eV±0.2 eV, assigned to Zn-O bond, oxygen vacancies (V_o), and surface hydroxyl groups (OH⁻), respectively [8]. The peak at BE of 533.1 eV from ZnO_{NR}/Au: 0.01 could be assigned to C-O, C=O and H₂O species [8].

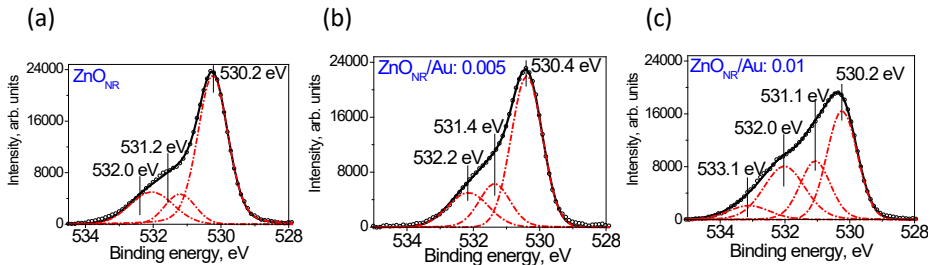


Figure 3.5. O 1s core-level spectra of (a) ZnO_{NR} layer, (b) ZnO_{NR}/Au: 0.005 composite, (c) ZnO_{NR}/Au: 0.01 composite.

The atomic ratios of the components, OH⁻/Zn-O and V_o/Zn-O, are summarized in Table 3.2. The atomic ratio of V_o/Zn-O and OH⁻/Zn-O is higher for ZnO_{NR}/Au composites compared to ZnO_{NR} layer (Table 3.2). For instance, the atomic ratio of OH⁻/Zn-O and V_o/Zn-O for ZnO_{NR}/Au: 0.01 composite is 0.7 and 0.5, respectively, being more than twice higher than that of bare ZnO_{NR} layer. The higher amount of OH⁻ and V_o from ZnO_{NR}/Au layers leads to more effective generation of hydroxyl radicals [8]. Thus, the increased PA of ZnO_{NR}/Au composites under UV light compared to that of ZnO_{NR} layer is achieved due to the increased amount of OH⁻ groups and V_o defects on the surface of ZnO_{NR} after its treatment with HAuCl₄ solution.

Table 3.2. The atomic ratios of V_o/Zn-O and OH⁻/Zn-O obtained from the O 1s core-level peaks and water contact angle values.

Sample	V _o /Zn-O	OH ⁻ /Zn-O	Water contact angle (°)
ZnO _{NR}	0.2	0.3	17-20
ZnO _{NR} /Au: 0.005	0.3	0.3	11-15
ZnO _{NR} /Au: 0.01	0.5	0.7	1-8

Water contact angles characterize the hydrophilicity or hydrophobicity of the measured surface [8]. In general, the lower water contact angle value is the more hydrophilic the surface is, which means there are more hydroxyl groups on the surface [8]. From this perspective, the results of water contact angle measurements are in good agreement with the XPS results. For instance, the surface of ZnO_{NR}/Au: 0.01 composite showed a lower water contact angle of 1-8° and higher amount of hydroxyl groups compared to bare ZnO_{NR} layer.

To summarize, the increased PA of ZnO_{NR}/Au composites under UV light is mainly due to the increased amount of surface hydroxyl groups on ZnO_{NR}. In addition, the effect of ZnO_{NR}/Au Schottky barrier for more efficient separation of photoinduced charge carriers should be considered as well. Nearly twice higher MO degradation efficiency under visible light irradiation by ZnO_{NR}/Au composites compared to that of ZnO_{NR} could be assigned to the Au nanoparticles induced surface plasmon resonance effect that increases the light absorption in the visible light spectral region.

3.2 NiO films deposited by pneumatic spray pyrolysis method

In this section, the structural, morphological, and optical properties, surface chemical composition, and photocatalytic activity of NiO films deposited by PSP method have been studied. The results have been published in paper [II].

3.2.1 Structural, morphological, and optical properties of NiO films

NiO films were deposited at $T_s=340-420$ °C from Ni(ac)₂ aqueous solution. The XRD patterns of deposited films are presented in Figure 3.6. Three reflections were found at $2\theta=37.47^\circ$, 43.26° , and 62.67° , corresponding to the (111), (200), and (220) planes of cubic NiO (bunsenite), respectively (PDF-2, 01-071-1179). The NiO crystallites in deposited films do not show preferential orientation because the intensity ratio of $I_{(111)}/I_{(200)}$ is 0.5-0.7, similar to that in NiO powder ($I_{(111)}/I_{(200)}=0.669$, PDF-2, 01-071-1179). The full width at half maximum (FWHM) of the (200) reflection was used to calculate the NiO crystallite size in sprayed films by Scherrer formula. It was found that the crystallite size increased with increasing the deposition temperature, being 4 nm, 6 nm, 8 nm, and 10 nm at $T_s=300$ °C, 340 °C, 380 °C and 420 °C, respectively. The crystallite size values are in agreement with that reported for sprayed NiO films produced from Ni(ac)₂ aqueous solution [147, 192]. For instance, the crystallite size of NiO in sprayed films increased from 6 nm to 10 nm by increasing the deposition temperature from 400 °C to 500 °C [147].

However, the films produced from alcoholic solution were amorphous according to XRD as no reflections were detected on diffraction patterns of the samples deposited at different temperatures. For this reason, Raman spectroscopy was applied to further investigate the phase composition of deposited films.

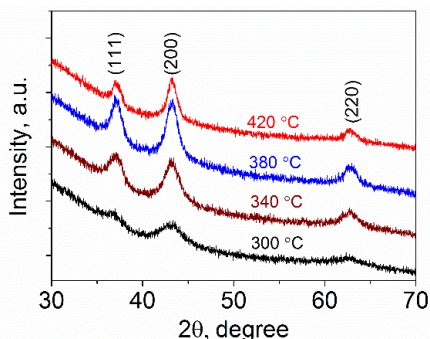


Figure 3.6. XRD patterns of NiO films deposited from Ni(ac)₂ aqueous solution at $T_s=300-420$ °C.

Raman spectra of NiO films deposited at $T_s=300-420$ °C from aqueous and alcoholic solutions are presented in Figure 3.7. Irrespective of the solvent used, the Raman spectra of the sprayed films are quite similar and consist of two broad Raman bands centered at

around 500 cm^{-1} and 1095 cm^{-1} , that could be assigned to one phonon transverse optical mode (1P TO) and two-phonon longitudinal optical mode (2P LO) of NiO [209-212], respectively. The 2P LO band was detectable only when films deposited at $T_s \geq 380\text{ }^\circ\text{C}$.

The appearance of 1P TO band in Raman spectra is characteristic of defective, nonstoichiometric NiO produced by wet-chemical methods including spray pyrolysis [212, 213], hydrothermal growth [214], chemical bath deposition [215] and electrodeposition [216]. The 1P TO band in Raman spectra is absent or negligible from stoichiometric NiO single crystal [217] and high-purity NiO samples produced by electron beam evaporation [213] or epitaxial growth [218]. Therefore, Raman spectroscopy studies confirmed the formation of defective NiO phase from both aqueous and alcohol-based solutions.

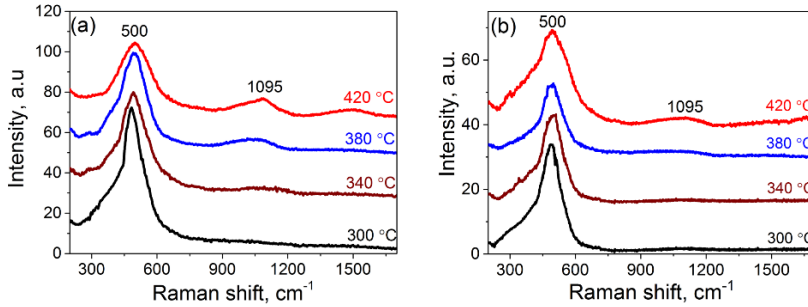


Figure 3.7. Raman spectra of NiO films deposited at $T_s=300\text{-}420\text{ }^\circ\text{C}$ from (a) $\text{Ni}(\text{ac})_2$ aqueous solution, (b) $\text{Ni}(\text{ac})_2$ alcoholic solution.

Cross-sectional SEM images of NiO films produced from aqueous and alcoholic solution clearly indicates the film thickness reduced with increasing the deposition temperature (Figure 3.8). By increasing the T_s from $340\text{ }^\circ\text{C}$ to $420\text{ }^\circ\text{C}$, the thickness of NiO films produced from aqueous solution decreased from ca. 830 nm to ca. 430 nm , whereas the thickness of the films deposited from alcoholic solution reduced from ca. 180 nm to ca. 20 nm . The reduction in film thickness with higher deposition temperature is a feature of spray pyrolysis techniques as precursor solution droplets are repelled from the reaction area at higher temperatures [147, 191, 194].

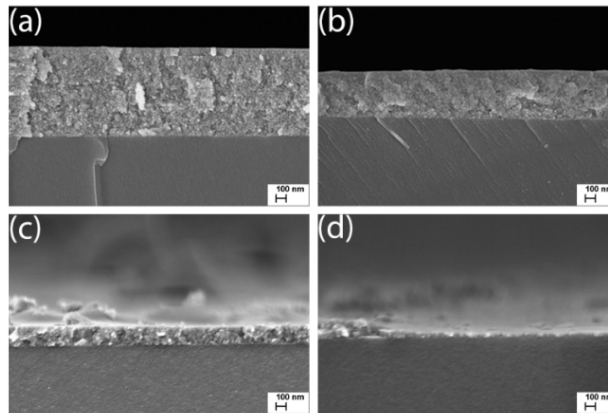


Figure 3.8. SEM cross-sectional images of NiO films from $\text{Ni}(\text{ac})_2$ aqueous solution: (a) $T_s=340\text{ }^\circ\text{C}$, (b) $T_s=420\text{ }^\circ\text{C}$, and $\text{Ni}(\text{ac})_2$ alcoholic solution (c) $T_s=340\text{ }^\circ\text{C}$, (d) $T_s=420\text{ }^\circ\text{C}$.

The total transmittance spectra of the NiO films (Fig.4 in [II]) showed that optical transmittance of the films increases with increasing the deposition temperature irrespective of the solvent used. Furthermore, the total transmittance in the visible light range (300–800 nm) of NiO films produced from alcoholic solutions was higher than that of films produced from aqueous solutions. One of the reasons could be the lower thickness of NiO film grown from alcoholic solution.

The bandgap of NiO films were determined from absorption data using Tauc plots (Fig.5 in [II]). Independent of the deposition temperature, the sprayed NiO films showed direct bandgaps of 3.4 eV and 4.0 eV when produced from aqueous solution and alcoholic solution, respectively. The larger bandgap of NiO film produced from alcoholic solution compared to aqueous solution is probably due the fact that the films were amorphous according to XRD.

The obtained bandgap values correspond to the reported ones in the literature [143, 145, 146, 192, 219]. For example, the E_g values of sprayed NiO films produced from acetate precursor in aqueous solution were 3.5 eV [146] at $T_s=330$ °C and 3.43 eV [192] at $T_s=450$ °C. NiO films produced from chloride precursor in aqueous solution possessed similar bandgap values of 3.4 eV [143, 219]. The E_g value of NiO film prepared from alcoholic solution (ethanol:water =9:1, vol. ratio) was 3.87 eV when grown at $T_s=450$ °C [145].

In summary, XRD confirmed that films produced by spray from Ni(ac)₂ aqueous solution at $T_s=340-420$ °C were of crystalline cubic NiO phase, whereas films produced from Ni(ac)₂ alcoholic solution were amorphous. Raman spectroscopy study revealed that films were of defective NiO irrespective of solvent used for the synthesis. SEM study showed that film thickness decreased with increasing the deposition temperature independent of solvent type and films from alcohol-based solutions were thinner than those obtained by spray of aqueous solutions. UV-Vis spectroscopy study demonstrated that the bandgap of NiO films produced from Ni(ac)₂ aqueous solution and alcoholic solution were 3.4 eV and 4.0 eV, respectively, independent of deposition temperature.

3.2.2 Photocatalytic activity of NiO films

The degradation curves of MO in aqueous solution under UV irradiation by NiO films deposited at different T_s using aqueous and alcoholic solutions are presented in Figure 3.9 (a) and (b), respectively. Irrespective of the solvent type, the degradation efficiency of MO by NiO films decreased with increasing the film deposition temperature. For NiO films produced from aqueous solutions, MO degradation efficiency reached 45% within 3 h under UV-A irradiation by the films grown at $T_s=300$ °C, dropped to 11% for the NiO films grown at $T_s=420$ °C. Similar tendency was observed for the films grown from alcoholic solution. The MO degradation efficiency was 31% within 3 h under UV-B for the films grown at $T_s=300$ °C, and decreased to 5% for the film grown at 420 °C.

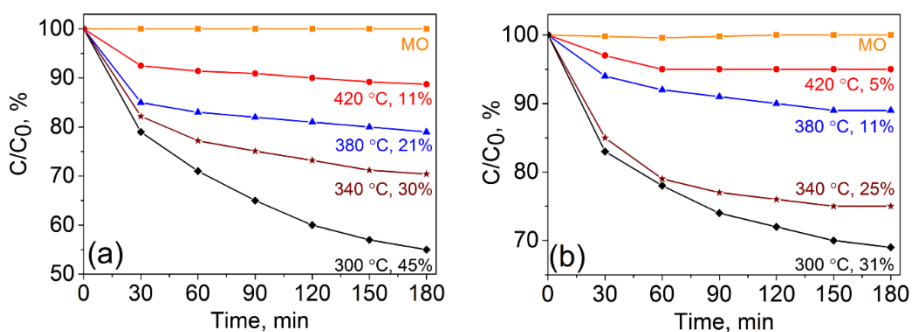


Figure 3.9. MO degradation curves in presence of NiO films deposited by spray at different T_s from (a) $Ni(ac)_2$ aqueous solution under UV-A irradiation; and from (b) $Ni(ac)_2$ alcohol-based solution under UV-B irradiation.

It should be marked out that NiO films produced from alcoholic solution exhibited lower MO degradation efficiencies compared to those grown from aqueous solution (25% vs 30%, $T_s=340$ °C). The possible reason could be the much lower thickness of the films produced from alcoholic solution (180 nm) compared to the NiO films grown from aqueous solution (830 nm) according to SEM study. It has been reported that the higher PA was observed for TiO_2 film with increased thickness [220].

The NiO films obtained in this study demonstrated 45% MO degradation efficiency, which is comparable or even higher than shown by NiO particles or fibers [221-223]. It has been reported that hydrothermal grown NiO nanoparticles possessed 22% MO degradation efficiency under UV-C light in 90 min [221]. NiO nanoparticles prepared by precipitation in solution showed 30% MO degradation efficiency under UV-A light in 180 min [222]. It has been also reported that NiO nanofibers prepared by electrospinning were capable to degrade 40% MO under UV-A light in 160 min [223].

To investigate the reason behind the lower MO degradation efficiency of NiO films grown at higher temperatures, XPS measurements were performed to study NiO film surface chemical composition (see section 3.2.3).

3.2.3 Surface chemical composition and wettability of NiO films

In this section, surface chemical composition and surface wettability of NiO films were analyzed. Based on the analyzed data, the effect of deposition temperature on the PA of NiO films was explained.

The O 1s and Ni 2p_{3/2} core-level spectra of NiO films grown from aqueous solutions in the temperature range of 300-420 °C are presented in Figure 3.10 a and b, respectively. The O 1s, Ni 2p_{3/2}, and C 1s core-level spectra of NiO films are presented Fig. 6 in [II] and the peak positions and assignments are summarized in table 1 in [II].

In the O 1s core-level spectra (Figure 3.10 a), four peaks were resolved at BE of 529.4 ± 0.1 eV, 531.0 eV, 531.9 ± 0.1 eV, and 532.8 ± 0.2 eV. The peak at BE of 529.4 ± 0.1 eV belongs to the Ni-O bond [145, 192, 224]. The peak at BE of 531.0 ± 0.1 eV can be assigned to different species, either $Ni(OH)_2$ [225, 226], $NiO(OH)$ [224], Ni_2O_3 [145, 197, 227] or V_o [8, 225]. The peak at BE of 531.9 ± 0.1 eV is usually assigned to the surface hydroxyl groups (OH^-) [8, 228, 229]. The weak peak at 532.8 ± 0.2 eV could be assigned to C-O, C=O or adsorbed H_2O [8].

In the Ni 2p_{3/2} core-level spectra (Figure 3.10 b), six peaks were detected including three satellite peaks at 860.8 ± 0.1 eV, 863.7 ± 0.1 eV and 866.6 ± 0.2 eV due to shake up effect, and three main peaks at BE of 853.8 ± 0.1 eV, 855.4 ± 0.2 eV, and 857.6 ± 0.3 eV [195, 224]. The peaks at BE of 853.8 ± 0.1 eV and 855.4 ± 0.2 eV are assigned to Ni-O bond in NiO [225].

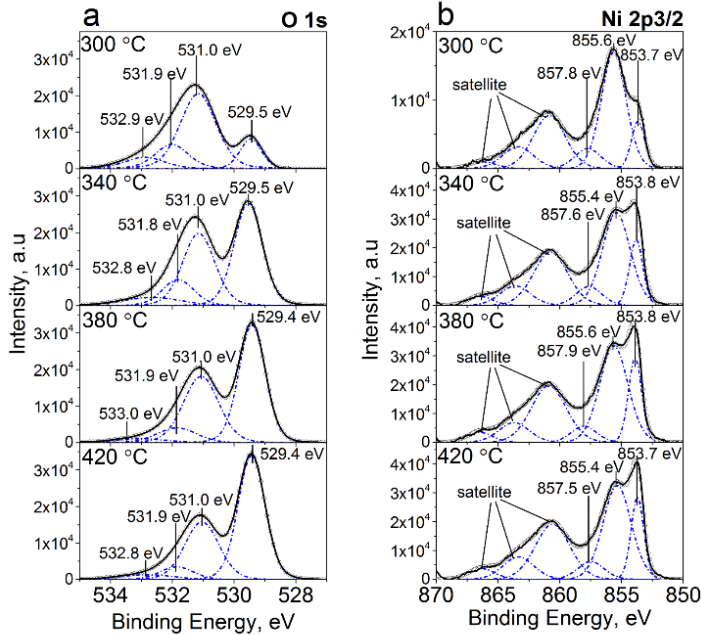


Figure 3.10. Core-level spectra of NiO films deposited at $T_s=300-420$ °C from $Ni(ac)_2$ aqueous solution: (a) O 1s. (b) Ni 2p_{3/2}.

At the same time the peak at BE of 855.4 eV has also been assigned to Ni(OH)₂ [195, 224] as well as to Ni₂O₃ [197]. However, in case of stoichiometric Ni₂O₃, the peaks are centered at BE of 852.5 and 867.5 eV [230], that are missing in spectra of our samples, and thus, the 855.4 eV peak most probably could be assigned to Ni(OH)₂. The weak peak at 857.6 eV probably belongs to Ni(OH)₂, a characteristic subband in the Ni 2p_{3/2} core-level spectrum of stoichiometric Ni(OH)₂ [225].

The peak positions and shape of Ni 2p_{3/2} core-level spectra of our samples are in agreement with those reported for NiO films produced by wet chemical methods such as spray pyrolysis, chemical bath deposition, hydrothermal growth and spin coating techniques [145, 197, 227, 228, 231].

To get further understanding of the effect of deposition temperature on the surface chemical composition of NiO films, the ratios of peak components were calculated, results are summarized in Table 3.3. It can be seen that the ratios of Ni(OH)₂/NiO and OH⁻/NiO, calculated from O 1s core-level spectra, decreased nearly 5.6 and 10 folds, respectively, with increasing the deposition temperature from 300 to 420 °C. Similarly, the ratio of Ni(OH)₂/NiO from Ni 2p_{3/2} core-level spectra drops nearly two times, from 4.62 to 2.38, by increasing the deposition temperature from 300 to 420 °C. It should be noticed that NiO films produced from alcoholic solutions showed a similar tendency as the films produced from aqueous solution.

Table 3.3. O 1s and Ni 2p_{3/2} core-level peak component ratios in NiO films obtained by spray of Ni(ac)₂ solutions at various deposition temperatures.

Solvent type	T _s (°C)	O 1s			Ni 2p _{3/2}
		at%/at%			at%/at%
		Ni(OH) ₂ /NiO	OH ⁻ /NiO	OH _{ads} /NiO	Ni(OH) ₂ /NiO
aqueous	300	3.31	1.35	0.89	4.62
	340	0.84	0.28	0.15	2.95
	380	0.75	0.19	0.07	2.43
	420	0.59	0.13	0.06	2.38
alcoholic	340	0.98	1.03	0.37	2.74

To summarize, the increase in the NiO film deposition temperature significantly reduces the amount of hydroxyl group containing species on the film surface. It is commonly known that hydroxides or hydroxyl groups on the surface are critical species to generate hydroxyl radicals that participate in the decomposition of pollutants [8]. Higher amount of hydroxides or hydroxyl groups on the surface leads to higher degradation efficiency [8]. Hence, the decreased MO degradation efficiency by NiO films grown at elevated deposition temperatures is due to the decreased amount of hydroxyl-containing species on the film surface.

Additional evident to prove the lower amount of hydroxyl groups on the surface of NiO films at higher temperature can be found from water contact angle values, presented in Table 3.4. It appears that the water contact angle values increase with increasing the deposition temperature of NiO films. For the NiO films produced from aqueous solution, the water contact angle increased from 8 to 35° and for the films produced from alcoholic solutions, the water contact angle increased from 10 to 45° when increasing the T_s from 300 to 420 °C. The higher the water contact angle value, the more hydrophobic the surface, indicating less hydroxyl groups on the surface. Therefore, the obtained results from water contact angle measurements are in good agreement with the results of XPS analysis.

Table 3.4. Water contact angle values of NiO films deposited at various temperatures from Ni(ac)₂ aqueous and alcoholic solutions.

T _s (°C)	Water contact angle (°)	
	NiO from aqueous solution	NiO from alcoholic solution
300	8	10
340	13	18
380	25	26
420	35	45

In this study, we showed that NiO films produced by simple and cost-efficient PSP method demonstrated the ability to photocatalytically degrade MO pollutant under UV irradiation. It was shown that NiO film deposition temperature is the technology key parameter controlling the film surface chemical composition that, in turn, determines the film photocatalytic activity. Notably, the decreased amount of surface hydroxyl groups in the films grown at higher temperatures is responsible for the reduced MO

degradation efficiency. At the same time, it should be recognized that PSP technique does not allow fabrication of NiO uniformly thin conformal coatings with controlled thicknesses as required for core-shell heterostructures. For that reason, study on USP deposition of NiO thin films was carried through.

3.3 ZnO/NiO heterostructures by ultrasonic spray of NiO films on ZnO films and ZnO_{NR}

This section summarizes the results of the studies on deposition of NiO thin films by USP and its application in ZnO/NiO bilayer and ZnO/NiO core-shell heterostructures as potentially efficient photocatalysts. The results of the study have been published in the paper [III].

3.3.1 Effect of deposition temperature on structural, morphological, and optical properties of NiO films

NiO films were deposited by USP method using Ni(acac)₂ as Ni source material dissolved in ethanol. Ni(acac)₂ solution with 10 mM concentration was sprayed onto glass substrates at T_s=350-500 °C using 12 spray cycles. The XRD patterns of NiO films deposited at T_s= 350-500 °C are presented in Figure 3.11. As can be seen the main reflection is centered at 2θ=43.51° corresponding to the (200) plane of cubic NiO (PDF-2, 01-071-1179), while the reflections corresponding to (111) and (220) planes are weak. The preferential orientation of the NiO crystallites in films is along the (200) plane as the intensity ratio of I₍₂₀₀₎/I₍₁₁₁₎ is in the range of 6 to 13, being much higher than that of the powder reference of NiO (I₍₂₀₀₎/I₍₁₁₁₎=1.49, PDF-2, 01-071-1179). The NiO crystallite sizes, calculated from the FWHM of the (200) reflection using the Scherrer formula [26], are presented in Table 3.5. Increasing the T_s from 350 to 500 °C increases the NiO crystallite size from 17 to 30 nm. Annealing NiO films in air at T_{an}=600 °C resulted in larger crystallite size in case the films were deposited at T_s=350-450 °C, while the crystallite size remained the same of ca 30 nm after annealing when the film was grown at T_s=500 °C (Table 3.5).

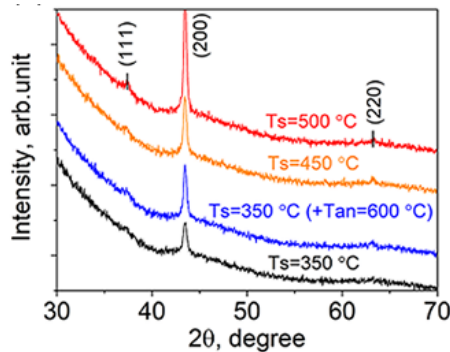


Figure 3.11. XRD patterns of NiO films deposited onto glass substrates at T_s=350-500 °C from Ni(acac)₂ alcoholic solution and the NiO film deposited at T_s= 350 °C followed by annealing at T_{an}=600 °C for 1h in air.

Table 3.5. The film thickness (d), crystallite size (D) and bandgap (E_g) of NiO films deposited onto glass substrate at $T_s=350-500$ °C from Ni(acac)₂ alcoholic solution and after annealing at $T_{an}=600$ °C for 1h in air.

T_s (°C)	d (nm)	D (nm)		E_g (eV)	
		As-dep	$T_{an}=600$ °C	As-dep	$T_{an}=600$ °C
350	30	17	24	3.8	3.7
400	45	22	25	3.7	3.7
450	60	25	30	3.7	3.7
500	70	30	30	3.7	3.7

The SEM images of NiO films are shown in Fig.1c in [III]. Independent of the T_s , the films possessed a uniform surface with fine-grained structure. According to the cross-sectional images, the thickness of NiO films increased from ca. 30 to 70 nm when increasing the T_s from 350 to 500 °C (Table 3.5). The increased thickness at higher T_s is commonly observed for metal oxide films (TiO₂, ZrO_x) produced from acetylacetonate precursor by spray method [229, 232].

The direct bandgap values of NiO films are summarized in Table 3.5. The E_g of as-deposited NiO films grown at $T_s=350$ °C is 3.8 eV and decreased to 3.7 eV when $T_s \geq 350$ °C. Annealing at $T_{an}=600$ °C did not affect the E_g value of the films grown at $T_s=400-500$ °C, all the films have a similar E_g value of 3.7 eV. The slightly higher E_g value of 3.8 eV of the film grown at 350 °C is probably due to the presence of some residues which are removed by annealing.

In summary, crystalline and uniform NiO films with $E_g=3.7$ eV were successfully fabricated from a nickel acetylacetonate precursor by USP method for the first time.

3.3.2 ZnO/NiO bilayer heterostructures: effect of NiO growth temperature

In this subsection, NiO films were deposited at different temperatures by USP onto ZnO films to find out the optimal NiO growth temperature to prepare photocatalytically active ZnO/NiO bilayer heterostructure. Ni(acac)₂ solution with concentration of 10 mM was sprayed on ZnO film at $T_s=350-500$ °C using 12 spray cycles.

XRD patterns of NiO film and ZnO/NiO(500) bilayer heterostructure which are presented in Figure 3.12 (a). The XRD pattern of NiO film showed a reflection at 2θ of 43.56° corresponding to the (200) plane of NiO, whereas the XRD pattern of ZnO/NiO(500) bilayer heterostructure exhibited several reflections at 2θ of 31.79°, 34.48°, 36.36°, 47.67°, 63.04°, 68.17° corresponding to the (100), (002), (101), (102), (103), (112) planes of ZnO and at 2θ of 43.31° belonging to the (200) plane of NiO [94]. Hence, XRD data confirmed that NiO film was grown on ZnO film.

The conductivity type of ZnO and NiO layers were measured by two-point hot probe method. Hot-probe measurements confirmed that ZnO film is a n-type and NiO film is a p-type semiconductor material. Current-voltage (I-V) characterization of the ZnO/NiO(500) bilayer heterostructure after post-annealing at $T_{an}=600$ °C demonstrated a pronounced rectifying characteristic (Figure 3.12 (b)), indicating the formation of the n-p heterojunction.

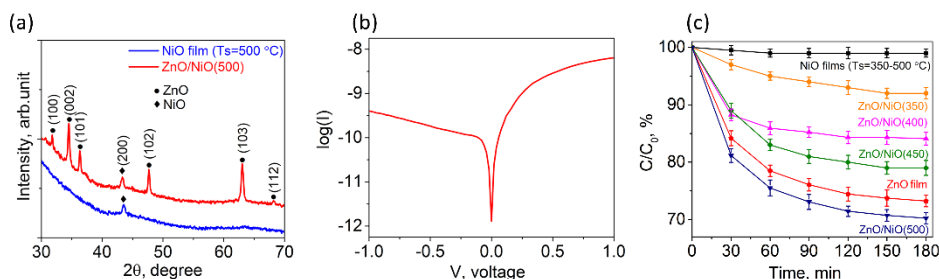


Figure 3.12. (a) XRD patterns of NiO film deposited onto glass substrate at $T_s=500$ °C from $Ni(acac)_2$ alcoholic solution and ZnO/NiO(500) bilayer heterostructure. (b) I-V curve of ZnO/NiO bilayer on ITO glass (NiO was deposited at $T_s=500$ °C using 12 spray cycles, ZnO/NiO bilayer was annealed at $T_{an}=600$ °C for 1h in air). (c) Degradation curves of MB by as-deposited samples under UV-B illumination: NiO films ($T_s=350-500$ °C) onto glass, ZnO film onto glass, and ZnO/NiO(350), ZnO/NiO(400), ZnO/NiO(450), ZnO/NiO(500) bilayer heterostructures.

The PA of ZnO/NiO bilayer heterostructures was measured by photodegradation of MB under UV-B light. The MB degradation curves of as-deposited ZnO/NiO bilayer heterostructures as well as their singular components are presented in Figure 3.12 (c). The degradation efficiencies and degradation rate constants (k) are summarized in Table 3.6. Negligible degradation efficiency of ca. 1% was achieved by NiO films regardless of the deposition temperature in the range of 350-500 °C, whereas the MB degradation efficiencies by as-deposited ZnO/NiO bilayer heterostructures increased from 8 to 30% with increasing the deposition temperature of NiO from 350 to 500 °C. The 30% MB degradation efficiency by the ZnO/NiO bilayer heterostructure with NiO grown at 500 °C (ZnO/NiO(500)) was already higher than bare ZnO film (26%). Post-deposition annealing at 600 °C increased the degradation efficiencies of ZnO/NiO bilayer heterostructures when NiO was grown at $T_s=350-450$ °C (Table 3.6). However, no changes in degradation efficiency were observed from ZnO/NiO(500) bilayer heterostructure after annealing at 600 °C.

Table 3.6. Degradation efficiencies (η) of MB and degradation rate constants (k) by as-deposited samples from $Ni(acac)_2$ alcoholic solution and samples annealed at $T_{an}=600$ °C in air for 1h: NiO films ($T_s=350-500$ °C); ZnO film; and ZnO/NiO(350), ZnO/NiO(400), ZnO/NiO(450), and ZnO/NiO(500) bilayer heterostructures.

Samples	η (%)		k (min^{-1})	
	As-dep	$T_{an}=600^\circ\text{C}$	As-dep	$T_{an}=600^\circ\text{C}$
NiO film	1	2	-	-
ZnO film	26	32	0.0015	0.0021
ZnO/NiO(350)	8	13	0.0005	0.0007
ZnO/NiO(400)	15	20	0.0008	0.0011
ZnO/NiO(450)	21	26	0.0012	0.0015
ZnO/NiO(500)	30	30	0.0017	0.0018

Performed experiment clearly showed that NiO deposition at higher temperatures and post-deposition annealing at 600 °C are crucial to fabricate ZnO/NiO bilayer heterostructures with enhanced photocatalytic activity.

3.3.3 ZnO_{NR}/NiO core-shell heterostructures: effect of NiO shell thickness

In this subsection, the results on the formation and characterization of ZnO_{NR}/NiO core-shell heterostructure are presented and discussed. The deposition temperature of NiO was fixed at 500 °C according to the results obtained from ZnO/NiO bilayer studies. Here we focus on impact of NiO shell thickness on ZnO_{NR} on ZnO_{NR}/NiO core-shell properties. NiO shell thickness was varied by changing the number of spray cycles (1, 2, or 4 cycles).

To find out the optimal concentration of Ni(acac)₂ solution to deposit a uniform NiO shell on ZnO_{NR}, NiO shell was sprayed on ZnO_{NR} from 10 mM and 5 mM Ni(acac)₂ solutions by using 2 spray cycles. The SEM images of the fabricated ZnO_{NR}/NiO core-shell heterostructures and bare ZnO_{NR} are presented in Figure 3.13 (a). As can be seen from Figure 3.13 (a), the bare ZnO_{NR} layers consist of elongated rods with hexagonal shape on the top of rods and the diameter of the rods is ca. 100 nm. ZnO_{NR} layers are composed of hexagonally shaped elongated ZnO crystals with average diameter of ca. 100 nm. ZnO_{NR}/NiO core-shell heterostructure produced from 10 mM Ni(acac)₂ solution with 2 spray cycles demonstrated a coverage of nanosized grains on the surface of ZnO_{NR}. However, by decreasing the concentration of Ni(acac)₂ solution from 10 mM to 5 mM, a more uniform, denser and smoother coverage was formed on the surface of ZnO_{NR} (Figure 3.13 (a)). Thus, 5 mM Ni(acac)₂ solution was selected to deposit NiO onto ZnO_{NR} to fabricate ZnO_{NR}/NiO core-shell structures to study their PA.

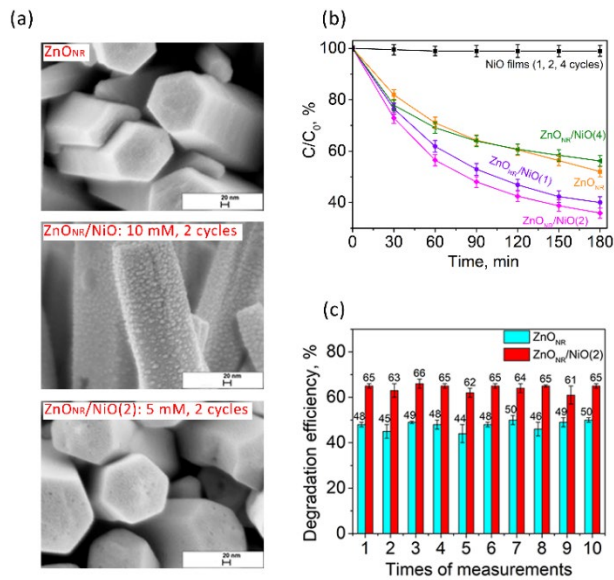


Figure 3.13. (a) SEM images of ZnO_{NR}, ZnO_{NR}/NiO core-shell heterostructures with NiO from 10 mM and 5 mM Ni(acac)₂ alcoholic solution using 2 spray cycles. (b) Degradation curves of MB by as-deposited samples under UV-B illumination: NiO films (1,2,4 spray cycles) onto glass, ZnO_{NR}, and ZnO_{NR}/NiO(1), ZnO_{NR}/NiO(2), ZnO_{NR}/NiO(4) core-shell heterostructures. (c) Reusability test of photodegradation of MB by ZnO_{NR} and ZnO_{NR}/NiO(2) core-shell heterostructures.

The MB degradation curves by as-deposited ZnO_{NR}/NiO core-shell heterostructures as well as their components, NiO films and ZnO_{NR}, are shown in Figure 3.13 (b), and the corresponding degradation efficiencies and degradation rate constants (k) are summarized in Table 3.7. NiO films showed negligible degradation efficiency, being ca. 1%, irrespective

of the number of spray cycles. Meanwhile, ZnO_{NR}/NiO core-shell heterostructures with NiO thickness related to 1 or 2 spray cycles exhibited degradation efficiencies of 60% and 64%, respectively, being higher than 48% obtained from bare ZnO_{NR}. However, a thicker NiO layer deposited from 4 spray cycles in ZnO_{NR}/NiO core-shell heterostructure decreases the degradation efficiency dramatically, from 64 % to 44 %, indicating that the optimization of NiO shell thickness is critical to enhance the PA of ZnO_{NR}/NiO core-shell heterostructure.

The PA results of ZnO_{NR}/NiO core-shell heterostructures annealed at 600 °C are summarized in Table 3.7. In general, annealing leads to a higher PA of all the ZnO_{NR}/NiO core-shell heterostructure. For instance, the MB degradation efficiency by ZnO_{NR}/NiO(2) increased from 64% to 70%. Therefore, annealing is an important procedure to increase the PA of ZnO_{NR}/NiO core-shell heterostructure probably due to the improvement of the material properties and the quality of heterojunction.

Notably, higher PA of core-shell heterostructure photocatalysts compared to their single components has been observed by other researchers. For instance, Periyannan et al. [107] reported that ZnO_{NR}/NiO core-shell heterostructure obtained by sputtering NiO on hydrothermally grown ZnO_{NR} possessed 58% RhB degradation efficiency under UV light in 3 hours compared to 54% from bare ZnO_{NR}. Montero et al. [103] reported that ZnO_{NR}/Cu_xO core-shell heterostructure showed 65% degradation efficiency towards orange II dye under UV light in 3 hours compared to 55% of bare ZnO_{NR}.

The degradation rate constant (k) values before and after annealing at 600 °C are shown in Table 3. As the most photocatalytically active sample, ZnO_{NR}/NiO(2)-600 demonstrated a degradation rate constant (k) value of 0.0072 min⁻¹, being 1.7 times higher than that of bare ZnO_{NR}.

Table 3.7. Degradation efficiencies (η) of MB and degradation rate constants (k) by as-deposited samples from Ni(acac)₂ alcoholic solution and samples annealed at T_{an}=600 °C in air for 1h: NiO films onto glass substrate; ZnO_{NR}; and ZnO_{NR}/NiO(1), ZnO_{NR}/NiO(2), ZnO_{NR}/NiO(4) core-shell heterostructures.

Samples	η (%)		k (min ⁻¹)	
	As-dep	T _{an} =600 °C	As-dep	T _{an} =600 °C
NiO films (1,2,4 spray cycles)	1	2	-	-
ZnO _{NR}	48	53	0.0034	0.0041
ZnO _{NR} /NiO(1)	60	65	0.0051	0.0057
ZnO _{NR} /NiO(2)	64	70	0.0055	0.0072
ZnO _{NR} /NiO(4)	44	50	0.0029	0.0038

The reliability and stability of the photocatalyst are essential for practical application. For this purpose, three parallel samples of ZnO_{NR} prepared under similar deposition conditions and three parallel samples of ZnO_{NR}/NiO(2) core-shell heterostructures prepared under similar deposition conditions were used to repeat the MB photodegradation test for 10 times. The results of photodegradation tests were presented in Figure 3.13 (c), numbers on the graph indicate the averaged degradation efficiency. The obtained results indicated that both ZnO_{NR} and ZnO_{NR}/NiO(2) core-shell heterostructure are stable and reusable for at least 10 times measurements.

Surface chemical composition of ZnO_{NR}/NiO core-shell heterostructures

XPS was used to confirm the presence of NiO on the surface of ZnO_{NR} since NiO was not detected by XRD due to the low film thickness and can be hardly seen from the SEM image (Figure 3.13 (a)). The Zn 2p_{3/2}, Ni 2p, and O 1s core-level spectra of ZnO_{NR}-600, ZnO_{NR}/NiO(2)-600, and ZnO_{NR}/NiO(4)-600 are presented in Figure 3.14 (a), (b), and (c), respectively. The BE of Zn 2p_{3/2} of ZnO_{NR}-600 is centered at 1020.7 eV (Figure 3.14 (a)), corresponding to the reported BE value of Zn 2p_{3/2} from ZnO [233-235]. The Zn 2p_{3/2} peak intensity decreases significantly for ZnO_{NR}/NiO(2)-600 and ZnO_{NR}/NiO(4)-600 compared to ZnO_{NR}-600. The peaks at BE of 852.5±0.3 eV and 870.9±0.3 eV are usually assigned to Ni 2p_{3/2} and Ni 2p_{1/2} of NiO in spectra of ZnO_{NR}/NiO(2)-600 and ZnO_{NR}/NiO(4)-600, respectively (Figure 3.14 (b)) [26, 175].

In O 1s spectra of ZnO_{NR}-600 (Figure 3.14 (c)), three peaks centered at BE of 530.2 eV, 531.8 eV and 532.9 eV are assigned to Zn-O bond, surface hydroxyl groups (OH⁻), and surface H₂O, respectively [8, 236, 237]. After the coverage of NiO on the surface of ZnO_{NR}, An additional peak at BE of 528.8±0.1 eV in the O 1s spectra was observed, belonging to characteristic of Ni-O bond [26, 238].

It should be noted that the BE of Zn 2p_{3/2} of ZnO_{NR}/NiO(2)-600 and ZnO_{NR}/NiO(4)-600 heterostructures is shifted by 0.9 eV and 1.1 eV, respectively, towards lower values compared to the BE of Zn 2p_{3/2} of ZnO_{NR}-600 (Figure 3.14 (a), Table 3.8). The shifts in the BE of Zn2p spectra of ZnO/NiO heterostructures have been observed in several reports [107, 239, 240]. For instance, Periyannan et al. [107] observed a similar shift of 1.1 eV to lower BE, while Tian et al. [239] and Zhang et al. [240] observed a 0.6 eV and 0.9 eV shift toward higher BE, respectively, in BE of Zn 2p_{3/2} from different ZnO/NiO heterostructures compared to bare ZnO. It seems like these obtained shifts in BE are in contradictory to some extent [107, 239, 240]. Our results appear to support the ones reported by Periyannan et al. [107] instead of those reported by Tian et al. [239] and Zhang et al. [240].

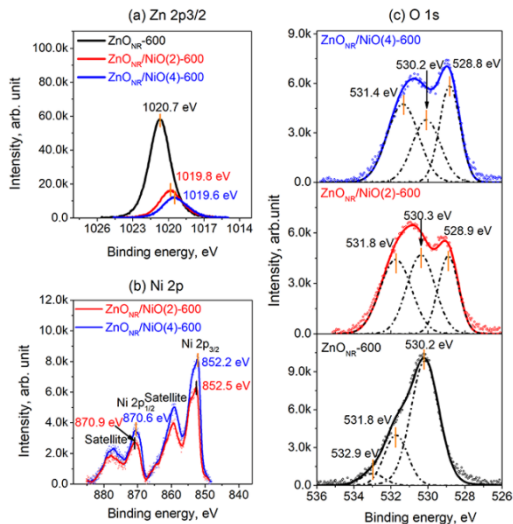


Figure 3.14. XPS core-level spectra from ZnO_{NR}-600, ZnO_{NR}/NiO(2)-600, and ZnO_{NR}/NiO(4)-600: (a) Zn 2p_{3/2}, (b) Ni 2p, (c) O 1s.

To elucidate the cause of the shift of BE of Zn 2p_{3/2} from ZnO_{NR}/NiO core-shell heterostructure, the Zn_{LMM} Auger spectra of ZnO_{NR}-600, ZnO_{NR}/NiO(2)-600 and ZnO_{NR}/NiO(4)-600 were analyzed. The kinetic energy of Zn_{LMM} and Auger parameter are presented in Table 3.8.

Table 3.8. Binding energy (BE) of O 1s, Ni 2p, Zn 2p_{3/2} core levels, and kinetic energy (KE) of Zn_{LMM} and the modified Auger parameter (α') for ZnO_{NR}-600, ZnO_{NR}/NiO(2)-600, and ZnO_{NR}/NiO(4)-600.

Sample name	BE (eV)						KE (eV)		α' (eV)
	O 1s				Ni 2p _{3/2}	Ni 2p _{1/2}	Zn 2p _{3/2}	Zn _{LMM}	
	ZnO	OH	H ₂ O	NiO					
ZnO _{NR} -600	530.2	531.8	532.9	-	-	-	1020.7	988.5	2009.2
ZnO _{NR} /NiO(2)-600	530.3	531.8	-	528.9	852.5	870.9	1019.8	987.4	2007.2
ZnO _{NR} /NiO(4)-600	530.2	531.4	-	528.8	852.2	870.6	1019.6	987.9	2007.3

As can be seen from Table 3.8, there is a significant difference of 1.9-2.0 eV between the modified Auger parameter values (α') of pristine ZnO_{NR} and ZnO_{NR}/NiO heterostructures. This difference confirms the existence of built-in electric field at the heterojunction interface.

Band diagram of ZnO_{NR}/NiO core-shell heterostructures and MB degradation mechanism

The MB degradation mechanism by the ZnO_{NR}/NiO core-shell heterostructure is discussed on base of the energetic diagram of the heterostructure composed using experimental results of KP and PYS analysis. The work functions of ZnO_{NR}-600 and ZnO_{NR}/NiO(2)-600 are measured by KP and the results are presented in Fig. 5 (a) in [III]. The work function values of ZnO_{NR}-600 and ZnO_{NR}/NiO(2)-600 are 4.42 eV and 4.70 eV, respectively (Table 3.9). Compared with ZnO_{NR}-600, the higher work function value of ZnO_{NR}/NiO(2)-600 proves the existence of NiO thin films on the surface of ZnO_{NR}.

Table 3.9. Work function (Φ), ionization energy (E_i) and the energy difference between Fermi level (E_f) and valence band maximum (E_{VBM}) of ZnO_{NR}-600 and ZnO_{NR}/NiO(2)-600.

Sample	Φ (± 0.04 eV)	E_i (± 0.03 eV)	$E_f - E_{VBM}$ (± 0.05 eV)
ZnO _{NR} -600	4.42	6.29	-1.87
ZnO _{NR} /NiO(2)-600	4.70	5.41	-0.71

The ionization energy (E_i) of the ZnO_{NR}-600 and ZnO_{NR}/NiO(2)-600 was measured by PYS and the corresponding spectra are presented in Fig. 5 (b) and (c) in [III], respectively. The E_i values of ZnO_{NR}-600 and ZnO_{NR}/NiO(2)-600 are 6.29 eV and 5.40 eV, respectively (Table 3.9). To draw the band diagram of ZnO_{NR}/NiO heterojunction, the difference between valence band maximum (E_{VBM}) and Fermi level (E_f) is calculated as the difference between the work function (Φ) and E_i , $E_f - E_{VBM} = \Phi - E_i$. The conduction band minimum (CBM) is calculated as $E_{CBM} = E_{VBM} + E_g$ by using the bandgap of the hydrothermally grown ZnO_{NR} of 3.27 eV [236] and of the USP grown NiO of 3.70 eV (Table 3.5). With the known VBM and CBM positions, the energy band diagram of the ZnO_{NR}/NiO heterostructure can be presented as shown in Figure 3.15. As can be seen from the energy band diagram, it shows a n-type conductivity for the ZnO_{NR} and a p-type conductivity for the NiO films corresponding to the results of the hot point probe measurements in chapter 3.2. In addition, a rectifying current-voltage characteristic is predicted.

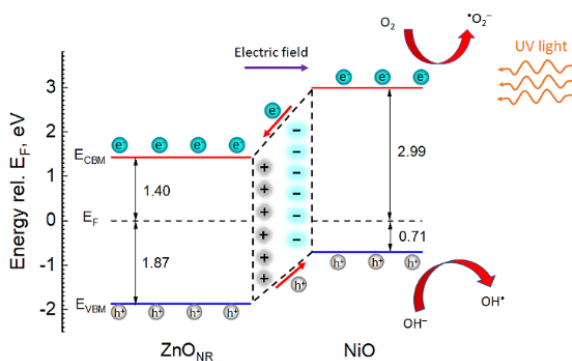


Figure 3.15. Energy band diagram of $\text{ZnO}_{\text{NR}}/\text{NiO}(2)\text{-600}$ heterostructure.

It is worth noting that in most of the PA studies the formation of ZnO/NiO heterojunction is proposed based on the PA results rather than relying on actual energetic parameters of the heterostructure [94, 96, 204-206]. For instance, Hameed et al. [204] claimed the formation of ZnO/NiO heterojunction only by comparing the MB degradation efficiencies from ZnO/NiO NPs and its singular components. Similarly, Tian et al. [96] and Liu et al. [206] concluded the formation of ZnO/NiO heterojunction based on the difference in MB degradation efficiency by ZnO/NiO particles and bare ZnO. However, none of aforementioned studies confirmed the formation of ZnO/NiO heterojunction via experimentally measured energetic parameters.

For this reason, the band diagram of the $\text{ZnO}_{\text{NR}}/\text{NiO}$ heterojunction based on directly measured experimental data (Figure 3.15) and the MB photocatalytic degradation mechanism are proposed.

Following the classical concept of heterojunction formation [241], the electrons transfer from ZnO to NiO and holes transfer from NiO to ZnO until the system reaches thermodynamic equilibrium and an inner electric field forms at the heterointerface. When ZnO/NiO heterostructure is irradiated by UV light, the electron hole pairs are generated in both ZnO and NiO, and electrons from valence band (VB) could be excited to the conduction band (CB) in both materials with simultaneous formation of the same amount of holes in valence band. However, our experimentally proven band alignment for the p-NiO/n-ZnO heterojunction (Figure 3.15) supports transfer of the photogenerated electrons from CB of NiO to the CB of ZnO, and transfer of photogenerated holes from VB of ZnO to VB of NiO, indicating that the electrons and holes are efficiently separated. The electrons from the ZnO and holes from the NiO will be injected into the reaction medium and participate in chemical reactions to degrade different organic pollutants. The electrons interact with dissolved O_2 molecules and produce the superoxide radical anion ($^{\bullet}\text{O}_2^-$). The photogenerated holes are trapped by OH^- forming hydroxyl radical species ($^{\bullet}\text{OH}$). Formed radicals are the main species that degrade the organic dye molecule to carbon dioxide and water. Thus, this study clearly demonstrated that efficient separation of charge carriers at $\text{ZnO}_{\text{NR}}/\text{NiO}$ heterointerface determines the boost of the photocatalytic performance.

Conclusions

This thesis was focused on the development of strategies for the synthesis of photocatalytically efficient ZnO nanorod and NiO film based materials by low cost chemical solution methods such as hydrothermal growth and chemical spray pyrolysis. The novelty of this study is summarized as follows. Firstly, Au nanoparticles were synthesized by spin-coating of H₂AuCl₄ solution onto ZnO_{NR} layers followed by thermal treatment to form ZnO_{NR}/Au composites with enhanced PA. The mechanism behind the increased PA upon H₂AuCl₄ treatment was described and proved. Secondly, we showed that the NiO film deposition temperature is the main technological parameter that controls the content of hydroxyl groups on the surface, mainly responsible for the photocatalytic performance of pneumatically sprayed films from a nickel acetate solution. Thirdly, we demonstrated that homogeneous crystalline films of NiO with a cubic structure could be fabricated on different substrates via employing a robust ultrasonic spray technique and nickel acetylacetonate as a source material. Moreover, for the first time ultrasonically sprayed NiO film was applied onto ZnO_{NR} layer to form ZnO_{NR}/NiO core-shell heterostructures with significantly enhanced photocatalytic performance compared to pristine ZnO_{NR}. The formation of ZnO_{NR}/NiO n-p core shell heterostructure was confirmed applying advanced physical characterization techniques.

The main conclusions from this dissertation are summarized as follows:

1. ZnO_{NR}/Au composites were fabricated by spin-coating of H₂AuCl₄ solution onto ZnO_{NR} layers followed by thermal treatment at 400 °C, the formation of Au nanoparticles was confirmed by XRD and SEM. The dimensions of Au nanoparticles were in a direct correlation with H₂AuCl₄ solution concentration. According to XPS study, ZnO_{NR}/Au composites contain higher amount of hydroxyl groups on the surface and therefore possess higher MO degradation efficiency under UV light compared to bare ZnO_{NR}. Employment of H₂AuCl₄ solution with concentration of 0.01 mol/L resulted in ZnO_{NR}/Au composite showing the highest MO degradation efficiency of 94 % in 3 h compared to 65% by bare ZnO_{NR} under UV light irradiation. Nearly twice higher MO degradation efficiency under visible light by ZnO_{NR}/Au composites (ca. 40% in 3 h) compared to that by pristine ZnO_{NR} (21% in 3 h) is explained by occurrence the absorption band in the visible spectral region, at 500-600 nm due to the surface plasmon resonance effect.

2. NiO thin films were fabricated by pneumatic spray technique at deposition temperatures of 300-420 °C using nickel acetate as a precursor material in different solvents (aqueous and alcohol based). The formation of NiO was confirmed by XRD and Raman spectroscopy methods. Deposition temperature and solvent type affect the structural, optical properties, and surface chemical composition of pneumatically sprayed NiO films. Films prepared from aqueous solution are of polycrystalline NiO with crystallite size of 4-10 nm, but films from alcoholic solution are amorphous according to XRD study. Bandgap of NiO films produced from aqueous and alcoholic solutions is 3.4 eV and 4.0 eV, respectively, irrespective of the deposition temperature. Deposition temperature is the main technological parameter that controls the content of hydroxyl groups on the surface, and therefore the photocatalytic performance of NiO films. The MO degradation efficiency under UV light by NiO films produced at 300 °C from aqueous solution was 45% in 3 h and 11% in 3h for the film grown at 420 °C. The decrease in PA of NiO films with increasing the deposition temperature correlates to the decrease in the amount of hydroxyl groups on the surface of NiO film.

3. The strategy for synthesis of ZnO_{NR}/NiO n-p core-shell heterostructures with improved photocatalytic activity was developed.

Firstly, homogenous, transparent polycrystalline NiO films with E_g of 3.7 eV were fabricated by ultrasonic spray pyrolysis technique using nickel acetylacetonate as precursor material.

Secondly, the NiO layer deposition temperature of 500 °C was found to be optimal for ZnO/NiO bilayer heterostructure fabrication as the MB degradation efficiency by ZnO/NiO bilayer increased from 8 to 30% with increasing the NiO deposition temperature from 350 to 500 °C. Rectifying I-V characteristic of ZnO/NiO contact confirms the formation of ZnO/NiO n-p heterostructure.

Thirdly, the optimum preparation conditions of photocatalytically efficient ZnO_{NR}/NiO core-shell heterostructures were determined: NiO film deposition from two USP cycles at 500 °C followed by annealing heterostructure at 600 °C in air. The formation of ZnO_{NR}/NiO n-p core shell heterostructure was confirmed applying advanced physical characterization techniques. XPS analysis confirmed the formation of NiO shell on ZnO core and showed a 1.9–2.0 eV difference in modified Auger parameter between ZnO_{NR} and ZnO_{NR}/NiO core-shell heterostructure, validating the presence of built-in electric field at the interface. A type-II band diagram between NiO and ZnO_{NR} is proposed based on Kelvin probe and photoelectron yield spectroscopy measurements.

ZnO_{NR}/NiO core-shell heterostructure showed MB degradation efficiency of 70% compared to 53% by ZnO_{NR} as measured under UV irradiation for 3 h. The increased photocatalytic performance of ZnO_{NR}/NiO heterostructures is due to the improved separation of photogenerated electron-hole pairs.

References

- [1] Advanced Oxidation Processes for Water Treatment: Fundamentals and Applications. ed. M.I. Stefan. **2017**: IWA Publishing, <https://doi.org/10.2166/9781780407197>.
- [2] Pillai S.C., McGuinness N.B., Byrne C., Han C., Lalley J., Nadagouda M., Falaras P., Kontos A.G., Gracia-Pinilla M.A., O'Shea K., Mangalaraja R.V., Christophoridis C., Triantis T., Hiskia A., and Dionysiou D.D. Photocatalysis as an effective advanced oxidation process, in *Advanced Oxidation Processes for Water Treatment: Fundamentals and Applications*. M.I. Stefan, Editor. **2017**, IWA Publishing.
- [3] Olga M.I., Vincent R., Guillaume L., and Damien L. TiO₂- and ZnO-Based Materials for Photocatalysis: Material Properties, Device Architecture and Emerging Concepts, in *Semiconductor Photocatalysis*. C. Wenbin, Editor. **2016**, IntechOpen: Rijeka.
- [4] Ong C.B., Ng L.Y., and Mohammad A.W. A review of ZnO nanoparticles as solar photocatalysts: Synthesis, mechanisms and applications. *Renewable & Sustainable Energy Reviews*, **2018**, 81, 536-551, <https://doi.org/10.1016/j.rser.2017.08.020>.
- [5] Akbari A., Sabouri Z., Hosseini H.A., Hashemzadeh A., Khatami M., and Darroudi M. Effect of nickel oxide nanoparticles as a photocatalyst in dyes degradation and evaluation of effective parameters in their removal from aqueous environments. *Inorganic Chemistry Communications*, **2020**, 115, 107867, <https://doi.org/10.1016/j.inoche.2020.107867>.
- [6] Ikram M., Rashid M., Haider A., Naz S., Haider J., Raza A., Ansar M.T., Uddin M.K., Ali N.M., Ahmed S.S., Imran M., Dilpazir S., Khan Q., and Maqbool M. A review of photocatalytic characterization, and environmental cleaning, of metal oxide nanostructured materials. *Sustainable Materials and Technologies*, **2021**, 30, e00343, <https://doi.org/10.1016/j.susmat.2021.e00343>.
- [7] Gromōko I. ZnO Nanostructured Layers by Wet Chemical Deposition Methods: Growth, Surface Properties, Photocatalytic Capability. *PhD thesis*. **2018**, Tallinn University of Technology.
- [8] Gromyko I., Krunks M., Dedova T., Katerski A., Klauson D., and Oja Acik I. Surface properties of sprayed and electrodeposited ZnO rod layers. *Applied Surface Science*, **2017**, 405, 521-528, <https://doi.org/10.1016/j.apsusc.2017.02.065>.
- [9] Dedova T., Krunks M., Oja Acik I., Klauson D., Volobujeva O., and Mere A. Hierarchical nanostructures of ZnO obtained by spray pyrolysis. *Materials Chemistry and Physics*, **2013**, 141, 69-75, <https://doi.org/10.1016/j.matchemphys.2013.04.026>.
- [10] Xu C., Ravi Anusuyadevi P., Aymonier C., Luque R., and Marre S. Nanostructured materials for photocatalysis. *Chemical Society Reviews*, **2019**, 48, 3868-3902, <https://doi.org/10.1039/C9CS00102F>.
- [11] Saravanan A., Kumar P.S., Vo D.V.N., Yaashikaa P.R., Karishma S., Jeevanantham S., Gayathri B., and Bharathi V.D. Photocatalysis for removal of environmental pollutants and fuel production: a review. *Environmental Chemistry Letters*, **2021**, 19, 441-463, <https://doi.org/10.1007/s10311-020-01077-8>.
- [12] Gunti S., Kumar A., and Ram M.K. Nanostructured photocatalysis in the visible spectrum for the decontamination of air and water. *International Materials Reviews*, **2018**, 63, 257-282, <https://doi.org/10.1080/09506608.2017.1379264>.

- [13] Zhang F., Wang X., Liu H., Liu C., Wan Y., Long Y., and Cai Z. Recent Advances and Applications of Semiconductor Photocatalytic Technology. *Applied Sciences*, **2019**, 9, 2489, <https://doi.org/10.3390/app9122489>.
- [14] Mashuri S.I.S., Ibrahim M.L., Kasim M.F., Mastuli M.S., Rashid U., Abdullah A.H., Islam A., Mijan N.A., Tan Y.H., Mansir N., Kaus N.H.M., and Hin T.Y.Y. Photocatalysis for Organic Wastewater Treatment: From the Basis to Current Challenges for Society. *Catalysts*, **2020**, 10, 1260, <https://doi.org/10.3390/catal10111260>.
- [15] Ibhaddon A.O. and Fitzpatrick P. Heterogeneous Photocatalysis: Recent Advances and Applications. *Catalysts*, **2013**, 3, 189-218, <https://doi.org/10.3390/catal3010189>.
- [16] Samsudin E.M., Goh S.N., Wu T.Y., Ling T.T., Abd Hamid S.B., and Juan J.C. Evaluation on the Photocatalytic Degradation Activity of Reactive Blue 4 using Pure Anatase Nano-TiO₂. *Sains Malaysiana*, **2015**, 44, 1011-1019, <https://doi.org/10.17576/jsm-2015-4407-13>.
- [17] Akpan U.G. and Hameed B.H. Parameters affecting the photocatalytic degradation of dyes using TiO₂-based photocatalysts: A review. *Journal of Hazardous Materials*, **2009**, 170, 520-529, <https://doi.org/10.1016/j.jhazmat.2009.05.039>.
- [18] Chong M.N., Jin B., Chow C.W.K., and Saint C. Recent developments in photocatalytic water treatment technology: A review. *Water Research*, **2010**, 44, 2997-3027, <https://doi.org/10.1016/j.watres.2010.02.039>.
- [19] Jo W.K. and Tayade R.J. Recent developments in photocatalytic dye degradation upon irradiation with energy-efficient light emitting diodes. *Chinese Journal of Catalysis*, **2014**, 35, 1781-1792, [https://doi.org/10.1016/s1872-2067\(14\)60205-9](https://doi.org/10.1016/s1872-2067(14)60205-9).
- [20] Bhatkhande D.S., Pangarkar V.G., and Beenackers A. Photocatalytic degradation for environmental applications - a review. *Journal of Chemical Technology and Biotechnology*, **2002**, 77, 102-116, <https://doi.org/10.1002/jctb.532>.
- [21] Wang M., Han J., Hu Y., Guo R., and Yin Y. Carbon-Incorporated NiO/TiO₂ Mesoporous Shells with p-n Heterojunctions for Efficient Visible Light Photocatalysis. *ACS Applied Materials & Interfaces*, **2016**, 8, 29511-29521, <https://doi.org/10.1021/acsami.6b10480>.
- [22] Prakash K., Kumar P.S., Pandiaraj S., Saravanakumar K., and Karuthapandian S. Controllable synthesis of SnO₂ photocatalyst with superior photocatalytic activity for the degradation of methylene blue dye solution. *Journal of Experimental Nanoscience*, **2016**, 11, 1138-1155, <https://doi.org/10.1080/17458080.2016.1188222>.
- [23] Murillo-Sierra J.C., Hernández-Ramírez A., Hinojosa-Reyes L., and Guzmán-Mar J.L. A review on the development of visible light-responsive WO₃-based photocatalysts for environmental applications. *Chemical Engineering Journal Advances*, **2021**, 5, 100070, <https://doi.org/10.1016/j.cej.2020.100070>.
- [24] Elgohary E.A., Mohamed Y.M.A., El Nazer H.A., Baaloudj O., Alyami M.S.S., El Jery A., Assadi A.A., and Amrane A. A Review of the Use of Semiconductors as Catalysts in the Photocatalytic Inactivation of Microorganisms. *Catalysts*, **2021**, 11, 1498, <https://doi.org/10.3390/catal11121498>.
- [25] Zhang Y.-H., Liu M.-M., Chen J.-L., Fang S.-M., and Zhou P.-P. Recent advances in Cu₂O-based composites for photocatalysis: a review. *Dalton Transactions*, **2021**, 50, 4091-4111, <https://doi.org/10.1039/D0DT04434B>.
- [26] Chen Z., Dedova T., Acik I.O., Danilson M., and Krunks M. Nickel oxide films by chemical spray: Effect of deposition temperature and solvent type on structural, optical, and surface properties. *Applied Surface Science*, **2021**, 548, 149118, <https://doi.org/10.1016/j.apsusc.2021.149118>.

- [27] Gupta S.M. and Tripathi M. An Overview of Commonly Used Semiconductor Nanoparticles in Photocatalysis. *High Energy Chemistry*, **2012**, 46, 1-9, <https://doi.org/10.1134/s0018143912010134>.
- [28] Lee G.-J. and Wu J.J. Recent developments in ZnS photocatalysts from synthesis to photocatalytic applications — A review. *Powder Technology*, **2017**, 318, 8-22, <https://doi.org/10.1016/j.powtec.2017.05.022>.
- [29] Asadzadeh-Khaneghah S. and Habibi-Yangjeh A. g-C₃N₄/carbon dot-based nanocomposites serve as efficacious photocatalysts for environmental purification and energy generation: A review. *Journal of Cleaner Production*, **2020**, 276, 124319, <https://doi.org/10.1016/j.jclepro.2020.124319>.
- [30] Zhang Y., Hu Y., Zeng H.M., Zhong L., Liu K.W., Cao H.M., Li W., and Yan H.J. Silicon carbide recovered from photovoltaic industry waste as photocatalysts for hydrogen production. *Journal of Hazardous Materials*, **2017**, 329, 22-29, <https://doi.org/10.1016/j.jhazmat.2017.01.023>.
- [31] Kang X.L., Liu S.H., Dai Z.D., He Y.P., Song X.Z., and Tan Z.Q. Titanium Dioxide: From Engineering to Applications. *Catalysts*, **2019**, 9, 191, <https://doi.org/10.3390/catal9020191>.
- [32] Klauson D., Šakarašvili M., Pronina N., Krichevskaya M., Kärber E., and Mikli V. Aqueous photocatalytic degradation of selected micropollutants by Pd-modified titanium dioxide in three photoreactor types. *Environmental Technology*, **2017**, 38, 860-871, <https://doi.org/10.1080/09593330.2016.1214185>.
- [33] Klauson D., Portjanskaya E., Budarnaja O., Krichevskaya M., and Preis S. The synthesis of sulphur and boron-containing titania photocatalysts and the evaluation of their photocatalytic activity. *Catalysis Communications*, **2010**, 11, 715-720, <https://doi.org/10.1016/j.catcom.2010.02.001>.
- [34] Klauson D., Krichevskaya M., Borissova M., and Preis S. Aqueous photocatalytic oxidation of sulfamethizole. *Environmental Technology*, **2010**, 31, 1547-1555, <https://doi.org/10.1080/09593331003789537>.
- [35] Klauson D., Babkina J., Stepanova K., Krichevskaya M., and Preis S. Aqueous photocatalytic oxidation of amoxicillin. *Catalysis Today*, **2010**, 151, 39-45, <https://doi.org/10.1016/j.cattod.2010.01.015>.
- [36] Klauson D., Budarnaja O., Stepanova K., Krichevskaya M., Dedova T., Käkinen A., and Preis S. Selective performance of sol-gel synthesised titanium dioxide photocatalysts in aqueous oxidation of various-type organic pollutants. *Kinetics and Catalysis*, **2014**, 55, 47-55, <https://doi.org/10.1134/S0023158414010030>.
- [37] Dundar I., Krichevskaya M., Katerski A., and Acik I.O. TiO₂ thin films by ultrasonic spray pyrolysis as photocatalytic material for air purification. *Royal Society Open Science*, **2019**, 6, 181578, <https://doi.org/doi:10.1098/rsos.181578>.
- [38] Spiridonova J., Katerski A., Danilson M., Krichevskaya M., Krunks M., and Oja Acik I. Effect of the Titanium Isopropoxide:Acetylacetone Molar Ratio on the Photocatalytic Activity of TiO₂ Thin Films. *Molecules*, **2019**, 24, 4326, <https://doi.org/doi:10.3390/molecules24234326>.
- [39] Ding M., Yang H., Yan T., Wang C., Deng X., Zhang S., Huang J., Shao M., and Xu X. Fabrication of Hierarchical ZnO@NiO Core-Shell Heterostructures for Improved Photocatalytic Performance. *Nanoscale Research Letters*, **2018**, 13, 260, <https://doi.org/10.1186/s11671-018-2676-1>.
- [40] Klingshirn C. ZnO: From basics towards applications. *Physica Status Solidi B-Basic Solid State Physics*, **2007**, 244, 3027-3073, <https://doi.org/10.1002/pspb.200743072>.

- [41] Janotti A. and Van de Walle C.G. Fundamentals of zinc oxide as a semiconductor. *Reports on Progress in Physics*, **2009**, 72, 126501, <https://doi.org/10.1088/0034-4885/72/12/126501>.
- [42] Sharma D.K., Shukla S., Sharma K.K., and Kumar V. A review on ZnO: Fundamental properties and applications. *Materials Today: Proceedings*, **2022**, 49, 3028-3035, <https://doi.org/10.1016/j.matpr.2020.10.238>.
- [43] Dhiman P., Rana G., Kumar A., Sharma G., Vo D.-V.N., and Naushad M. ZnO-based heterostructures as photocatalysts for hydrogen generation and depollution: a review. *Environmental Chemistry Letters*, **2022**, 1047–1081, <https://doi.org/10.1007/s10311-021-01361-1>.
- [44] Kumar R., Anandan S., Hembram K., and Rao T.N. Efficient ZnO-Based Visible-Light-Driven Photocatalyst for Antibacterial Applications. *ACS Applied Materials & Interfaces*, **2014**, 6, 13138-13148, <https://doi.org/10.1021/am502915v>.
- [45] Chen X., Wu Z., Liu D., and Gao Z. Preparation of ZnO Photocatalyst for the Efficient and Rapid Photocatalytic Degradation of Azo Dyes. *Nanoscale Research Letters*, **2017**, 12, 143, <https://doi.org/10.1186/s11671-017-1904-4>.
- [46] Tian C., Zhang Q., Wu A., Jiang M., Liang Z., Jiang B., and Fu H. Cost-effective large-scale synthesis of ZnO photocatalyst with excellent performance for dye photodegradation. *Chemical Communications*, **2012**, 48, 2858-2860, <https://doi.org/10.1039/C2CC16434E>.
- [47] Ghule L.A., Patil A.A., Sapnar K.B., Dhole S.D., and Garadkar K.M. Photocatalytic degradation of methyl orange using ZnO nanorods. *Toxicological & Environmental Chemistry*, **2011**, 93, 623-634, <https://doi.org/10.1080/02772248.2011.560852>.
- [48] Kumar N., Mittal H., Reddy L., Nair P., Ngila J.C., and Parashar V. Morphogenesis of ZnO nanostructures: role of acetate (COO⁻) and nitrate (NO₃⁻) ligand donors from zinc salt precursors in synthesis and morphology dependent photocatalytic properties. *RSC Advances*, **2015**, 5, 38801-38809, <https://doi.org/10.1039/C5RA04162G>.
- [49] Zeng J.H., Jin B.B., and Wang Y.F. Facet enhanced photocatalytic effect with uniform single-crystalline zinc oxide nanodisks. *Chemical Physics Letters*, **2009**, 472, 90-95, <https://doi.org/10.1016/j.cplett.2009.02.082>.
- [50] Sahu K., kuriakose S., Singh J., Satpati B., and Mohapatra S. Facile synthesis of ZnO nanoplates and nanoparticle aggregates for highly efficient photocatalytic degradation of organic dyes. *Journal of Physics and Chemistry of Solids*, **2018**, 121, 186-195, <https://doi.org/10.1016/j.jpics.2018.04.023>.
- [51] Mohammad A., Kapoor K., and Mobin S.M. Improved Photocatalytic Degradation of Organic Dyes by ZnO-Nanoflowers. *Chemistryselect*, **2016**, 1, 3483-3490, <https://doi.org/10.1002/slct.201600476>.
- [52] Suresh D., Udayabhanu, Nethravathi P.C., Lingaraju K., Rajanaika H., Sharma S.C., and Nagabhushana H. EGCG assisted green synthesis of ZnO nanopowders: Photodegradative, antimicrobial and antioxidant activities. *Spectrochimica Acta Part A: Molecular and Biomolecular Spectroscopy*, **2015**, 136, 1467-1474, <https://doi.org/10.1016/j.saa.2014.10.038>.
- [53] Yu F.C., Hu H.L., Wang B.L., Li H.S., Song T.Y., Xu B.Y., He L., Wang S., and Duan H.Y. Effects of Al doping on defect behaviors of ZnO thin film as a photocatalyst. *Materials Science-Poland*, **2019**, 37, 437-445, <https://doi.org/10.2478/msp-2019-0050>.

- [54] Boughelout A., Macaluso R., Kechouane M., and Trari M. Photocatalysis of rhodamine B and methyl orange degradation under solar light on ZnO and Cu₂O thin films. *Reaction Kinetics Mechanisms and Catalysis*, **2020**, 129, 1115-1130, <https://doi.org/10.1007/s11144-020-01741-8>.
- [55] Lv J., Gong W., Huang K., Zhu J., Meng F., Song X., and Sun Z. Effect of annealing temperature on photocatalytic activity of ZnO thin films prepared by sol-gel method. *Superlattices and Microstructures*, **2011**, 50, 98-106, <https://doi.org/10.1016/j.spmi.2011.05.003>.
- [56] Di Mauro A., Cantarella M., Nicotra G., Privitera V., and Impellizzeri G. Low temperature atomic layer deposition of ZnO: Applications in photocatalysis. *Applied Catalysis B: Environmental*, **2016**, 196, 68-76, <https://doi.org/10.1016/j.apcatb.2016.05.015>.
- [57] Ouhaibi A., Saoula N., Ghamnia M., Dahamni M.A., and Guerbous L. Effect of Deposition Temperature on Morphological, Optical, and Photocatalytic Properties of ZnO Thin Films Synthesized by Ultrasonic Spray Pyrolysis Method. *Crystal Research and Technology*, 2100224, <https://doi.org/10.1002/crat.202100224>.
- [58] Toporovska L.R., Hryzak A.M., Turko B.I., Rudyk V.P., Tsybul'skyi V.S., and Serkiz R.Y. Photocatalytic properties of zinc oxide nanorods grown by different methods. *Optical and Quantum Electronics*, **2017**, 49, 408, <https://doi.org/10.1007/s11082-017-1254-6>.
- [59] Chen Y.L., Kuo L.-C., Tseng M.L., Chen H.M., Chen C.-K., Huang H.J., Liu R.-S., and Tsai D.P. ZnO nanorod optical disk photocatalytic reactor for photodegradation of methyl orange. *Optics Express*, **2013**, 21, 7240-7249, <https://doi.org/10.1364/OE.21.007240>.
- [60] Xu L., Zheng G., Wang J., Lai M., Miao J., Xian F., Gu F., and Sun T. Leaf-like ZnO nanostructure and its excellent photocatalytic activity. *Materials Letters*, **2014**, 122, 1-4, <https://doi.org/10.1016/j.matlet.2014.01.182>.
- [61] Roza L., Fauzia V., and Rahman M.Y.A. Tailoring the active surface sites of ZnO nanorods on the glass substrate for photocatalytic activity enhancement. *Surfaces and Interfaces*, **2019**, 15, 117-124, <https://doi.org/10.1016/j.surfin.2019.02.009>.
- [62] Li X.Y., Wang J., Yang J.H., Lang J.H., Cao J., Liu F.Z., Fan H.G., Gao M., and Jiang Y.H. Size-controlled fabrication of ZnO micro/nanorod arrays and their photocatalytic performance. *Materials Chemistry and Physics*, **2013**, 141, 929-935, <https://doi.org/10.1016/j.matchemphys.2013.06.028>.
- [63] Pathak T.K., Kroon R.E., and Swart H.C. Photocatalytic and biological applications of Ag and Au doped ZnO nanomaterial synthesized by combustion. *Vacuum*, **2018**, 157, 508-513, <https://doi.org/10.1016/j.vacuum.2018.09.020>.
- [64] Lee Y., Fujimoto T., Yamanaka S., and Kuga Y. Evaluation of photocatalysis of Au supported ZnO prepared by the spray pyrolysis method. *Advanced Powder Technology*, **2021**, 32, 1619-1626, <https://doi.org/10.1016/j.apt.2021.03.025>.
- [65] Haldar K.K., Biswas R., Tanwar S., Sen T., and Lahtinen J. One-Pot Synthesis of Au Embedded ZnO Nanorods Composite Heterostructures with Excellent Photocatalytic Properties. *Chemistryselect*, **2018**, 3, 7882-7890, <https://doi.org/10.1002/slct.201801234>.
- [66] Misra M., Kapur P., and Singla M.L. Surface plasmon quenched of near band edge emission and enhanced visible photocatalytic activity of Au@ZnO core-shell nanostructure. *Applied Catalysis B-Environmental*, **2014**, 150, 605-611, <https://doi.org/10.1016/j.apcatb.2014.01.006>.

- [67] Chamjangali M.A., Bagherian G., Bahramian B., and Rad B.F. Synthesis and application of multiple rods gold-zinc oxide nanostructures in the photocatalytic degradation of methyl orange. *International Journal of Environmental Science and Technology*, **2015**, 12, 151-160, <https://doi.org/10.1007/s13762-014-0669-x>.
- [68] Zhu X., Wang J., Yang D., Liu J., He L., Tang M., Feng W., and Wu X. Fabrication, characterization and high photocatalytic activity of Ag–ZnO heterojunctions under UV-visible light. *RSC Advances*, **2021**, 11, 27257-27266, <https://doi.org/10.1039/D1RA05060E>.
- [69] Zheng Y., Zheng L., Zhan Y., Lin X., Zheng Q., and Wei K. Ag/ZnO Heterostructure Nanocrystals: Synthesis, Characterization, and Photocatalysis. *Inorganic Chemistry*, **2007**, 46, 6980-6986, <https://doi.org/10.1021/ic700688f>.
- [70] Pawinrat P., Mekasuwandumrong O., and Panpranot J. Synthesis of Au–ZnO and Pt–ZnO nanocomposites by one-step flame spray pyrolysis and its application for photocatalytic degradation of dyes. *Catalysis Communications*, **2009**, 10, 1380-1385, <https://doi.org/10.1016/j.catcom.2009.03.002>.
- [71] Peng S.-Y., Yang L., Yu L., Li X.-Y., Zhou Y.-Z., Lv Y., and Zhu F. Well-defined Pd anchoring on the surface of porous ZnO nanocomposites with excellent photocatalytic activity and good reusability for the removal of phenol from water. *New Journal of Chemistry*, **2019**, 43, 18034-18040, <https://doi.org/10.1039/C9NJ04127C>.
- [72] Zhang Y., Wang Q., Xu J., and Ma S. Synthesis of Pd/ZnO nanocomposites with high photocatalytic performance by a solvothermal method. *Applied Surface Science*, **2012**, 258, 10104-10109, <https://doi.org/10.1016/j.apsusc.2012.06.083>.
- [73] Yu C., Yang K., Zhou W., Fan Q., Wei L., and Yu J.C. Preparation, characterization and photocatalytic performance of noble metals (Ag, Pd, Pt, Rh) deposited on sponge-like ZnO microcuboids. *Journal of Physics and Chemistry of Solids*, **2013**, 74, 1714-1720, <https://doi.org/10.1016/j.jpcs.2013.06.014>.
- [74] Fragua D.M., Abargues R., Rodriguez-Canto P.J., Sanchez-Royo J.F., Agouram S., and Martinez-Pastor J.P. Au-ZnO Nanocomposite Films for Plasmonic Photocatalysis. *Advanced Materials Interfaces*, **2015**, 2, 10, <https://doi.org/10.1002/admi.201500156>.
- [75] Khiari M., Gilliot M., Lejeune M., Lazar F., and Hadjadj A. Effects of Ag Nanoparticles on Zinc Oxide Photocatalytic Performance. *Coatings*, **2021**, 11, 400, <https://doi.org/10.3390/coatings11040400>.
- [76] Yang T.H., Huang L.D., Harn Y.W., Lin C.C., Chang J.K., Wu C.I., and Wu J.M. High Density Unaggregated Au Nanoparticles on ZnO Nanorod Arrays Function as Efficient and Recyclable Photocatalysts for Environmental Purification. *Small*, **2013**, 9, 3169-3182, <https://doi.org/10.1002/sml.201300424>.
- [77] Lu J., Wang H., Peng D., Chen T., Dong S., and Chang Y. Synthesis and properties of Au/ZnO nanorods as a plasmonic photocatalyst. *Physica E: Low-dimensional Systems and Nanostructures*, **2016**, 78, 41-48, <https://doi.org/10.1016/j.physe.2015.11.035>.
- [78] Liu X., Li Z., Zhao W., Zhao C., Yang J., and Wang Y. Zinc Oxide nanorod/Au composite arrays and their enhanced photocatalytic properties. *Journal of Colloid and Interface Science*, **2014**, 432, 170-175, <https://doi.org/10.1016/j.jcis.2014.06.008>.

- [79] Sun Y.Y., Jiang L., Zeng T., Wei J., Liu L., Jin Y., Jiao Z.F., and Sun X.S. Synthesis of Au-ZnO hybrid nanostructure arrays and their enhanced photocatalytic activity. *New Journal of Chemistry*, **2015**, 39, 2943-2948, <https://doi.org/10.1039/c5nj00124b>.
- [80] Wu J.-J. and Tseng C.-H. Photocatalytic properties of nc-Au/ZnO nanorod composites. *Applied Catalysis B: Environmental*, **2006**, 66, 51-57, <https://doi.org/10.1016/j.apcatb.2006.02.013>.
- [81] Ren C., Yang B., Wu M., Xu J., Fu Z., lv Y., Guo T., Zhao Y., and Zhu C. Synthesis of Ag/ZnO nanorods array with enhanced photocatalytic performance. *Journal of Hazardous Materials*, **2010**, 182, 123-129, <https://doi.org/10.1016/j.jhazmat.2010.05.141>.
- [82] Mahardika T., Putri N.A., Putri A.E., Fauzia V., Roza L., Sugihartono I., and Herbani Y. Rapid and low temperature synthesis of Ag nanoparticles on the ZnO nanorods for photocatalytic activity improvement. *Results in Physics*, **2019**, 13, 102209, <https://doi.org/10.1016/j.rinp.2019.102209>.
- [83] Wu Z., Xue Y., Wang H., Wu Y., and Yu H. ZnO nanorods/Pt and ZnO nanorods/Ag heteronanostructure arrays with enhanced photocatalytic degradation of dyes. *RSC Advances*, **2014**, 4, 59009-59016, <https://doi.org/10.1039/C4RA10753E>.
- [84] Arifin M., Roza L., and Fauzia V. Bayberry-like Pt nanoparticle decorated ZnO nanorods for the photocatalytic application. *Results in Physics*, **2019**, 15, 102678, <https://doi.org/10.1016/j.rinp.2019.102678>.
- [85] Güy N. and Özacar M. The influence of noble metals on photocatalytic activity of ZnO for Congo red degradation. *International Journal of Hydrogen Energy*, **2016**, 41, 20100-20112, <https://doi.org/10.1016/j.ijhydene.2016.07.063>.
- [86] Hou W.B. and Cronin S.B. A Review of Surface Plasmon Resonance-Enhanced Photocatalysis. *Advanced Functional Materials*, **2013**, 23, 1612-1619, <https://doi.org/10.1002/adfm.201202148>.
- [87] Liu H., Hu Y., Zhang Z., Liu X., Jia H., and Xu B. Synthesis of spherical Ag/ZnO heterostructural composites with excellent photocatalytic activity under visible light and UV irradiation. *Applied Surface Science*, **2015**, 355, 644-652, <https://doi.org/10.1016/j.apsusc.2015.07.012>.
- [88] Wu J.J. and Tseng C.H. Photocatalytic properties of nc-Au/ZnO nanorod composites. *Applied Catalysis B-Environmental*, **2006**, 66, 51-57, <https://doi.org/10.1016/j.apcatb.2006.02.013>.
- [89] Pathak T.K., Swart H.C., and Kroon R.E. Structural and plasmonic properties of noble metal doped ZnO nanomaterials. *Physica B-Condensed Matter*, **2018**, 535, 114-118, <https://doi.org/10.1016/j.physb.2017.06.074>.
- [90] Vaiano V., Jaramillo-Paez C.A., Matarangolo M., Navío J.A., and del Carmen Hidalgo M. UV and visible-light driven photocatalytic removal of caffeine using ZnO modified with different noble metals (Pt, Ag and Au). *Materials Research Bulletin*, **2019**, 112, 251-260, <https://doi.org/10.1016/j.materresbull.2018.12.034>.
- [91] Low J.X., Yu J.G., Jaroniec M., Wageh S., and Al-Ghamdi A.A. Heterojunction Photocatalysts. *Advanced Materials*, **2017**, 29, 1601694, <https://doi.org/10.1002/adma.201601694>.
- [92] Wang Y., Li S., Shi H., and Yu K. Facile synthesis of p-type Cu₂O/n-type ZnO nano-heterojunctions with novel photoluminescence properties, enhanced field emission and photocatalytic activities. *Nanoscale*, **2012**, 4, 7817-7824, <https://doi.org/10.1039/C2NR32797J>.

- [93] Zhu L., Li H., Liu Z., Xia P., Xie Y., and Xiong D. Synthesis of the 0D/3D CuO/ZnO Heterojunction with Enhanced Photocatalytic Activity. *The Journal of Physical Chemistry C*, **2018**, 122, 9531-9539, <https://doi.org/10.1021/acs.jpcc.8b01933>.
- [94] Thampy U.S.U., Mahesh A., Sibi K.S., Jawahar I.N., and Biju V. Enhanced photocatalytic activity of ZnO-NiO nanocomposites synthesized through a facile sonochemical route. *Sn Applied Sciences*, **2019**, 1, 1478, <https://doi.org/10.1007/s42452-019-1426-z>.
- [95] Xiao M., Lu Y., Li Y., Song H., Zhu L., and Ye Z. A new type of p-type NiO/n-type ZnO nano-heterojunctions with enhanced photocatalytic activity. *RSC Advances*, **2014**, 4, 34649-34653, <https://doi.org/10.1039/C4RA04600E>.
- [96] Tian F. and Liu Y. Synthesis of p-type NiO/n-type ZnO heterostructure and its enhanced photocatalytic activity. *Scripta Materialia*, **2013**, 69, 417-419, <https://doi.org/10.1016/j.scriptamat.2013.05.040>.
- [97] Abdul Rahman I., Ayob M.T.M., and Radiman S. Enhanced Photocatalytic Performance of NiO-Decorated ZnO Nanowhiskers for Methylene Blue Degradation. *Journal of Nanotechnology*, **2014**, 2014, 212694, <https://doi.org/10.1155/2014/212694>.
- [98] Sabzehmeidani M.M., Karimi H., and Ghaedi M. Electrospinning preparation of NiO/ZnO composite nanofibers for photodegradation of binary mixture of rhodamine B and methylene blue in aqueous solution: Central composite optimization. *Applied Organometallic Chemistry*, **2018**, 32, e4335, <https://doi.org/10.1002/aoc.4335>.
- [99] Kanjwal M.A., Chronakis I.S., and Barakat N.A.M. Electrospun NiO, ZnO and composite NiO-ZnO nanofibers/photocatalytic degradation of dairy effluent. *Ceramics International*, **2015**, 41, 12229-12236, <https://doi.org/10.1016/j.ceramint.2015.06.045>.
- [100] Zhang Z.Y., Shao C.L., Li X.H., Wang C.H., Zhang M.Y., and Liu Y.C. Electrospun Nanofibers of p-Type NiO/n-Type ZnO Heterojunctions with Enhanced Photocatalytic Activity. *ACS Applied Materials & Interfaces*, **2010**, 2, 2915-2923, <https://doi.org/10.1021/am100618h>.
- [101] Yu X., Chen H., Ji Q., Chen Y., Wei Y., Zhao N., and Yao B. p-Cu₂O/n-ZnO heterojunction thin films with enhanced photoelectrochemical properties and photocatalytic activities for norfloxacin. *Chemosphere*, **2021**, 267, 129285, <https://doi.org/10.1016/j.chemosphere.2020.129285>.
- [102] Zou X., Fan H., Tian Y., and Yan S. Synthesis of Cu₂O/ZnO hetero-nanorod arrays with enhanced visible light-driven photocatalytic activity. *CrystEngComm*, **2014**, 16, 1149-1156, <https://doi.org/10.1039/C3CE42144A>.
- [103] Montero J., Welearegay T., Thyr J., Stopfel H., Dedova T., Acik I.O., and Österlund L. Copper-zinc oxide heterojunction catalysts exhibiting enhanced photocatalytic activity prepared by a hybrid deposition method. *RSC Advances*, **2021**, 11, 10224-10234, <https://doi.org/10.1039/D1RA00691F>.
- [104] Wei A., Xiong L., Sun L., Liu Y.J., and Li W.W. CuO Nanoparticle Modified ZnO Nanorods with Improved Photocatalytic Activity. *Chinese Physics Letters*, **2013**, 30, 046202, <https://doi.org/10.1088/0256-307x/30/4/046202>.
- [105] Huang J.H., Chen J.X., Tu Y.F., Tian Y., Zhou D., Zheng G., Sang J.P., and Fu Q.M. Preparation and photocatalytic activity of CuO/ZnO composite nanostructured films. *Materials Research Express*, **2019**, 6, 015035, <https://doi.org/10.1088/2053-1591/aae6ff>.

- [106] Pal S., Maiti S., Maiti U.N., and Chattopadhyay K.K. Low temperature solution processed ZnO/CuO heterojunction photocatalyst for visible light induced photo-degradation of organic pollutants. *CrystEngComm*, **2015**, 17, 1464-1476, <https://doi.org/10.1039/C4CE02159B>.
- [107] Periyannan S., Manceri L., Nguyen N.D., Klein A., Jaegermann W., Colson P., Henrist C., and Cloots R. Influence of ZnO Surface Modification on the Photocatalytic Performance of ZnO/NiO Thin Films. *Catalysis Letters*, **2019**, 149, 1813-1824, <https://doi.org/10.1007/s10562-019-02781-z>.
- [108] Wang H.L., Zhang L.S., Chen Z.G., Hu J.Q., Li S.J., Wang Z.H., Liu J.S., and Wang X.C. Semiconductor heterojunction photocatalysts: design, construction, and photocatalytic performances. *Chemical Society Reviews*, **2014**, 43, 5234-5244, <https://doi.org/10.1039/c4cs00126e>.
- [109] Poornajar M., Marashi P., Haghshenas Fatmehsari D., and Kolahdouz Esfahani M. Synthesis of ZnO nanorods via chemical bath deposition method: The effects of physicochemical factors. *Ceramics International*, **2016**, 42, 173-184, <https://doi.org/10.1016/j.ceramint.2015.08.073>.
- [110] Cao B. and Cai W. From ZnO Nanorods to Nanoplates: Chemical Bath Deposition Growth and Surface-Related Emissions. *The Journal of Physical Chemistry C*, **2008**, 112, 680-685, <https://doi.org/10.1021/jp076870l>.
- [111] Li X., Wang J., Yang J., Lang J., Lü S., Wei M., Meng X., Kou C., and Li X. Comparison of photocatalytic activity of ZnO rod arrays with various diameter sizes and orientation. *Journal of Alloys and Compounds*, **2013**, 580, 205-210, <https://doi.org/10.1016/j.jallcom.2013.05.037>.
- [112] Abdulrahman A.F., Ahmed S.M., Ahmed N.M., and Almessiere M.A. Enhancement of ZnO Nanorods Properties Using Modified Chemical Bath Deposition Method: Effect of Precursor Concentration. *Crystals*, **2020**, 10, 386, <https://doi.org/10.3390/cryst10050386>.
- [113] Akhmad Herman Yuwono L.S.N.S.D.D.G.R.A.S.C.H. Nanostructural Growth Investigation of ZnO Nanorods Derived from Chemical Bath Deposition for Transparent Heater Application. *International Journal of Technology*, **2018**, 9, 291-319, <https://doi.org/10.14716/ijtech.v9i6.2452>.
- [114] Kardeş M. and Öztürk K. Photocatalyst ZnO nanorod arrays on glass substrates: the critical role of seed layer in nanorod alignment and photocatalytic efficiencies. *Chemical Engineering Communications*, **2020**, 207, 1522-1535, <https://doi.org/10.1080/00986445.2019.1660651>.
- [115] Li X., Wang J., Yang J., Lang J., Cao J., Liu F., Fan H., Gao M., and Jiang Y. Size-controlled fabrication of ZnO micro/nanorod arrays and their photocatalytic performance. *Materials Chemistry and Physics*, **2013**, 141, 929-935, <https://doi.org/10.1016/j.matchemphys.2013.06.028>.
- [116] Fragalà M.E., Di Mauro A., Cristaldi D.A., Cantarella M., Impellizzeri G., and Privitera V. ZnO nanorods grown on ultrathin ZnO seed layers: Application in water treatment. *Journal of Photochemistry and Photobiology A: Chemistry*, **2017**, 332, 497-504, <https://doi.org/10.1016/j.jphotochem.2016.09.032>.
- [117] Baruah S. and Dutta J. Hydrothermal growth of ZnO nanostructures. *Science and Technology of Advanced Materials*, **2009**, 10, 18, <https://doi.org/10.1088/1468-6996/10/1/013001>.

- [118] Asim N., Ahmadi S., Alghoul M.A., Hammadi F.Y., Saeedfar K., and Sopian K. Research and Development Aspects on Chemical Preparation Techniques of Photoanodes for Dye Sensitized Solar Cells. *International Journal of Photoenergy*, **2014**, 2014, 518156, <https://doi.org/10.1155/2014/518156>.
- [119] Qiu J., Guo M., and Wang X. Electrodeposition of Hierarchical ZnO Nanorod-Nanosheet Structures and Their Applications in Dye-Sensitized Solar Cells. *ACS Applied Materials & Interfaces*, **2011**, 3, 2358-2367, <https://doi.org/10.1021/am2002789>.
- [120] Skompska M. and Zarebska K. Electrodeposition of ZnO Nanorod Arrays on Transparent Conducting Substrates—a Review. *Electrochimica Acta*, **2014**, 127, 467-488, <https://doi.org/10.1016/j.electacta.2014.02.049>.
- [121] Wang X., Li X., Zhang Q., Lu Z., Song H., and Wang Y. Electrodeposition of ZnO Nanorods with Synergistic Photocatalytic and Self-Cleaning Effects. *Journal of Electronic Materials*, **2021**, 50, 4954-4961, <https://doi.org/10.1007/s11664-021-08958-w>.
- [122] Lu H., Zhang M., and Guo M. Controllable electrodeposition of ZnO nanorod arrays on flexible stainless steel mesh substrate for photocatalytic degradation of Rhodamine B. *Applied Surface Science*, **2014**, 317, 672-681, <https://doi.org/10.1016/j.apsusc.2014.08.153>.
- [123] Lin Y., Yang J., and Zhou X. Controlled synthesis of oriented ZnO nanorod arrays by seed-layer-free electrochemical deposition. *Applied Surface Science*, **2011**, 258, 1491-1494, <https://doi.org/10.1016/j.apsusc.2011.09.113>.
- [124] Krunk M., Dedova T., and Oja Açıık I. Spray pyrolysis deposition of zinc oxide nanostructured layers. *Thin Solid Films*, **2006**, 515, 1157-1160, <https://doi.org/10.1016/j.tsf.2006.07.134>.
- [125] Dedova T., Krunk M., Grossberg M., Volobujeva O., and Oja Acik I. A novel deposition method to grow ZnO nanorods: Spray pyrolysis. *Superlattices and Microstructures*, **2007**, 42, 444-450, <https://doi.org/10.1016/j.spmi.2007.04.010>.
- [126] Dedova T., Klauson J., Badre C., Pauporté T., Nisumaa R., Mere A., Volobujeva O., and Krunk M. Chemical spray deposition of zinc oxide nanostructured layers from zinc acetate solutions. *physica status solidi (a)*, **2008**, 205, 2355-2359, <https://doi.org/10.1002/pssa.200779440>.
- [127] Zhao Q.X., Klason P., and Willander M. Growth of ZnO nanostructures by vapor-liquid-solid method. *Applied Physics A*, **2007**, 88, 27-30, <https://doi.org/10.1007/s00339-007-3958-0>.
- [128] Giri P.K., Dhara S., and Chakraborty R. Effect of ZnO seed layer on the catalytic growth of vertically aligned ZnO nanorod arrays. *Materials Chemistry and Physics*, **2010**, 122, 18-22, <https://doi.org/10.1016/j.matchemphys.2010.02.027>.
- [129] Zhang Z., Wang S.J., Yu T., and Wu T. Controlling the Growth Mechanism of ZnO Nanowires by Selecting Catalysts. *The Journal of Physical Chemistry C*, **2007**, 111, 17500-17505, <https://doi.org/10.1021/jp075296a>.
- [130] Nandi R. and Major S.S. The mechanism of growth of ZnO nanorods by reactive sputtering. *Applied Surface Science*, **2017**, 399, 305-312, <https://doi.org/10.1016/j.apsusc.2016.12.097>.
- [131] Chen M.T. and Ting J.M. Sputter deposition of ZnO nanorods/thin-film structures on Si. *Thin Solid Films*, **2006**, 494, 250-254, <https://doi.org/10.1016/j.tsf.2005.08.134>.

- [132] Baratto C. Growth and properties of ZnO nanorods by RF-sputtering for detection of toxic gases. *RSC Advances*, **2018**, 8, 32038-32043, <https://doi.org/10.1039/c8ra05357j>.
- [133] Liang Y.-C., Lung T.-W., and Xu N.-C. Photoexcited Properties of Tin Sulfide Nanosheet-Decorated ZnO Nanorod Heterostructures. *Nanoscale Research Letters*, **2017**, 12, 258, <https://doi.org/10.1186/s11671-017-2022-z>.
- [134] Sun Y., Fuge G.M., and Ashfold M.N.R. Growth mechanisms for ZnO nanorods formed by pulsed laser deposition. *Superlattices and Microstructures*, **2006**, 39, 33-40, <https://doi.org/10.1016/j.spmi.2005.08.029>.
- [135] Choopun S., Tabata H., and Kawai T. Self-assembly ZnO nanorods by pulsed laser deposition under argon atmosphere. *Journal of Crystal Growth*, **2005**, 274, 167-172, <https://doi.org/10.1016/j.jcrysgro.2004.10.017>.
- [136] Song J. and Lim S. Effect of Seed Layer on the Growth of ZnO Nanorods. *The Journal of Physical Chemistry C*, **2007**, 111, 596-600, <https://doi.org/10.1021/jp0655017>.
- [137] Horachit C., Moonnoi S., Ruankham P., Choopun S., and Intaniwet A. Effects of precursor concentration on hydrothermally grown ZnO nanorods as electron transporting layer in perovskite solar cells. *Materials Today: Proceedings*, **2017**, 17, 1217-1223, <https://doi.org/10.1016/j.matpr.2019.06.001>.
- [138] Guo M., Diao P., Wang X., and Cai S. The effect of hydrothermal growth temperature on preparation and photoelectrochemical performance of ZnO nanorod array films. *Journal of Solid State Chemistry*, **2005**, 178, 3210-3215, <https://doi.org/10.1016/j.jssc.2005.07.013>.
- [139] Mohd Fudzi L., Zainal Z., Lim H.N., Chang S.-K., Holi A.M., and Sarif@Mohd Ali M. Effect of Temperature and Growth Time on Vertically Aligned ZnO Nanorods by Simplified Hydrothermal Technique for Photoelectrochemical Cells. *Materials*, **2018**, 11, 704, <https://doi.org/doi:10.3390/ma11050704>.
- [140] Amin G., Asif M.H., Zainelabdin A., Zaman S., Nur O., and Willander M. Influence of pH, Precursor Concentration, Growth Time, and Temperature on the Morphology of ZnO Nanostructures Grown by the Hydrothermal Method. *Journal of Nanomaterials*, **2011**, 2011, 269692, <https://doi.org/10.1155/2011/269692>.
- [141] Yang G. and Park S.J. Conventional and Microwave Hydrothermal Synthesis and Application of Functional Materials: A Review. *Materials*, **2019**, 12, 1177, <https://doi.org/10.3390/ma12071177>.
- [142] Shi W., Song S., and Zhang H. Hydrothermal synthetic strategies of inorganic semiconducting nanostructures. *Chemical Society Reviews*, **2013**, 42, 5714-5743, <https://doi.org/10.1039/C3CS60012B>.
- [143] Patil P.S. and Kadam L.D. Preparation and characterization of spray pyrolyzed nickel oxide (NiO) thin films. *Applied Surface Science*, **2002**, 199, 211-221, [https://doi.org/10.1016/S0169-4332\(02\)00839-5](https://doi.org/10.1016/S0169-4332(02)00839-5).
- [144] Desai J.D., Min S.K., Jung K.D., and Joo O.S. Spray pyrolytic synthesis of large area NiOx thin films from aqueous nickel acetate solutions. *Applied Surface Science*, **2006**, 253, 1781-1786, <https://doi.org/10.1016/j.apsusc.2006.03.009>.
- [145] Kumar N., Lee H.B., Hwang S., and Kang J.-W. Large-area, green solvent spray deposited nickel oxide films for scalable fabrication of triple-cation perovskite solar cells. *Journal of Materials Chemistry A*, **2020**, 8, 3357-3368, <https://doi.org/10.1039/C9TA13528F>.

- [146] Ukoba K.O., Eloka-Eboka A.C., and Inambao F.L. Review of nanostructured NiO thin film deposition using the spray pyrolysis technique. *Renewable & Sustainable Energy Reviews*, **2018**, 82, 2900-2915, <https://doi.org/10.1016/j.rser.2017.10.041>.
- [147] Krunk M., Soon J., Unt T., Mere A., and Mikli V. Deposition of p-type NiO films by chemical spray pyrolysis. *Vacuum*, **2014**, 107, 242-246, <https://doi.org/10.1016/j.vacuum.2014.02.013>.
- [148] Joshi U.S., Matsumoto Y., Itaka K., Sumiya M., and Koinuma H. Combinatorial synthesis of Li-doped NiO thin films and their transparent conducting properties. *Applied Surface Science*, **2006**, 252, 2524-2528, <https://doi.org/10.1016/j.apsusc.2005.03.239>.
- [149] Renaud A., Chavillon B., Cario L., Pleux L.L., Szuwarski N., Pellegrin Y., Blart E., Gautron E., Odobel F., and Jobic S. Origin of the Black Color of NiO Used as Photocathode in p-Type Dye-Sensitized Solar Cells. *The Journal of Physical Chemistry C*, **2013**, 117, 22478-22483, <https://doi.org/10.1021/jp4055457>.
- [150] Seo S., Park I.J., Kim M., Lee S., Bae C., Jung H.S., Park N.-G., Kim J.Y., and Shin H. An ultra-thin, un-doped NiO hole transporting layer of highly efficient (16.4%) organic-inorganic hybrid perovskite solar cells. *Nanoscale*, **2016**, 8, 11403-11412, <https://doi.org/10.1039/C6NR01601D>.
- [151] Taeno M., Maestre D., and Cremades A. An approach to emerging optical and optoelectronic applications based on NiO micro- and nanostructures. *Nanophotonics*, **2021**, 10, 1785-1799, <https://doi.org/10.1515/nanoph-2021-0041>.
- [152] Lv P.P., Zhao H.L., Zeng Z.P., Gao C.H., Liu X., and Zhang T.H. Self-assembled three-dimensional hierarchical NiO nano/microspheres as high-performance anode material for lithium ion batteries. *Applied Surface Science*, **2015**, 329, 301-305, <https://doi.org/10.1016/j.apsusc.2014.12.170>.
- [153] Browne M.P., Nolan H., Berner N.C., Duesberg G.S., Colavita P.E., and Lyons M.E.G. Electrochromic Nickel Oxide Films for Smart Window Applications. *International Journal of Electrochemical Science*, **2016**, 11, 6636-6647, <https://doi.org/10.20964/2016.08.38>.
- [154] Nakate U.T., Ahmad R., Patil P., Yu Y.T., and Hahn Y.-B. Ultra thin NiO nanosheets for high performance hydrogen gas sensor device. *Applied Surface Science*, **2020**, 506, 144971, <https://doi.org/10.1016/j.apsusc.2019.144971>.
- [155] Yang D., Du F., Ren Y., Kang T., Hu P., Teng F., and Fan H. A high-performance NiO/TiO₂ UV photodetector: the influence of the NiO layer position. *Journal of Materials Chemistry C*, **2021**, 9, 14146-14153, <https://doi.org/10.1039/D1TC02687A>.
- [156] Huang C.X., Hao C., Zheng W.H., Zhou S.S., Yang L.Z., Wang X.H., Jiang C.L., and Zhu L.L. Synthesis of polyaniline/nickel oxide/sulfonated graphene ternary composite for all-solid-state asymmetric supercapacitor. *Applied Surface Science*, **2020**, 505, 144589, <https://doi.org/10.1016/j.apsusc.2019.144589>.
- [157] Ahmad J., Majid K., and Dar M.A. Controlled synthesis of p-type NiO/n-type GO nanocomposite with enhanced photocatalytic activity and study of temperature effect on the photocatalytic activity of the nanocomposite. *Applied Surface Science*, **2018**, 457, 417-426, <https://doi.org/10.1016/j.apsusc.2018.06.200>.

- [158] Christy A.J., Suresh S., and Nehru L.C. Enhanced antibacterial and photocatalytic activities of nickel oxide nanostructures. *Optik*, **2021**, 237, 166731, <https://doi.org/10.1016/j.ijleo.2021.166731>.
- [159] Zhang F., Liu Y.J., Liu Q.H., Li Q., Li H., Cai X.Y., and Wang Y.D. Synthesis and characterisation of Ni(OH)₂ and NiO nanosheets and their removal properties of azo dyes from aqueous solution. *Materials Technology*, **2013**, 28, 310-315, <https://doi.org/10.1179/1753555712Y.0000000052>.
- [160] Fazlali F., Mahjoub A.r., and Abazari R. A new route for synthesis of spherical NiO nanoparticles via emulsion nano-reactors with enhanced photocatalytic activity. *Solid State Sciences*, **2015**, 48, 263-269, <https://doi.org/10.1016/j.solidstate.sciences.2015.08.022>.
- [161] Gnanasekaran L., Hemamalini R., Saravanan R., Ravichandran K., Gracia F., Agarwal S., and Gupta V.K. Synthesis and characterization of metal oxides (CeO₂, CuO, NiO, Mn₃O₄, SnO₂ and ZnO) nanoparticles as photo catalysts for degradation of textile dyes. *Journal of Photochemistry and Photobiology B: Biology*, **2017**, 173, 43-49, <https://doi.org/10.1016/j.jphotobiol.2017.05.027>.
- [162] Duraisamy N., Kandiah K., Rajendran R., S P., R R., and Dhanaraj G. Electrochemical and photocatalytic investigation of nickel oxide for energy storage and wastewater treatment. *Research on Chemical Intermediates*, **2018**, 44, 5653-5667, <https://doi.org/10.1007/s11164-018-3446-5>.
- [163] Chaudhary S., Kaur Y., Jayee B., Chaudhary G.R., and Umar A. NiO nanodisks: Highly efficient visible-light driven photocatalyst, potential scaffold for seed germination of *Vigna Radiata* and antibacterial properties. *Journal of Cleaner Production*, **2018**, 190, 563-576, <https://doi.org/10.1016/j.jclepro.2018.04.110>.
- [164] Motahari F., Mozdianfard M.R., Soofivand F., and Salavati-Niasari M. NiO nanostructures: synthesis, characterization and photocatalyst application in dye wastewater treatment. *RSC Advances*, **2014**, 4, 27654-27660, <https://doi.org/10.1039/C4RA02697G>.
- [165] Wang Y., Zhang F., Wei L., Li G., and Zhang W. Facet-dependent photocatalytic performance of NiO oriented thin films prepared by pulsed laser deposition. *Physica B: Condensed Matter*, **2015**, 457, 194-197, <https://doi.org/10.1016/j.physb.2014.10.014>.
- [166] Al-Ghamdi A.A., Abdel-wahab M.S., Farghali A.A., and Hasan P.M.Z. Structural, optical and photo-catalytic activity of nanocrystalline NiO thin films. *Materials Research Bulletin*, **2016**, 75, 71-77, <https://doi.org/10.1016/j.materresbull.2015.11.027>.
- [167] Hayat K., Gondal M.A., Khaled M.M., and Ahmed S. Effect of operational key parameters on photocatalytic degradation of phenol using nano nickel oxide synthesized by sol-gel method. *Journal of Molecular Catalysis A: Chemical*, **2011**, 336, 64-71, <https://doi.org/10.1016/j.molcata.2010.12.011>.
- [168] Jana S., Samai S., Mitra B.C., Bera P., and Mondal A. Nickel oxide thin film from electrodeposited nickel sulfide thin film: peroxide sensing and photo-decomposition of phenol. *Dalton Trans.*, **2014**, 43, <https://doi.org/10.1039/c4dt01658k>.
- [169] Huang Y.F., Zhou Y.K., and Wang K.G. A kind of NiO nanofilm photocatalyst supported on nano-PAA substrate for efficient degradation of organic dye wastewater. *Environmental Science and Pollution Research*, **2020**, 27, 41503-41514, <https://doi.org/10.1007/s11356-020-10131-5>.

- [170] Chakhoum M.A., Boukhachem A., Ghamnia M., Benameur N., Mahdhi N., Raouadi K., and Amlouk M. An attempt to study (111) oriented NiO-like TCO thin films in terms of structural, optical properties and photocatalytic activities under strontium doping. *Spectrochimica Acta Part A: Molecular and Biomolecular Spectroscopy*, **2018**, 205, 649-660, <https://doi.org/10.1016/j.saa.2018.07.065>.
- [171] Chen J., Wang M., Han J., and Guo R. TiO₂ nanosheet/NiO nanorod hierarchical nanostructures: p–n heterojunctions towards efficient photocatalysis. *Journal of Colloid and Interface Science*, **2020**, 562, 313-321, <https://doi.org/10.1016/j.jcis.2019.12.031>.
- [172] Faisal M., Harraz F.A., Ismail A.A., El-Toni A.M., Al-Sayari S.A., Al-Hajry A., and Al-Assiri M.S. Novel mesoporous NiO/TiO₂ nanocomposites with enhanced photocatalytic activity under visible light illumination. *Ceramics International*, **2018**, 44, 7047-7056, <https://doi.org/10.1016/j.ceramint.2018.01.140>.
- [173] Chen C.-J., Liao C.-H., Hsu K.-C., Wu Y.-T., and Wu J.C.S. P–N junction mechanism on improved NiO/TiO₂ photocatalyst. *Catalysis Communications*, **2011**, 12, 1307-1310, <https://doi.org/10.1016/j.catcom.2011.05.009>.
- [174] Wang H., Gong Q., Huang H., Gao T., Yuan Z., and Zhou G. P-n heterostructured TiO₂/NiO double-shelled hollow spheres for the photocatalytic degradation of papermaking wastewater. *Materials Research Bulletin*, **2018**, 107, 397-406, <https://doi.org/10.1016/j.materresbull.2018.08.016>.
- [175] Peck M.A. and Langell M.A. Comparison of Nanoscaled and Bulk NiO Structural and Environmental Characteristics by XRD, XAFS, and XPS. *Chemistry of Materials*, **2012**, 24, 4483-4490, <https://doi.org/10.1021/cm300739y>.
- [176] Al-Ghamdi A.A., Mahmoud W.E., Yaghmour S.J., and Al-Marzouki F.M. Structure and optical properties of nanocrystalline NiO thin film synthesized by sol–gel spin-coating method. *Journal of Alloys and Compounds*, **2009**, 486, 9-13, <https://doi.org/10.1016/j.jallcom.2009.06.139>.
- [177] Zrikem K., Song G., Aghzzaf A.A., Amjoud M., Mezzane D., and Rougier A. UV treatment for enhanced electrochromic properties of spin coated NiO thin films. *Superlattices and Microstructures*, **2019**, 127, 35-42, <https://doi.org/10.1016/j.spmi.2018.03.042>.
- [178] Taşköprü T., Turan E., and Zor M. Characterization of NiO films deposited by homemade spin coater. *International Journal of Hydrogen Energy*, **2016**, 41, 6965-6971, <https://doi.org/10.1016/j.ijhydene.2015.12.008>.
- [179] Haider A.J., Al- Anbari R., Sami H.M., and Haider M.J. Photocatalytic Activity of Nickel Oxide. *Journal of Materials Research and Technology*, **2019**, 8, 2802-2808, <https://doi.org/10.1016/j.jmrt.2019.02.018>.
- [180] Koussi-Daoud S., Majerus O., Schaming D., and Pauporté T. Electrodeposition of NiO Films and Inverse Opal Organized Layers from Polar Aprotic Solvent-Based Electrolyte. *Electrochimica Acta*, **2016**, 219, 638-646, <https://doi.org/10.1016/j.electacta.2016.10.074>.
- [181] Pham N.S., Phan P.T.Q., and Le V.X. Porous NiO via pulsed electrodeposition towards enhanced electrochromic properties. *Journal of Applied Electrochemistry*, <https://doi.org/10.1007/s10800-022-01716-8>.
- [182] Ghalmi Y., Habelhames F., Sayah A., Bahloul A., Nessark B., Shalabi M., and Nunzi J.M. Capacitance performance of NiO thin films synthesized by direct and pulse potentiostatic methods. *Ionics*, **2019**, 25, 6025-6033, <https://doi.org/10.1007/s11581-019-03159-2>.

- [183] Qi X.Y., Su G., Bo G.S., Cao L.X., and Liu W. Synthesis of NiO and NiO/TiO₂ films with electrochromic and photocatalytic activities. *Surface & Coatings Technology*, **2015**, 272, 79-85, <https://doi.org/10.1016/j.surfcoat.2015.04.020>.
- [184] Hotový I., Huran J., Spiess L., Čapkovic R., and Haščík Š. Preparation and characterization of NiO thin films for gas sensor applications. *Vacuum*, **2000**, 58, 300-307, [https://doi.org/10.1016/S0042-207X\(00\)00182-2](https://doi.org/10.1016/S0042-207X(00)00182-2).
- [185] Wang H., Zhao Y., Li X., Zhen Z., Li H., Wang J., and Tang M. Effect of Sputtering Temperature on Structure and Optical Properties of NiO Films Fabricated by Magnetron Sputtering. *Journal of Electronic Materials*, **2017**, 46, 4052-4056, <https://doi.org/10.1007/s11664-017-5453-5>.
- [186] Fasaki I., Koutoulaki A., Kompitsas M., and Charitidis C. Structural, electrical and mechanical properties of NiO thin films grown by pulsed laser deposition. *Applied Surface Science*, **2010**, 257, 429-433, <https://doi.org/10.1016/j.apsusc.2010.07.006>.
- [187] Mooney J.B. and Radding S.B. Spray Pyrolysis Processing. *Annual Review of Materials Science*, **1982**, 12, 81-101, <https://doi.org/10.1146/annurev.ms.12.080182.000501>.
- [188] Perednis D. and Gauckler L.J. Thin film deposition using spray pyrolysis. *Journal of Electroceramics*, **2005**, 14, 103-111, <https://doi.org/10.1007/s10832-005-0870-x>.
- [189] Jung D.S., Park S.B., and Kang Y.C. Design of particles by spray pyrolysis and recent progress in its application. *Korean Journal of Chemical Engineering*, **2010**, 27, 1621-1645, <https://doi.org/10.1007/s11814-010-0402-5>.
- [190] Patil P.S. Versatility of chemical spray pyrolysis technique. *Materials Chemistry and Physics*, **1999**, 59, 185-198, [https://doi.org/10.1016/S0254-0584\(99\)00049-8](https://doi.org/10.1016/S0254-0584(99)00049-8).
- [191] Kamal H., Elmaghraby E.K., Ali S.A., and Abdel-Hady K. Characterization of nickel oxide films deposited at different substrate temperatures using spray pyrolysis. *Journal of Crystal Growth*, **2004**, 262, 424-434, <https://doi.org/10.1016/j.jcrysgro.2003.10.090>.
- [192] Gomaa M.M., Yazdi G.R., Schmidt S., Boshta M., Khranovskyy V., Eriksson F., Farag B.S., Osman M.B.S., and Yakimova R. Effect of precursor solutions on the structural and optical properties of sprayed NiO thin films. *Materials Science in Semiconductor Processing*, **2017**, 64, 32-38, <https://doi.org/10.1016/j.mssp.2017.03.009>.
- [193] Kate R.S., Bulakhe S.C., and Deokate R.J. Effect of Substrate Temperature on Properties of Nickel Oxide (NiO) Thin Films by Spray Pyrolysis. *Journal of Electronic Materials*, **2019**, 48, 3220-3228, <https://doi.org/10.1007/s11664-019-07074-0>.
- [194] Mahmoud S.A., Alshomer S., and Tarawnh M.a.A. Structural and optical dispersion characterisation of sprayed nickel oxide thin films. *Journal of Modern Physics*, **2011**, 2, 1178-1186, <https://doi.org/10.4236/jmp.2011.210147>.
- [195] Reguig B.A., Regragui M., Morsli M., Khelil A., Addou M., and Bernede J.C. Effect of the precursor solution concentration on the NiO thin film properties deposited by spray pyrolysis. *Solar Energy Materials and Solar Cells*, **2006**, 90, 1381-1392, <https://doi.org/10.1016/j.solmat.2005.10.003>.
- [196] Yadav A.A. and Chavan U.J. Influence of substrate temperature on electrochemical supercapacitive performance of spray deposited nickel oxide thin films. *Journal of Electroanalytical Chemistry*, **2016**, 782, 36-42, <https://doi.org/10.1016/j.jelechem.2016.10.006>.

- [197] Chan X.H., Jennings J.R., Hossain M.A., Yu K.K.Z., and Wang Q. Characteristics of p-NiO Thin Films Prepared by Spray Pyrolysis and Their Application in CdS-sensitized Photocathodes. *Journal of the Electrochemical Society*, **2011**, 158, H733-H740, <https://doi.org/10.1149/1.3590742>.
- [198] Messing G.L., Zhang S.C., and Jayanthi G.V. Ceramic Powder Synthesis by Spray-Pyrolysis. *Journal of the American Ceramic Society*, **1993**, 76, 2707-2726, <https://doi.org/10.1111/j.1151-2916.1993.tb04007.x>.
- [199] Wang W.-N., Purwanto A., Lenggono I.W., Okuyama K., Chang H., and Jang H.D. Investigation on the Correlations between Droplet and Particle Size Distribution in Ultrasonic Spray Pyrolysis. *Industrial & Engineering Chemistry Research*, **2008**, 47, 1650-1659, <https://doi.org/10.1021/ie070821d>.
- [200] Wang S.-Y., Wang W., Wang W.-Z., and Du Y.-W. Preparation and characterization of highly oriented NiO(200) films by a pulse ultrasonic spray pyrolysis method. *Materials Science and Engineering: B*, **2002**, 90, 133-137, [https://doi.org/10.1016/S0921-5107\(01\)00922-9](https://doi.org/10.1016/S0921-5107(01)00922-9).
- [201] Scheideler W.J., Rolston N., Zhao O., Zhang J.B., and Dauskardt R.H. Rapid Aqueous Spray Fabrication of Robust NiO_x: A Simple and Scalable Platform for Efficient Perovskite Solar Cells. *Advanced Energy Materials*, **2019**, 9, 1803600, <https://doi.org/10.1002/aenm.201803600>.
- [202] Tenent R.C., Gillaspie D.T., Miedaner A., Parilla P.A., Curtis C.J., and Dillon A.C. Fast-Switching Electrochromic Li+-Doped NiO Films by Ultrasonic Spray Deposition. *Journal of the Electrochemical Society*, **2010**, 157, H318-H322, <https://doi.org/10.1149/1.3279992>.
- [203] Denayer J., Bister G., Simonis P., Colson P., Maho A., Aubry P., Vertruyen B., Henrist C., Lardot V., Cambier F., and Cloots R. Surfactant-assisted ultrasonic spray pyrolysis of nickel oxide and lithium-doped nickel oxide thin films, toward electrochromic applications. *Applied Surface Science*, **2014**, 321, 61-69, <https://doi.org/10.1016/j.apsusc.2014.09.128>.
- [204] Hameed A., Montini T., Gombac V., and Fornasiero P. Photocatalytic decolourization of dyes on NiO-ZnO nano-composites. *Photochemical & Photobiological Sciences*, **2009**, 8, 677-682, <https://doi.org/10.1039/B817396F>.
- [205] Derikvandi H. and Nezamzadeh-Ejehieh A. Increased photocatalytic activity of NiO and ZnO in photodegradation of a model drug aqueous solution: Effect of coupling, supporting, particles size and calcination temperature. *Journal of Hazardous Materials*, **2017**, 321, 629-638, <https://doi.org/10.1016/j.jhazmat.2016.09.056>.
- [206] Liu Y., Li G., Mi R., Deng C., and Gao P. An environment-benign method for the synthesis of p-NiO/n-ZnO heterostructure with excellent performance for gas sensing and photocatalysis. *Sensors and Actuators B: Chemical*, **2014**, 191, 537-544, <https://doi.org/10.1016/j.snb.2013.10.068>.
- [207] Nazim M., Khan A.A.P., Asiri A.M., and Kim J.H. Exploring Rapid Photocatalytic Degradation of Organic Pollutants with Porous CuO Nanosheets: Synthesis, Dye Removal, and Kinetic Studies at Room Temperature. *ACS Omega*, **2021**, 6, 2601-2612, <https://doi.org/10.1021/acsomega.0c04747>.
- [208] Otto K., Oja Acik I., Krunks M., Tõnsuaadu K., and Mere A. Thermal decomposition study of HAuCl₄·3H₂O and AgNO₃ as precursors for plasmonic metal nanoparticles. *Journal of Thermal Analysis and Calorimetry*, **2014**, 118, 1065-1072, <https://doi.org/10.1007/s10973-014-3814-3>.

- [209] Nkosi S.S., Yalisi B., Motaung D.E., Keartland J., Sideras-Haddad E., Forbes A., and Mwakikunga B.W. Antiferromagnetic-paramagnetic state transition of NiO synthesized by pulsed laser deposition. *Applied Surface Science*, **2013**, 265, 860-864, <https://doi.org/10.1016/j.apsusc.2012.11.134>.
- [210] Marciuš M., Ristić M., Ivanda M., and Musić S. Formation and microstructure of nickel oxide films. *Journal of Alloys and Compounds*, **2012**, 541, 238-243, <https://doi.org/10.1016/j.jallcom.2012.07.021>.
- [211] Mrabet C., Ben Amor M., Boukhachem A., Amlouk M., and Manoubi T. Physical properties of La-doped NiO sprayed thin films for optoelectronic and sensor applications. *Ceramics International*, **2016**, 42, 5963-5978, <https://doi.org/10.1016/j.ceramint.2015.12.144>.
- [212] Chandoul F., Moussa H., Jouini K., Boukhachem A., Hosni F., Fayache M.S., and Schneider R. Investigation of the properties of nanostructured nickel oxide NiO thin films irradiated at different γ -doses. *Journal of Materials Science: Materials in Electronics*, **2019**, 30, 348-358, <https://doi.org/10.1007/s10854-018-0299-z>.
- [213] Jiang D.Y., Qin J.M., Wang X., Gao S., Liang Q.C., and Zhao J.X. Optical properties of NiO thin films fabricated by electron beam evaporation. *Vacuum*, **2012**, 86, 1083-1086, <https://doi.org/10.1016/j.vacuum.2011.10.003>.
- [214] Kumari L., Li W.Z., Vannoy C.H., Leblanc R.M., and Wang D.Z. Vertically aligned and interconnected nickel oxide nanowalls fabricated by hydrothermal route. *Crystal Research and Technology*, **2009**, 44, 495-499, <https://doi.org/10.1002/crat.200800583>.
- [215] Vidales-Hurtado M.A. and Mendoza-Galvan A. Electrochromism in nickel oxide-based thin films obtained by chemical bath deposition. *Solid State Ionics*, **2008**, 179, 2065-2068, <https://doi.org/10.1016/j.ssi.2008.07.003>.
- [216] Bodurov G., Stefchev P., Ivanova T., and Gesheva K. Investigation of electrodeposited NiO films as electrochromic material for counter electrodes in "Smart Windows". *Materials Letters*, **2014**, 117, 270-272, <https://doi.org/10.1016/j.matlet.2013.11.118>.
- [217] Dietz R.E., Parisot G.I., and Meixner A.E. Infrared Absorption and Raman Scattering by Two-Magnon Processes in NiO. *Physical Review B*, **1971**, 4, 7, <https://doi.org/10.1103/PhysRevB.4.2302>.
- [218] Mironova-Ulmane N., Kuzmin A., Sildos I., and Pars M. Polarisation dependent Raman study of single-crystal nickel oxide. *Central European Journal of Physics*, **2011**, 9, 1096-1099, <https://doi.org/10.2478/s11534-010-0130-9>.
- [219] Gowthami V., Perumal P., Sivakumar R., and Sanjeeviraja C. Structural and optical studies on nickel oxide thin film prepared by nebulizer spray technique. *Physica B-Condensed Matter*, **2014**, 452, 1-6, <https://doi.org/10.1016/j.physb.2014.06.030>.
- [220] Dundar I., Mere A., Mikli V., Krunk M., and Oja Acik I. Thickness Effect on Photocatalytic Activity of TiO₂ Thin Films Fabricated by Ultrasonic Spray Pyrolysis. *Catalysts*, **2020**, 10, 1058, <https://doi.org/10.3390/catal10091058>.
- [221] Karimi-Shamsabadi M., Behpour M., Babaheidari A.K., and Saberi Z. Efficiently enhancing photocatalytic activity of NiO-ZnO doped onto nanozeoliteX by synergistic effects of p-n heterojunction, supporting and zeolite nanoparticles in photo-degradation of Eriochrome Black T and Methyl Orange. *Journal of Photochemistry and Photobiology a-Chemistry*, **2017**, 346, 133-143, <https://doi.org/10.1016/j.jphotochem.2017.05.038>.

- [222] Tian F.S. and Liu Y.L. Synthesis of p-type NiO/n-type ZnO heterostructure and its enhanced photocatalytic activity. *Scripta Materialia*, **2013**, 69, 417-419, <https://doi.org/10.1016/j.scriptamat.2013.05.040>.
- [223] Li J.N., Zhao F., Zhang L., Zhang M.Y., Jiang H.F., Li S., and Li J.F. Electrospun hollow ZnO/NiO heterostructures with enhanced photocatalytic activity. *RSC Advances*, **2015**, 5, 67610-67616, <https://doi.org/10.1039/c5ra08903d>.
- [224] Liu S.Y., Liu R., Chen Y., Ho S.H., Kim J.H., and So F. Nickel Oxide Hole Injection/Transport Layers for Efficient Solution-Processed Organic Light-Emitting Diodes. *Chemistry of Materials*, **2014**, 26, 4528-4534, <https://doi.org/10.1021/cm501898y>.
- [225] Biesinger M.C., Lau L.W.M., Gerson A.R., and Smart R.S.C. The role of the Auger parameter in XPS studies of nickel metal, halides and oxides. *Physical Chemistry Chemical Physics*, **2012**, 14, 2434-2442, <https://doi.org/10.1039/c2cp22419d>.
- [226] Gomaa M.M., RezaYazdi G., Rodner M., Greczynski G., Boshta M., Osman M.B.S., Khranovskyy V., Eriksson J., and Yakimova R. Exploring NiO nanosize structures for ammonia sensing. *Journal of Materials Science-Materials in Electronics*, **2018**, 29, 11870-11877, <https://doi.org/10.1007/s10854-018-9287-6>.
- [227] Tian Y., Gong L.G., Qi X.Q., Yang Y.B., and Zhao X.D. Effect of Substrate Temperature on the Optical and Electrical Properties of Nitrogen-Doped NiO Thin Films. *Coatings*, **2019**, 9, 634, <https://doi.org/10.3390/coatings9100634>.
- [228] Berkat L., Cattin L., Reguig A., Regragui M., and Bernede J.C. Comparison of the physico-chemical properties of NiO thin films deposited by chemical bath deposition and by spray pyrolysis. *Materials Chemistry and Physics*, **2005**, 89, 11-20, <https://doi.org/10.1016/j.matchemphys.2004.07.005>.
- [229] Dundar I., Krichevskaya M., Katerski A., and Acik I.O. TiO₂ thin films by ultrasonic spray pyrolysis as photocatalytic material for air purification. *Royal Society Open Science*, **2019**, 6, 181578, <https://doi.org/10.1098/rsos.181578>.
- [230] Mansour A.N. and Melendres C.A. Characterization of Ni₂O₃·6H₂O by XPS. *Surface Science Spectra*, **1994**, 3, 263, <https://doi.org/10.1116/1.1247755>.
- [231] Xi S., Zhu Y.L., Yang Y.T., Jiang S.L., and Tang Z.R. Facile Synthesis of Free-Standing NiO/MnO₂ Core-Shell Nanoflakes on Carbon Cloth for Flexible Supercapacitors. *Nanoscale Research Letters*, **2017**, 12, 171, <https://doi.org/10.1186/s11671-017-1939-6>.
- [232] Oluwabi A.T., Katerski A., Carlos E., Branquinho R., Mere A., Krunks M., Fortunato E., Pereira L., and Oja Acik I. Application of ultrasonic sprayed zirconium oxide dielectric in zinc tin oxide-based thin film transistor. *Journal of Materials Chemistry C*, **2020**, 8, 3730-3739, <https://doi.org/10.1039/C9TC05127A>.
- [233] Claros M., Setka M., Jimenez Y.P., and Vallejos S. AACVD Synthesis and Characterization of Iron and Copper Oxides Modified ZnO Structured Films. *Nanomaterials*, **2020**, 10, 471, <https://doi.org/10.3390/nano10030471>.
- [234] Pal A., Dey T.K., Singhal A., Bindal R.C., and Tewari P.K. Nano-ZnO impregnated inorganic-polymer hybrid thinfilm nanocomposite nanofiltration membranes: an investigation of variation in structure, morphology and transport properties. *RSC Advances*, **2015**, 5, 34134-34151, <https://doi.org/10.1039/c4ra14854a>.
- [235] Wang M., Jiang L., Kim E.J., and Hahn S.H. Electronic structure and optical properties of Zn(OH)₂: LDA+U calculations and intense yellow luminescence. *RSC Advances*, **2015**, 5, 87496-87503, <https://doi.org/10.1039/C5RA17024A>.

- [236] Dedova T., Acik I.O., Chen Z., Katerski A., Balmassov K., Gromyko I., Nagyné-Kovács T., Szilágyi I.M., and Krunk M. Enhanced photocatalytic activity of ZnO nanorods by surface treatment with H₂AuCl₄: Synergic effects through an electron scavenging, plasmon resonance and surface hydroxylation. *Materials Chemistry and Physics*, **2020**, 245, 122767, <https://doi.org/10.1016/j.matchemphys.2020.122767>.
- [237] Al-Gaashani R., Radiman S., Daud A.R., Tabet N., and Al-Douri Y. XPS and optical studies of different morphologies of ZnO nanostructures prepared by microwave methods. *Ceramics International*, **2013**, 39, 2283-2292, <https://doi.org/10.1016/j.ceramint.2012.08.075>.
- [238] Sakamoto K., Hayashi F., Sato K., Hirano M., and Ohtsu N. XPS spectral analysis for a multiple oxide comprising NiO, TiO₂, and NiTiO₃. *Applied Surface Science*, **2020**, 526, 146729, <https://doi.org/10.1016/j.apsusc.2020.146729>.
- [239] Tian H., Fan H., Dong G., Ma L., and Ma J. NiO/ZnO p–n heterostructures and their gas sensing properties for reduced operating temperature. *RSC Advances*, **2016**, 6, 109091-109098, <https://doi.org/10.1039/C6RA19520B>.
- [240] Zhang Z., Shao C., Li X., Wang C., Zhang M., and Liu Y. Electrospun Nanofibers of p-Type NiO/n-Type ZnO Heterojunctions with Enhanced Photocatalytic Activity. *ACS Applied Materials & Interfaces*, **2010**, 2, 2915-2923, <https://doi.org/10.1021/am100618h>.
- [241] Spalatu N., Krautmann R., Katerski A., Karber E., Josepson R., Hiie J., Acik I.O., and Krunk M. Screening and optimization of processing temperature for Sb₂Se₃ thin film growth protocol: Interrelation between grain structure, interface intermixing and solar cell performance. *Solar Energy Materials and Solar Cells*, **2021**, 225, 111045, <https://doi.org/10.1016/j.solmat.2021.111045>.

Acknowledgements

I would like to express my most sincerely thanks to my supervisors Prof. Malle Krunk and Senior researcher Dr. Tatjana Dedova for their careful guidance, support, patience, and motivation during the years of my doctoral study.

I would like to extend my sincere thanks to Prof. Ilona Oja Açıık, the co-authors and colleagues at Laboratory of Thin Film Chemical Technologies and Department of Materials and Environmental Technology for their insightful comments and suggestions. I am thankful to Dr. Mati Danilson for the XPS measurements and Dr. Valdek Mikli, Dr. Olga Volobujeva for the SEM measurements at Laboratory of Photovoltaic Materials, TalTech. I am thankful to Dr. Natalia Maticiuc for the XPS measurements and Dr. Marin Rusu for the KP and PYS measurements at Helmholtz-Zentrum Berlin.

I would like to acknowledge the following research projects for financing support for my PhD study.: The research projects financed by the Estonian Research Council: IUT 19-4 “Thin films and nanomaterials by wet-chemical methods for next-generation photovoltaics”, PRG627 “Antimony-chalcogenide thin films for next-generation semi-transparent solar cells applicable in electricity producing windows”, the Estonian Centre of Excellence project TK141 (TAR16016EK) “Advanced materials and high-technology devices for energy recuperation systems”, the European Commission’s H2020 programme under the ERA Chair project 5GSOLAR grant agreement No 952509, and ASTRA “TUT Institutional Development Programme for 2016-2022” Graduate School of Functional Materials and Technologies (2014-2020.4.01.16-0032).

I am deeply thankful to my family members for their unwavering support and belief in me.

Abstract

Development of ZnO Nanorod and NiO Thin Film based Materials for Photocatalytic Applications

Photocatalysis as one of the advanced oxidation processes emerged as promising technology for wastewater treatment. Photocatalysis employs semiconductors (TiO_2 , ZnO, NiO, CdS, etc) as photocatalysts that under light irradiation are able to degrade various organic pollutants. Among these semiconductors, TiO_2 is the mostly studied photocatalyst due to its excellent photocatalytic activity, nontoxicity, and chemical stability. In addition, ZnO is also considered as a promising photocatalytic material due to its abundance, low cost, and ease of synthesis in various morphologies. Nonetheless, ZnO photocatalyst suffers from rapid recombination of photogenerated electron-hole pairs, thereby decreasing photocatalytic activity. To suppress the recombination of photogenerated carriers and improve photocatalytic performance, ZnO has been coupled with noble metals or semiconductors. NiO is another promising metal oxide based photocatalyst that attracted great interest by scientists worldwide. NiO has been used for photocatalytic studies due to its tunable bandgap, low cost, chemical stability and ability to mineralize organic pollutants. As a p-type semiconductor, NiO is also a suitable candidate for coupling with ZnO to form a p-n heterojunction to suppress the recombination of photogenerated electron-hole pairs and improve photocatalytic activity of ZnO.

To date, ZnO and NiO based photocatalysts have been mainly studied in their powder form. However, photocatalyst in powder form has the severe disadvantages such as particle agglomeration and difficulty of separation from wastewater, causing secondary pollution. From this perspective, developing photocatalysts immobilized on substrates is a more suitable approach that allows ease of separation and recovery of photocatalyst from wastewater. Therefore, the forms of ZnO nanorods (ZnO_{NR}) and NiO films grown on substrates have been chosen for this study.

The overall aim of this thesis was to develop the strategies for the synthesis of ZnO nanorods and NiO film based materials as efficient photocatalytic coatings on glass substrates by low-cost chemical solution methods such as hydrothermal growth and chemical spray pyrolysis. To reach the aim, three main tasks were set: 1) to synthesize $\text{ZnO}_{\text{NR}}/\text{Au}$ composite through the surface treatment of ZnO_{NR} by HAuCl_4 solution and to study the physico-chemical properties of the composite; 2) to synthesize NiO films by pneumatic spray pyrolysis technique using nickel acetate as precursor material and to study the effect of deposition temperature and solvent type on the physico-chemical properties and PA of NiO films; 3) to synthesize thin continuous layers of NiO by ultrasonic spray method using nickel acetylacetonate as precursor material, to characterize the physico-chemical properties in NiO films, apply NiO film to form ZnO/NiO bilayer and $\text{ZnO}_{\text{NR}}/\text{NiO}$ core-shell heterostructures and to study photocatalytic performance of heterostructures.

$\text{ZnO}_{\text{NR}}/\text{Au}$ composites were fabricated by spin-coating HAuCl_4 solutions with different concentrations, 0.005, 0.01, and 0.03 mol/L onto hydrothermally grown ZnO_{NR} surfaces followed by thermal annealing at 400 °C. XRD and SEM studies confirmed the formation of Au nanoparticles (NPs) on ZnO_{NR} . The size of Au NPs is ca. 20-70 nm depending on the concentration of HAuCl_4 solution. The absorbance spectra of $\text{ZnO}_{\text{NR}}/\text{Au}$ composites indicated the increase of optical absorbance in the visible light range. XPS study revealed

the 2.5 fold increase in the amount of surface hydroxyl groups from ZnO_{NR}/Au composite with Au NPs from 0.01 mol/L HAuCl₄ solution, compared to bare ZnO_{NR}. Employment of HAuCl₄ solution with concentration of 0.01 mol/L resulted in ZnO_{NR}/Au composite showing the highest MO degradation efficiency of 94 % in 3 h compared to 65% by bare ZnO_{NR} under UV light irradiation. Nearly twice higher MO degradation efficiency under visible light by ZnO_{NR}/Au composites (ca 40 % in 3 h) compared to that by pristine ZnO_{NR} (21 % in 3 h) is explained by occurrence the absorption band in visible spectral region, at 500-600 nm due to the surface plasmon resonance effect.

NiO films were synthesized at 300-420 °C from nickel acetate aqueous and alcoholic solutions by pneumatic spray pyrolysis method. Films prepared from aqueous solution are of polycrystalline NiO with crystallite size of 4-10 nm, but films from alcoholic solution are amorphous according to XRD study. Bandgap of NiO films produced from aqueous and alcoholic solutions is 3.4 eV and 4.0 eV, respectively, irrespective of the deposition temperature. It was found that the temperature is a key factor that influences the photocatalytic activity of the films. The photocatalytically more active NiO films were grown at 300 °C. The surfaces of those films were highly hydrophilic (water contact angle = 8°) and contain relatively high amount of hydroxide groups (atomic ratio of Ni(OH)₂/NiO= 3.31). The amount of surface hydroxyl groups gradually decreases with an increase in deposition temperature, with subsequent decrease in the PA of MO. The MO degradation efficiency under UV light by NiO films produced at 300 °C from aqueous solution was 45% in 3 h and decreased to 11% in 3h for the film grown at 420 °C. The decrease in PA of NiO films with increasing the deposition temperature correlates to the decrease in the amount of hydroxyl groups on the surface of NiO film.

It was shown that homogenous transparent polycrystalline NiO films with E_g of 3.7 eV are obtained by ultrasonic spray pyrolysis technique at temperatures 350-500 °C using nickel acetylacetonate as precursor material. The NiO layer deposition temperature of 500 °C was found to be optimal for ZnO/NiO heterostructure fabrication as the MB degradation efficiency by ZnO/NiO bilayer increased from 8 to 30% with increasing the NiO deposition temperature from 350 to 500 °C. Results of the study showed that photocatalytically efficient ZnO_{NR}/NiO core-shell heterostructures could be obtained using for NiO shell deposition two USP cycles at 500 °C followed by annealing the heterostructure at 600 °C in air. ZnO_{NR}/NiO core-shell heterostructure with the shell thickness from two spray cycles show MB degradation efficiency of 70% compared to 53% by ZnO_{NR} as measured under UV irradiation for 3 h.

The formation of ZnO_{NR}/NiO n-p core shell heterostructure was confirmed applying advanced physical characterization techniques. XPS analysis confirmed the formation of NiO shell on ZnO core and showed a 1.9–2.0 eV difference in modified Auger parameter between ZnO_{NR} and ZnO_{NR}/NiO core-shell heterostructure, validating the presence of built-in electric field at the interface. A type-II band diagram between NiO and ZnO_{NR} is proposed based on Kelvin probe and photoelectron yield spectroscopy measurements. In this study we proved that enhanced photocatalytic performance of ZnO_{NR}/NiO heterostructures is due to improved separation of photogenerated in ZnO electron–hole pairs at n-p heterointerface.

The novelty of the thesis lies in the following: 1) Au NPs were produced by spin-coating of HAuCl₄ solution onto ZnO_{NR} layers followed by heat treatment to form ZnO_{NR}/Au composite with enhanced PA 2) by systematic study the effect of deposition conditions on surface properties of pneumatically sprayed NiO films we showed that the deposition temperature is the main technological parameter controlling the content of surface

hydroxyl groups on the film surface, and consequently, the film photocatalytic performance 3) homogeneous crystalline films of NiO with cubic structure can be successfully grown on different substrates by employing a robust ultrasonic spray technique and nickel acetylacetonate as a source material. For the first time ultrasonically sprayed NiO film was applied to ZnO_{NR} layer to form ZnO_{NR}/NiO core-shell heterostructure demonstrating significantly enhanced photocatalytic performance compared to pristine ZnO_{NR}.

In this thesis study feasible, cost-effective and scientifically evidenced strategies for the synthesis of ZnO nanorod and NiO film based materials as efficient photocatalysts on glass substrates by chemical solution methods such as hydrothermal growth and chemical spray pyrolysis are presented.

Lühikokkuvõte

ZnO nanovarrastel ja NiO õhukestel kiledel baseeruvate fotokatalüütiliste materjalide arendus

Fotokatalüüs on üks eesrindlikest süvaoksüdatsiooni protsessidest orgaaniliste jääkainete lagundamiseks reovees. Fotokatalüüsi protsessis kasutatakse fotokatalüsaatoritena pooljuhtmaterjale nagu TiO_2 , ZnO, NiO, CdS, jt. Pooljuhi valgustamisel valgusega, mille kvandi energia on suurem kui pooljuhi keelutsooni laius, tekitatakse elektron-auk paare, mis pooljuhi pinnal omakorda tekitavad vabu radikaale, mille toimel orgaanilised saasteained lagundatakse. TiO_2 on kõige laialdasemalt uuritud materjal tänu oma väga heale fotokatalüütilisele võimekusele, mittetoksisusele ja keemilisele stabiilsusele. ZnO-d peetakse samuti üheks paljulubavaks fotokatalüütiliseks materjaliks tänu oma keelutsoonile, laialdasele levikule, odavusele, mittetoksisusele, ning erinevate morfoloogiatega sünteesi lihtsusele. ZnO kui fotokatalüsaatori peamiseks puuduseks on fotogenereeritud elektron-aukpaaride kiire rekombinatsioon, mis oluliselt vähendab materjali fotokatalüütilist aktiivsust. Fotogenereeritud laengukandjate paremaks eraldamiseks ja seekaudu fotokatalüütilise võimekuse parendamise üheks strateegiaks on ZnO/metall (Au, Ag) või ZnO/pooljuht struktuuride loomine. NiO on samuti üks perspektiivne fotokatalüütiline materjal, mis on viimasel ajal pälvinud paljude uurijate tähelepanu tänu tema muudetavale keelutsooni laiusele, odavusele, keemilisele stabiilsusele ja võimekusele lagundada orgaanilisi saasteaineid. NiO kui p-tüüpi juhtivusega pooljuhtmaterjal on sobilik ZnO/NiO n-p heterostruktuuri valmistamiseks, millel on suurem fotokatalüüsi võimekus kui struktuuri komponentidel eraldi.

Praeguseks on ZnO ja NiO fotokatalüsaatoritena uuritud peamiselt pulbri kujul. Pulbrilisel fotokatalüsaatoril on aga tõsised puudused nagu osakeste aglomeratsioon ja raskused reoveest eraldamisel, mis omakorda võib põhjustada sekundaarset reostust. Sellest vaatenurgast on aluspindadele immobiliseeritud fotokatalüsaatorite arendamine palju sobivam lahendus, mis võimaldab fotokatalüsaatori hõlpsat eraldamist reoveest ning materjali taaskasutamist. Just seetõttu on uurimistöo objektideks valitud klaasalustele kasvatatud ZnO nanovarrastest koosnevad kihid (ZnO_{NR}) ja NiO kiled. Käesoleva doktoritöö põhieesmärk oli ZnO nanovarrastel ja NiO kiledel baseeruvate tõhusate fotokatalüütiliste katete sünteesi strateegiate väljatöötamine. Materjalide sünteesiks kasutati odavaid keemilisi meetodeid nagu hüdrotermaalne kasvatamine ja keemiline pihustuspürolüüs.

Doktoritöö eesmärgi saavutamiseks seati kolm peamist ülesannet: 1) sünteesida $\text{ZnO}_{\text{NR}}/\text{Au}$ komposiit kasutades ZnO_{NR} pinnatöötluseks HAuCl_4 lahust ja uurida komposiidi füüsikalisi-keemilisi omadusi; 2) kasvatada NiO-kiled pneumaatilise pihustuspürolüüsi meetodil kasutades lähtematerjalina nikkelatsetaati, ning uurida sadestustemperatuuri ja lahusti tüübi mõju NiO kiledel füüsikalisi-keemilistele omadustele ja fotokatalüütilisele aktiivsusele; 3) sünteesida NiO õhukesed kiled ultraheli pihustuse meetodil kasutades lähtematerjalina nikkelatsetüülatsiooni, iseloomustada NiO kiledel füüsikalisi-keemilisi omadusi, kasutada NiO kilesid ZnO/NiO õhukesekilise ning $\text{ZnO}_{\text{NR}}/\text{NiO}$ heterostruktuuride valmistamiseks. Uurida struktuuride fotokatalüütilist võimekust.

$\text{ZnO}_{\text{NR}}/\text{Au}$ komposiidid valmistati HAuCl_4 lahuse (0,005; 0,01; 0,03 mol/L) kandmisel ZnO_{NR} kihtidele, millele järgnes termiline töötlemine 400 °C juures. Au nanoosakeste moodustumist kinnitasid XRD ja SEM analüüsid. Au nanoosakeste mõõdud vahemikus 20-70 nm olid otseses korrelatsioonis HAuCl_4 lahuse kontsentratsiooniga. $\text{ZnO}_{\text{NR}}/\text{Au}$

komposiitide optilised spektrid näitasid neeldumise kasvu spektri nähtavas osas. XPS uuringu kohaselt on ZnO_{NR}/Au komposiidi, mis valmistati HAuCl₄ 0,01 mol/L lahusest, pinnal 2,5 korda rohkem hüdroksüülrühmi kui ZnO_{NR} pinnal ja seetõttu on neil ka suurem MO lagundamise võimekus. HAuCl₄ 0,01 mol/L lahuse kasutamine andis tulemuseks ZnO_{NR}/Au komposiidi, mis UV kiirguse all lagundas 94 % MO-st 3 tunni jooksul, samas kui Au-ga katmata ZnO_{NR} vaid 65%. ZnO_{NR}/Au komposiit näitas peaaegu kaks korda suuremat MO lagundamise võimekust nähtava valguse all (ca 40% 3 tunni jooksul) võrreldes ZnO_{NR}-ga (21% 3 tunni jooksul). ZnO_{NR}/Au komposiitide suurem fotokatalüütiline võimekus nähtava valguse all on seletatav Au nanoosakeste plasmonresonants efektiga, mis tekitab neeldumise spektri nähtavas osas 500–600 nm juures.

NiO õhukesed kiled valmistati pneumaatilise pihustuspürolüüsi meetodiga sadestustemperatuuridel 300–420 °C kasutades lähteainena nikkelatsetaati ning erinevaid lahusteid (vesi, alkohol). NiO moodustumist kinnitasid XRD ja Raman spektroskoopia meetodid. Leiti, et sadestustemperatuur ja lahusti tüüp mõjutavad pneumaatiliselt pihustatud NiO kilede struktuurseid ja optilisi omadusi ning kilede pinna keemilist koostist. Vesilahusest valmistatud NiO kiled on polükristalsed, kristalliidi suurusega 4-10 nm, samas kui alkoholilahusest sadestatud kiled on XRD uuringu kohaselt amorfseid. Vesi- ja alkoholilahustest valmistatud NiO kilede keelutsooni laius on vastavalt 3,4 eV ja 4,0 eV sõltumata sadestustemperatuurist. XPS analüüsi järgi on sadestustemperatuur peamine tehnoloogiline parameeter, mis kontrollib hüdroksüülrühmade kogust kile pinnal ja seetõttu ka NiO kilede fotokatalüütilist võimekust. Vesilahusest 300 °C juures valmistatud NiO kiled on võimelised lagundama UV kiirguse all 3 tunni jooksul 45% analüüsivast MO-st samal ajal kui 420 °C juures kasvatatud kiled vaid 11 %. NiO kilede fotokatalüütilise aktiivsuse vähenemine sadestustemperatuuri tõstmisel korreleerub hüdroksüülrühmade koguse vähenemisega NiO kilede pinnal.

Doktoritöös töötati välja kõrge fotokatalüütilise võimekusega ZnO_{NR}/NiO n-p tuumkoorik heterostruktuuride sünteesi strateegia, kasutades esmakordselt NiO kooriku valmistamiseks ultrahelipihustuspürolüüsi meetodit. Esiteks, kasutades lähteainena nikkelatsetüülatsönaati valmistati ultraheli pihustuspürolüüsi meetodil NiO homogeensed, optiliselt läbipaistvad, polükristallilised NiO kiled, mille E_g on 3,7 eV. Teiseks leiti, et ZnO/NiO heterostruktuuri valmistamiseks on NiO kihi optimaalne sadestustemperatuur ca. 500 °C. MB lagunemise efektiivsus kilise ZnO/NiO struktuuri poolt suurenes 8%-lt 30%-le kui NiO sadestustemperatuuri tõsteti 350-lt 500 °C-le. ZnO/NiO kontakti volt-ampere karakteristikute mõõtmine kinnitas n-p heterostruktuuri moodustumist. Kolmandaks, määrati fotokatalüütiliselt tõhusate ZnO nanovarrastel baseeruvate ZnO_{NR}/NiO heterostruktuuride optimaalsed valmistamise tingimused: NiO kile sadestamine kahest ultraheli pihustussüklist 500 °C juures, millele järgnes heterostruktuuri lõõmutamine õhus 600 °C juures. ZnO_{NR}/NiO n-p heterostruktuuri moodustumist kinnitas XPS-analüüs, mis näitas NiO kooriku moodustumist ZnO nanovarraste pinnal ning 1,9–2,0 eV erinevust modifitseeritud Augeri parameetrites ZnO_{NR} ja ZnO_{NR}/NiO heterostruktuuri puhul, mis omakorda valideeris sisemise elektrivälja tekke. Kelvini sondi, fotoelektronide saagise spektroskoopia ja keelutsooni laiuse mõõtmiste tulemuste põhjal koostati ZnO_{NR}/NiO heterostruktuuri tsoonidiagramm. ZnO_{NR}/NiO heterostruktuur näitas UV kiirguse all MB lagunemise efektiivsust 70% 3 tunni jooksul samas kui ZnO_{NR} lagundas samades tingimustes 53% MB-st. ZnO_{NR}/NiO heterostruktuuride suurenenud fotokatalüütiline võimekus on tingitud fotogenereeritud elektron-auk paaride efektiivsemast eraldamisest p-n siirde poolt.

Töö uudsus seisneb järgmises: 1) Esmakordselt valmistati Au nanoosakesed ZnO_{NR} peale kasutades selleks $HAuCl_4$ lahuse pindvurritamist millele järgnes kuumutamine õhu keskkonnas. Tulemusena saadi ZnO_{NR}/Au struktuurid, mis olid fotokatalüütiliselt tunduvalt efektiivsemad lagundama MO-d kui ZnO_{NR} kihid nii UV kiirguse kui nähtava valguse all. 2) Uurimistöö tulemusena tõestati, et pneumaatilise pihustamise meetodil on võimalik valmistada hea fotokatalüütilise võimekusega NiO kilesid, kusjuures sadestustemperatuur on peamine tehnoloogiline parameeter, mis määrab hüdroksüülrühmade kontsentratsiooni kilede pinnal ja see omakorda kilede fotokatalüütilise võimekuse lagundada MO-d kui saasteainet. 3) Töös näidati esmakordselt, et ultrahelipihustuse meetodil on võimalik valmistada õhukesi, ühtlase pinnaga, kristallilisi NiO kilesid kasutades lähteainena nikkelatsetüülatsenaati. Esmakordselt kasutati ultrahelipihustuse meetodit NiO kooriku sadestamiseks ZnO_{NR} tuumale, määrati optimaalsed tehnoloogilised tingimused ZnO_{NR}/NiO tuum-koorik n-p heterostruktuuride valmistamiseks, n-p heterostruktuuri moodustumine tõestati struktuuri füüsikaliste parameetrite mõõtmiste kaudu.

Kokkuvõttes, doktoritöös töötati välja tehnoloogiliselt lihtsalt teostatavad, kuluefektiivsed ja teaduslikult põhjendatud strateegiad ZnO nanovarrastel ja NiO õhukestel kiledel baseeruvate efektiivsete fotokatalüütiliste materjalide valmistamiseks keemilistel vedeliksadestuse meetoditel.

Appendix 1

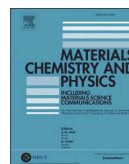
Publication I

T. Dedova, I. Oja Acik, Z. Chen, A. Katerski, K. Balmassov, I. Gromyko, T. Nagyné-Kovács, I.M. Szilágyi, and M. Krunk. Enhanced photocatalytic activity of ZnO nanorods by surface treatment with H₂AuCl₄: Synergic effects through an electron scavenging, plasmon resonance and surface hydroxylation. *Materials Chemistry and Physics*, 245, 122767, 2020, <https://doi.org/10.1016/j.matchemphys.2020.122767>.



Contents lists available at ScienceDirect

Materials Chemistry and Physics

journal homepage: www.elsevier.com/locate/matchemphys

Enhanced photocatalytic activity of ZnO nanorods by surface treatment with H₂AuCl₄: Synergic effects through an electron scavenging, plasmon resonance and surface hydroxylation

T. Dedova^{a,*}, I. Oja Acik^a, Z. Chen^a, A. Katerski^a, K. Balmassov^a, I. Gromyko^a,
T. Nagyné-Kovács^b, I.M. Szilágyi^b, M. Krunks^a

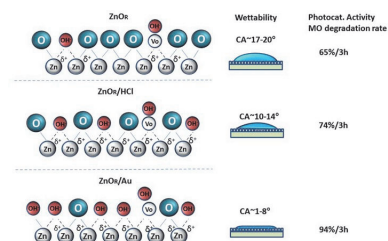
^a Department of Materials and Environmental Technology, Tallinn University of Technology, Ehitajate tee 5, 19086, Tallinn, Estonia

^b Department of Inorganic and Analytical Chemistry, Budapest University of Technology and Economics, H-1111, Budapest, Muegyetem rakpart 3, Hungary

HIGHLIGHTS

- ZnO_R/Au layers possess enhanced photocatalytic activity over ZnO_R layers.
- ZnO_R surface becomes more hydroxylated after treatment with H₂AuCl₄.
- Surface hydroxylation lead to a greater photocatalytic activity of ZnO_R/Au layers.
- Electron scavenging, plasmon resonance and hydroxylation together improve PA.

GRAPHICAL ABSTRACT



ARTICLE INFO

Keywords:

Hydrothermal growth
ZnO nanorods
Plasmon
Hydroxylation
Photocatalytic activity

ABSTRACT

In this research, we demonstrate an enhanced photocatalytic activity (PA) of ZnO_R/Au composites compared to PA of plain ZnO_R structures. The ZnO_R were produced by a hydrothermal growth method and the surface treatment of the ZnO_R crystals was carried out with H₂AuCl₄ using a spin coating technique. In this study, methyl orange was chosen to evaluate the photocatalytic activity of the ZnO_R and ZnO_R/Au. The highest degradation efficiency of MO was achieved with ZnO_R/Au layers. The XPS and wettability measurements have confirmed the increase in the amount of hydroxyl groups on the surface of the ZnO_R/Au. Taking into account the physical and chemical characterizations of the samples, the enhanced photocatalytic activity of the ZnO_R/Au composites has been attributed to the three main issues 1) an effective charge carriers separation due to proper ZnO and Au bands alignment where the gold acts as an electron scavenger, 2) surface plasmon resonance from Au nanoparticles 3) increase of the hydroxylation of the ZnO_R crystals surface after H₂AuCl₄ interaction with ZnO_R surface.

1. Introduction

Currently, environmental investigations around the world [1,2] have

gained increasing attention in environmental problems related to the removal of toxic organic substances (dyes, antibiotics, e.t.c.) from wastewater. Ultimately, research activities on wastewater treatment

* Corresponding author.

E-mail address: tatjana.dedova@taltech.ee (T. Dedova).

<https://doi.org/10.1016/j.matchemphys.2020.122767>

Received 2 September 2019; Received in revised form 17 January 2020; Accepted 4 February 2020

Available online 8 February 2020

0254-0584/© 2020 Elsevier B.V. All rights reserved.

methods have focused on advanced oxidation processes (AOP), mainly due to the complete degradation of a wide range of organic contaminants that are resistant to conventional purification methods of water, absence of waste disposal problems and low cost [3]. Among the AOPs, a heterogeneous photocatalysis, a new wastewater treatment technique, is a rapidly growing research area in recent decades [3,4]. The heterogeneous photocatalysis that uses semiconductor catalysts (TiO_2 , ZnO, Fe_2O_3 , CdS, GaP, and ZnS) has demonstrated its effectiveness in the degradation of a wide range of organic compounds into easily biodegradable compounds, and eventually mineralized them into harmless carbon dioxide and water [4].

In the field of photocatalysis today, ZnO has become the main candidate in the ecological environmental management system due to its non-toxicity, profitability, a near UV band gap value (3.37 eV), its excellent capacity to grow in many different nanostructured forms (wires, rods, platelets, etc.), strong oxidation capacity and chemical and optical stability [5,6].

However, a major obstacle to achieving highly efficient photocatalytic performance is the rapid recombination of pairs of photo-generated electron-holes in ZnO nanosystems [7].

Therefore, much effort has been expended to increase the charge separation and transport by coupling ZnO with other materials [7–10]. The combination of plasmonic metal nanoparticles (Au, Ag, Pd) with semiconductors has been considered as an effective approach to improve the photocatalytic efficiency of the resulting hybrid semiconductor/plasmonic particle structure. Benefits of such a composite structure are known, such as improving the absorption of sunlight through the surface plasmon resonance, an improvement in the separation of the charge carrier due to the proper correct position of the energetic band of the gold nanoparticles and semiconductors, where gold acts as an electron scavenger [11].

Currently, the number of studies on the photocatalytic activity of such Au/ZnO composites is growing rapidly, however, the most of the studies still comprise the powder forms of photocatalysts [12–19].

The powdery photocatalyst has several serious problems that limit its practical application for the remediation of wastewater. These are difficulties of separation and recovery, high tendency to the aggregation of nanoparticles, low capacity of adsorption of hydrophobic contaminants, difficulties in the uniform distribution of particles.

One of the effective solutions to overcome the problems caused by the nanoparticles could be the photocatalyst with a defined crystalline structure attached to the substrate. The 1D nanostructures such as nanorods, nanowires or nanoarrays are a good choice due to their high open surface area and their easy preparation on various substrates. So far there are very limited amount of studies on photocatalysis of Au/ZnO composit with ZnO rod-like morphology attached to the substrates. J. Wu et al. [20] have studied the photocatalytic activity of MO degradation by using CVD deposited ZnO films, ZnO nanorods and Au/ZnO nanorod composites on Si with different size and density of Au particles. It was shown that the highest photocatalytic activity to degrade MO solution (15 ppm) was achieved by Au/ZnO nanorod composit samples. For example, the degradation rate of MO by Au/ZnO nanorod samples was ca. 70–83%, compared to ca.50% for ZnO nanorod sample without gold and 5% for ZnO film sample for 3 h under UV light (365 nm). The authors have shown that high density and smaller Au nanoparticles diameters (5 nm) induce greater MO decomposition ability (83%/3h) compared to the larger, 30 nm large Au particles (PA is 70%/3h) or lower density 5–15 nm large Au particles (PA is ca.75%/3h) [20]. J. Lu et al. [21] have studied the photocatalytic activity of Au/ZnO nanorod vs. ZnO nanorod samples, where nanorods were produced by hydrothermal growth and nanorods were immersed to the HAuCl_4 - ammonia solution at pH 8–9 at 70 °C for 1h and model pollutant was MO (5 ppm, 300 W Xe lamp). It has been shown that Au/ZnO samples have superior PA activity over ZnO samples, being 87–100%/3h for Au/ZnO samples (3h) and ca.65%/3h for ZnO samples [21]. It was found that optimal Au concentration to achieve maximum PA performance is 0.25 and 0.75

mmol/L and highest Au concentration studied in this paper 1 mmol/L lowered PA activity of Au/ZnO samples up to 87%/3h. Da-Ren Hang et al. [22] have reported the increased PA activity of hydrothermally grown ZnO rod samples (91%/2h of 10 ppm MB, 500 W UV lamp) compared to pristine ZnO photocatalyst (ca. 35%/2h of 10 ppm MB, 500 W UV lamp).

X. Liu [23] has also reported the enhanced PA of Au/ZnO rod samples, where ZnO rods were grown by chemical bath and immersed into HAuCl_4 solution. The PA of Au/ZnO sample over MO pollutant was 90%/3h vs. 50%/3h for pristine ZnO sample. Thus, the Au decoration of either random ZnO crystals or ZnO nanorods structure lead to increase in photocatalytic activity of the photocatalyst independent of the pollutant.

The enhanced photocatalysis of Au/ZnO composites over ZnO rods is usually referred to so called physical reasons, such as enhanced charge separation due to proper Au and ZnO bands alignment (scavenging effect) or plasmonic effect, leaving behind the chemical interaction of an acid (HAuCl_4) or ammonia with ZnO crystals surface. In this study additionally to systematic PA activity study under UV and visible light we study the influence of the surface composition of Au/ZnO on PA after chemical treatment of ZnO with HAuCl_4 .

Another problem that complicates the comparison of results from one study to another is a wide range of model pollutants used, their different concentrations, different types of irradiation sources and the power used in several studies. Therefore, the study that covers several parameters in a study represents high scientific value.

For this study, ZnO crystals were grown using a hydrothermal growth technique, which is one of the most popular methods for growing ZnO nanostructured materials at present. The relevance of the hydrothermal method is also supported by the greater number of publications on the hydrothermal growth of ZnO compared to the publications on other synthesis methods (according to ISI Web of Science Hydrothermal growth, ZnO ca. 3700 publications for a period of 2008–2018). However, most hydrothermally developed nanostructures are loose, are not bound to the substrate structures, and by this growth method, the growth of c-axis oriented ZnO nanorod crystals which are highly crystalline and vertically attached to the glass substrate is still challenging.

The important topics addressed in this study are 1) the practical way to synthesis elongated, highly crystalline, fixed to substrate ZnO nanorods by the hydrothermal growth method and their derivatives, ZnO/Au composites 2) comparative study on the photocatalytic activity of ZnO and ZnO/Au layers using UV and VIS light sources in the same study 3) establishing the synergetic mechanism that explains the improvement of the photocatalytic efficiency of ZnO/Au layers over the bare ZnO, including not only the physical backgrounds (electron scavenging and plasmon resonance) established earlier, but also the chemical reasons, such as changing the surface composition of Au/ZnO composites after the chemical interaction of HAuCl_4 acid and ZnO during the decoration of ZnO with Au nanoparticles.

2. Experimental details

2.1. Samples preparation

The soda-lime glass substrates were cut into pieces with a specific size of $38 \times 9 \times 1.1$ mm³. After that, the substrates were cleaned with detergent solution, deionized water, and isopropanol in an ultrasound bath, dried and washed thoroughly with deionized water. Properly cleaned glass substrates were placed in a heated tin bath for the preparation of the ZnO seed layer. The seed layers have been prepared by the spray pyrolysis method. The precursor solution was nebulized with the aid of a pneumatic spraying head, which operates in a pulsating feed mode (5 s of power, 20 s of pause). The precursor solution (20 ml) is composed of 0.05 mol/l of zinc acetate solution ($\text{Zn}(\text{CH}_3\text{COO})_2$) solution of 2/3 vol of the isopropanol/water mixture. The bath temperature (T_s)

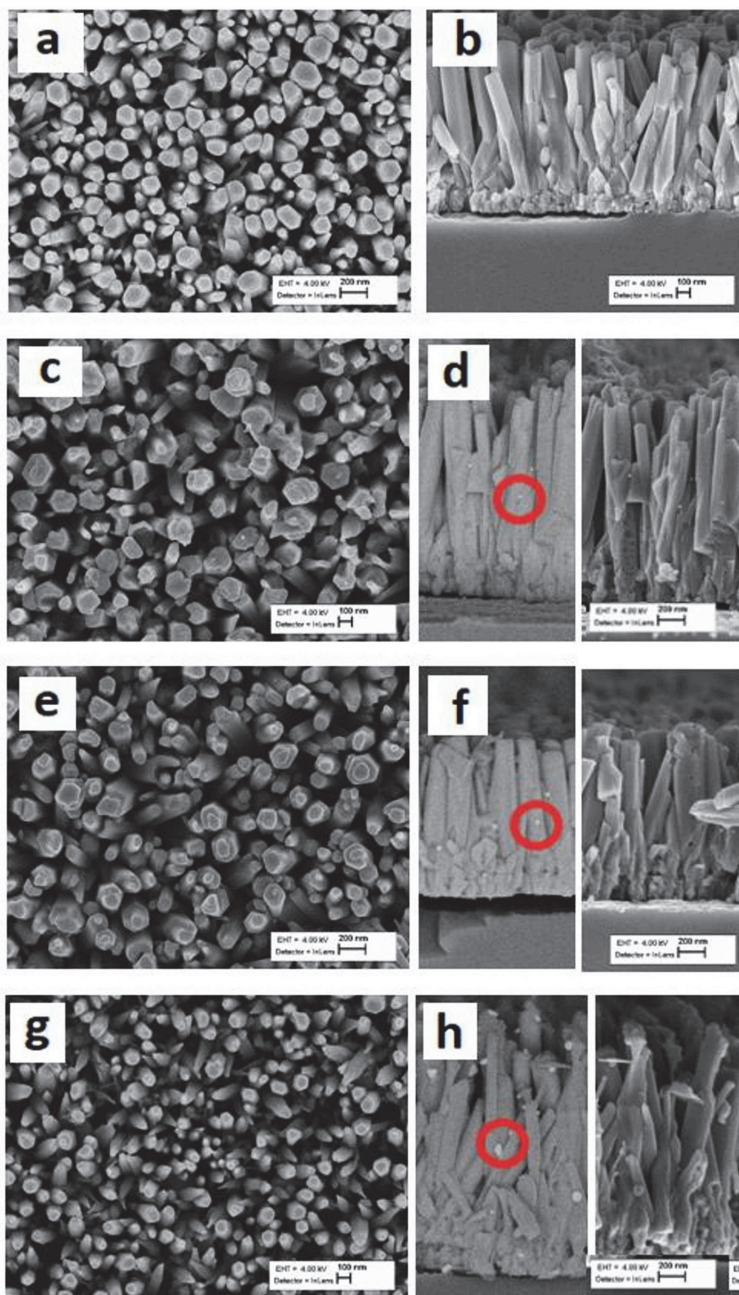


Fig. 1. SEM and back-scattered electron images of ZnO_R and ZnO_R/Au layers a) ZnO_R surface; b) ZnO_R cross-sections; c) ZnO_R/Au 0.005 mol/L surface; d) ZnO_R/Au 0.005 mol/L cross-sections; e) ZnO_R/Au 0.01 mol/L surface; f) ZnO_R/Au 0.01 mol/L cross-sections; g) ZnO_R/Au 0.03 mol/L surface; h) ZnO_R/Au 0.03 mol/L cross-sections.

was set at 500 °C and the air flow was adjusted to 8L/min. According to SEM, the morphology of the seed layer represented a flat and compact structure composed of round crystals of 30 nm thickness. The thickness of the seed layer was ca. 80 nm.

For the hydrothermal synthesis, the glass substrates covered with

ZnO seed coatings were mounted simultaneously in 40 ml of the reactor baker with a mixture of 0.1 mol/L zinc nitrate hexahydrate ($\text{Zn}(\text{NO}_3)_2 \cdot 6\text{H}_2\text{O}$, Sigma-Aldrich, 99.9%) and hexamethylenetetramine ($(\text{CH}_2)_6\text{N}_4$, HMT) 0.1 mol/L aqueous solutions. The reactor baker was then mounted in a steel autoclave and the reaction proceeded for 2 h at

120 °C.

The freshly prepared ZnO_R layers, thoroughly washed with deionized water and washed with deionized water in ultrasound bath (1 min), proceeded with the treatment with HAuCl₄ (HAuCl₄ - Sigma-Aldrich 99.9%). The HAuCl₄ acid solution in ethanol was dropped (2 drops with a 0–100 μm pipette) on the surface of the rods and centrifuged [24–26]. The spinning regime was 5s at 500 rpm and 30 s at 3000 rpm. The concentrations studied of HAuCl₄ were 0.005 mol/L, 0.01 mol/L and 0.03 mol/L. The highest concentrations were not studied due to the partial dissolution of ZnO according to Ref. [26]. Then, the samples were dried at 100 °C for 30 min and annealed at 400 °C for 20 min. The ZnO_R reference sample without Au particles proceeded to a heat treatment procedure similar to the ZnO_R/Au composite. Parallel to the treatment with HAuCl₄, we treat specific sample of ZnO_R with a solution of HCl alone using the concentration of 0.01 mol/L.

2.2. Samples characterization

The high-resolution scanning electron microscope (SEM) studied the dimensions and shape of the gold nanoparticles and ZnO_R rods in Zeiss HR FESEM Ultra 55 at an operating voltage of 10 kV.

The phase composition and the structure of ZnO_R and ZnO_R/Au were studied on an XRD machine. The XRD patterns were recorded using a Rigaku Ultima IV diffractometer with CuKα radiation ($\lambda = 1.5406 \text{ \AA}$, 40 kV at 40 mA) and the D/teX Ultra silicone strip detector. The crystalline phases were identified using the XRD reference files (PDF-2 file collection) of the International Center for Diffraction Data (ICDD, Pennsylvania, USA).

The absorbance spectra of the ZnO_R arrays and the ZnO_R arrays with Au nanoparticles were recorded in the Jasco V-670 UV-VIS-NIR spectrophotometer equipped with an integrating sphere. The spectra were taken in the wavelength range of 300–2200 nm.

X-ray photoelectron spectroscopy (XPS) study was performed on the Kratos Analytical AXIS ULTRA DLD spectrometer equipped with the monochromatic X-ray source Al Kα and the achromatic anodic X-ray source Mg Kα/Al Kα. All the spectra have been charge-corrected by taking C1s peak (BE = 285.0eV) as reference.

The photocatalytic activity of the ZnO_R, ZnO_R/Au and ZnO_R/HCl samples were estimated by the degradation of the Methyl Orange (MO) dye, concentration changes with time. The concentrations of the dye were monitored every 30 min in the Jasco V-670 UV-VIS-NIR spectrophotometer. The Philips Mercury lamp (15W*2 lamps, model TL-D, $\lambda_{\text{max}} = 365 \text{ nm}$) was used as a UV source and Philips Master TL-D Super 80 (15W*2 lamps, $\lambda_{\text{max}} = 550 \text{ nm}$) for the visible light photodegradation tests. The ZnO-photocatalyst rod samples (substrate surface area of one sample is 3.42 cm² and weight of ZnO nanorod layer sample (photocatalyst) on glass substrate is 1.5 mg, (glasses were weighted before and after the deposition) were mounted in a 5 ml UV-cuvette filled with 4 ml of dye solution. The initial concentration of MO solution was 0.015037 mg/L (15 ppm). The standard measurement of MO concentration took place at a wavelength of 464 nm. The study on the stability of photocatalyst, 10 repetitive cycles has been performed, 3h duration for each cycle. To identify the reactive species actively taken part in photocatalytic degradation process, we performed photocatalytic measurement mounting the samples into MO solution containing scavenger solutions. The isopropanol was used to scavenge the hydroxyl radicals, ammonium oxalate was used to catch the holes, p-quinone was used to bound superoxide radicals. The degradation efficiency took place 1 h. The concentration of scavenger was 1 mmol/L.

3. Results and discussion

3.1. Morphology, structural and optical properties of the layers

The surface and cross-sectional SEM images of the ZnO_R and ZnO_R/Au layers studied here are presented in Fig. 1. According to Fig. 1, the

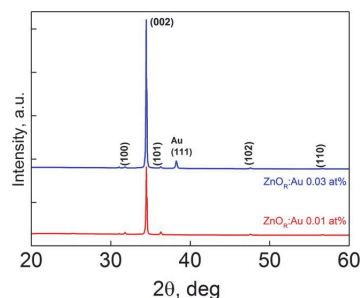


Fig. 2. XRD patterns of ZnO_R/Au layers deposited from the HAuCl₄ solution with concentration of 0.01 mol/L and 0.03 mol/L.

glass substrates have a dense, uniform coverage of elongated ZnO rod crystals. The vertical orientation of the crystals prevails, the most of the crystals have a well-defined hexagonal shape and a flat (002) top plane termination, while others, minorities, have a sharp, pencil-shaped top tip. The average lengths of the crystals are $L = \text{ca. } 1 \text{ }\mu\text{m}$, and the diameters vary from 50 to 150 nm. After treatment with HAuCl₄, the gold nanoparticles are formed in the facets of the ZnO_R crystals. The diameters of Au-NPs vary from 20 to 60 nm depending on the concentration of HAuCl₄ used. The smallest particles with $d = \text{ca. } 20 \text{ nm}$ were detected on the surface of ZnO_R, treated with HAuCl₄ solution with a concentration of 0.005mol/L, the largest $d = \text{ca. } 60\text{--}70 \text{ nm}$ with a concentration of HAuCl₄ of 0.03mol/L. The back-scattered electron SEM images (Fig. 1 d, f, h left) provide a clear representation of Au points and positions due to a greater difference in conductivity between Au and ZnO.

The crystalline structure and the composition of the phases of the samples were characterized by XRD analysis. Regardless of the presence of gold in the lateral facets of the rods, all the samples studied are composed of wurtzite ZnO. The XRD patterns acquired from hydrothermally grown ZnO_R crystals covered with gold nanoparticles are shown in Fig. 2. The main reflections in 2θ of 31.77, 34.42, 36.25, 47.54, 56.6° correspond to planes (100), (002), (101), (102) and (110) of hexagonal ZnO. The strong and narrow predominant reflection at 34.40° from (002) plane of ZnO indicates the formation of highly crystalline, c-axis perpendicular to the substrate oriented ZnO crystals. The ratio of the intensities of (002) and (101) reflections ($I_{(002)}/I_{(101)}$) is 68 and characteristic for the highly dense, well-aligned vertically oriented ZnO nanorod arrays. For a powder sample, ($I_{(002)}/I_{(101)}$) is 0.44.

The presence of Au nanoparticles as a separate phase can be detected in the XRD diffractogram only for ZnO_R covered with Au using a higher concentration of HAuCl₄ solution. The Au-NPs deposited from HAuCl₄ with a concentration of 0.03 mol/L are clearly detectable at 2θ of 38.1° corresponding to the plane (111) of metallic Au (cubic phase). XRD did

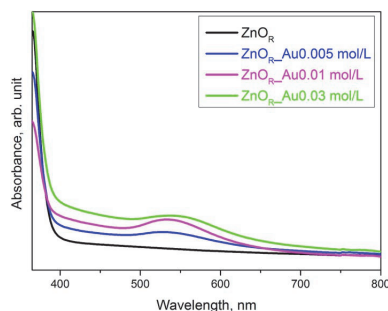


Fig. 3. Absorption spectra of ZnO_R and ZnO_R/Au layers.

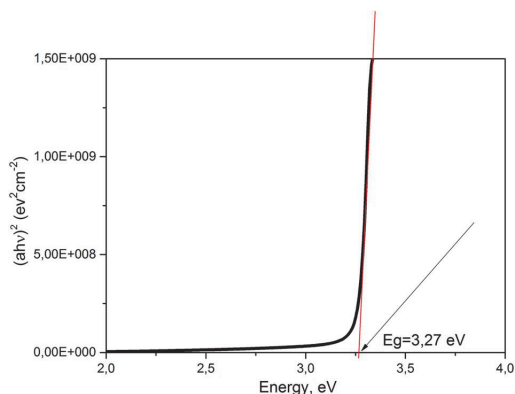


Fig. 4. $(\alpha h\nu)^2$ vs. energy plot of ZnO_R sample. Band gap determination from Tauc's plot.

not detect any sign of Au-NPs for the samples produced using the lowest concentration of $H AuCl_4$ solution of 0.005 and 0.01 mol/L.

The absorbance spectra of the ZnO_R and ZnO_R arrays covered with Au-NPs were measured in the wavelength range of 300–2200 nm and the range of 300–800 nm is presented in Fig. 3. The absorption band in the region of 500–600 nm with a maximum of 550 nm could be associated with the effect of plasmon resonance exiting from the gold nanoparticles [26,27]. The higher the concentration of the gold precursor used to produce the gold nanoparticles, the higher the absorbance value.

The band gap energies were determined from the Tauc graph shown in Fig. 4 as an example. Regardless of the presence of gold nanoparticles or not, all ZnO_R samples have almost similar band gap energy values, E_g , in the range of 3.25–3.27 eV. This is an additional confirmation that the gold particles are a separate unit distributed in the crystal facets of ZnO_R .

3.2. Photocatalytic activity and the surface properties of the layers

3.2.1. Photocatalytic activity

The photocatalytic activity (PA) of the samples studied was recorded in the degradation rate of the methylene orange (MO) dye. The MO is a well-known and frequently used model contaminant to evaluate the

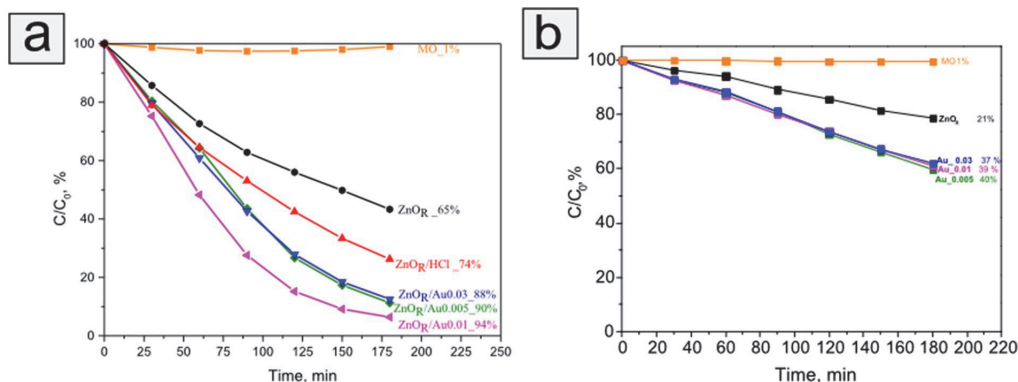


Fig. 5. MO (15 ppm) degradation rate C/C_0 vs. time of MO, ZnO_R , ZnO_R/HCl , ZnO_R/Au 0.005 mol/L, ZnO_R/Au 0.01 mol/L, ZnO_R/Au 0.03 mol/L a) under UV light (30 W Hg lamp) and b) under visible light (30 W luminescence lamp) illumination.

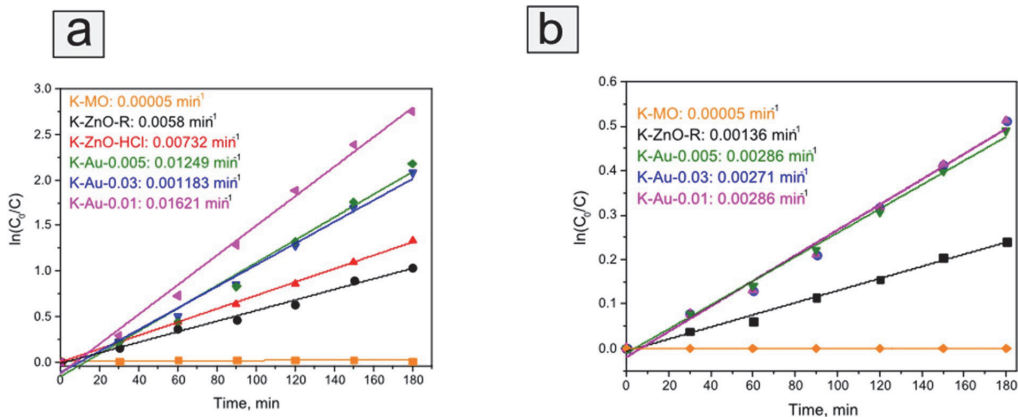


Fig. 6. Plots of $\ln(C_0/C_t)$ vs. illumination time of the samples: ZnO_R , ZnO_R/HCl , ZnO_R/Au 0.005 mol/L, ZnO_R/Au 0.01 mol/L, ZnO_R/Au 0.03 mol/L a) under UV light (30 W Hg lamp) and b) under visible light (30 W luminescence lamp) illumination.

Table 1

k_{obs} , R^2 of ZnO_R , ZnO_R/HCl , ZnO_R/Au 0.005 mol/L, ZnO_R/Au 0.01 mol/L, ZnO_R/Au 0.03 mol/L (left) under UV light (30 W Hg lamp) and right) under visible light (30 W luminescence lamp) illumination.

Sample name	UV light illumination		VIS light illumination	
	k_{obs}	R^2	k_{obs}	R^2
ZnO_R	0.006	0.9955	0.0014	0.9918
$\text{ZnO}_R/\text{Au}0.005$	0.013	0.9773	0.0028	0.9877
$\text{ZnO}_R/\text{Au}0.01$	0.016	0.9907	0.0028	0.9877
$\text{ZnO}_R/\text{Au}0.03$	0.001	0.9872	0.0027	0.9953
ZnO_R/HCl	0.007	0.9984	N/A	N/A

photocatalytic activity of several photocatalysts.

Degradation rate of MO, curves C/CO as a function of time, under UV and visible light without (MO) and with photocatalyst layers (ZnO_R , ZnO_R/Au 0.005 mol/L, ZnO_R/Au 0.01 mol/L, ZnO_R/Au 0.03 mol/L, ZnO/HCl) are presented in Fig. 5. As the photocatalytic degradation of MO obeys the first-order kinetics [28] the graphs of $\ln(\text{C}/\text{C}_0)$ vs. illumination time represent the straight line. The slope of the linear regression is equal to the apparent first order rate constant, k_{obs} . The graphs of $\ln(\text{C}/\text{C}_0)$ vs. illumination time are presented in Fig. 6. The apparent first-order rate constant, the k_{obs} , and the correlation coefficients (R^2) are presented in Table 1. As can be seen in Table 1, all the correlation coefficients are greater than 0.95, which reveals that the photodegradation of the dyes fits well with the chosen kinetic model.

According to the values of k_{obs} and the percentages of MO discoloration over time, photocatalysts illuminated with UV light were performed more efficiently compared to those illuminated with visible light.

For example, ZnO_R samples have shown ca. 65% degradation efficiency for 3 h under UV light, and only 21% degradation of MO was achieved under visible light illumination during the same time. The k_{obs} of the illuminated UV light of ZnO_R are almost 6 times higher than the same sample treated with the VIS light source, being 0.006 and 0.001, respectively.

The clear improvement of the photocatalytic performance due to the presence of Au in a ZnO_R sample surface is clearly demonstrated by the values of k_{obs} as well as the graphs of C/CO vs. time. Gold-coated nanorods compared to bare rods have shown an increase in degradation efficiency of 30% under UV light and 20% under visible light. The samples of PA of ZnO_R/Au are ca. 90% and 40% for 3 h for UV and VIS light, respectively, and simple ZnO_R PA is ca. 65% and 21% for 3 h, for UV and VIS, respectively.

The reaction rate constant, K_{obs} , of bare ZnO_R is as high as ca. 3 times of ZnO_R/Au 0.01, being ca.0.006 and 0.016, respectively, for UV light and 2 times higher than ZnO_R/Au 0.01 (k_{obs} 0.0014 and 0.0028, respectively) for VIS light illumination.

It was observed that the ZnO_R sample treated with only HCl solution keeping the procedure and concentration mode similar to the samples

Table 2

XPS analysis data of atomic ratios of the Vo/Zn–O and OH/Zn–O obtained from the O1s core level peaks and water contact angle values.

Sample	$[\text{Vo}]/[\text{Me}-\text{O}]$	$[\text{OH}]/[\text{Me}-\text{O}]$	CA°
ZnO_R	0.2	0.3	17–20
ZnO_R/Au 0.005	0.3	0.3	N/A
ZnO_R/Au 0.01	0.5	0.7	1–8
ZnO_R/HCl	N/A	N/A	10–14

treated with HAuCl_4 , has shown a better photocatalytic performance than the bare ZnO_R sample. The ZnO_R/HCl k_{obs} are 1.17 times higher than the ZnO_R sample (0.007 vs. 0.006, respectively) and the ZnO_R/HCl PA is 1.4 times higher than the ZnO_R sample (74% vs. 65%, respectively).

The results of photocatalytic degradation under UV light are in a good correspondence with those reported in a literature by J. Lu et al. [21] who reported 87–100% degradation of 5 ppm MO (300 W illumination) for 3h by ZnO_R/Au and 65%/3h by pristine ZnO_R grown also hydrothermally.

To further understand the chemical reasons behind the difference in photocatalytic behaviour after an interaction of ZnO_R crystals with HAuCl_4 acid, the ZnO_R photocatalysts, ZnO_R/Au and ZnO/HCl samples proceeded to XPS analysis and surface wettability characterizations.

3.2.2. Surface properties of the layers via XPS study and wettability studies

The surface composition of ZnO_R and ZnO_R/Au 0.005 mol/L and ZnO_R/Au 0.01 mol/L samples were studied by XPS. Insofar as a relative amount of hydroxyl groups and oxygen vacancies are the driving components of the photocatalytic activity, the O1s core level spectra of those samples were plotted and analyzed. The asymmetric core level peaks of O1s were deconvoluted using Lorentzian-Gaussian fitting analysis (pseudo-Voigt function) and presented in Fig. 7 for ZnO_R , ZnO_R/Au 0.005 mol/L and ZnO_R/Au 0.01 mol/L in a, b and c, respectively.

In the O1s core level spectrum of all the samples, three well-defined deconvoluted peaks were observed. The peaks in the binding energy values (BE) of 530.2 ± 0.2 eV are attributed to the Me–O bond, in our case Zn–O [29], BE of 531.1 ± 0.3 to the oxygen-deficient region, i.e. oxygen vacancies (Vo) [30–33], BE of $532 \text{ eV} \pm 0.2$ eV belong to the surface hydroxyl groups (–OH) [34], and 533.1 eV belong to the species CO, C = O and H_2O [35,36]. The atomic concentrations of all the components (Zn–O, Vo, –OH, H_2O) found in the O1s core level spectrum were calculated from the integrated area of the O1s spectrum using the cross sections of Scofield. The atomic relationships of the components, OH/Zn–O and Vo/Zn–O, are summarized in Table 2.

As shown in Table 2, the relative amount of $[\text{Vo}]/[\text{Me}-\text{O}]$ and $[\text{OH}]/[\text{Me}-\text{O}]$ is higher for the samples covered with gold nanoparticles. The relative amount of $[\text{OH}]/[\text{Me}-\text{O}]$ for the sample ZnO_R/Au 0.01 mol/l is 0.7 being more than twice as high as compared to $[\text{OH}]/[\text{Me}-\text{O}] = 0.3$ of the bare ZnO_R .

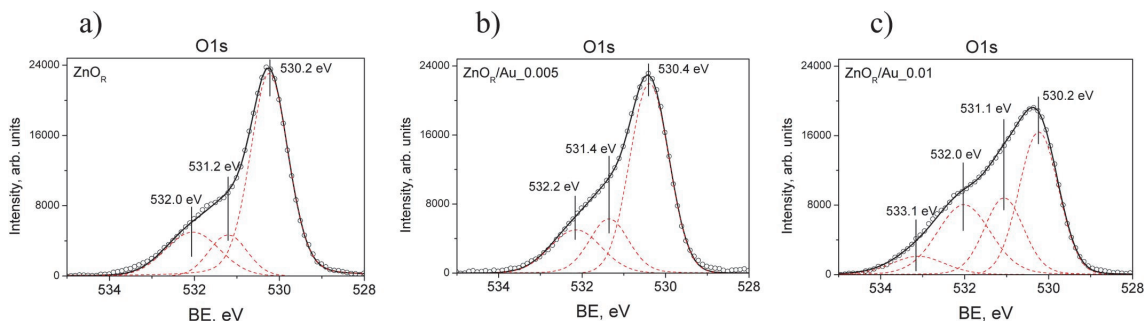


Fig. 7. O1s core level spectrum of a) ZnO_R , b) ZnO_R/Au 0.005 mol/L, c) ZnO_R/Au 0.01 mol/L.

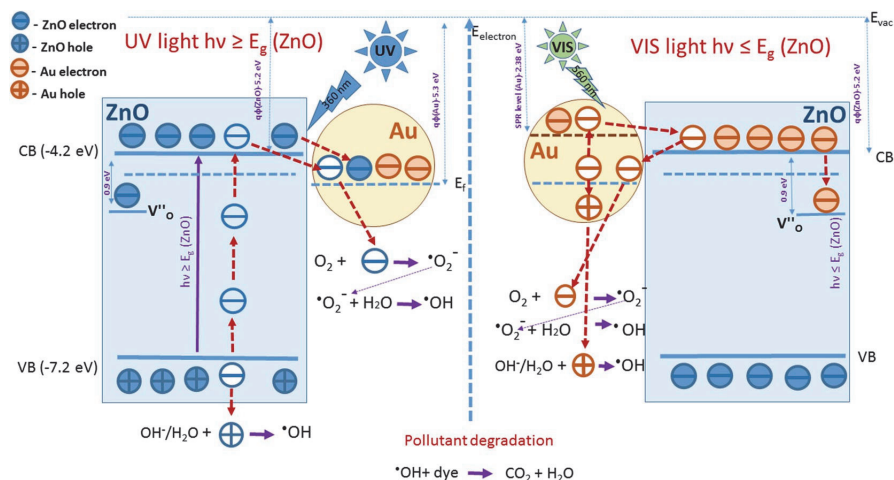


Fig. 8. Schematic diagrams showing the charge carriers transportation processes in ZnO_R/Au structures and physico chemical interaction reactions to radical formation in case of UV and VIS light illumination.

Another test to estimate the relative content of OH groups on the surface could be made by measurements of surface wettability. It is well known that the amount of OH groups on the surface is directly proportional to the water contact angle (WCA). The greater the number of WCA, the smaller the number of OH groups on the surface, the greater the hydrophobicity of the surface and vice versa. In our case, the wettability measurements support the XPS results. The hydrophilicity increases with the treatment of the ZnO_R structures with an acid solution, the WCA values are in the range of 1–8°, 10–14 and 17–20 for ZnO_R/Au 0.01, ZnO_R/HCl 0.01 and ZnO_R samples, respectively. This supports the presence of a greater amount of hydroxyl groups on the surface treated with acid solution samples compared to bare rods.

The greater amount of hydroxyl groups is reflected in the higher photocatalytic behavior of the ZnO_R/Au samples compared to ZnO_R samples showing PA of ca. 90%/3h and 65%/3h under UV light, respectively (Fig. 5a). The greater number of OH groups on the surface in the case of the ZnO_R/Au samples can be explained as follows: According to thermal decomposition studies in H₂AuCl₄ [37], the main by-product of gas decomposition is HCl. Therefore, the HCl formed during the heating of H₂AuCl₄ reacts with the surface of the ZnO crystal with the formation of ZnCl₂. The latter, a highly hygroscopic compound (Lewis acid) is known which immediately absorbs moisture from the environment and is transformed into "OH groups" containing zinc hydroxychloride, which makes the surface more hydroxylated. To test this assumption, we treated the surface of the ZnO_R crystal with HCl acid (0.01 mol/L), proceeding with a procedure exactly similar procedure as we treated the samples with H₂AuCl₄ and we measured the photocatalytic activity of this sample with UV irradiation. The photocatalytic performance value of this sample, ZnO_R/HCl (Fig. 5a), is between the PA of the pristine ZnO_R and ZnO_R/Au, being 74%/3h, 65%/3h and ca. 90%/3h, respectively. Therefore, the acid treatment changes the surfaces of the ZnO_R layers making the surface more hydroxylated, resulting in greater photocatalytic activity.

The higher the concentration of H₂AuCl₄, the more HCl gas evolves and reacts with the surface of the ZnO crystals and, therefore, the greater number of OH species are formed. However, the higher concentrations of H₂AuCl₄ (0.03 and higher) may already be detrimental to the integrity of the ZnO nanorod, subsequently worsening the photocatalytic activity of the crystals. Therefore, a moderate or low concentration of H₂AuCl₄ acid is better for the treatment of the surface of the crystals due to the hydroxylation effect of the surface. In addition, the ZnO_R/Au samples

have an additional beneficial impact on the photocatalytic activity that arises from the plasmonic effect of the gold nanoparticles and proper gold ZnO band positions, making an Au as a charge scavenger suppressing the losses of the charge carriers from the recombination.

3.3. Mechanism behind the photocatalytic activity

Taking into account the studies of absorbance spectra, XPS, wettability and photocatalytic activity, we propose the synergic mechanism responsible for increasing the photocatalytic performance of the ZnO_R/Au samples. The mechanism includes both the physical and chemical aspects.

Fig. 8 illustrates the schematic diagrams showing the charge transport processes in ZnO_R/Au hybrid structures and explains the enhanced photocatalytic performance of the samples under UV and VIS light illumination. The mechanism and the charge pathways differ for the UV and VIS light sources.

3.3.1. UV light illumination. Charge transport. Au is a charge scavenger

Under UV illumination, the ZnO_R/Au structures receive high energy ($E \geq E_g$ of ZnO), over which the electrons of the ZnO conduction band are transferred to their valence band. The charge transport path is illustrated in Fig. 8 as white circles with the corresponding charges, negative "-" corresponds to the electron and positive "+" to the holes. As the Fermi level of Au is located slightly below the CB of ZnO, the excited and positioned electrons in CB move down to the Fermi level of Au. Therefore, Au acts here as an electron scavenger, efficiently suppressing the losses of the charge carriers from the recombination. In turn, the electrons (already moved to the Fermi level of Au from the ZnO CB and the electrons belonging to the Au and located on Fermi level of gold) actively participate in a reduction reaction with oxygen that is generally adsorbed to the semiconductor surface from the air with formation of so-called active reactive species. These are the first superoxide radical ion ($\bullet\text{O}_2^-$), which then reacts with the water molecule and forms $\bullet\text{OH}$ radicals [38–40].

The holes left in the valence band after the ZnO electrons are elevated to the CB react with the OH groups (either those adsorbed to the surface from humid air or H₂O in the aqueous solution) with the formation of the $\bullet\text{OH}$ radical. Both reactive species, $\bullet\text{OH}$ and superoxide radicals ($\bullet\text{O}_2^-$) act destructively on the dye molecule [41]. Finally, the dye molecule under the influence of these radicals decomposes into

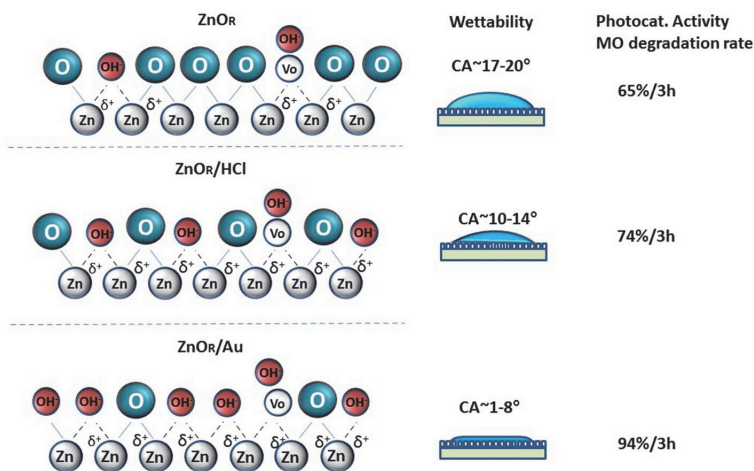


Fig. 9. Illustration of the surface composition and wettability of ZnO_R , ZnO_R/HCl and ZnO_R/Au .

harmless CO_2 and H_2O .

3.3.2. VIS light illumination. Charge transport. Surface plasmon resonance

When the ZnO_R/Au structures are illuminated with visible light, the surface electron of gold is excited and elevated to the higher energy states normally referred to as the surface plasmon resonance (SPR) level, located ca. 2.38 eV from the vacuum level in the energy diagram, Fig. 8 right. The SPR level energetically has a higher position than the conduction band of ZnO, and the electrons of gold are transferred to the CB of ZnO. From the CB of ZnO, they move again to the E_f of gold (as in the case of the illumination with UV light) from where they meet and react with the oxygen, forming first the superoxide ion ($\bullet\text{O}_2^-$) and then reacting with OH groups (on a surface or in water) that leads to $\bullet\text{OH}$ radical formation. Parallel to these reactions, hole left behind after electron elevation to the higher level, was accepted, with OH groups forming $\bullet\text{OH}$ radicals. All the radical species, formed during these charge carriers interactions with the molecules, react with the dye molecule, decomposing it into CO_2 and H_2O .

In the case of illumination with VIS light, there are no ZnO electrons excited in the ZnO conduction band, nor are holes formed in the ZnO valence band. The energy of VIS light is not as powerful compared to the energy of UV light for electrons to be extremely fast and active. This is the main reason why the photocatalytic degradation behavior of the ZnO_R/Au samples illuminated under visible light remains behind those illuminated with powerful UV light.

3.3.3. Chemical interaction of ZnO_R with HAuCl_4 acid. Chemical composition of ZnO_R surfaces

Another important part of the photodegradation mechanism of the dye is a "chemical part" or surface composition of the photocatalyst after an interaction of ZnO_R with HAuCl_4 acid. Fig. 9 has an illustrative reproduction of the ZnO_R , ZnO_R/HCl and ZnO_R/Au surfaces and their wettability.

One of the key components on the surface that plays a key role in photocatalysis is adsorbed to the surface of the photocatalyst OH groups [42,43].

According to the XPS and wettability studies, the relative amount of OH groups on a surface is greater after surface treatment of ZnO_R with an acid solution, either with HCl or HAuCl_4 . OH groups are primary components required for the reactions no. 2a and 2b in Fig. 8 (reaction of an electron with OH groups on the surface with the formation of $\bullet\text{OH}$ radical), the photocatalytic activity directly depends on the amount of

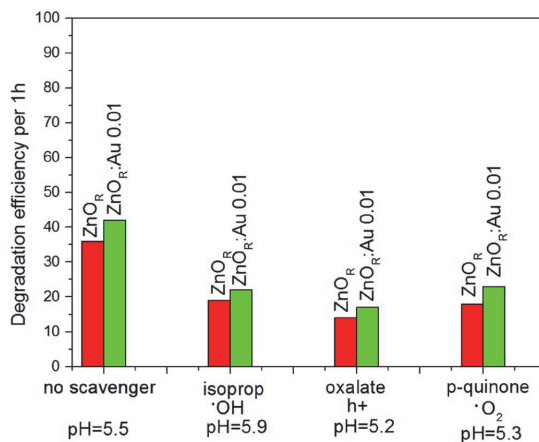


Fig. 10. MO degradation tests by ZnO_R and $\text{ZnO}_R:\text{Au}$ 0.01 photocatalysts with scavenging solutions.

OH groups adsorbed on the surface. In addition, there are many studies that reveal that more hydroxylated surfaces offer better photocatalytic performance [42–44]. $\bullet\text{OH}$ radicals are more active photocatalytically than superoxide radicals [45], therefore, reactions 2a and 2b are the most important to produce OH radicals.

Thus, the hydroxylated chemical surfaces of the ZnO_R surfaces after HAuCl_4 treatment is an another important benefit additionally to a physical issues that give rise to an increased photocatalytic activity.

To prove the existence and prevailing of the reactive species in the solution, we performed so called scavenging test. The isopropanol was used to scavenge the hydroxyl radicals, ammonium oxalate was used to catch the holes, p-quinone was used to bound superoxide radical particles. The degradation efficiency took place 1 h and results are presented in Fig. 10. As can be seen from Fig. 10, the presence of isopropanol, oxalate and p-quinone in MO solution has decreased the photocatalytic efficiency nearly twice compared to the photodegradation rate of unscavenged MO solution. Results show that hydroxo, superoxide radicals and holes are present and taking part in photocatalytic process of MO degradation.

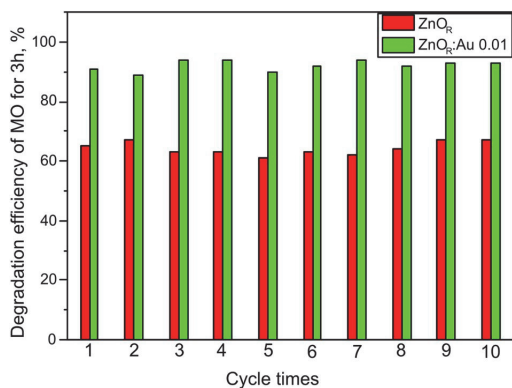


Fig. 11. Recycled photoactivity tests with duration 3h for ZnO_R (left column) and ZnO_R:Au 0.01 (right column).

Table 3

The pH values of the degradative solution before and after irradiation with UV light.

Solution	pH before UV illum	pH after UV illum
Methyl orange (MO)	6.1	5.5
MO + isopropyl alcohol	6.4	5.9
MO + oxalate	5.3	5.2
MO + p-quinone	6.5	5.3

3.4. Stability of ZnO_R and Au/ZnO_R photocatalysts

Furthermore, we have tested the stability of chosen photocatalyst and measured photocatalytic activity for at least 10 times (Fig. 11). Each cycle continued for 3 h. We have also performed the monitoring of pH of MO solution before and after the photocatalytic activity and SEM study of the ZnO_R structures after 10 cycles. The results of pH study are summarized in Table 3 and SEM study of 10 cycles performed by ZnO_R

photocatalysts are presented in Fig. 11.

The stability test results have shown excellent stability of the ZnO_R and Au/ZnO_R photocatalysts. The MO degradation efficiency of ca. 65 and 94% for ZnO_R and ZnO_R:Au 0.01 samples, respectively, was demonstrated after 10 cycles with duration of 3h each.

Moreover, the SEM photos which were taken from the ZnO_R samples after 10 cycles clearly demonstrate the preserved initial rod shaped morphology of ZnO_R layers. The SEM images of ZnO_R and ZnO_R:Au 0.01 nanorods are shown in Fig. 12 a and b, respectively. Thus, ZnO_R samples are stable at pH range of 5.5–6.5 for multiple recycling times. The excellent stability of ZnO_R photocatalysts in MO solution was demonstrated by Refs. [22,23].

4. Conclusions

This article deals with the photocatalytic activity of ZnO_R/Au composites and the reasons behind the increase in photocatalytic activity of these samples compared to pristine ZnO_R structures.

Regardless of the type of illumination, the ZnO_R/Au composites have shown the highest photocatalytic activity, achieving 94% degradation of MO for 3h ($k = 0.016 \text{ min}^{-1}$), compared to ZnO_R with a degradation efficiency of 65% for 3h ($k = 0.006 \text{ min}^{-1}$) under UV illumination. Under irradiation of visible light, the photocatalytic efficiency of the ZnO_R sample is 21%/3h ($k = 0.0014$) compared to 40%/3h ($k = 0.0028$) for the ZnO_R/Au sample.

According to an XPS study, the ZnO_R/Au samples contain up to 2.5 times more hydroxyl groups on a surface compared to the ZnO_R samples. The XPS study is supported by wettability studies, where the water contact angle values of the ZnO_R/Au samples are up to 20 times lower compared to the ZnO_R sample.

Here we report, summarize and illustrate a synergistic mechanism behind enhanced photocatalytic performance of ZnO_R/Au samples that includes following issues together 1) an enhancement in sunlight absorption through a surface plasmon resonance phenomenon and 2) an improvement in charge carrier separation due to the proper energetic band positions of the semiconductor and gold nanoparticle, where gold acts as an electron scavenger; and 3) ZnO_R surface hydroxylation after an interaction with the acidic HAUCl₄ solution. The hydroxyl surface of

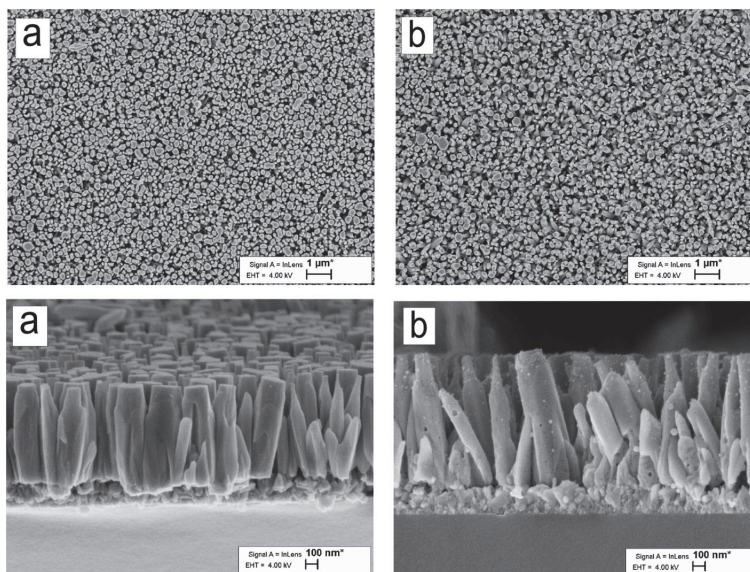


Fig. 12. SEM images of ZnO_R(a) and ZnO_R:Au0.01 (b) after 10 cycles in MO solution (pH 6.1-5.5).

ZnO_R contains a greater amount of hydroxyl groups (OH groups) on the surface, which in turn are transformed into highly reactive radical molecules (•OH, •O²⁻ radicals) that actively destroy the pollutant molecule into harmless CO₂ and H₂O.

Besides that the ZnO_R and ZnO_R:Au samples possess excellent stability, preserving the stable photocatalytic activity and rod shape morphology even after 10 cycles of MO degradation.

Acknowledgements

The authors thank Dr. M. Danilson for recording the XPS spectra, Dr. V. Mikli for recording the SEM images and Dr. A. Mere for a fruitful discussion on a physical part of the paper.

This study was financially supported by the Estonian Ministry of Education and Research, institutional research funding projects IUT 19-4, PRG627 and by the EU through ERDF under project TK141 "Advanced materials and high-technology devices for energy recuperation systems" (2014-2020.4.01.15-0011).

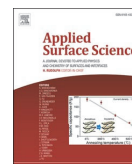
A GINOP-2.2.1-15-2017-00084, an NRDI K 124212 and an NRDI TNN_16 123631 grants are acknowledged. The work performed within project VEKOP-2.3.2-16-2017-00013 was supported by the European Union and the State of Hungary, co-financed by the European Regional Development Fund. The research reported in this paper was supported by the Higher Education Excellence Program of the Ministry of Human Capacities in the frame of Nanotechnology and Materials Science research area of Budapest University of Technology (BME FIKP-NAT).

References

- [1] S. Kuriakose, K. Sahu, S.A. Khan, A. Tripathi, D.K. Avasthi, S. Mohapatra, Facile synthesis of Au-ZnO plasmonic nanohybrids for highly efficient photocatalytic degradation of methylene blue, *Opt. Mater.* 64 (2017) 47–52.
- [2] L.L. Sun, D.X. Zhao, Z.M. Song, C.X. Shan, Z.H. Zhang, B.H. Li, D.Z. Shen, Gold nanoparticles modified ZnO nanorods with improved photocatalytic activity, *J. Colloid Interface Sci.* 363 (1) (2011) 175–181.
- [3] S.N. Ahmed, W. Haider, Heterogeneous photocatalysis and its potential applications in water and wastewater treatment: a review, *Nanotechnology* 29 (34) (2018) 30.
- [4] M.N. Chong, B. Jin, C.W.K. Chow, C. Saint, Recent developments in photocatalytic water treatment technology: a review, *Water Res.* 44 (10) (2010) 2997–3027.
- [5] K.M. Lee, C.W. Lai, K.S. Ngai, J.C. Juan, Recent developments of zinc oxide based photocatalyst in water treatment technology: a review, *Water Res.* 88 (2016) 428–448.
- [6] B. Xue, Y.Q. Zou, High photocatalytic activity of ZnO-graphene composite, *J. Colloid Interface Sci.* 529 (2018) 306–313.
- [7] B. Panigrahy, D.D. Sarma, Enhanced photocatalytic efficiency of AuPd nanoalloy decorated ZnO-reduced graphene oxide nanocomposites, *RSC Adv.* 5 (12) (2015) 8918–8928.
- [8] P. Li, Z. Wei, T. Wu, Q. Peng, Y.D. Li, Au-ZnO hybrid nanopillars and their photocatalytic properties, *J. Am. Chem. Soc.* 133 (15) (2011) 5660–5663.
- [9] Y.Z. Chen, D.Q. Zeng, K. Zhang, A.L. Lu, L.S. Wang, D.L. Peng, Au-ZnO hybrid nanoflowers, nanomultipods and nanopillars: one-pot reaction synthesis and photocatalytic properties, *Nanoscale* 6 (2) (2014) 874–881.
- [10] M.N. Tahir, F. Natalio, M.A. Cambaz, M. Panthofer, R. Branscheid, U. Kolb, W. Tremel, Controlled synthesis of linear and branched Au@ZnO hybrid nanocrystals and their photocatalytic properties, *Nanoscale* 5 (20) (2013) 9944–9949.
- [11] P. She, K.L. Xu, Y.X. Shang, Q.R. He, S. Zeng, S.Y. Yin, G.L. Lu, S. Liang, H. Sun, Z. N. Liu, ZnO nanodisks decorated with Au nanorods for enhanced photocurrent generation and photocatalytic activity, *New J. Chem.* 42 (5) (2018) 3315–3321.
- [12] C.B. Ong, L.Y. Ng, A.W. Mohammad, A review of ZnO nanoparticles as solar photocatalysts: synthesis, mechanisms and applications, *Renew. Sustain. Energy Rev.* 81 (2018) 536–551.
- [13] K.X. Yao, X. Liu, L. Zhao, H.C. Zeng, Y. Han, Site-specific growth of Au particles on ZnO nanopillars under ultraviolet illumination, *Nanoscale* 3 (10) (2011) 4195–4200.
- [14] T.T. Jiang, X.Y. Qin, Y. Sun, M. Yu, UV photocatalytic activity of Au@ZnO core-shell nanostructure with enhanced UV emission, *RSC Adv.* 5 (80) (2015) 65595–65599.
- [15] H.B. Zeng, W.P. Cai, P.S. Liu, X.X. Xu, H.J. Zhou, C. Klingshirn, H. Kalt, ZnO-based hollow nanoparticles by selective etching: elimination and reconstruction of metal-semiconductor interface, improvement of blue emission and photocatalysis, *ACS Nano* 2 (8) (2008) 1661–1670.
- [16] S. Sarkar, A. Makhil, T. Bora, S. Baruah, J. Dutta, S.K. Pal, Photosensitive excited state dynamics in ZnO-Au nanocomposites and their implications in photocatalysis and dye-sensitized solar cells, *Phys. Chem. Chem. Phys.* 13 (27) (2011) 12488–12496.
- [17] W.H. Lin, Y.H. Chiu, P.W. Shao, Y.J. Hsu, Metal-particle-decorated ZnO nanocrystals: photocatalysis and charge dynamics, *ACS Appl. Mater. Interfaces* 8 (48) (2016) 32754–32763.
- [18] C. Mondal, J. Pal, M. Ganguly, A.K. Sinha, J. Jana, T. Pal, A one pot synthesis of Au-ZnO nanocomposites for plasmon-enhanced sunlight driven photocatalytic activity, *New J. Chem.* 38 (7) (2014) 2999–3005.
- [19] T.Y. Liu, W. Chen, Y.X. Hua, X.H. Liu, Au/ZnO nanoarchitectures with Au as both supporter and antenna of visible-light, *Appl. Surf. Sci.* 392 (2017) 616–623.
- [20] J.-J. Wu, C.-H. Tseng, Photocatalytic properties of nc-Au/ZnO nanorod composites, *Appl. Catal. B Environ.* 66 (1) (2006) 51–57.
- [21] J. Lu, H. Wang, D. Peng, T. Chen, S. Dong, Y. Chang, Synthesis and properties of Au/ZnO nanorods as a plasmonic photocatalyst, *Phys. E Low-dimens. Syst. Nanostruct.* 78 (2016) 41–48.
- [22] D.R. Hang, S.E. Islam, C.H. Chen, K.H. Sharma, Full solution-processed synthesis and mechanisms of a recyclable and bifunctional Au/ZnO plasmonic platform for enhanced UV/vis photocatalysis and optical properties, *Chem. Eur J.* 22 (42) (2016) 14950–14961.
- [23] X. Liu, Z. Li, W. Zhao, C. Zhao, J. Yang, Y. Wang, Zinc Oxide nanorod/Au composite arrays and their enhanced photocatalytic properties, *J. Colloid Interface Sci.* 432 (2014) 170–175.
- [24] I.O. Acik, L. Dolgov, M. Krunks, A. Mere, V. Mikli, S. Pikker, A. Loot, I. Sildos, Surface plasmon resonance caused by gold nanoparticles formed on sprayed TiO₂ films, *Thin Solid Films* 553 (2014) 144–147.
- [25] I.O. Acik, N.G. Oyekoya, A. Mere, A. Loot, L. Dolgov, V. Mikli, M. Krunks, I. Sildos, Plasmonic TiO₂:Au composite layers deposited in situ by chemical spray pyrolysis, *Surf. Coating Technol.* 271 (2015) 27–31.
- [26] I. Gromyko, I.O. Acik, M. Krunks, T. Dedova, A. Katerski, A. Mere, V. Mikli, R. Vessart, Surface plasmon resonance in ZnO nanorod arrays caused by gold nanoparticles for solar cell application, in: P. Mascher, et al. (Eds.), *Physica Status Solidi C: Current Topics in Solid State Physics*, vol. 12, 2015, pp. 1338–1343. No 12.
- [27] T. Dedova, M. Krunks, I.O. Acik, D. Klauon, O. Volobujeva, A. Mere, Hierarchical nanostructures of ZnO obtained by spray pyrolysis, *Mater. Chem. Phys.* 141 (1) (2013) 69–75.
- [28] L. Zhang, H.Z. Li, Y. Liu, Z. Tian, B. Yang, Z.B. Sun, S.Q. Yan, Adsorption-photocatalytic degradation of methyl orange over a facile one-step hydrothermally synthesized TiO₂/ZnO-NH₂-RGO nanocomposite, *RSC Adv.* 4 (89) (2014) 48703–48711.
- [29] I. Gromyko, M. Krunks, T. Dedova, A. Katerski, D. Klauon, I.O. Acik, Surface properties of sprayed and electrodeposited ZnO rod layers, *Appl. Surf. Sci.* 405 (2017) 521–528.
- [30] X.Y. Zhang, J.Q. Qin, Y.N. Xue, P.F. Yu, B. Zhang, L.M. Wang, R.P. Liu, Effect of aspect ratio and surface defects on the photocatalytic activity of ZnO nanorods, *Sci. Rep.* 4 (2014).
- [31] J.H. Zheng, Q. Jiang, J.S. Lian, Synthesis and optical properties of flower-like ZnO nanorods by thermal evaporation method, *Appl. Surf. Sci.* 257 (11) (2011) 5083–5087.
- [32] C.Y. Mao, L. Fang, H. Zhang, W.J. Li, F. Wu, G.P. Qin, H.B. Ruan, C.Y. Kong, Effect of B doping on optical, electrical properties and defects of ZnO films, *J. Alloys Compd.* 676 (2016) 135–141.
- [33] A. Sahai, N. Goswami, Probing the dominance of interstitial oxygen defects in ZnO nanoparticles through structural and optical characterizations, *Ceram. Int.* 40 (9) (2014) 14569–14578.
- [34] E. McCafferty, J.P. Wrightman, Determination of the concentration of surface hydroxyl groups on metal oxide films by a quantitative XPS method, *Surf. Interface Anal.* 26 (8) (1998) 549–564.
- [35] L. Grzadzziel, M. Krzywiecki, Ambience-related adsorbates on CuPc surface-Photoemission and thermal desorption spectroscopy studies for control of organic electronics degradation processes, *Synth. Met.* 210 (2015) 141–147.
- [36] E. De la Rosa, S. Sepulveda-Guzman, B. Rejeja-Jayan, A. Torres, P. Salas, N. Elizondo, M.J. Yacamán, Controlling the growth and luminescence properties of well-faceted ZnO nanorods, *J. Phys. Chem. C* 111 (24) (2007) 8489–8495.
- [37] K. Otto, I.O. Acik, M. Krunks, K. Tonsuadu, A. Mere, Thermal decomposition study of H₂AuCl₄ center dot 3H₂O and AgNO₃ as precursors for plasmonic metal nanoparticles, *J. Therm. Anal. Calorim.* 118 (2) (2014) 1065–1072.
- [38] K. Connelly, A.K. Wahab, H. Idriss, Photoreaction of Au/TiO₂ for hydrogen production from renewables: a review on the synergistic effect between anatase and rutile phases of TiO₂, *Mater. Renew. Sustain. Energy* 1 (2012) 3.
- [39] I.A. Shkrob, M.C. Sauer, Hole scavenging and photo-stimulated recombination of electron-hole pairs in aqueous TiO₂ nanoparticles, *J. Phys. Chem. B* 108 (33) (2004) 12497–12511.
- [40] F.L. Deepak (Ed.), *Metal Nanoparticles and Clusters: Advances in Synthesis, Properties and Applications*, Springer International, Portugal, 2018, p. 18.
- [41] A. Ajmal, I. Majeed, R.N. Malik, H. Idriss, M.A. Nadeem, Principles and mechanisms of photocatalytic dye degradation on TiO₂ based photocatalysts: a comparative overview, *RSC Adv.* 4 (70) (2014) 37003–37026.
- [42] A. Di Paola, M. Bellardita, L. Palmisano, Z. Barbierikova, V. Brezova, Influence of crystallinity and OH surface density on the photocatalytic activity of TiO₂ powders, *J. Photochem. Photobiol. Chem.* 273 (2014) 59–67.
- [43] C.Y. Wu, K.J. Tu, J.P. Deng, Y.S. Lo, C.H. Wu, Markedly enhanced surface hydroxyl groups of TiO₂ nanoparticles with superior water-dispersibility for photocatalysis, *Materials* 10 (5) (2017).
- [44] H.P. Suryawanshi, S.G. Bachhav, D.R. Patil, The effect of adsorbed hydroxyl content on the surface of TiO₂ nanorod array and its photocatalytic degradation study, *Curr. Catal.* 7 (3) (2018).
- [45] NIST Chemical Kinetics Database.

Publication II

Z. Chen, T. Dedova, I. Oja Acik, M. Danilson, and M. Krunks. Nickel oxide films by chemical spray: Effect of deposition temperature and solvent type on structural, optical, and surface properties. *Applied Surface Science*, 548, 149118, 2021, <https://doi.org/10.1016/j.apsusc.2021.149118>.



Full Length Article

Nickel oxide films by chemical spray: Effect of deposition temperature and solvent type on structural, optical, and surface properties

Zengjun Chen^a, Tatjana Dedova^a, Ilona Oja Acik^a, Mati Danilson^b, Malle Krunks^{a,*}^a Laboratory of Thin Films Chemical Technologies, Department of Materials and Environmental Technology, Tallinn University of Technology, Ehitajate tee 5, 19086 Tallinn, Estonia^b Laboratory of Optoelectronic Materials Physics, Department of Materials and Environmental Technology, Tallinn University of Technology, Ehitajate tee 5, 19086 Tallinn, Estonia

ARTICLE INFO

Keywords:

NiO film
Spray pyrolysis
Surface chemical composition
Photocatalytic activity

ABSTRACT

Nickel(II) oxide (NiO) films were grown via spray pyrolysis method. The effects of deposition temperature (Ts) and solvent type (aqueous, alcoholic) on the properties of the NiO films were studied. It was found that Ts significantly influenced the surface chemical composition, wettability, and photocatalytic activity (PA) toward degradation of methyl orange (MO) pollutant. The solvent type significantly affected the optical and structural properties of the NiO films. In accordance with the XRD and Raman studies, all deposited NiO films were nanocrystalline defective NiO. According to the XPS study, the OH⁻/Ni-O ratio decreased from 3.31 to 0.59 for the films grown from aqueous solutions at Ts = 300 and 420 °C, respectively, indicating that the surfaces of films grown at lower temperatures were richer in hydroxyl groups. Photocatalytic degradation efficiency was primarily affected by the hydroxyl group content on the surface. The NiO films grown at lower Ts (Ts = 300 °C) demonstrated 4-fold higher degradation efficiency toward MO degradation, at 45% over 3 h, relative to that of the films grown at Ts = 420 °C (11% over 3 h).

1. Introduction

Nickel oxide (NiO) is an important p-type semiconductor with a wide bandgap of 3.0–4.3 eV [1–5]. It has a cubic structure and antiferromagnetic nature. The p-type conductivity is related to non-stoichiometric defects such as Ni vacancies and O interstitials, and can be enhanced, for example, by substituting Ni sites with Li [6,7]. Owing to its chemical stability and electrical and optical properties such as p-type conductivity and a wide span of transmittance in the visible range, NiO has attracted increasing attention for use in various applications including solar cells [8], photocatalysts [9], sensors [10,11], batteries [12], smart windows [13] and supercapacitors [14].

Several techniques have been reported for the synthesis of NiO thin films, including sputtering [15], chemical bath deposition [16], spin coating [17], electrodeposition [18], hydrothermal growth [11] and spray pyrolysis [1,2,6]. Among other techniques, spray pyrolysis is recognised as an important and facile technology for the production of powdered materials and thin films owing to its simplicity, cost-effectiveness, and potential for large-scale industrial production [19–22].

Nickel chloride [23,24], nickel nitrate [24,25], nickel acetate [6,24,26], and nickel acetylacetonate [4,27] have been used as precursors to deposit NiO films by spray pyrolysis. The precursor type strongly affects the crystallinity and homogeneity of the obtained NiO films. It has been reported that NiO films produced from chloride precursors show higher crystallinity and roughness than films produced from acetate and nitrate solutions [24]. Films produced from chloride precursors could even be porous and contain chlorine residues [23].

Deposition temperature is one of the most important parameters influencing the film properties. However, only a few studies have investigated the effect of deposition temperature on the properties of NiO films [6,23–25]. NiO films produced by spray pyrolysis are usually obtained in the growth temperature range of 300–500 °C [6,23–25]. As a rule, an increase in deposition temperature results in a larger crystallite size, irrespective of the precursor. In general, the crystallite size of NiO films produced from chloride precursors is usually higher than that of those obtained from acetate precursors. For example, Kamal et al. [23] reported that the crystallite size of NiO films deposited from a chloride precursor increased from 30 nm to 35 nm by increasing the growth temperature from 300 to 375 °C. Krunks et al. [6] reported that the

* Corresponding author.

E-mail address: malle.krunks@taltech.ee (M. Krunks).

crystallite size of NiO films produced from acetate precursor increased from 6 nm to 10 nm upon increasing the substrate temperature (Ts) from 400 to 500 °C. Gomaa et al. [24] reported that the crystallite size of NiO deposited from an acetate precursor was 10 nm, which was smaller than that of NiO deposited from a chloride precursor (57 nm) at Ts = 450 °C. To date, the effect of deposition temperature on the chemical composition of NiO films has been scarcely studied [23].

The bandgap of NiO films is also influenced by deposition temperature. Films produced from aqueous solution of nitrate precursor showed an increase in bandgap from 3.1 eV to 4.0 eV as Ts was increased from 350 to 390 °C [25]. The bandgap of NiO obtained from a chloride precursor was found to range from 3.04 eV to 3.28 eV by varying the substrate temperature from 425 to 500 °C [28]. In contrast, Mahmoud et al. [26] reported that the bandgap of NiO obtained from an acetate precursor decreased from 3.46 eV to 3.17 eV upon increasing Ts from 275 to 350 °C. As for NiO prepared from alcoholic solutions, it has been reported that the bandgap of NiO obtained by spraying nickel acetylacetonate in an alcoholic solution (ethanol:water = 9:1, vol%) at Ts = 450 °C was in the range of 3.71–3.87 eV [4].

To date, only one study has compared the properties of NiO films obtained from aqueous and alcoholic solutions [6]. The films obtained by spraying alcoholic solutions are usually thinner and smoother compared to those obtained from aqueous solutions [6].

The surface chemical composition of sprayed NiO films was studied in films obtained at a fixed substrate temperature [24,27,29]. For example, Gomaa et al. [24] studied the surface chemical composition of NiO films from different precursors deposited at Ts = 450 °C. It was shown that NiO produced from an acetate precursor contained a higher amount of surface carbon species and had lower Ni/O ratio than those deposited from nitrate and chloride precursors. Chan et al. [29] reported that the surface of a NiO film obtained from an acetylacetonate precursor at Ts = 450 °C contained NiO and Ni₂O₃ phases. Reguig et al. [27] have shown that the surface of sprayed NiO films produced from a chloride precursor at Ts = 350 °C also contained the Ni(OH)₂ phase in addition to the NiO and Ni₂O₃ phases. However, there are no studies in the literature on how different deposition temperatures affect the surface chemical composition of sprayed NiO films.

NiO has also been studied for its photocatalytic activity (PA), and is accepted as an alternative photocatalyst to TiO₂ and ZnO because of its low material cost, high stability, low toxicity, and ability to degrade organic pollutants [30–35]. It has been reported that NiO is a prospective material for heterostructures, viz. NiO/ZnO for more efficient separation of charge carriers resulting in higher PA [36,37].

The PA of NiO is mostly reported and studied in its powdered form due to its high surface area [34,35]. However, powdered photocatalysts have serious drawbacks, such as problems with separation and reusability. Therefore, thin film immobilised on a substrate is viewed as a superior photocatalyst. To date, the PA of sprayed NiO thin films has been studied only by Chakhom et al. [31]. This author reported that the degradation efficiency of the sprayed NiO film prepared from a nickel chloride precursor at Ts = 450 °C on methylene blue in water was 90% in 3 h under UV light irradiation.

In this manuscript, we present a systematic study on the influences of film growth temperature (in the range of 300–420 °C) and solvent type (aqueous or alcohol based) on the structural, optical, morphological properties and surface chemical composition of sprayed NiO films. Moreover, we determined the correlation between the surface chemical composition, wettability, and photocatalytic activity toward degradation of methyl orange by NiO films.

2. Experimental

2.1. Sample preparation

Nickel(II) acetate tetrahydrate (Ni(CH₃COO)₂·4H₂O, 99%, Sigma-Aldrich) was used as the precursor. The precursor was dissolved in

double-deionised (DI) water to prepare the aqueous solution and in a mixture of water and isopropanol (water: isopropanol = 2:3, vol%) to obtain the alcoholic solution. The pH of the solution was adjusted to 5 to prevent hydrolysis of the precursor in the solution. The precursor concentration in the prepared solution was fixed at 0.05 mol/L for both aqueous and alcoholic solutions. The volume of the spray solution was fixed to 50 mL for the aqueous solution and 150 mL for the alcoholic solution. The films were deposited using a homemade pneumatic spray pyrolysis set-up. The distance between the nozzle and substrate was 25 cm. The carrier gas flow rate was 8 L/min, and the solution spray rate was 2 mL/min. Soda-lime glasses (40 × 8 × 1 mm³) were used as substrates. The substrates were thoroughly cleaned using a detergent solution and then washed in DI water. After that, the substrates were sonicated in ethanol for 20 min. Substrate temperatures between 300 °C and 420 °C, at intervals of 40 °C, were used for both aqueous and alcoholic solutions to study the effect of deposition temperature on the film properties.

2.2. Characterisation

X-ray diffraction (XRD) was used to investigate the phase composition and structural properties of the prepared samples. XRD patterns were recorded using a Rigaku Ultima IV diffractometer with Cu K α radiation (λ = 1.5406 Å, 40 kV at 40 mA) and a D/teX Ultra silicon strip detector. The measurements were performed in 2 theta/theta configurations with a scan range of 30–70°, with a step of 0.02° and a scanning speed of 5° min⁻¹.

Raman spectroscopy was used to study the phase composition of the sprayed films. The measurements were conducted at room temperature using a Horiba Jobin Yvon Labram HR 800 spectrometer in backscattering geometry. The excitation wavelength was 532 nm, while the power density was sufficiently low to prevent excessive heating of the sample area of ~100 μ m² over 100 s of data acquisition.

The surface morphology of the samples was investigated by scanning electron microscopy (SEM) using a Zeiss HR Ultra 55 FESEM instrument at an accelerating voltage of 4.0 kV. The film thickness was measured from cross-sectional images of the samples.

The total transmittance (T) and reflectance (R) spectra of the NiO films were recorded on a Jasco V-670 UV-VIS-NIR spectrophotometer equipped with an integrating sphere. The spectra were recorded in the wavelength range of 300–1000 nm. The optical direct bandgap (E_g) of NiO was determined by extrapolation of the linear portion of the (ah ν)² vs. h ν plot (Tauc plot) to meet the x-axis. To draw a Tauc plot, the absorption coefficient, α , was calculated using Eq. (1):

$$\alpha = \frac{1}{d} \ln\left(\frac{1-R}{T}\right) \quad (1)$$

where α is the absorption coefficient, d is the thickness of the film, T is the total transmittance, and R is the total reflectance. X-ray photoelectron spectroscopy (XPS) was performed using a Kratos Analytical AXIS ULTRA DLD spectrometer (Manchester, England) in conjunction with a 165-mm hemispherical electron energy analyser (Kratos Analytical, Manchester, England), and a delay-line detector (Kratos Analytical, Manchester, England) was used to investigate the chemical composition of the surfaces of the NiO thin films. The analysis was carried out with monochromatic Al K α X-rays (1486.6 eV) operating at 15 kV and 150 W.

The Fourier-Transform Infrared (FTIR) transmittance spectra of the NiO films were measured using the KBr pellet method (2 mg of NiO film was scratched from the substrate and thoroughly ground with 198 mg of previously dried KBr powder) in the spectral region of 4000–400 cm⁻¹ on a Perkin Elmer GX-1 spectrometer.

The surface wettability of the deposited films was investigated by measuring the static water contact angle (CA) on a DSA 25 (KRÜSS optronic GmbH) at room temperature at three randomly selected locations on the film surface. CA values were calculated using the sessile

drop fitting method. The samples were cleaned under UV-A irradiation (15 W, $\lambda_{\max} = 365$ nm) before the wettability test and PA test. The PA was measured in the photodegradation of methyl orange (MO) dye under UV-A irradiation (Philips, Hg, TL-D, 15 W, $\lambda_{\max} = 365$ nm) for the NiO samples prepared from aqueous solution and UV-B irradiation (Philips, Hg, PL-L, 36 W, $\lambda_{\max} = 315$ nm) for the samples prepared from alcoholic solution. The initial concentration of the aqueous solution of MO (C_0) was 10 ppm and the volume was 3 mL. The concentration of MO in the solution at a given time (C) was determined by recording the absorbance intensity at 464 nm using a Jasco V-670 UV-VIS-NIR spectrophotometer. The measured absorbance intensity was automatically correlated to the MO concentration in accordance with the previously recorded calibration curve of absorbance intensity vs. known MO concentrations. The absorbance intensity of MO at 464 nm was recorded every 30 min for 3 h. The photodegradation efficiency of MO was calculated from Eq. (2):

$$\eta = (C_0 - C)/C_0 \times 100\% \quad (2)$$

where η is the photodegradation efficiency (%), C_0 (mg/L) is the concentration of the MO solution before UV irradiation, and C (mg/L) is the concentration of the MO solution after the irradiation time.

3. Results and discussion

3.1. Structural, morphological, and optical properties

The XRD patterns of the films prepared from the aqueous solution are presented in Fig. 1. Three well-pronounced reflections at $2\theta = 37.47^\circ$, 43.26° , and 62.67° corresponding to the (111), (200), and (220) crystal planes of cubic NiO (bunsenite) can be clearly seen in Fig. 1. The films did not exhibit any preferential orientation of the crystallites, as the intensity ratio of $I_{(111)}/I_{(200)}$ was in the range of 0.5 to 0.7, which is close to that of the powdered form of NiO ($I_{(111)}/I_{(200)} = 0.669$, PDF-2, 01-071-1179). The crystallite size of the NiO films, as calculated from the FWHM of the (200) reflection by the Scherrer formula increased with the increase in deposition temperature, with values of 4, 6, 8, and 10 nm for the films grown at 300 °C, 340 °C, 380 °C, and 420 °C, respectively. The crystallite size values are in good agreement with those reported for NiO films grown by spray of a nickel acetate solution [6,24]. For example, it has been reported that the crystallite size in sprayed NiO films increased from 6 nm to 10 nm upon increasing the substrate temperature from 400 to 500 °C [6].

The XRD patterns of the films produced from alcoholic solutions showed very broad and weak reflections, indicating that the films were X-ray amorphous. However, the Raman investigations, which detect short-range ordering of the material, clearly revealed the formation of

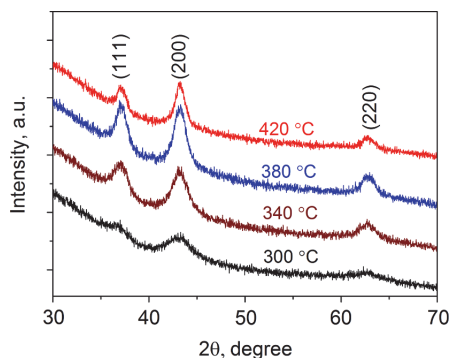


Fig. 1. XRD patterns of NiO films deposited from aqueous solution at $T_s = 300$ – 420 °C.

NiO. Fig. 2 shows the Raman spectra of NiO films in the wavenumber range of 200–1700 cm^{-1} . The profiles of Raman spectra of NiO films grown from aqueous and alcoholic solutions are quite similar, and consist of two wide Raman bands centred at approximately 500 cm^{-1} and 1095 cm^{-1} , which were assigned to the one-phonon transverse optical modes (1P TO) and two-phonon longitudinal optical mode (2P LO) of NiO [38–41], respectively. A weak 2P LO band was detectable only for samples deposited at $T_s \geq 380$ °C.

In many studies, the appearance of the 1P TO band in Raman spectra is characteristic of nanocrystalline, nonstoichiometric NiO produced by wet-chemical methods, such as spray pyrolysis [41,42], hydrothermal growth [43], chemical bath deposition [44] and electrodeposition [45]. The 1P TO sub-bands at 390 cm^{-1} and 460 cm^{-1} were well-pronounced in the Raman spectra of Ni(OH)₂-rich NiO produced by wet-chemical methods [43]. It is worth mentioning that the 1P TO band, a sign of defective material [46], is either missing or negligible in the Raman spectra of stoichiometric defect-free NiO single crystals [47], as well as in the spectra of NiO samples prepared by methods that produce high-quality materials such as electron beam evaporation [42] or epitaxial growth [48]. Thus, the Raman spectroscopy studies confirmed the formation of nanocrystalline defective NiO films from both aqueous and alcohol-based solutions. The SEM images clearly indicate that the film thickness decreased with an increase in the deposition temperature. As can be seen in Fig. 3, the film thickness decreased nearly two-fold from ca. 830 nm to ca. 430 nm with an increase in the deposition temperature from 340 to 420 °C for the films produced from aqueous solution. The thickness of the films deposited from the alcoholic solution dropped from ca. 180 nm to ca. 20 nm as T_s was increased from 340 to 420 °C. The decrease in film thickness with increasing deposition temperature has been reported frequently in the literature and is a characteristic feature of the spray pyrolysis process due to repulsion of the precursor containing droplets from the reaction zone at higher substrate temperatures [6,23,26]. According to the transmittance spectra of the NiO films presented in Fig. 4, two general trends can be observed. First, with an increase in the deposition temperature, the total transmittance of the films increased independently of the solvent used. The second trend is that the films produced from an alcoholic solution exhibited higher transmittance in the visible spectrum range than the NiO films deposited from aqueous solutions. This is probably due to the decrease in film thickness with increasing film growth temperature, and when using an alcohol-based solvent as described above. The Tauc plots of the NiO films deposited at 420 °C from aqueous (a) and alcoholic (b) solutions are shown in Fig. 5. The direct bandgap values were approximately 3.4 eV for the films produced from aqueous solution and 4.0 eV for the films produced from the alcoholic solution, irrespective of the deposition temperature. The larger bandgap of 4.0 eV in the film obtained from the alcoholic solution is most probably due to the amorphous nature of the samples, in comparison to the crystalline NiO films obtained from aqueous solution. The bandgap values obtained are in good agreement with the values for NiO films obtained by spray pyrolysis reported in the literature [1,4,5,24,49]. For example, the bandgap of a sprayed NiO film (aqueous solution, acetate precursor) was 3.5 eV [5] when grown at $T_s = 330$ °C, and 3.43 eV [24] when grown at $T_s = 450$ °C. Similar bandgap values of approximately 3.4 eV have been reported for NiO films grown from chloride precursors [1,49]. The higher bandgap value of 3.87 eV was reported for NiO films prepared from alcoholic solution (ethanol: water = 9:1, vol%, $T_s = 450$ °C, acetylacetonate precursor) [4].

Summarising the previous sections, the XRD study confirmed the formation of a cubic NiO film by spraying of an aqueous solution independent of T_s . Raman spectroscopy confirmed the formation of nanocrystalline defective NiO irrespective of T_s or solvent type. The thickness of the films was altered by both deposition temperature and solvent type. The Eg values of NiO films obtained from alcoholic solution were higher (ca. 4 eV) than those produced from aqueous solution (ca. 3.4 eV) due to the amorphous nature of the films.

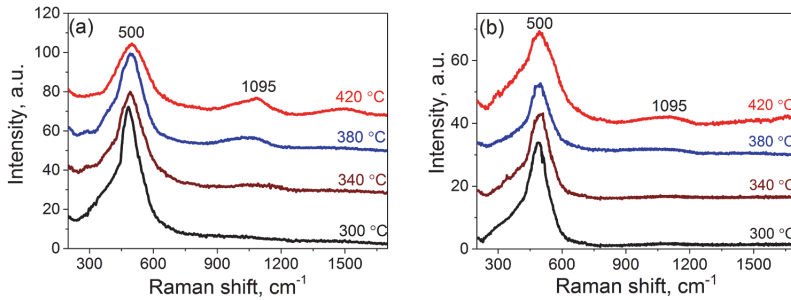


Fig. 2. Raman spectra of NiO films deposited from (a) aqueous solution and (b) alcoholic solution at $T_s = 300\text{--}420\text{ }^\circ\text{C}$.

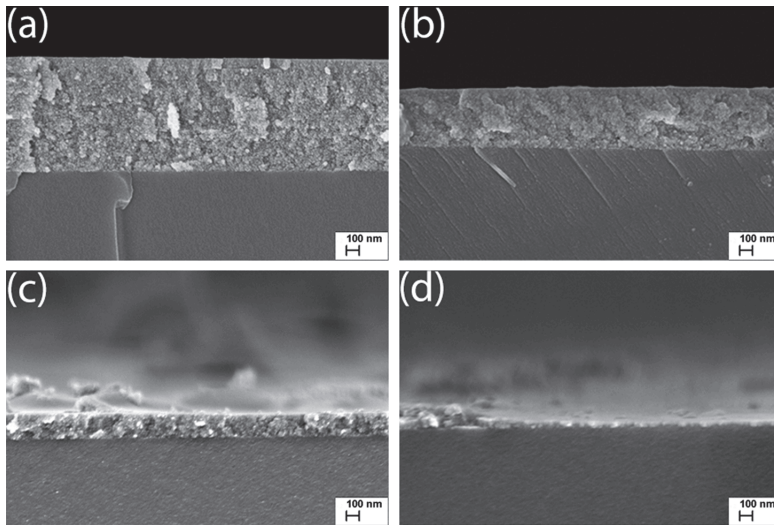


Fig. 3. SEM cross-sectional images of NiO films obtained from aqueous solution at (a) $T_s = 340\text{ }^\circ\text{C}$ and (b) $T_s = 420\text{ }^\circ\text{C}$, and from alcoholic solution at (c) $T_s = 340\text{ }^\circ\text{C}$ and (d) $T_s = 420\text{ }^\circ\text{C}$.

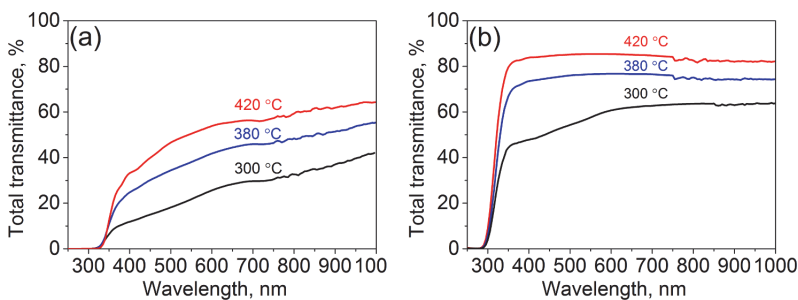


Fig. 4. Total transmittance (T) spectra of NiO films deposited from (a) aqueous solution and (b) alcoholic solution at $T_s = 300\text{--}420\text{ }^\circ\text{C}$.

3.2. Surface chemical composition

The O 1s core-level spectra of NiO films deposited at various temperatures (Fig. 6a) are resolved into two well-pronounced peaks centred at binding energies (BE) of around $529.4 \pm 0.1\text{ eV}$ and 531.0 eV , and two weak peaks centred at around $531.9 \pm 0.1\text{ eV}$ and $532.8 \pm 0.2\text{ eV}$. The peak observed at a BE of $529.4 \pm 0.1\text{ eV}$ corresponds to the

metal–oxygen bond in NiO [4,24,50]. The peak at a BE of $531.0 \pm 0.1\text{ eV}$ can be assigned to several species, including $\text{Ni}(\text{OH})_2$ [51,52], $\text{NiO}(\text{OH})$ [50], Ni_2O_3 [4,29,53] or V_o [51,54]. Beisinger et al. [51] suggested that in the case of stoichiometric NiO with purity of 99.998%, the O 1s core-level peak at 531 eV corresponds to defects in NiO crystals rather than to hydroxide species. A similar assignment of the peak at 531 eV to defects in stoichiometric NiO was supported by other researchers [27,51]. On

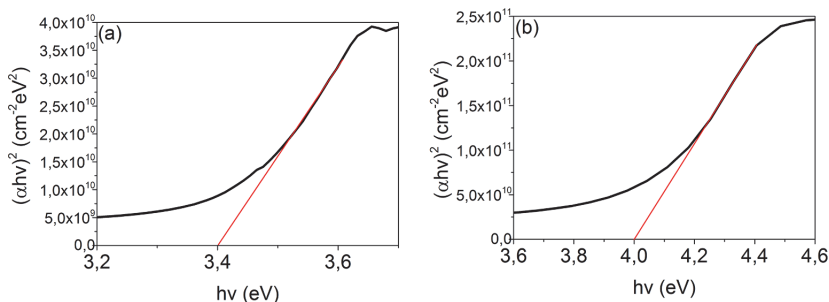


Fig. 5. Tauc plots of the NiO film deposited from (a) aqueous solution and (b) alcoholic solution at 420 °C.

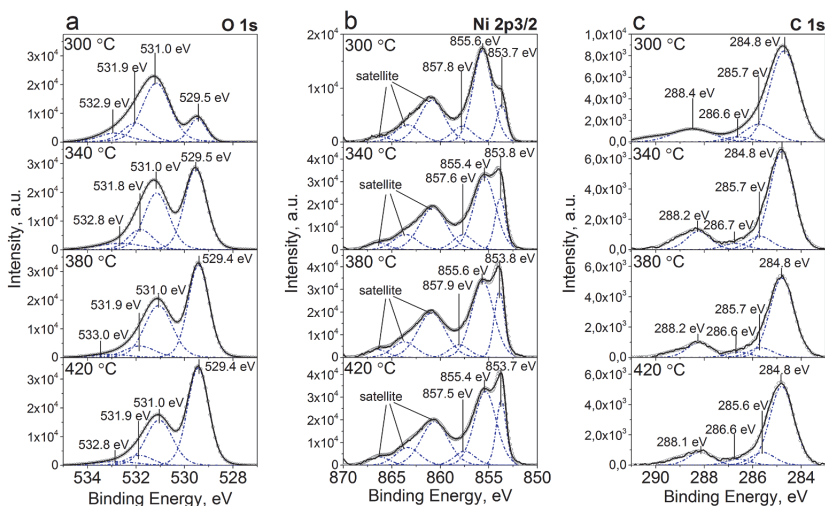


Fig. 6. XPS core-level spectra of NiO films deposited from aqueous solution at $T_s = 300\text{--}420$ °C: (a) O 1s; (b) Ni 2p_{3/2}; (c) C 1s.

the other hand, the same XPS peak at 531 eV was assigned to Ni(OH)₂ in the case of stoichiometric Ni(OH)₂ powder [51]. It is known that oxygen defects such as oxygen vacancies enhance the adsorption of hydroxyl groups. Such interdependency between oxygen defects and hydroxyl groups is very characteristic of materials, particularly oxides, grown by wet chemical methods [54]. The 531 eV band is always present in the O 1s spectra of NiO layers prepared by wet chemical methods, including spray pyrolysis, and is often assigned to Ni(OH)₂ [27,50,55]. A peak at a BE of 531.9 ± 0.1 eV is commonly assigned to surface hydroxyl groups (OH⁻) [54–56] and a weak peak at 532.8 ± 0.2 eV is usually assigned to C–O, C=O, or adsorbed H₂O [54].

In the Ni 2p_{3/2} core-level spectra (Fig. 6b), six peaks were clearly detected, namely the main peaks at BEs of 853.8 ± 0.1 eV, 855.4 ± 0.2 eV, and 857.6 ± 0.3 eV, and the others, satellite and shake up effect peaks, at 860.8 ± 0.1 eV, 863.7 ± 0.1 eV, and 866.6 ± 0.2 eV [27,50]. In accordance with the National Institute of Standards and Technology (NIST) Database and a study presented by Beisinger et al. [51], the Ni 2p_{3/2} core-level spectrum presents a multiple splitting structure, with two major bands at BEs of 853.8 and 855.4 eV both belonging to the stoichiometric NiO and an 855.4 eV/853.8 eV peak intensity ratio of 0.2. At the same time, the band at a BE of 855.4 eV is the main band characteristic of the stoichiometric Ni(OH)₂ phase [27,50]. In addition, in some studies, the 855.4 eV band is assigned to an Ni³⁺ species (most often to Ni₂O₃) [29]. However, according to the XPS spectra of the stoichiometric Ni₂O₃ compound, the main characteristic Ni 2p_{3/2} core-

level bands are centred at BEs of 852.5 and 867.5 eV [57]. Thus, in our case, the weak peak at 857.6 eV probably corresponds to Ni(OH)₂, a characteristic sub-band in the Ni 2p_{3/2} core-level spectra of stoichiometric Ni(OH)₂ powder [51]. The shape and main band positions of the Ni 2p_{3/2} core-level spectra of our NiO layers are very similar to those reported for NiO films produced by wet chemical methods, including spray pyrolysis, chemical bath deposition, hydrothermal growth, and spin coating techniques [4,29,53,55,58].

In the C 1s spectra (Fig. 6c), the peaks at BEs of 284.8 ± 0.1 eV, 285.7 ± 0.1 eV, 286.6 ± 0.1 eV, and 288.2 ± 0.1 eV are usually assigned to C–C, C–O, C=O, and O–C=O, respectively [54].

The main peak positions and assignments of the O 1s, Ni 2p, and C 1s core-level spectra are presented in Table 1.

The quantitative ratios of the main species on the NiO surface as calculated from the integrated areas of the resolved O 1s, Ni 2p_{3/2}, and C 1s core-level spectra, are summarised in Table 2.

As can be seen from Table 2, there was a significant decrease in the proportion of hydroxyl groups on the NiO surfaces with increasing film growth temperature. For example, the Ni(OH)₂/NiO ratio calculated from the O 1s core-level spectra of NiO films deposited from aqueous solution decreased by nearly 5.6-fold, from 3.31 to 0.59 for the films grown at $T_s = 300$ and 420 °C, respectively. Again, the OH⁻/NiO ratio obtained from the O 1s core-level spectra decreased 10-fold as growth temperature was increased from 300 to 420 °C. A slightly less-pronounced but still perceptible decrease in the Ni(OH)₂/NiO ratio

Table 1
Core level spectra peak positions and peak assignments of O 1s, Ni 2p, C 1s core level spectra.

Ts (°C)	O 1s BE (eV)				Ni 2p3/2 BE (eV)		C 1s BE (eV)			
	NiO	Ni(OH) ₂ , Ni ₂ O ₃ , V _o	OH ⁻	C-O, OH _{ads}	NiO	Ni(OH) ₂ , Ni ₂ O ₃ , V _o	C-C	C-O	C=O	O-C=O
300	529.5	531.0	531.9	532.9	853.7	855.6	284.8	285.7	286.6	288.4
340	529.5	531.0	531.8	532.8	853.8	855.4	284.8	285.7	286.7	288.2
380	529.4	531.0	531.9	533.0	853.8	855.6	284.8	285.7	286.6	288.2
420	529.4	531.0	531.9	532.8	853.7	855.4	284.8	285.6	286.6	288.1

Table 2
O1s, Ni2p and C1s core level peak component ratios in NiO films obtained by spray of nickel acetate solutions at various deposition temperatures.

Solvent type	Ts (°C)	O 1s			Ni 2p3/2		C 1s		
		Ni(OH) ₂ /NiO	OH ⁻ /NiO at%/at%	OH _{ads} /NiO	Ni(OH) ₂ /NiO at%/at%	C-O/C-C	C=O/C-C at%/at%	O-C=O/C-C	
aqueous	300	3.31	1.35	0.89	4.62	0.21	0.05	0.20	
	340	0.84	0.28	0.15	2.95	0.14	0.06	0.19	
	380	0.75	0.19	0.07	2.43	0.12	0.07	0.19	
	420	0.59	0.13	0.06	2.38	0.16	0.08	0.17	
alcoholic	340	0.98	1.03	0.37	2.74	0.09	0.02	0.08	

was observed between NiO films sprayed at Ts = 300 and 420 °C, with the ratio decreasing from 4.62 to 2.38, respectively, as calculated from the Ni 2p3/2 core-level spectra.

The CA measurements were in good agreement with the XPS analysis. The CA values presented in Table 3 increased with increasing deposition temperature of the NiO films. For example, the NiO films produced at Ts = 300 °C were of superhydrophilic nature, with CA values of 8° and 10° for samples deposited from aqueous and alcoholic solutions, respectively. The CA value of NiO film synthesised at Ts = 420 °C increased 4-fold from that of the films produced at Ts = 300 °C, and were 35° and 45° for NiO grown using alcoholic and aqueous solvents, respectively and were in good agreement with reduced amount of hydroxyl groups on the surface of films grown at higher temperatures (Table 2).

The presence of hydroxyl groups in the studied NiO films and the gradual decrease in their presence with increasing Ts was also supported by the FTIR study presented in Fig. 7. The FTIR spectra of NiO films deposited from aqueous solution at temperatures of 300–420 °C (Fig. 7) indicate that the films grown from nickel acetate in this temperature range did not correspond to the pure NiO phase, and contained several residuals. A wide band in the region of 3200–3600 cm⁻¹ is characteristic of the O-H stretching vibration [59] and a band centred at 1630 cm⁻¹ represents a distinctive H-O-H bending vibration mode [1]. The films also contained some carbon-related species, as evidenced by the bands centred at 1000 cm⁻¹ and at 1390 cm⁻¹ corresponding to C-O vibration and O-C=O symmetric and non-symmetric stretching vibration modes, respectively [60,61]. It should be noted that the peak positions in the spectra were not affected by the film growth temperature but the intensity of vibrations weakened with increasing film deposition temperature, indicating a decrease in the amount of functional group in the film bulk. Only a band in the region 400–850 cm⁻¹, characteristic of Ni-O stretching vibrations [61], became narrower when deposited at higher

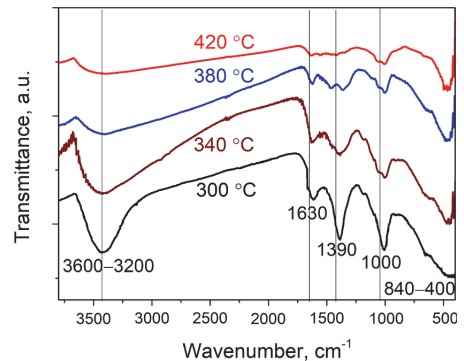


Fig. 7. FTIR spectra of NiO films deposited from aqueous solution at 300, 340, 380, and 420 °C.

temperatures, indicating the strengthening of the Ni–O bond. From the C 1s core-level spectra, the ratios of C-O/C-C, C=O/C-C, and O-C=O did not vary greatly with increasing Ts (Table 2). This result indicates that carbon-containing species on the film surface have a minor effect on the wettability properties, although carbon-containing organics may contaminate the surface and contribute to higher CA values. Thus, according to the XPS study, the surface of the NiO films was mainly composed of NiO and Ni(OH)₂ components, along with a relatively low amount of carbon-containing species. The proportion of Ni(OH)₂/NiO decreased significantly with increasing deposition temperature in the range of 300–420 °C which is in a good correlation with increase in water contact angle values of samples grown at higher temperature.

3.3. Photocatalytic degradation of methyl orange

The degradation curves of methyl orange (MO) under UV irradiation in the presence of NiO films deposited at different Ts from aqueous and alcoholic solutions are presented in Fig. 8a and b, respectively. In accordance with Fig. 8, lower deposition temperatures of the NiO films led to higher photocatalytic activity. For example, the films deposited from aqueous solution at Ts = 300 °C showed a degradation efficiency of 45% in 3 h, and efficiency decreased to 11% over 3 h when the NiO film was sprayed at Ts = 420 °C. A similar dependence was observed for the

Table 3
Water contact angle values of NiO films deposited at various temperatures using different solvents.

Ts (°C)	Water contact angle (°)	
	NiO from aqueous solution	NiO from alcoholic solution
300	8	10
340	13	18
380	25	26
420	35	45

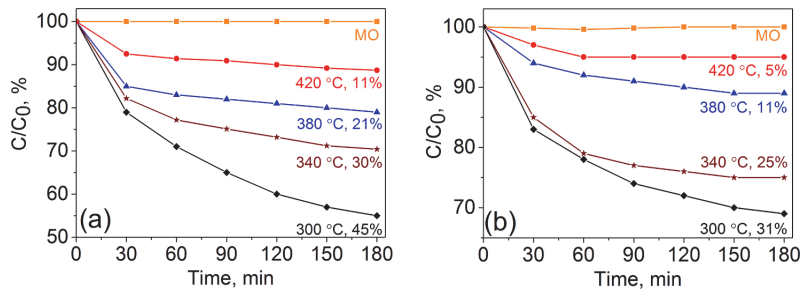


Fig. 8. Photocatalytic MO degradation curves in the presence of NiO films deposited by spraying at different Ts from (a) aqueous solution (UVA irradiation) and (b) alcohol-based solution (UVB irradiation).

films grown from alcoholic solutions. The degradation efficiency of the NiO film grown from alcoholic solutions at Ts = 300 °C was 31%, and only 5% when grown at Ts = 420 °C.

Surface hydroxyl groups are known to play a major role in photocatalysis [54], and hydrophilic surfaces abundant in hydroxyl groups usually demonstrate much higher PA than hydrophobic surfaces [54,62]. The wettability study clearly showed that the CA decreased with decreasing Ts, indicating that the surfaces of the NiO films became more hydrophilic, and the XPS study showed a clear increase in the amount of hydroxyl groups present with decreasing deposition temperature. Thus, the PA of the sprayed NiO samples in this study was directly correlated with the amount of hydroxyl species on the surface of the NiO driven by the deposition temperature of the films.

As can be seen from Fig. 8, the overall degradation efficiency values of the NiO layers grown from the alcoholic solution were slightly lower than those of the samples obtained from aqueous solution. A proposed reason for this is the much lower thickness of the films obtained from alcoholic solution (20 nm) in comparison to that grown from aqueous solution (430 nm) at Ts = 420 °C (Fig. 3).

The photocatalytic degradation efficiency values in the degradation of MO by the NiO films presented in this study are comparable to or even higher than those of NiO particles or fibres published in the literature. For example, Maryam et al. [34] and Tian et al. [63] reported MO degradation efficiency of 22% over 1.5 h and 30% over 3 h, respectively, in the presence of NiO particles. Li et al. [64] reported photocatalytically active NiO nanofibers with a MO degradation efficiency of 40% over 2.5 h.

4. Conclusions

Herein, the structural, optical, properties, and surface chemical compositions of NiO films grown by spray pyrolysis from a nickel acetate precursor have been systematically studied in relation to the growth temperature and solvent type. It was found that deposition temperature was the main technological parameter controlling the surface chemical composition and wettability of NiO films. According to the XPS spectra, in addition to the main NiO phase, the surfaces of the sprayed films contain Ni(OH)₂ and surface hydroxyl groups, which decreased in quantity with increasing film deposition temperature. According to XPS and wettability studies, NiO films grown at lower Ts (Ts = 300 °C) were superhydrophilic (CA = 8°) and had hydroxyl group-rich surfaces with subsequently high photocatalytic capability in the degradation of MO (degradation efficiency ca. 45% in 3 h for NiO films grown from aqueous solution). An increase in Ts led to a decrease in the amount of hydroxyl groups, an increase in the CA (45°), and a decrease in photocatalytic (degradation efficiency ca. 11% in 3 h for NiO films grown from aqueous solution at Ts = 420 °C). A similar correlation between the surface chemical composition and wetting properties was found for the films grown from alcoholic solution.

The solvent type significantly influenced the crystallinity and Eg

values of the NiO films. The crystallite size increased from 4 nm to 10 nm upon increasing the Ts from 340 to 420 °C for the NiO film produced from aqueous solution. The NiO film produced from the alcoholic solution exhibited an amorphous nature. The Eg of the films obtained from alcoholic solution was 4.0 eV, in comparison to the 3.4 eV for NiO films grown from aqueous solution, which was independent of the film growth temperature.

CRedit authorship contribution statement

Zengjun Chen: Conceptualization, Data curation, Formal analysis, Methodology, Software, Writing - original draft. **Tatjana Dedova:** Data curation, Supervision, Validation, Visualization, Writing - review & editing. **Iлона Oja Acik:** Supervision, Validation, Project administration, Funding acquisition. **Mati Danilson:** Formal analysis, Resources, Software. **Malle Krunk:** Conceptualization, Data curation, Formal analysis, Funding acquisition, Validation, Visualization, Supervision, Writing - review & editing.

Declaration of Competing Interest

The authors declare that they have no known competing financial interests or personal relationships that could have appeared to influence the work reported in this paper.

Acknowledgement

This study was funded by the Estonian Research Council project PRG627 "Antimony chalcogenide thin films for next-generation semi-transparent solar cells applicable in electricity producing windows", the Estonian Centre of Excellence project TK141 (TAR16016EK) "Advanced materials and high-technology devices for energy recuperation systems", the European Commission's H2020 programme under the ERA Chair project 5GSOLAR grant agreement No 952509, and ASTRA "TUT Institutional Development Programme for 2016-2022" Graduate School of Functional Materials and Technologies (2014-2020.4.01.16-0032).

Dr. Valdek Mikli is thanked for recording the SEM images.

References

- [1] P.S. Patil, L.D. Kadam, Preparation and characterization of spray pyrolyzed nickel oxide (NiO) thin films, *Appl. Surf. Sci.* 199 (2002) 211–221, [https://doi.org/10.1016/S0169-4332\(02\)00839-5](https://doi.org/10.1016/S0169-4332(02)00839-5).
- [2] J.D. Desai, S.K. Min, K.D. Jung, O.S. Joo, Spray pyrolytic synthesis of large area NiO_x thin films from aqueous nickel acetate solutions, *Appl. Surf. Sci.* 253 (2006) 1781–1786, <https://doi.org/10.1016/j.apsusc.2006.03.009>.
- [3] J.C. Sun, P.D. Li, R.X. Gao, X. Lu, C.R. Li, Y.Y. Lang, X.W. Zhang, J.M. Bian, Piezotronic effect enhanced photo-detector based on ZnO nano-arrays/NiO structure, *Appl. Surf. Sci.* 427 (2018) 613–619, <https://doi.org/10.1016/j.apsusc.2017.09.023>.
- [4] N. Kumar, H.B. Lee, S. Hwang, J.-W. Kang, Large-area, green solvent spray deposited nickel oxide films for scalable fabrication of triple-cation perovskite solar

- cells, *J. Mater. Chem. A* 8 (2020) 3357–3368, <https://doi.org/10.1039/C9TA13528F>.
- [5] K.O. Ukoba, A.C. Eloka-Eboka, F.L. Inambao, Review of nanostructured NiO thin film deposition using the spray pyrolysis technique, *Renew. Sust. Energ. Rev.* 82 (2018) 2900–2915, <https://doi.org/10.1016/j.rser.2017.10.041>.
- [6] M. Krunk, J. Soon, T. Unt, A. Mere, V. Mikli, Deposition of p-type NiO films by chemical spray pyrolysis, *Vacuum* 107 (2014) 242–246, <https://doi.org/10.1016/j.vacuum.2014.02.013>.
- [7] U.S. Joshi, Y. Matsumoto, K. Itaka, M. Sumiya, H. Koinuma, Combinatorial synthesis of Li-doped NiO thin films and their transparent conducting properties, *Appl. Surf. Sci.* 252 (2006) 2524–2528, <https://doi.org/10.1016/j.apsusc.2005.03.239>.
- [8] W. Maiaugree, N. Kongrakaiwoot, A. Tangtrakarn, S. Saekow, S. Pimanpang, V. Amornkithamrong, Efficiency enhancement for dye-sensitized solar cells with a porous NiO/Pt counter electrode, *Appl. Surf. Sci.* 289 (2014) 72–76, <https://doi.org/10.1016/j.apsusc.2013.10.100>.
- [9] J. Ahmad, K. Majid, M.A. Dar, Controlled synthesis of p-type NiO/n-type GO nanocomposite with enhanced photocatalytic activity and study of temperature effect on the photocatalytic activity of the nanocomposite, *Appl. Surf. Sci.* 457 (2018) 417–426, <https://doi.org/10.1016/j.apsusc.2018.06.200>.
- [10] M. Fouladgar, S. Ahmadzadeh, Application of a nanostructured sensor based on NiO nanoparticles modified carbon paste electrode for determination of methyldopa in the presence of folic acid, *Appl. Surf. Sci.* 379 (2016) 150–155, <https://doi.org/10.1016/j.apsusc.2016.04.026>.
- [11] U.T. Nakate, R. Ahmad, P. Patil, Y.T. Yu, Y.B. Hahn, Ultra thin NiO nanosheets for high performance hydrogen gas sensor device, *Appl. Surf. Sci.* 506 (2020), <https://doi.org/10.1016/j.apsusc.2019.144971>.
- [12] P.P. Lv, H.L. Zhao, Z.P. Zeng, C.H. Gao, X. Liu, T.H. Zhang, Self-assembled three-dimensional hierarchical NiO nano/microspheres as high-performance anode material for lithium ion batteries, *Appl. Surf. Sci.* 329 (2015) 301–305, <https://doi.org/10.1016/j.apsusc.2014.12.170>.
- [13] M.P. Browne, H. Nolan, N.C. Berner, G.S. Duesberg, P.E. Colavita, M.E.G. Lyons, Electrochromic nickel oxide films for smart window applications, *Int. J. Electrochem. Sci.* 11 (2016) 6636–6647, <https://doi.org/10.20964/2016.08.38>.
- [14] C.X. Huang, C. Hao, W.H. Zheng, S.S. Zhou, L.Z. Yang, X.H. Wang, C.L. Jiang, L. L. Zhu, Synthesis of polyaniline/nickel oxide/sulfonated graphene ternary composite for all-solid-state asymmetric supercapacitor, *Appl. Surf. Sci.* 505 (2020), <https://doi.org/10.1016/j.apsusc.2019.144589>.
- [15] J. Keraudy, A. Ferrer, M. Richard-Plouet, J. Hamon, A. Goulet, P.Y. Jouan, Nitrogen doping on NiO by reactive magnetron sputtering: a new pathway to dynamically tune the optical and electrical properties, *Appl. Surf. Sci.* 409 (2017) 77–84, <https://doi.org/10.1016/j.apsusc.2017.02.229>.
- [16] H. Yang, J.H. Yu, H.J. Seo, R.H. Jeong, J.H. Boo, Improved electrochromic properties of nanoporous NiO film by NiO flake with thickness controlled by aluminum, *Appl. Surf. Sci.* 461 (2018) 88–92, <https://doi.org/10.1016/j.apsusc.2018.05.231>.
- [17] Y.M. Lee, C.H. Hsu, H.W. Chen, Structural, optical, and electrical properties of p-type NiO films and composite TiO₂/NiO electrodes for solid-state dye-sensitized solar cells, *Appl. Surf. Sci.* 255 (2009) 4658–4663, <https://doi.org/10.1016/j.apsusc.2008.12.014>.
- [18] Q.Y. Xi, G. Gao, H. Zhou, Y.X. Zhao, C.Q. Wu, L.D. Wang, Y.Q. Lei, J.W. Xu, Highly efficient inverted perovskite solar cells mediated by electrodeposition-processed NiO NPs hole-selective contact with different energy structure and surface property, *Appl. Surf. Sci.* 463 (2019) 1107–1116, <https://doi.org/10.1016/j.apsusc.2018.09.019>.
- [19] L. Cattin, B.A. Reguig, A. Khelil, M. Morsli, K. Benchouk, J.C. Bernede, Properties of NiO thin films deposited by chemical spray pyrolysis using different precursor solutions, *Appl. Surf. Sci.* 254 (2008) 5814–5821, <https://doi.org/10.1016/j.apsusc.2008.03.071>.
- [20] A. Juma, I.O. Acik, A.T. Oluwabi, A. Mere, V. Mikli, M. Danilson, M. Krunk, Zirconium doped TiO₂ thin films deposited by chemical spray pyrolysis, *Appl. Surf. Sci.* 387 (2016) 539–545, <https://doi.org/10.1016/j.apsusc.2016.06.093>.
- [21] I.O. Acik, V. Kiisk, M. Krunk, I. Sildos, A. Junolainen, M. Danilson, A. Mere, V. Mikli, Characterisation of samarium and nitrogen co-doped TiO₂ films prepared by chemical spray pyrolysis, *Appl. Surf. Sci.* 261 (2012) 735–741, <https://doi.org/10.1016/j.apsusc.2012.08.090>.
- [22] I.O. Acik, A. Junolainen, V. Mikli, M. Danilson, M. Krunk, Growth of ultra-thin TiO₂ films by spray pyrolysis on different substrates, *Appl. Surf. Sci.* 256 (2009) 1391–1394, <https://doi.org/10.1016/j.apsusc.2009.08.101>.
- [23] H. Kamal, E.K. Elmaghraby, S.A. Ali, K. Abdel-Hady, Characterization of nickel oxide films deposited at different substrate temperatures using spray pyrolysis, *J. Cryst. Growth* 262 (2004) 424–434, <https://doi.org/10.1016/j.jcrysgro.2003.10.090>.
- [24] M.M. Gomaa, G.R. Yazdi, S. Schmidt, M. Boshta, V. Khranovskyy, F. Eriksson, B. S. Farag, M.B.S. Osman, R. Yakimova, Effect of precursor solutions on the structural and optical properties of sprayed NiO thin films, *Mater. Sci. Semicond. Process.* 64 (2017) 32–38, <https://doi.org/10.1016/j.mssp.2017.03.009>.
- [25] R.S. Kate, S.C. Bulakhe, R.J. Deokate, Effect of substrate temperature on properties of nickel oxide (NiO) thin films by spray pyrolysis, *J. Electron. Mater.* 48 (2019) 3220–3228, <https://doi.org/10.1007/s11664-019-07074-0>.
- [26] S.A. Mahmoud, S. Alshomer, M.A.A. Tarawneh, Structural and optical dispersion characterisation of sprayed nickel oxide thin films, *J. Mod. Phys.* 2 (2011) 1178–1186, <https://doi.org/10.4236/jmp.2011.210147>.
- [27] B.A. Reguig, M. Regragui, M. Morsli, A. Khelil, M. Addou, J.C. Bernede, Effect of the precursor solution concentration on the NiO thin film properties deposited by spray pyrolysis, *Sol. Energy Mater. Sol. Cells.* 90 (2006) 1381–1392, <https://doi.org/10.1016/j.solmat.2005.10.003>.
- [28] A.A. Yadav, U.J. Chavan, Influence of substrate temperature on electrochemical supercapacitive performance of spray deposited nickel oxide thin films, *J. Electroanal. Chem.* 782 (2016) 36–42, <https://doi.org/10.1016/j.jelechem.2016.10.006>.
- [29] X.H. Chan, J.R. Jennings, M.A. Hossain, K.K.Z. Yu, Q. Wang, Characteristics of p-NiO thin films prepared by spray pyrolysis and their application in CdS-sensitized photocathodes, *J. Electrochem. Soc.* 158 (2011) H733–H740.
- [30] A.A. Al-Ghamdi, M.S. Abdel-wahab, A.A. Farghali, P.M.Z. Hasan, Structural, optical and photo-catalytic activity of nanocrystalline NiO thin films, *Mater. Res. Bull.* 75 (2016) 71–77, <https://doi.org/10.1016/j.materresbull.2015.11.027>.
- [31] M.A. Chakhom, A. Boukhachem, M. Ghamnia, N. Benamer, N. Mandhi, K. Raoudi, M. Amlouk, An attempt to study (111) oriented NiO-like TCO thin films in terms of structural, optical properties and photocatalytic activities under strontium doping, *Spectrochim. Acta A* 205 (2018) 649–660, <https://doi.org/10.1016/j.saa.2018.07.065>.
- [32] S. Jana, S. Samai, B.C. Mitra, P. Bera, A. Mondal, Nickel oxide thin film from electrodeposited nickel sulfide thin film: peroxide sensing and photo-decomposition of phenol, *Dalton Trans.* 43 (2014) 13096–13104, <https://doi.org/10.1039/c4dt01658k>.
- [33] X.C. Hu, G.H. Wang, J. Wang, Z.F. Hu, Y.R. Su, Step-scheme NiO/BiOI heterojunction photocatalyst for rhodamine photo-degradation, *Appl. Surf. Sci.* 511 (2020), <https://doi.org/10.1016/j.apsusc.2020.145499>.
- [34] M. Karimi-Shamsabadi, M. Behpour, A.K. Babaheidari, Z. Saberi, Efficiently enhancing photocatalytic activity of NiO-ZnO doped onto nanozeoliteX by synergistic effects of p-n heterojunction, supporting and zeolite nanoparticles in photo-degradation of Eriochrome Black T and Methyl Orange, *J. Photochem. Photobiol. A: Chem.* 346 (2017) 133–143, <https://doi.org/10.1016/j.jphtchem.2017.05.038>.
- [35] A.K. Ramasami, M.V. Reddy, G.R. Balakrishna, Combustion synthesis and characterization of NiO nanoparticles, *Mater. Sci. Semicond. Process.* 40 (2015) 194–202, <https://doi.org/10.1016/j.mssp.2015.06.017>.
- [36] Y. Liu, G. Li, R. Mi, C. Deng, P. Gao, An environment-benign method for the synthesis of p-NiO/n-ZnO heterostructure with excellent performance for gas sensing and photocatalysis, *Sens. Actuators B Chem.* 191 (2014) 537–544, <https://doi.org/10.1016/j.snb.2013.10.068>.
- [37] Z.Y. Zhang, C.L. Shao, X.H. Li, C.H. Wang, M.Y. Zhang, Y.C. Liu, Electrospun nanofibers of p-Type NiO/n-Type ZnO heterojunctions with enhanced photocatalytic activity, *ACS Appl. Mater. Interfaces* 2 (2010) 2915–2923, <https://doi.org/10.1021/am100618h>.
- [38] S.S. Nkosi, B. Yalisi, D.E. Motaung, J. Keartland, E. Sideras-Haddad, A. Forbes, B. W. Mwakikunga, Antiferromagnetic-paramagnetic state transition of NiO synthesized by pulsed laser deposition, *Appl. Surf. Sci.* 265 (2013) 860–864, <https://doi.org/10.1016/j.apsusc.2012.11.134>.
- [39] M. Marciuc, M. Ristić, M. Ivanda, S. Musić, Formation and microstructure of nickel oxide films, *J. Alloys Compd.* 541 (2012) 238–243, <https://doi.org/10.1016/j.jallcom.2012.07.021>.
- [40] C. Mrabet, M. Ben Amor, A. Boukhachem, M. Amlouk, T. Manoubi, Physical properties of La-doped NiO sprayed thin films for optoelectronic and sensor applications, *Ceram. Int.* 42 (2016) 5963–5978, <https://doi.org/10.1016/j.ceramint.2015.12.144>.
- [41] F. Chandoul, H. Moussa, K. Jouini, A. Boukhachem, F. Hosni, M.S. Fayache, R. Schneider, Investigation of the properties of nanostructured nickel oxide NiO thin films irradiated at different γ-doses, *J. Mater. Sci. Mater. Electron.* 30 (2019) 348–358, <https://doi.org/10.1007/s10854-018-0299-z>.
- [42] D.Y. Jiang, J.M. Qin, X. Wang, S. Gao, Q.C. Liang, J.X. Zhao, Optical properties of NiO thin films fabricated by electron beam evaporation, *Vacuum* 86 (2012) 1083–1086, <https://doi.org/10.1016/j.vacuum.2011.10.003>.
- [43] L. Kumari, W.Z. Li, C.H. Vannoy, R.M. Leblanc, D.Z. Wang, Vertically aligned and interconnected nickel oxide nanowalls fabricated by hydrothermal route, *Cryst. Res. Technol.* 44 (2009) 495–499, <https://doi.org/10.1002/crat.200800583>.
- [44] M.A. Vidales-Hurtado, A. Mendoza-Galvan, Electrochromism in nickel oxide-based thin films obtained by chemical bath deposition, *Solid State Ion.* 179 (2008) 2065–2068, <https://doi.org/10.1016/j.ssi.2008.07.003>.
- [45] G. Bodurov, P. Stefech, T. Ivanova, K. Gesheva, Investigation of electrodeposited NiO films as electrochromic material for counter electrodes in “Smart Windows”, *Mater. Lett.* 117 (2014) 270–272, <https://doi.org/10.1016/j.matlet.2013.11.118>.
- [46] N. Mironova-Ulmane, A. Kuzmin, I. Sildos, L. Puust, J. Grabis, Magnon and phonon excitations in nanosized NiO, *Latv. J. Phys. Tech. Sci.* 56 (2019) 61–72, <https://doi.org/10.2478/lpts-2019-0014>.
- [47] R.E. Dietz, G.I. Parisot, A.E. Meixner, Infrared absorption and raman scattering by two-magnon processes in NiO, *Phys. Rev. B* 4 (1971), <https://doi.org/10.1103/PhysRevB.4.2302>.
- [48] N. Mironova-Ulmane, A. Kuzmin, I. Sildos, M. Pars, Polarisation dependent Raman study of single-crystal nickel oxide, *Cent. Eur. J. Phys.* 9 (2011) 1096–1099, <https://doi.org/10.2478/s11534-010-0130-9>.
- [49] V. Gowthami, P. Perumal, R. Sivakumar, C. Sanjeeviraja, Structural and optical studies on nickel oxide thin film prepared by nebulizer spray technique, *Phys. B Condens. Matter.* 452 (2014) 1–6, <https://doi.org/10.1016/j.physb.2014.06.030>.
- [50] S.Y. Liu, R. Liu, Y. Chen, S.H. Ho, J.H. Kim, F. So, Nickel oxide hole injection/transport layers for efficient solution-processed organic light-emitting diodes, *Chem. Mater.* 26 (2014) 4528–4534, <https://doi.org/10.1021/cm501898y>.
- [51] M.C. Biesinger, L.W.M. Lau, A.R. Gerson, R.S.C. Smart, The role of the Auger parameter in XPS studies of nickel metal, halides and oxides, *Phys. Chem. Chem. Phys.* 14 (2012) 2434–2442, <https://doi.org/10.1039/c2cp22419d>.

- [52] M.M. Goma, G. RezaYazdi, M. Rodner, G. Greczynski, M. Boshta, M.B.S. Osman, V. Khranovskyy, J. Eriksson, R. Yakimova, Exploring NiO nanosize structures for ammonia sensing, *J. Mater. Sci. Mater. Electron.* 29 (2018) 11870–11877, <https://doi.org/10.1007/s10854-018-9287-6>.
- [53] Y. Tian, L.G. Gong, X.Q. Qi, Y.B. Yang, X.D. Zhao, Effect of substrate temperature on the optical and electrical properties of nitrogen-doped NiO thin films, *Coatings* 9 (2019), <https://doi.org/10.3390/coatings9100634>.
- [54] I. Gromyko, M. Krunks, T. Dedova, A. Katerski, D. Klauson, I. Oja Acik, Surface properties of sprayed and electrodeposited ZnO rod layers, *Appl. Surf. Sci.* 405 (2017) 521–528, <https://doi.org/10.1016/j.apsusc.2017.02.065>.
- [55] L. Berkat, L. Cattin, A. Reguig, M. Regragui, J.C. Bernede, Comparison of the physico-chemical properties of NiO thin films deposited by chemical bath deposition and by spray pyrolysis, *Mater. Chem. Phys.* 89 (2005) 11–20, <https://doi.org/10.1016/j.matchemphys.2004.07.005>.
- [56] I. Dundar, M. Krichevskaya, A. Katerski, I.O. Acik, TiO₂ thin films by ultrasonic spray pyrolysis as photocatalytic material for air purification, *Royal Soc. Open Sci.* 6 (2019), <https://doi.org/10.1098/rsos.181578>.
- [57] A.N. Mansour, C.A. Melendres, Characterization of Ni₂O₃·6H₂O by XPS, *Surf. Sci. Spectra.* 3 (1994) 263, <https://doi.org/10.1116/1.1247755>.
- [58] S. Xi, Y.L. Zhu, Y.T. Yang, S.L. Jiang, Z.R. Tang, Facile Synthesis of free-standing NiO/MnO₂ core-shell nanoflakes on carbon cloth for flexible supercapacitors, *Nanoscale Res. Lett.* 12 (2017), <https://doi.org/10.1186/s11671-017-1939-6>.
- [59] Y. Zhu, W. Chu, N. Wang, T. Lin, W. Yang, J. Wen, X.S. Zhao, Self-assembled Ni/NiO/RGO heterostructures for high-performance supercapacitors, *RSC Adv.* 5 (2015) 77958–77964, <https://doi.org/10.1039/C5RA14790E>.
- [60] A. Rahdar, M. Aliahmad, Y. Azizi, NiO nanoparticles: synthesis and characterization, *J. Nanostruct.* 5 (2015) 145–151, <https://doi.org/10.7508/jns.2015.02.009>.
- [61] M.R. Das, A. Roy, S. Mpelane, A. Mukherjee, P. Mitra, S. Das, Influence of dipping cycle on SILAR synthesized NiO thin film for improved electrochemical performance, *Electrochim. Acta* 273 (2018) 105–114, <https://doi.org/10.1016/j.electacta.2018.04.024>.
- [62] B.J. Cha, S. Saqlain, H.O. Seo, Y.D. Kim, Hydrophilic surface modification of TiO₂ to produce a highly sustainable photocatalyst for outdoor air purification, *Appl. Surf. Sci.* 479 (2019) 31–38, <https://doi.org/10.1016/j.apsusc.2019.01.261>.
- [63] F.S. Tian, Y.L. Liu, Synthesis of p-type NiO/n-type ZnO heterostructure and its enhanced photocatalytic activity, *Scr. Mater.* 69 (2013) 417–419, <https://doi.org/10.1016/j.scriptamat.2013.05.040>.
- [64] J.N. Li, F. Zhao, L. Zhang, M.Y. Zhang, H.F. Jiang, S. Li, J.F. Li, Electrospun hollow ZnO/NiO heterostructures with enhanced photocatalytic activity, *RSC Adv.* 5 (2015) 67610–67616, <https://doi.org/10.1039/c5ra08903d>.

Publication III

Z. Chen, T. Dedova, N. Spalatu, N. Maticiuc, M. Rusu, A. Katerski, I. Oja Acik, T. Unold, and M. Krunks. ZnO/NiO heterostructure with enhanced photocatalytic activity obtained by ultrasonic spray of a NiO shell onto ZnO nanorods. *Colloids and Surfaces A: Physicochemical and Engineering Aspects*, 648, 129366, 2022, <https://doi.org/10.1016/j.colsurfa.2022.129366>.



Contents lists available at ScienceDirect

Colloids and Surfaces A: Physicochemical and Engineering Aspects

journal homepage: www.elsevier.com/locate/colsurfa

ZnO/NiO heterostructures with enhanced photocatalytic activity obtained by ultrasonic spraying of a NiO shell onto ZnO nanorods

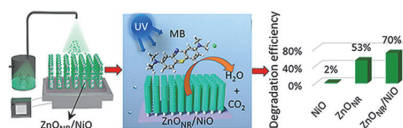
Zengjun Chen^a, Tatjana Dedova^a, Nicolae Spalatu^a, Natalia Maticiu^b, Marin Rusu^c, Atanas Katerski^a, Ilona Oja Acik^a, Thomas Unold^c, Malle Krunks^{a,*}

^a Laboratory of Thin Films Chemical Technologies, Department of Materials and Environmental Technology, Tallinn University of Technology, Ehitajate tee 5, 19086 Tallinn, Estonia

^b Competence Centre Photovoltaics Berlin (PVCoMB), Helmholtz-Zentrum Berlin für Materialien und Energie (HZB), Schwarzschildstraße 3, 12489 Berlin, Germany

^c Struktur und Dynamik von Energiematerialien, Helmholtz-Zentrum Berlin für Materialien und Energie, Lise-Meitner Campus, Hahn-Meitner-Platz 1, 14109 Berlin, Germany

GRAPHICAL ABSTRACT



ARTICLE INFO

Keywords:

NiO film
Ultrasonic spray
n-ZnO/p-NiO photocatalyst
n-ZnO/p-NiO band diagram
Methylene blue
Photocatalytic degradation

ABSTRACT

Degradation of organic pollutants such as methylene blue (MB) from water resources is currently of particular interest. Employment of a heterojunction device with optimized layer properties and proper interface engineering can enhance the photocatalytic performance by taking advantage of efficient charge separation. In this work, we develop an efficient photocatalytic system for the MB degradation based on ZnO nanorod (ZnO_{NR})/NiO core-shell heterostructure with an optimized chemical and electronic structure for achieving record MB degradation efficiency of ~70%. ZnO_{NR} were grown by hydrothermal technique, whereas homogeneous crystalline NiO thin films were prepared by a robust and easy for up-scaling method of ultrasonic spray pyrolysis (USP). The optimum preparation conditions of photocatalytically efficient ZnO_{NR}/NiO heterostructures imply NiO film deposition from two USP cycles at 500 °C followed by air annealing heterostructures at 600 °C. The photocatalytic performance of ZnO_{NR}/NiO core-shell structure was investigated in comparison to counterpart layers and ZnO/NiO bilayer system. Chemical composition and band alignment at the ZnO_{NR}/NiO interface were investigated by X-ray photoelectron spectroscopy, Kelvin probe and photoelectron yield spectroscopy. Current transport studies indicated the presence of built-in electric field at the n-ZnO/p-NiO heterointerface responsible for the enhanced photocatalytic activity and based on this the degradation mechanism of MB is discussed.

* Correspondence to: Department of Materials and Environmental Technology, Tallinn University of Technology, Ehitajate tee 5, 19086 Tallinn, Estonia.

E-mail addresses: zengjun.chen@taltech.ee (Z. Chen), tatjana.dedova@taltech.ee (T. Dedova), nicolae.spalatu@taltech.ee (N. Spalatu), natalia.maticiu@helmholtz-berlin.de (N. Maticiu), rusu@helmholtz-berlin.de (M. Rusu), atanas.katerski@taltech.ee (A. Katerski), ilona.oja@taltech.ee (I.O. Acik), unold@helmholtz-berlin.de (T. Unold), malle.krunks@taltech.ee (M. Krunks).

<https://doi.org/10.1016/j.colsurfa.2022.129366>

Received 4 April 2022; Received in revised form 27 May 2022; Accepted 29 May 2022

Available online 31 May 2022

0927-7757/© 2022 The Author(s). Published by Elsevier B.V. This is an open access article under the CC BY-NC-ND license (<http://creativecommons.org/licenses/by-nc-nd/4.0/>).

1. Introduction

The removal of organic pollutants from water resources is currently of particular concern and photocatalysis is considered a prospective technology for the decomposition of organic pollutants [1]. Among various materials, ZnO is considered an excellent photocatalyst due to its suitable bandgap (~3.37 eV), high photocatalytic activity (PA), biocompatibility, and low cost [2]. It has been reported that ZnO is capable of degrading various organic pollutants, such as methylene blue (MB) [3], methyl orange [4], rhodamine B [5], and acridine orange [6]. However, one major drawback of ZnO as a photocatalyst is its complex point-defect structure, which promotes rapid recombination of photo-generated electron-hole pairs, inhibiting its PA [7–9] and retarding its practical application. One way to overcome this drawback is to couple ZnO with another semiconductor to form a heterojunction [10–14]. In a p-n heterojunction, photogenerated electron-hole pairs are separated by the gradients in their electrochemical potential and the asymmetric conductivity types in the n and p layers [12]. Therefore, a properly engineered heterojunction photocatalyst has the potential for higher PA because of the spatial separation of photogenerated electron-hole pairs. The most commonly used p-type metal oxide semiconductors to form a heterostructure with ZnO are Cu_xO [10,15–17] and NiO [11–13,18,19]. NiO has also been studied as a photocatalyst [20,21] due to its tunable bandgap (3.0–4.3 eV) [22], low material cost and high chemical stability. However, the PA of single NiO is much worse than that of ZnO. The higher PA of ZnO/NiO heterostructures than of either NiO or ZnO has been demonstrated in several studies [8,11–13,18,19,23–26].

In the majority of these studies, the ZnO/NiO photocatalyst was in powder form. For example, Thampany et al. [18] found that ZnO/NiO nanocomposites synthesized by the sonochemical route exhibited an MB degradation efficiency of 90 % in 1 h under sunlight irradiation, in contrast to efficiencies of 20 % and 40 % for degradation by NiO and ZnO alone, respectively. Tian et al. [13] reported that ZnO/NiO nanoparticles grown by precipitation in solution showed a methyl orange degradation efficiency of 100 % under UV illumination over 25 min, in contrast to efficiencies of 10 % and 40 % for NiO and ZnO, respectively. It was also reported that ZnO/NiO nanoparticles prepared by precipitation in solution had a rhodamine B degradation efficiency of 90 % in 200 min under UV light irradiation, in contrast to values of 20 % for NiO and 80 % for ZnO [19]. A photocatalytic degradation efficiency of ca. 80 % for binary mixture of rhodamine B and methylene blue was also reported employing ZnO-NiO composite nanofibers [24].

Although nanopowders and nanofibers obtained such a high degradation efficiency, these approaches have severe drawbacks, such as particle agglomeration and the difficulty of separating photocatalyst from wastewater, causing secondary pollution. The development of heterogeneous photocatalysts immobilized on a substrate, such as a bilayer or core-shell heterostructure, is a more promising approach that allows easy separation and recovery of photocatalysts from polluted environment [11,12]. ZnO nanorod (ZnO_{NR}) layers have been used in ZnO_{NR}/CuO [10,27,28] and ZnO_{NR}/NiO core-shell heterostructures [11, 12] and have the advantage of an increased active surface area compared thin films. For example, ZnO_{NR}/CuO photocatalysts on a substrate, fabricated by solution methods exhibited a 85 % [27] and a 93 % [28] degradation efficiency of MB in 180 min under UV irradiation, being significantly higher than 50 % for ZnO. ZnO_{NR}/CuO core shell structure with CuO by sputtering showed a 80 % methyl orange degradation efficiency in 240 min under UV light compared to ZnO_{NR} [10].

Unlike ZnO_{NR}/CuO photocatalysts, photocatalytic performance of ZnO_{NR}/NiO structures has been studied only in few reports [11,12], although ZnO-NiO nanocomposite photocatalysts in powder and nanofiber form posed high capability to degrade different pollutants. In this perspective, Periyannan et al. [11] reported that ZnO_{NR}/NiO fabricated by sputtering NiO on ZnO_{NR} had a rhodamine B degradation efficiency of 58 % in 180 min under UV light irradiation, in contrast to 54 % for

ZnO_{NR}. Ding et al. [12] found that a ZnO/NiO hierarchical structure on carbon fiber cloth prepared by electrodeposition of NiO on ZnO exhibited a 95 % degradation efficiency of both rhodamine B and methylene orange in 180 min under UV light irradiation, in contrast to 35 % for NiO and 38 % for ZnO.

Although such approaches showed potential for high PA, there is still space for the development and optimization of ZnO/NiO heterojunction photocatalysts, to explore the full potential of this heterostructure. In particular, a specific focus should be set on the optimization of NiO shell properties. The effect of NiO shell thickness on the PA of ZnO_{NR}/NiO core-shell heterostructures was observed in one publication [12] but has never been systematically studied. Moreover, only few methods such as sputtering [11] and electrodeposition [12] were applied to deposit NiO shell. However, the ultrasonic spray pyrolysis (USP) method, a simple and easy for up-scaling method that allows fabrication of thin films with good uniformity and controlled thickness [29–31], has not been used for NiO film deposition to form ZnO/NiO heterostructure until now.

In this study, we investigated the deposition of NiO films by USP and its application in ZnO/NiO core-shell heterostructure. Employment of such heterostructure with optimized NiO shell thickness and ZnO/NiO interface can enhance the photocatalytic performance by taking advantage of efficient charge separation. For NiO film deposition, the nickel acetylacetonate, that has been rarely used for NiO film deposition by spray method [32], was employed as a nickel source. The effect of NiO deposition temperature on the NiO film properties, ZnO/NiO bilayer heterostructure formation and PA for MB degradation was studied. Based on the results, the most suitable temperature for NiO shell deposition onto ZnO_{NR} was selected to optimize NiO shell thickness in the ZnO_{NR}/NiO core-shell heterostructure. Characterization techniques of X-ray photoelectron spectroscopy (XPS), Kelvin probe (KP) analysis and photoelectron yield spectroscopy (PYS) were applied experimentally to prove the formation of n-p junction. As a proof of concept, we developed an efficient ZnO_{NR}/NiO core-shell photocatalytic system with an optimized chemical and electronic structure, which allowed achieving a record MB degradation efficiency of ~70 %.

2. Experimental

2.1. Sample preparation

Three types of samples were prepared on borosilicate glass with a size of 25 × 9 × 1 mm³: (i) NiO thin films, (ii) NiO films deposited onto ZnO films (ZnO/NiO bilayer heterostructures) and (iii) NiO films deposited on ZnO nanorods (ZnO_{NR}/NiO core-shell heterostructures). The glass substrates were thoroughly precleaned with detergent solution, double deionized water, and ethanol in an ultrasonic bath.

2.1.1. Deposition of NiO films

NiO films were grown by the USP method at substrate temperatures (T_s) of 350, 400, 450, and 500 °C. Nickel acetylacetonate (Ni(C₅H₇O₂)₂, 96 %, Sigma-Aldrich Chemie GmbH, Germany) was used as the precursor to deposit NiO. The precursor was dissolved in ethanol to prepare a 10 mM solution. The air flow transporting precursor droplets from the nebulizer to the hot plate was set to 8 L/min. The spray rate was 4 mL/min, and the number of spray cycles was fixed at 12.

2.1.2. Deposition of ZnO films and ZnO nanorod layers

Zinc acetate dihydrate (Zn(CH₃COO)₂·2H₂O, 99.9 %, Sigma-Aldrich Chemie GmbH, Germany) was the precursor for the deposition of ZnO films as a component of the ZnO/NiO bilayer heterostructure and as a seed layer to grow ZnO nanorod layers (ZnO_{NR}). The precursor was dissolved in a mixture of water and isopropanol with a volume ratio of 2:3. The precursor concentration was 0.05 mol/L, and the volume of solution was 20 mL. A few drops of acetic acid were added to the zinc acetate solution to prevent hydrolysis of the precursor. The solution was nebulized with the help of a pneumatic sprayer, which operates in

pulsating mode (5 s spray, 20 s pause). The tin bath temperature was set to 450 °C, and an air flow of 6 L/min was used [33].

ZnO_{NR} was grown on a sprayed ZnO seed layer by a hydrothermal method [33]. Briefly, a glass substrate with a ZnO seed layer was placed into a reactor beaker that contained 40 mL of an aqueous solution of 0.1 mol/L zinc nitrate hexahydrate (Zn(NO₃)₂·6H₂O, 99.9 %, Sigma–Aldrich Chemie GmbH, Germany) and 0.1 mol/L hexamethylenetetramine ((CH₂)₆N₄). The reactor beaker was mounted in a steel autoclave, and the reaction was carried out at 120 °C for 2 h.

2.1.3. Preparation of ZnO/NiO heterostructures

To prepare ZnO/NiO bilayer heterostructures, a ZnO film was deposited first by pneumatic spraying, followed by deposition of a NiO film by USP at 350, 400, 450 and 500 °C. The corresponding ZnO/NiO bilayers were labeled ZnO/NiO(350), ZnO/NiO(400), ZnO/NiO(450), and ZnO/NiO(500). To keep the thickness of the NiO film similar when growing at different temperatures, the number of spray cycles was varied. We used 6, 4, 3, and 3 cycles for NiO grown at 350, 400, 450, and 500 °C, respectively.

To prepare ZnO_{NR}/NiO core-shell heterostructures, NiO films were deposited by USP onto hydrothermally grown ZnO_{NR} using 5 mM nickel acetylacetonate (Ni(acac)₂) in ethanol solution. The substrate temperature for NiO shell deposition was fixed to 500 °C. To vary the thickness of the NiO shell on ZnO_{NR}, 1, 2, and 4 cycles were used, and the corresponding ZnO_{NR}/NiO core-shell samples were labeled ZnO_{NR}/NiO(1), ZnO_{NR}/NiO(2), and ZnO_{NR}/NiO(4), respectively. A schematic illustration of the ZnO/NiO heterostructures is presented in Scheme 1.

A postdeposition annealing procedure was applied for all samples, including NiO films, ZnO_{NR} layers, ZnO/NiO bilayers and ZnO_{NR}/NiO core-shell heterostructures. Annealing was performed at temperature (T_{an}) of 600 °C for 1 h in air, and the samples were labeled accordingly. For example, ZnO_{NR}, ZnO_{NR}/NiO(2), and ZnO_{NR}/NiO(4) annealed at 600 °C were named ZnO_{NR}-600, ZnO_{NR}/NiO(2)-600, and ZnO_{NR}/NiO(4)-600, respectively.

2.2. Characterization methods

X-ray diffraction (XRD), scanning electron microscopy (SEM), and UV–VIS–NIR spectrophotometry were used to measure the XRD patterns, surface morphology and cross section, and total transmittance (T) and reflectance (R) spectra of the samples, respectively. The details on

the measurements and calculation of the optical parameters have been reported elsewhere [20].

The current-voltage (I-V) curves of the ZnO/NiO bilayer (NiO: T_s = 500 °C, 12 cycles) heterostructures on indium tin oxide (ITO) glass substrates were measured at room temperature in the dark by using a two-point probe method with an AutoLab PGSTAT-30. The contact material was graphite deposited from an aqueous graphite ink (Alfa Aesar).

The hot probe method in 2-contact configuration was used to determine the n-type or p-type conductivity of ZnO and NiO films.

The XPS spectra were measured with a standard XPS laboratory system based on a nonmonochromatic X-ray source from SPECS with a Mg anode providing an excitation energy of 1253.6 eV [34]. All XPS spectra were measured at room temperature at a pressure of 5×10^{-6} Pa. The energy analyzer was calibrated by fixing the C 1s binding energy at 285.0 eV.

KP and PYS analysis were used to measure the work function (Φ) and ionization energy (E_i) of the prepared samples, respectively, using a KP Technology SKP5050-APS02 instrument under ambient N₂ in the dark. The details of the measurements and calculation of the work function and ionization energy have been described elsewhere [35].

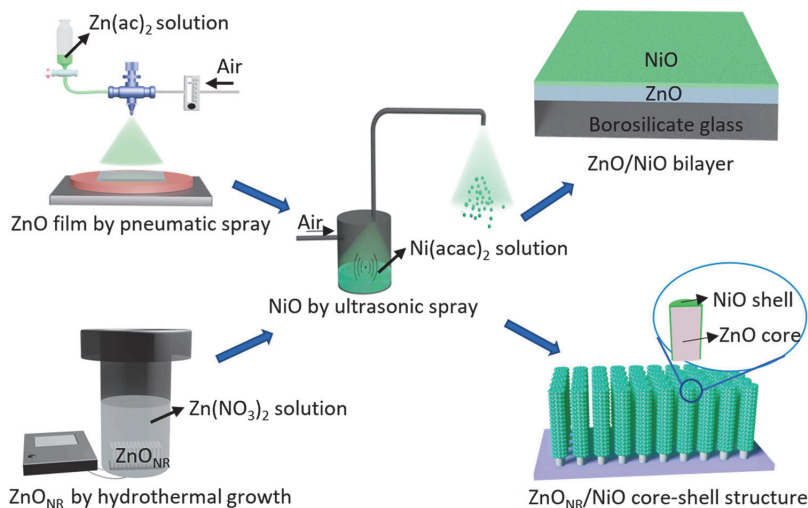
The photodegradation of MB dye was measured under UV-B irradiation (Philips, Hg, PL-L, 36 W, $\lambda_{\text{max}} = 315$ nm) as described elsewhere [20]. Prior to the test, the samples were subjected to a cleaning procedure under UV-A irradiation (15 W, $\lambda_{\text{max}} = 365$ nm) for 30 min. The initial concentration of MB aqueous solution (C₀) was set to 10 mg/L while keeping the volume at 2 mL. A Jasco V-670 UV–VIS–NIR spectrophotometer was used to measure the MB concentration at a given time (C) by recording the MB absorbance intensity at 660 nm. The absorbance spectra were recorded every 30 min for 3 h. The photodegradation efficiency of MB (η) was calculated according to Eq. (1) [20]:

$$\eta = (C_0 - C) / C_0 \times 100\% \quad (1)$$

The photodegradation kinetics of MB dye were estimated using the Langmuir-Hinshelwood model, and the reaction rate constant (k) was calculated from Eq. (2) [33]:

$$\ln(C_0/C) = kt \quad (2)$$

All the $\ln(C_0/C)$ vs. t curves follow a linear relationship with a correlation coefficient (R²) above 0.95, indicating that the



Scheme 1. Schematic illustration of the synthesis of ZnO/NiO heterostructures.

photodegradation of MB dye follows pseudo-first-order reaction kinetics. For each photodegradation measurement four samples, prepared under the same deposition conditions, were used. The standard deviations of degradation efficiencies were calculated.

To understand the role of different reactive species such as $\cdot\text{OH}$, $\cdot\text{O}_2^-$ and h^+ , in the photocatalytic degradation process, the photodegradation of MB in aqueous solution was measured by $\text{ZnO}_{\text{NR}}-600$ and $\text{ZnO}_{\text{NR}}/\text{NiO}(2)-600$ in the presence of tert-Butanol (t-BuOH) as $\cdot\text{OH}$ scavenger, p-Benzoquinone (p-BQ) as $\cdot\text{O}_2^-$ scavenger, and ammonium oxalate (AO) as h^+ scavenger, respectively. The concentration of scavengers in MB solution was set to 1 mmol/L. This measurement has been described elsewhere [36].

3. Results and discussion

3.1. NiO films prepared by USP: effect of growth temperature

First, we investigated the effects of USP deposition conditions on the properties of NiO films. XRD patterns of NiO films deposited at $T_s = 350\text{--}500^\circ\text{C}$ are presented in Fig. 1a. The films showed a main reflection at $2\Theta = 43.51^\circ$, corresponding to the (200) plane of cubic NiO (PDF-2, 01-071-1179), while reflections corresponding to the (111) and (220) planes were less intense. The films exhibited preferential orientation of the crystallites along the (200) plane, as the intensity ratio of $I_{(200)}/I_{(111)}$ was in the range of 6–13, which is much higher than that of the powder reference of NiO ($I_{(200)}/I_{(111)} = 1.49$, PDF-2, 01-071-1179). The crystallite size of the NiO films deposited at $T_s = 350\text{--}500^\circ\text{C}$ was calculated from the full width at half maximum (FWHM) of the (200) reflection using the Scherrer formula [20]. The values of crystallite size are presented in Table 1.

The crystallite size of NiO increased from 17 to 30 nm when T_s increased from 350 to 500 °C. It is widely accepted that films deposited from acetylacetonate precursors may contain organic residuals, which can hinder crystallite growth. A classical procedure to remove organic residuals is postdeposition annealing in air at elevated temperatures in the range of 500–600 °C [37]. Thus, we applied air annealing at $T_{\text{an}} = 600^\circ\text{C}$ for 1 h as the next step. Air annealing at $T_{\text{an}} = 600^\circ\text{C}$

Table 1

Film thickness (d), crystallite size (D) and bandgap (E_g) of NiO films deposited onto glass substrates at $T_s = 350\text{--}500^\circ\text{C}$ and after annealing at $T_{\text{an}} = 600^\circ\text{C}$ for 1 h in air. All the samples were obtained from 10 mM Ni(acac)₂ in ethanol solution using 12 spray cycles.

T_s ($^\circ\text{C}$)	d (nm)	D (nm)		E_g (eV)	
		As-dep	$T_{\text{an}} = 600^\circ\text{C}$	As-dep	$T_{\text{an}} = 600^\circ\text{C}$
350	30	17	24	3.8	3.7
400	45	22	25	3.7	3.7
450	60	25	30	3.7	3.7
500	70	30	30	3.7	3.7

resulted in a larger crystallite size of NiO films deposited at $T_s = 350\text{--}450^\circ\text{C}$ (Table 1), while the crystallite size of NiO deposited at $T_s = 500^\circ\text{C}$ remained the same at 30 nm after annealing.

The SEM images shown in Fig. 1c clearly demonstrate the uniformity and fine-grained structure of the sprayed NiO films independent of the deposition temperature. According to the SEM cross-sectional images, the film thickness increased from ca. 30 nm to ca. 70 nm when increasing T_s from 350 to 500 °C (Fig. 1c, Table 1). It is commonly observed that increasing the deposition temperature increases the thickness of metal oxide films (TiO₂, ZrO_x) produced from acetylacetonate precursors by the spray method [29,31]. The total transmittance spectra of NiO films presented in Fig. 1b indicate an overall optical transmittance of 60–80 % in the visible spectral region. The transmittance of the films grown at lower temperature (350 °C) was at least 10 % higher than the transmittance of the films deposited at 450 °C and 500 °C. The lower optical transparency of NiO films deposited at higher temperatures is probably due to the larger film thickness (Table 1). As-prepared films deposited at 350 °C had an E_g of 3.8 eV. Increasing the deposition temperature from 400 to 500 °C led to similar E_g values of 3.7 eV. Independent of the growth temperature, all the films annealed at 600 °C showed a similar direct bandgap of 3.7 eV (Table 1). The higher E_g value of the NiO film grown at 350 °C could be explained by the presence of some residues in the film that are removed by annealing at 600 °C.

In summary, it is confirmed for the first time that crystalline,

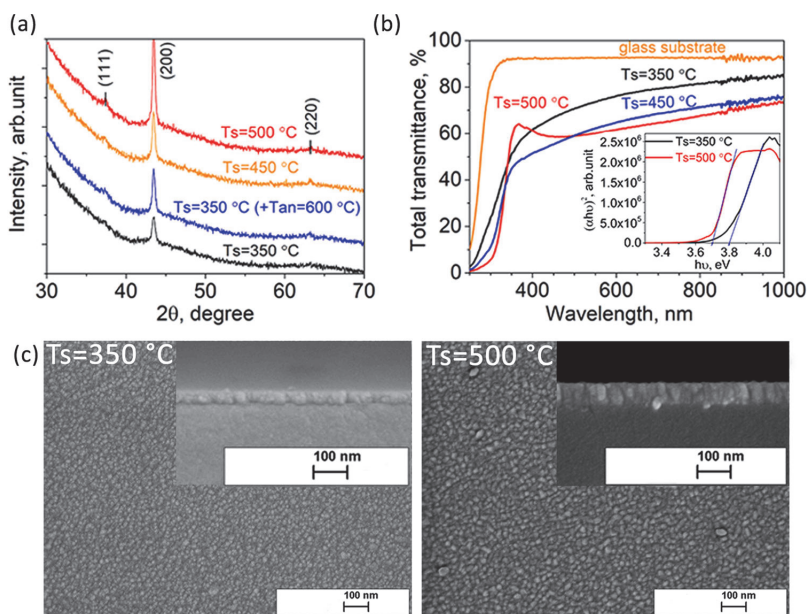


Fig. 1. (a) XRD patterns of NiO films deposited onto glass substrates at $T_s = 350\text{--}500^\circ\text{C}$ and a NiO film deposited at $T_s = 350^\circ\text{C}$ followed by annealing at $T_{\text{an}} = 600^\circ\text{C}$ for 1 h in air. (b) Total transmittance spectra of NiO films deposited onto glass substrates at $T_s = 350\text{--}500^\circ\text{C}$ (inset is the Tauc plot of NiO films deposited at 350 °C and 500 °C). (c) SEM surface and cross-sectional images (inset) of NiO films deposited onto glass substrates at $T_s = 350^\circ\text{C}$ and $T_s = 500^\circ\text{C}$. All the samples were obtained from 10 mM Ni(acac)₂ in ethanol solution using 12 spray cycles.

continuous NiO films with $E_g = 3.7$ eV can be successfully fabricated by the USP method using a nickel acetylacetonate precursor.

3.2. ZnO/NiO bilayer heterostructures: effect of NiO growth temperature

To study the effect of the NiO deposition temperature on the properties of ZnO/NiO bilayer heterostructures, NiO films were deposited onto ZnO at $T_s = 350$ – 500 °C. To keep the NiO film thickness similar at every deposition temperature, the number of spray cycles was varied; namely, 6, 4, 3 and 3 spray cycles at $T_s = 350, 400, 450,$ and 500 °C, respectively, were applied.

XRD patterns of the NiO film and ZnO/NiO bilayer heterostructure with NiO deposited at $T_s = 500$ °C are presented in Fig. 2a. The diffractogram of the NiO film showed a reflection at 2θ of 43.56° corresponding to the (200) plane of NiO. For the ZnO/NiO bilayer heterostructure, the XRD pattern showed several reflections at 2θ of $31.79^\circ, 34.48^\circ, 36.36^\circ, 47.67^\circ, 63.04^\circ,$ and 68.17° , corresponding to the (100), (002), (101), (102), (103), and (112) planes of ZnO, and at 2θ of 43.31° , corresponding to the (200) plane of NiO [18]. Thus, the XRD data confirmed that the NiO film was grown on the ZnO layer.

As a first attempt to prove the formation of a heterojunction between ZnO and NiO, the current-voltage characteristics were measured at room temperature. The current-voltage characteristics of the ZnO/NiO bilayer structure (Fig. 2b) showed pronounced rectifying behavior, indicating the formation of an n-p heterojunction. The conductivity type of each layer was measured by a hot probe, and the result indicated that the ZnO film is an n-type semiconductor material and the NiO film is a p-type semiconductor material.

To evaluate the photocatalytic performance of the as-deposited ZnO/NiO bilayer heterostructures as well as their constituent components, the NiO and ZnO films, MB dye degradation in aqueous solution under UV-B irradiation was measured and compared. The MB degradation curves of these samples are presented in Fig. 2c. The degradation efficiencies and degradation rate constant (k) values are summarized in Table 2.

As shown in Fig. 2c, independent of the deposition temperature, the NiO films possessed extremely low PA activity towards MB dye degradation, ca. 1%. In the case of ZnO/NiO bilayer photocatalysts, PA varied greatly depending on the NiO deposition temperature. The higher the deposition temperature of NiO was, the higher the PA value was (Fig. 2c). The highest degradation efficiency of 30% was achieved by the ZnO/NiO bilayer heterostructure with NiO grown at 500 °C (labeled ZnO/NiO(500) in Fig. 2c), in contrast to the value of 26% for the ZnO film. Annealing at 600 °C improved the degradation efficiency of ZnO/NiO bilayer heterostructures when NiO was grown in the range of 350 – 450 °C, as presented in Table 2. However, no changes in degradation efficiency were observed for NiO grown at 500 °C.

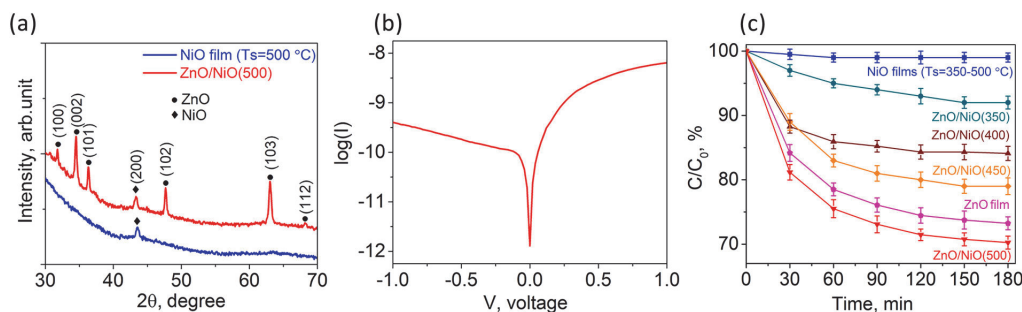


Fig. 2. (a) XRD patterns of NiO film deposited onto glass substrate at $T_s = 500$ °C and ZnO/NiO(500) bilayer heterostructure. (b) I-V curve of ZnO/NiO bilayer on ITO/glass (NiO was deposited at $T_s = 500$ °C using 12 spray cycles, ZnO/NiO bilayer was annealed at $T_{an} = 600$ °C for 1 h in air). (c) Degradation curves of MB by as-deposited samples under UV-B illumination: NiO films ($T_s = 350$ – 500 °C) on glass, ZnO film on glass, and ZnO/NiO(350), ZnO/NiO(400), ZnO/NiO(450), ZnO/NiO(500) bilayer heterostructures (number in bracket shows the NiO layer deposition temperature). NiO was deposited from 10 mM Ni(acac)₂ in ethanol solution.

Table 2

Degradation efficiencies of MB and degradation rate constants (k) obtained with as-deposited samples and samples annealed at $T_{an} = 600$ °C in air for 1 h: NiO films ($T_s = 350$ – 500 °C); ZnO film; and ZnO/NiO bilayer heterostructures with NiO grown at $T_s = 350, 400, 450$ and 500 °C. NiO was deposited from 10 mM Ni(acac)₂ in ethanol solution.

Sample	Degradation efficiency (%)		$k \times 10^{-3} (\text{min}^{-1})$	
	As-dep	$T_{an} = 600$ °C	As-dep	$T_{an} = 600$ °C
NiO film	1	2	–	–
ZnO film	26	32	1.49	2.04
ZnO/NiO(350)	8	13	0.45	0.77
ZnO/NiO(400)	15	20	0.75	1.12
ZnO/NiO(450)	21	26	1.17	1.45
ZnO/NiO(500)	30	30	1.65	1.83

According to the MB photodegradation results, the ZnO/NiO bilayer heterostructure with NiO grown at $T_s = 500$ °C showed the highest degradation efficiency and rate, which also exceeded the PA of the ZnO as-grown film. Annealing of bilayer structures at 600 °C enhances the degradation efficiency compared to their untreated counterparts; however, no improvement in the PA of ZnO/NiO(500) bilayer heterostructures was observed. One possible reason for this phenomenon could be the unoptimized thickness of the NiO layer in the ZnO/NiO bilayer heterostructures. Thus, we further aimed to study the effect of NiO shell thickness on the PA of ZnO/NiO core-shell heterostructures, as will be discussed in the next section.

3.3. ZnO_{NR}/NiO core-shell heterostructures: effect of NiO shell thickness

To take advantage of the high surface active area of nanostructured layers [38], ZnO_{NR} was used as the building block for ZnO_{NR}/NiO core-shell heterostructures. The thickness of the NiO shell on ZnO_{NR} was varied by changing the number of spray cycles (1, 2, or 4 cycles). The deposition temperature of NiO was set at 500 °C according to the results obtained in Section 3.2.

SEM images of the surface of ZnO_{NR} and ZnO_{NR}/NiO core-shell heterostructures are presented in Fig. 3a. The ZnO_{NR} layers are composed of hexagonally shaped elongated ZnO crystals with an average diameter of ca. 100 nm. The ZnO_{NR}/NiO core-shell heterostructure produced from 10 mM Ni(acac)₂ solution with 2 spray cycles reveals coverage by ZnO_{NR} crystals with dots of fine-grained NiO. However, upon decreasing the concentration of Ni(acac)₂ solution from 10 mM to 5 mM, more uniform, denser and smoother coverage, hardly distinguishable on ZnO_{NR} (Fig. 3a), was formed. It should be added that no diffraction peaks characteristic of NiO were detected in the XRD pattern of the ZnO_{NR}/NiO core-shell heterostructure (Fig. S1). Thus, 5 mM Ni(acac)₂ solution was used to deposit NiO onto ZnO_{NR} to form a

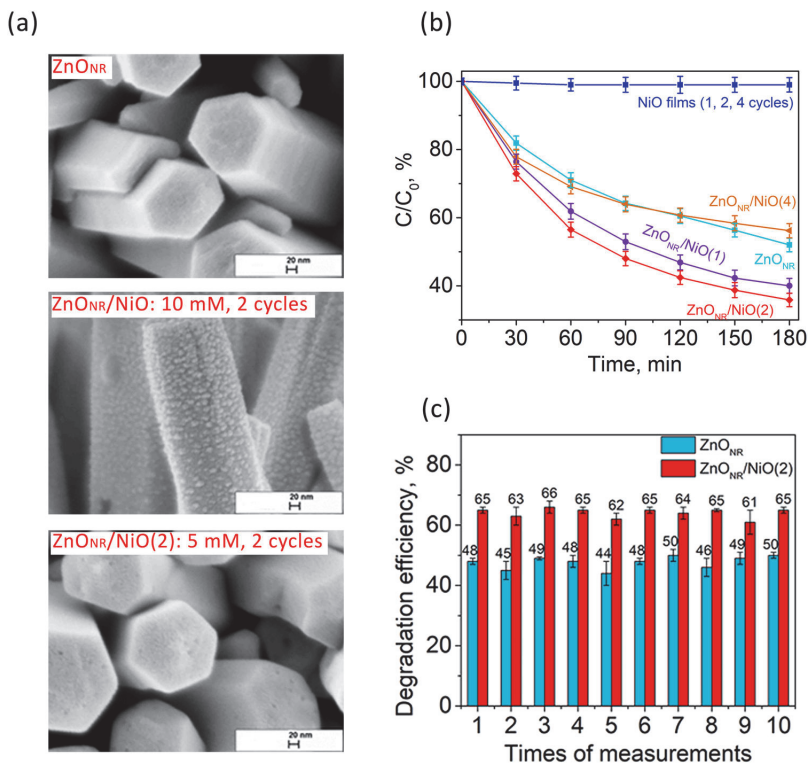


Fig. 3. (a) SEM images of ZnO_{NR} , $\text{ZnO}_{\text{NR}}/\text{NiO}$ core-shell heterostructures with NiO from 10 mM and 5 mM $\text{Ni}(\text{acac})_2$ solution using 2 spray cycles. (b) Degradation curves of MB by as-deposited samples under UV-B illumination: NiO films (1, 2, and 4 spray cycles) on glass, ZnO_{NR} , and $\text{ZnO}_{\text{NR}}/\text{NiO}(1)$, $\text{ZnO}_{\text{NR}}/\text{NiO}(2)$, $\text{ZnO}_{\text{NR}}/\text{NiO}(4)$ core-shell heterostructures; NiO in $\text{ZnO}_{\text{NR}}/\text{NiO}(1)$, $\text{ZnO}_{\text{NR}}/\text{NiO}(2)$, and $\text{ZnO}_{\text{NR}}/\text{NiO}(4)$ was deposited at $T_s = 500^\circ\text{C}$ from 5 mM $\text{Ni}(\text{acac})_2$ in ethanol solution using 1, 2, and 4 spray cycles, respectively. (c) Reusability test of photodegradation of MB by ZnO_{NR} and the $\text{ZnO}_{\text{NR}}/\text{NiO}(2)$ core-shell heterostructure.

$\text{ZnO}_{\text{NR}}/\text{NiO}$ core-shell structure.

The MB photocatalytic degradation curves for the as-deposited $\text{ZnO}_{\text{NR}}/\text{NiO}$ core-shell heterostructures and their components, NiO films and ZnO_{NR} , are shown in Fig. 3b, and the corresponding degradation efficiencies and k values are summarized in Table 3.

Independent of the number of spray cycles, the NiO films showed a negligible degradation efficiency of ca. 1%. Compared to the ZnO film (Table 2), ZnO_{NR} showed nearly twice the MB degradation efficiency, with a value of 48% (Table 3), which can be explained by the higher active surface area of the nanorod layer but may also imply contributions from different surface chemical components [39]. Moreover, $\text{ZnO}_{\text{NR}}/\text{NiO}$ core-shell heterostructures with NiO thicknesses corresponding to 1 or 2 spray cycles exhibited degradation efficiencies of 60% and 64%, respectively, which were higher than the degradation efficiency of 48% obtained by bare ZnO_{NR} . A thicker NiO layer (corresponding to 4 spray cycles) in the $\text{ZnO}_{\text{NR}}/\text{NiO}$ core-shell heterostructure

Table 3

Degradation efficiencies of MB and degradation rate constants (k) by as-deposited samples and samples annealed at $T_{\text{an}} = 600^\circ\text{C}$ in air for 1 h: NiO films; ZnO nanorods (ZnO_{NR}); and $\text{ZnO}_{\text{NR}}/\text{NiO}$ core-shell heterostructures with NiO from 1, 2 and 4 spray cycles. NiO was deposited at $T_s = 500^\circ\text{C}$ from 5 mM $\text{Ni}(\text{acac})_2$ in ethanol solution.

Sample	Degradation efficiency (%)		$k \times 10^{-3} (\text{min}^{-1})$	
	As-dep	$T_{\text{an}} = 600^\circ\text{C}$	As-dep	$T_{\text{an}} = 600^\circ\text{C}$
NiO films	1	2	–	–
ZnO_{NR}	48	53	3.42	4.13
$\text{ZnO}_{\text{NR}}/\text{NiO}(1)$	60	65	5.01	5.66
$\text{ZnO}_{\text{NR}}/\text{NiO}(2)$	64	70	5.51	7.21
$\text{ZnO}_{\text{NR}}/\text{NiO}(4)$	44	50	2.91	3.77

significantly decreased the degradation efficiency from 64% to 44%, showing that it is extremely important to optimize the shell layer thickness.

Similar to the bilayers (Section 3.2), postdeposition annealing at 600°C was applied to the $\text{ZnO}_{\text{NR}}/\text{NiO}$ core-shell heterostructures. Annealing resulted in enhancement of MB degradation efficiency, as summarized in Table 3. For instance, the MB degradation efficiency by $\text{ZnO}_{\text{NR}}/\text{NiO}(2)$ increased from 64% to 70%. Thus, annealing is an important procedure to improve the material properties and quality of heterojunctions.

It is worth mentioning that several research groups have reported the advantages of core-shell heterostructure photocatalysts. Periyannan et al. [11] reported that a $\text{ZnO}_{\text{NR}}/\text{NiO}$ core-shell heterostructure obtained by sputtering NiO on hydrothermally grown ZnO_{NR} exhibited a rhodamine-B degradation efficiency of 58% under UV light in 3 h, in contrast to 54% for bare ZnO_{NR} . For an alternative $\text{ZnO}_{\text{NR}}/\text{Cu}_x\text{O}$ core-shell heterostructure, Montero et al. [10] showed a 65% degradation efficiency towards orange II dye under UV light in 3 h, in contrast to 55% for bare ZnO_{NR} .

The k values before and after annealing at 600°C are presented in Table 3. For the best-performing $\text{ZnO}_{\text{NR}}/\text{NiO}(2)$ sample, the k value of $7.21 \times 10^{-3} \text{min}^{-1}$ was 1.7 times higher than that of bare ZnO_{NR} .

For practical applications, photocatalysts must be reliable and stable. Thus, a reusability test of MB photodegradation by ZnO_{NR} and the $\text{ZnO}_{\text{NR}}/\text{NiO}(2)$ core-shell heterostructure was performed, and the results are presented in Fig. 3c. The measurements were repeated ten times, and for each measurement point, three parallel samples were used. The results show high reproducibility and stability since both ZnO_{NR} and the $\text{ZnO}_{\text{NR}}/\text{NiO}(2)$ core-shell heterostructure still showed MB degradation efficiencies of ca. 44–50% and ca. 61–66%, which are comparable to the initial values.

3.4. XPS analysis of ZnO_{NR}/NiO core-shell heterostructures

XPS analysis was applied to prove the presence of NiO on the surface of ZnO_{NR} and to gain an understanding of the surface chemical composition of ZnO_{NR}-600, ZnO_{NR}/NiO(2)-600, and ZnO_{NR}/NiO(4)-600. The Zn 2p_{3/2}, Ni 2p, and O 1s core-level spectra of these samples are presented in Fig. 4(a), (b), and (c), respectively. The binding energy (BE) of Zn 2p_{3/2} of ZnO_{NR}-600 was centered at 1020.7 eV (Fig. 4a), corresponding to the reported BE value of Zn 2p_{3/2} from ZnO [40,41]. Compared to the result for ZnO_{NR}-600, the Zn 2p_{3/2} peak intensity was significantly decreased for the samples where NiO was deposited onto ZnO_{NR} using two (ZnO_{NR}/NiO(2)-600) or four spray cycles (ZnO_{NR}/NiO(4)-600). The peaks at BEs of 852.5 ± 0.3 eV and 870.9 ± 0.3 eV in the spectra of ZnO_{NR}/NiO(2)-600 and ZnO_{NR}/NiO(4)-600 are commonly assigned to Ni 2p_{3/2} and Ni 2p_{1/2} of NiO, respectively (Fig. 4b) [20]. The XPS spectra also confirmed that NiO was present on the surface of ZnO_{NR}, although NiO was not detected by XRD due to the low film thickness and can hardly be seen in the SEM image (Fig. 2a).

In the analysis of the O1s spectra of ZnO_{NR}-600, the best fit was achieved involving three peaks positioned at BEs of 530.2 eV, 531.8 eV and 532.9 eV, assigned to Zn-O bonds, surface hydroxyl groups (OH), and surface H₂O, respectively [33,39,42]. After covering the nanorods with NiO, a new contribution in the O 1s spectra was revealed at a BE of 528.8 ± 0.1 eV, characteristic of Ni-O bonds [20,43].

It is worth noting that for the ZnO_{NR}/NiO(2)-600 and ZnO_{NR}/NiO(4)-600 heterostructures, the BE of Zn 2p_{3/2} shifted by 0.9 eV and 1.1 eV, respectively, towards lower values compared to the BE of Zn 2p_{3/2} of ZnO_{NR}-600, positioned at 1020.7 eV (Fig. 4a, Table 4). Different reports can be found in the literature about the shift in the BE of Zn 2p emission as a result of ZnO coating with NiO forming a heterostructure. A similar shift in Zn 2p_{3/2} to a lower BE was observed for the ZnO_{NR}/NiO core-shell heterostructure prepared by Periyannan et al. [11]. In that study, a Zn 2p_{3/2} peak shift of 1.1 eV to lower BE values compared to that in pristine ZnO_{NR} was detected. In contrast, Tian et al. [44] reported that for a ZnO/NiO nanocomposite, the Zn 2p_{3/2} BE shifted by 0.6 eV to

a higher energy compared to that of ZnO. Zhang et al. [26] also observed a Zn 2p_{3/2} BE shift of 0.9 eV to a higher energy for a ZnO/NiO nanofiber structure compared to the corresponding value for ZnO nanofibers. Although ZnO/NiO heterostructures were characterized in all these studies, the obtained results are contradictory to some extent. Our results seem to support those reported by Periyannan et al. [11] rather than those reported by Tian et al. [44] and Zhang et al. [26].

To gain more clarity, the Zn_{1MM} Auger spectra of ZnO_{NR}-600, ZnO_{NR}/NiO(2)-600 and ZnO_{NR}/NiO(4)-600 were analyzed. The kinetic energy of Zn_{1MM} and Auger parameter results are presented in Table 4.

The most striking result of this analysis is the observation of a 1.9–2.0 eV difference between the modified Auger parameter values of pristine ZnO_{NR} and ZnO_{NR}/NiO heterostructures. Although the aforementioned BE shift observed by XPS has been related to the formation of heterojunctions, the changes in the Auger parameter confirm the existence of a built-in electric field at the heterojunction interface.

3.5. Band diagram of the ZnO_{NR}/NiO core-shell heterostructure and MB degradation mechanism

To understand the mechanism of photocatalytic degradation by ZnO_{NR}/NiO core-shell heterojunctions, the energetic diagram was evaluated by combining KP and PYS analysis data. The work functions of ZnO_{NR}-600 and ZnO_{NR}/NiO(2)-600 were measured in the dark, and the results are presented in Fig. 5a. The measured work functions of ZnO_{NR}-600 and ZnO_{NR}/NiO(2)-600 showed constant mean values within standard deviations of ± 2 meV, indicating stable surface electronic properties related to the surface chemical stability [35]. The work function was 4.42 eV for ZnO_{NR}-600 and 4.70 eV for ZnO_{NR}/NiO(2)-600. The higher work function value for ZnO_{NR}/NiO(2)-600 than ZnO_{NR}-600 proves the presence of the NiO thin film on the surface of ZnO_{NR}.

The ionization energy (E_i) of ZnO_{NR}-600 and ZnO_{NR}/NiO(2)-600 was measured by PYS. The PYS spectra are presented in Fig. 5b and c, respectively, and the E_i values are summarized in Table 5. The ionization energy is 6.29 eV for ZnO_{NR}-600 and 5.40 eV for ZnO_{NR}/NiO(2)-600. To draw the band diagram of the ZnO_{NR}/NiO heterojunction, the valence band maximum (E_{VBM}) relative to the Fermi level (E_F) was calculated as the difference between the work function (Φ) and ionization energy (E_i), $E_{VBM} = \Phi - E_i$, since Φ defines the E_F position relative to the local vacuum level and E_i is measured relative to the same local vacuum level. [35]. The conduction band minimum (CBM) was calculated as $E_{CBM} = E_{VBM} + E_g$ by using the bandgaps of the hydrothermally grown ZnO_{NR} (3.27 eV) [33] and USP-grown NiO (3.70 eV, Table 1). With the known VBM and CBM positions, the energy band diagram of the ZnO_{NR}/NiO heterostructure could be drawn as shown in Fig. 5d. Thus, the energy band diagram shows n-type conductivity for ZnO_{NR} and p-type conductivity for the NiO film, which agrees with the results of the hot probe measurements in Section 3.2. In addition, rectifying current-voltage behavior is predicted.

It is worth mentioning that in most PA studies, the formation of ZnO/NiO heterojunctions is proposed based on PA results rather than relying on the real energetic parameters of the heterostructure [8,13,18,23,25]. For instance, Thampy et al. [18] claimed that the increased MB degradation efficiency by ZnO/NiO nanoparticles is due to the formation of ZnO/NiO heterojunctions. Additionally, Hameed et al. [8] compared only the MB degradation efficiencies obtained with ZnO/NiO nanoparticles and their single components and concluded that ZnO/NiO heterojunction formation was responsible for the difference. Tian et al. [13] and Liu et al. [25] studied the degradation of methyl orange by ZnO/NiO particles and similarly concluded that the formation of a ZnO/NiO heterojunction was responsible, based only on the PA results. The band diagram was drawn based on compiled parameters from the literature [13,18,23,25]. However, none of the abovementioned studies provided experimentally measured energetic parameters. Thus, the

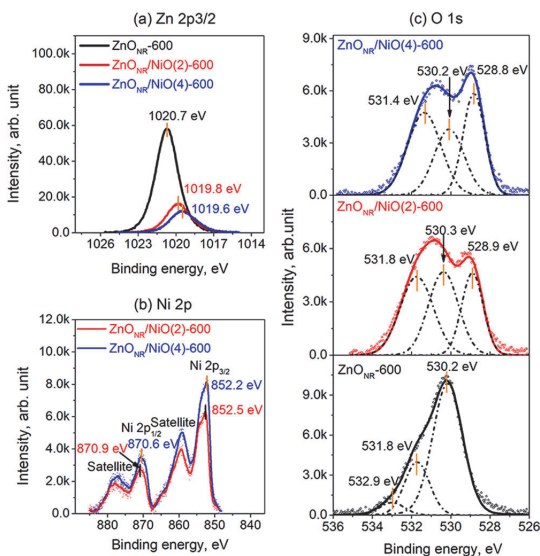


Fig. 4. XPS core-level spectra from ZnO_{NR}-600, ZnO_{NR}/NiO(2)-600, and ZnO_{NR}/NiO(4)-600: (a) Zn 2p_{3/2}, (b) Ni 2p, (c) O 1s. NiO in ZnO_{NR}/NiO(2)-600 and ZnO_{NR}/NiO(4)-600 was deposited at $T_s = 500$ °C from 5 mM Ni(acac)₂ in ethanol solution using 2 and 4 spray cycles, respectively. All the samples were annealed at 600 °C for 1 h in air.

Table 4

Binding energy (BE) of the O 1s, Ni 2p, Zn 2p_{3/2} core levels, kinetic energy of Zn_{LMM}, and the modified Auger parameter (α') for ZnO_{NR}-600, ZnO_{NR}/NiO(2)-600, and ZnO_{NR}/NiO(4)-600. NiO in ZnO_{NR}/NiO(2)-600 and ZnO_{NR}/NiO(4)-600 was deposited at $T_s = 500$ °C from 5 mM Ni(acac)₂ in ethanol solution using 2 and 4 spray cycles, respectively. All the samples were annealed at 600 °C for 1 h in air.

Sample name	BE (eV)							KE (eV) Zn _{LMM}	α' (eV)
	O 1s ZnO	OH	H ₂ O	NiO	Ni 2p _{3/2}	Ni 2p _{1/2}	Zn 2p _{3/2}		
ZnO _{NR} -600	530.2	531.8	532.9	–	–	–	1020.7	988.5	2009.2
ZnO _{NR} /NiO(2)-600	530.3	531.8	–	528.9	852.5	870.9	1019.8	987.4	2007.2
ZnO _{NR} /NiO(4)-600	530.2	531.4	–	528.8	852.2	870.6	1019.6	987.9	2007.3

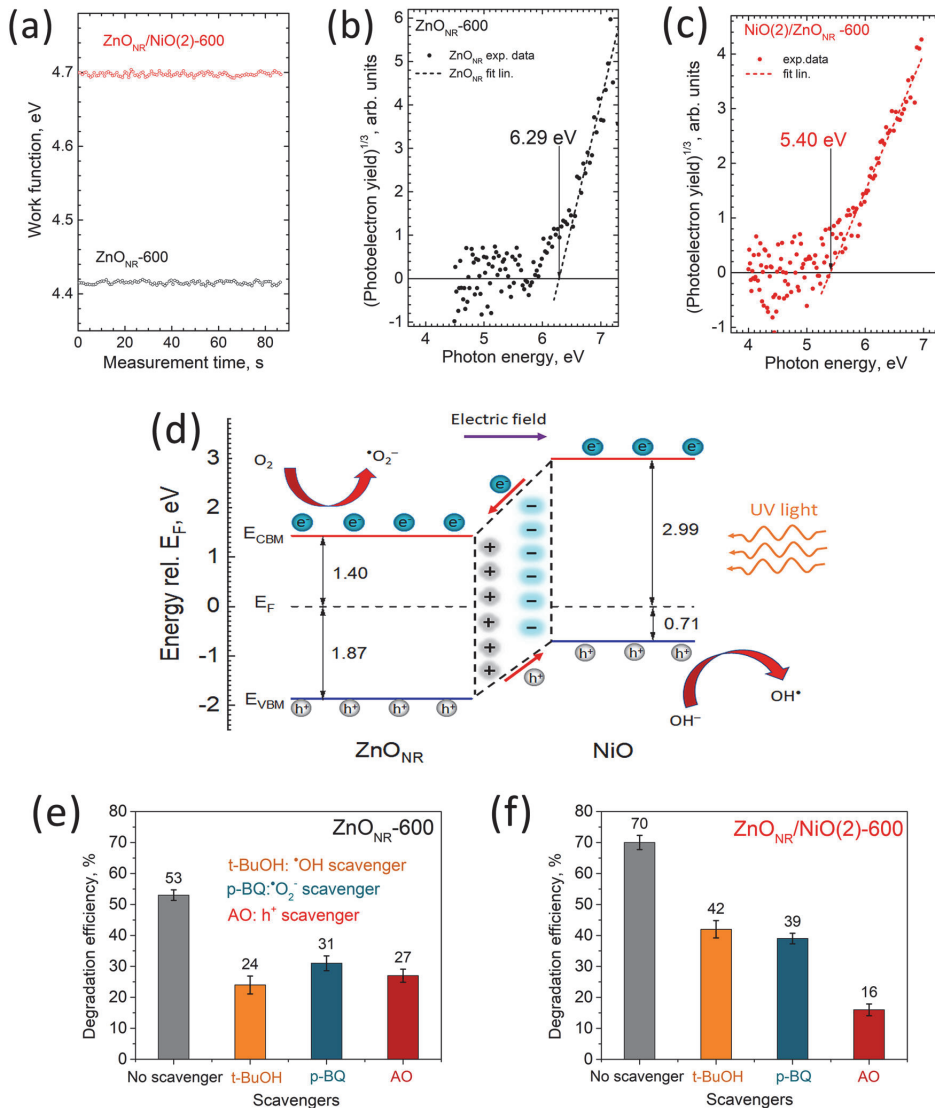


Fig. 5. (a) Time-dependent work function of ZnO_{NR}-600 and ZnO_{NR}/NiO(2)-600. (b) Photoelectron yield spectrum of ZnO_{NR}-600. (c) Photoelectron yield spectrum of ZnO_{NR}/NiO(2)-600. (d) Energy band diagram of ZnO_{NR}/NiO heterojunction. (e) Influence of [•]OH, [•]O₂⁻ and h⁺ scavengers on the MB degradation efficiency by ZnO_{NR}-600. (f) Influence of [•]OH, [•]O₂⁻ and h⁺ scavengers on the MB degradation efficiency by ZnO_{NR}/NiO(2)-600. NiO in ZnO_{NR}/NiO(2) heterostructure was deposited at $T_s = 500$ °C from 5 mM Ni(acac)₂ in ethanol solution using 2 spray cycles. All the samples were annealed at $T_{an} = 600$ °C for 1 h in air.

Table 5

Work function (Φ), ionization energy (E_i) and the energy difference between the Fermi level (E_F) and valence band maximum (E_{VBM}) of ZnO_{NR}-600 and ZnO_{NR}/NiO(2)-600. NiO was deposited at $T_s = 500$ °C from 5 mM Ni(acac)₂ in ethanol solution using 2 spray cycles. Both samples were annealed at 600 °C for 1 h in air.

Sample	Φ (± 0.04 eV)	E_i (± 0.03 eV)	$E_F - E_{VBM}$ (± 0.05 eV)
ZnO _{NR} -600	4.42	6.29	-1.87
ZnO _{NR} /NiO(2)-600	4.70	5.41	-0.71

band diagram of the ZnO_{NR}/NiO heterojunction based on directly measured experimental data (Fig. 5d) and the photocatalytic degradation mechanism was proposed here.

Following the classical concept of heterojunction formation [45], electrons transfer from ZnO to NiO and holes transfer from NiO to ZnO until the system reaches thermodynamic equilibrium and an inner electric field forms at the heterointerface. When the ZnO/NiO heterostructure is irradiated by UV light, electron-hole pairs are generated in both ZnO and NiO, and electrons from the valence band (VB) can be excited to the conduction band (CB) in both materials with the simultaneous formation of the same number of holes in the VB. However, our experimentally proven band alignment for the p-NiO/n-ZnO heterojunction (Fig. 5d) supports the transfer of photogenerated electrons from the CB of NiO to the CB of ZnO and the transfer of photogenerated holes from the VB of ZnO to the VB of NiO, indicating that the electrons and holes are efficiently separated. The electrons from ZnO and holes from NiO are injected into the reaction medium and participate in chemical reactions to degrade different organic pollutants. The electrons interact with dissolved O₂ molecules and produce superoxide radical ($^{\bullet}\text{O}_2^-$). The photogenerated holes are trapped by OH⁻, forming hydroxyl radical species ($^{\bullet}\text{OH}$).

To verify the role of $^{\bullet}\text{OH}$, $^{\bullet}\text{O}_2^-$ and h^+ in the photodegradation process, MB photodegradation measurements were performed in the presence of different scavengers (such as tert-Butanol as $^{\bullet}\text{OH}$ scavenger, p-Benzoquinone as $^{\bullet}\text{O}_2^-$ scavenger, and ammonium oxalate as h^+ scavenger). The results of the test are presented in Fig. 5e and f. Both ZnO_{NR}-600 and ZnO_{NR}/NiO(2)-600 exhibited lower degradation efficiency of MB in the presence of $^{\bullet}\text{OH}$, $^{\bullet}\text{O}_2^-$ and h^+ scavengers compared to that measured without adding a scavenger, indicating the active role $^{\bullet}\text{OH}$ and $^{\bullet}\text{O}_2^-$ species, as well as the role of the photogenerated carriers responsible for the generation of related radicals. The impact of the latest one is well supported by the enhanced photocatalytic activity of ZnO_{NR}/NiO heterojunction (compared to ZnO_{NR} alone, Fig. 5e) in which the photogenerated carriers are efficiently separated towards the surface and transferred to reactive surface sites. The reduced degradation efficiency of MB by ZnO_{NR}/NiO(2)-600 in the presence of the ammonium oxalate as h^+ scavenger (Fig. 5f) suggests that the photogenerated holes are efficiently transferred towards the surface of NiO shell contributing to the degradation efficiency of MB through the formation of $^{\bullet}\text{OH}$ radicals.

This study clearly demonstrated that the efficient separation of charge carriers at the ZnO_{NR}/NiO heterointerface boosts the photocatalytic performance.

4. Conclusions

In this study, we demonstrated for the first time that homogeneous crystalline films of NiO with cubic structure can be successfully grown on glass substrates by employing a robust ultrasonic spray technique and nickel acetylacetonate as a source material. Increasing the deposition temperature from 350 to 500 °C increased the NiO film thickness from ca. 30 to ca. 70 nm, and the mean crystallite size increased from ca. 17 to ca. 30 nm. Post-deposition annealing of as-grown films at 600 °C in air slightly increased the mean crystallite size. The films exhibited a direct

bandgap value of 3.7 eV after annealing.

NiO layers were applied to ZnO films and ZnO nanorods to fabricate ZnO/NiO bilayer and ZnO_{NR}/NiO core-shell heterostructures for which optimal preparation temperature and thickness were found. The photocatalytic degradation of MB by the NiO film, ZnO film, ZnO_{NR}, ZnO/NiO bilayer, and ZnO_{NR}/NiO core-shell heterostructure was analyzed under ultraviolet irradiation for 180 min. While the ZnO_{NR} showed a reasonable degradation efficiency of 48 %, NiO alone exhibited a negligible performance of 1–2 %. The record degradation efficiency of 70 % was achieved by ZnO_{NR}/NiO core-shell heterostructure, with optimized NiO shell thickness from two spray cycles, deposition temperature of 500 °C, and post-deposition air treatment at 600 °C.

Current-voltage characteristics of ZnO/NiO bilayer indicate the formation of rectifying behavior between n-type ZnO and p-type NiO film, being an approval of p-n junction formation. XPS analysis confirmed the formation of NiO shell on ZnO core and showed a 1.9–2.0 eV difference in modified Auger parameter between ZnO_{NR} and ZnO_{NR}/NiO core-shell heterostructure, validating the presence of built-in electric field at the interface. A type-II band diagram between NiO and ZnO_{NR} is proposed based on Kelvin probe and photoelectron yield spectroscopy measurements. Based on these results, the degradation mechanism of MB is discussed in which the built-in electric field at the heterointerface stimulated the enhanced photocatalytic activity.

To our knowledge, the achieved photocatalytic activity is the highest reported for the degradation of MB, employing ZnO_{NR}/NiO core-shell heterojunction concept. A similar ZnO_{NR}/NiO core-shell heterojunction photocatalyst was applied in one recent study [11], however, the degradation efficiency of 58 % was reported for a Rhodamine B pollutant. Our study provides an advanced and feasible proof of concept design for cost-effective heterojunction photocatalysts. Further research efforts on optimization of the related material and interfaces will allow subsequent improvement of photocatalytic activity and deployment of the device for wider range of pollutants.

CRediT authorship contribution statement

Zengjun Chen: Conceptualization, Formal analysis, Methodology, Software, Writing – original draft. **Tatjana Dedova:** Methodology, Supervision, Writing – review & editing. **Nicolae Spalatu:** Methodology, Formal analysis, Writing – review & editing. **Natalia Maticiu:** Formal analysis, Writing – review & editing. **Marin Rusu:** Formal analysis, Writing – review & editing. **Atanas Katerski:** Formal analysis, Writing – review & editing. **Iлона Oja Acik:** Project administration, Funding acquisition, Writing – review & editing. **Thomas Unold:** Writing – review & editing. **Malle Krunk:** Conceptualization, Methodology, Funding acquisition, Supervision, Writing – review & editing.

Declaration of Competing Interest

The authors declare that they have no known competing financial interests or personal relationships that could have appeared to influence the work reported in this paper.

Acknowledgement

This study was funded by the Estonian Research Council (project PRG627), the Archimedes SA (Estonian Centre of Excellence Project TK141 (TAR16016EK)), the European Commission's H2020 programme under the ERA Chair (grant agreement No 952509), and the ASTRA "TUT Institutional Development Programme for 2016–2022" Graduate School of Functional Materials and Technologies (2014–2020.4.01.16-0032).

Appendix A. Supporting information

Supplementary data associated with this article can be found in the

online version at [doi:10.1016/j.colsurfa.2022.129366](https://doi.org/10.1016/j.colsurfa.2022.129366).

References

- [1] U.I. Gaya, A.H. Abdullah, Heterogeneous photocatalytic degradation of organic contaminants over titanium dioxide: a review of fundamentals, progress and problems, *J. Photochem. Photobiol. C Photochem. Rev.* 9 (1) (2008) 1–12, <https://doi.org/10.1016/j.jphotochemrev.2007.12.003>.
- [2] K. Qi, B. Cheng, J. Yu, W. Ho, Review on the improvement of the photocatalytic and antibacterial activities of ZnO, *J. Alloy. Compd.* 727 (2017) 792–820, <https://doi.org/10.1016/j.jallcom.2017.08.142>.
- [3] F. Liu, M.Y. Guo, Y.H. Leung, A.B. Djurišić, A.M.C. Ng, W.K. Chan, Effect of starting properties and annealing on photocatalytic activity of ZnO nanoparticles, *Appl. Surf. Sci.* 283 (2013) 914–923, <https://doi.org/10.1016/j.apsusc.2013.07.043>.
- [4] M.Y. Guo, A.M.C. Ng, F. Liu, A.B. Djurišić, W.K. Chan, H. Su, K.S. Wong, Effect of native defects on photocatalytic properties of ZnO, *J. Phys. Chem. C* 115 (22) (2011) 11095–11101, <https://doi.org/10.1021/jp200926u>.
- [5] T. Varadavenkatesan, E. Lyubchik, S. Pai, A. Pugazhendhi, R. Vinayagam, R. Selvaraj, Photocatalytic degradation of Rhodamine B by zinc oxide nanoparticles synthesized using the leaf extract of *Cyanometra ramiflora*, *J. Photochem. Photobiol. B Biol.* 199 (2019), 111621, <https://doi.org/10.1016/j.jphotobiol.2019.111621>.
- [6] A. Umar, M.S. Akhtar, A. Al-Hajry, M.S. Al-Assiri, G.N. Dar, M. Saif Islam, Enhanced photocatalytic degradation of harmful dye and phenyl hydrazine chemical sensing using ZnO nanorods, *Chem. Eng. J.* 262 (2015) 588–596, <https://doi.org/10.1016/j.cej.2014.09.111>.
- [7] D. Lei, J. Xue, Q. Bi, C. Tang, L. Zhang, 3D/2D direct Z-scheme photocatalyst Zn₂SnO₄/CdS for simultaneous removal of Cr(VI) and organic pollutant, *Appl. Surf. Sci.* 517 (2020), 146300, <https://doi.org/10.1016/j.apsusc.2020.146300>.
- [8] A. Hameed, T. Montini, V. Gombac, P. Fornasiero, Photocatalytic decolorization of dyes on NiO–ZnO nano-composites, *Photochem. Photobiol. Sci.* 8 (5) (2009) 677–682, <https://doi.org/10.1039/B817396F>.
- [9] S. Balachandran, M. Swaminathan, Facile fabrication of heterostructured Bi₂O₃–ZnO photocatalyst and its enhanced photocatalytic activity, *J. Phys. Chem. C* 116 (50) (2012) 26306–26312, <https://doi.org/10.1021/jp306874z>.
- [10] J. Montero, T. Welearegay, J. Thyrr, H. Stopfel, T. Dedova, I.O. Acik, L. Österlund, Copper–zinc oxide heterojunction catalysts exhibiting enhanced photocatalytic activity prepared by a hybrid deposition method, *RSC Adv.* 11 (17) (2021) 10224–10234, <https://doi.org/10.1039/D1RA00691F>.
- [11] S. Periyannan, L. Mancerio, N.D. Nguyen, A. Klein, W. Jaegermann, P. Colson, C. Henrist, R. Cloots, Influence of ZnO surface modification on the photocatalytic performance of ZnO/NiO thin films, *Catal. Lett.* 149 (7) (2019) 1813–1824, <https://doi.org/10.1007/s10562-019-02781-z>.
- [12] M. Ding, H. Yang, T. Yan, C. Wang, X. Deng, S. Zhang, J. Huang, M. Shao, X. Xu, Fabrication of hierarchical ZnO@NiO core–shell heterostructures for improved photocatalytic performance, *Nanoscale Res. Lett.* 13 (1) (2018) 260, <https://doi.org/10.1186/s11671-018-2676-1>.
- [13] F. Tian, Y. Liu, Synthesis of p-type NiO/n-type ZnO heterostructure and its enhanced photocatalytic activity, *Scr. Mater.* 69 (5) (2013) 417–419, <https://doi.org/10.1016/j.scriptamat.2013.05.040>.
- [14] M. Wang, Y. Hu, J. Han, R. Guo, H. Xiong, Y. Yin, TiO₂/NiO hybrid shells: p–n junction photocatalysts with enhanced activity under visible light, *J. Mater. Chem. A* 3 (41) (2015) 20727–20735, <https://doi.org/10.1039/C5TA05839B>.
- [15] P. Nandi, D. Das, ZnO–Cu₂O heterostructure photocatalyst for efficient dye degradation, *J. Phys. Chem. Solids* 143 (2020), 109463, <https://doi.org/10.1016/j.jpcs.2020.109463>.
- [16] C. Liu, F. Meng, L. Zhang, D. Zhang, S. Wei, K. Qi, J. Fan, H. Zhang, X. Cui, CuO/ZnO heterojunction nanoarrays for enhanced photoelectrochemical water oxidation, *Appl. Surf. Sci.* 469 (2019) 276–282, <https://doi.org/10.1016/j.apsusc.2018.11.054>.
- [17] J. Yu, S. Zhuang, X. Xu, W. Zhu, B. Feng, J. Hu, Photogenerated electron reservoir in hetero-p–n CuO–ZnO nanocomposite device for visible-light-driven photocatalytic reduction of aqueous Cr(VI), *J. Mater. Chem. A* 3 (3) (2015) 1199–1207, <https://doi.org/10.1039/C4TA04526B>.
- [18] U.S.U. Thampy, A. Mahesh, K.S. Sibi, I.N. Jawahar, V. Biju, Enhanced photocatalytic activity of ZnO–NiO nanocomposites synthesized through a facile sonochemical route, *Snn Appl. Sci.* 1 (11) (2019) 15, <https://doi.org/10.1007/s42452-019-1426-z>.
- [19] M. Xiao, Y. Lu, Y. Li, H. Song, L. Zhu, Z. Ye, A new type of p-type NiO/n-type ZnO nano-heterojunctions with enhanced photocatalytic activity, *RSC Adv.* 4 (65) (2014) 34649–34653, <https://doi.org/10.1039/C4RA04600E>.
- [20] Z. Chen, T. Dedova, I.O. Acik, M. Danilson, M. Krunk, Nickel oxide films by chemical spray: effect of deposition temperature and solvent type on structural, optical, and surface properties, *Appl. Surf. Sci.* 548 (2021), 149118, <https://doi.org/10.1016/j.apsusc.2021.149118>.
- [21] A.A. Al-Ghamdi, M.S. Abdel-wahab, A.A. Farghali, P.M.Z. Hasan, Structural and photo-catalytic activity of nanocrystalline NiO thin films, *Mater. Res. Bull.* 75 (2016) 71–77, <https://doi.org/10.1016/j.materresbull.2015.11.027>.
- [22] K.O. Ukoba, A.C. Eloka-Eboka, F.L. Inambao, Review of nanostructured NiO thin film deposition using the spray pyrolysis technique, *Renew. Sustain. Energy Rev.* 82 (2018) 2900–2915, <https://doi.org/10.1016/j.rser.2017.10.041>.
- [23] H. Derikvandi, A. Nezamzadeh-Ejehi, Increased photocatalytic activity of NiO and ZnO in photodegradation of a model drug aqueous solution: effect of coupling, supporting, particles size and calcination temperature, *J. Hazard. Mater.* 321 (2017) 629–638, <https://doi.org/10.1016/j.jhazmat.2016.09.056>.
- [24] M.M. Sabzehmeidani, H. Karimi, M. Ghaedi, Electrospinning preparation of NiO/ZnO composite nanofibers for photodegradation of binary mixture of rhodamine B and methylene blue in aqueous solution: central composite optimization, *Appl. Organomet. Chem.* 32 (6) (2018), <https://doi.org/10.1002/aoc.4335>.
- [25] Y. Liu, G. Li, R. Mi, C. Deng, P. Gao, An environment-benign method for the synthesis of p-NiO/n-ZnO heterostructure with excellent performance for gas sensing and photocatalysis, *Sens. Actuators B Chem.* 191 (2014) 537–544, <https://doi.org/10.1016/j.snb.2013.10.068>.
- [26] Z. Zhang, C. Shao, X. Li, C. Wang, M. Zhang, Y. Liu, Electrospun nanofibers of p-type NiO/n-type ZnO heterojunctions with enhanced photocatalytic activity, *ACS Appl. Mater. Interfaces* 2 (10) (2010) 2915–2923, <https://doi.org/10.1021/am100618h>.
- [27] J.H. Huang, J.X. Chen, Y.F. Tu, Y. Tian, D. Zhou, G. Zheng, J.P. Sang, Q.M. Fu, Preparation and photocatalytic activity of CuO/ZnO composite nanostructured films, *Mater. Res. Express* 6 (1) (2019), <https://doi.org/10.1088/2053-1591/ae6ff>.
- [28] W. Jing, W. Gao, Z. Li, M. Peng, F. Han, Z. Wei, Z. Yang, Z. Jiang, Regulation of the volume flow rate of aqueous methyl blue solution and the wettability of CuO/ZnO nanorods to improve the photodegradation performance of related microfluidic reactors, *Langmuir* 37 (26) (2021) 7890–7906, <https://doi.org/10.1021/acs.langmuir.1c00407>.
- [29] I. Dunder, M. Krichevskaya, A. Katerski, I.O. Acik, TiO₂ thin films by ultrasonic spray pyrolysis as photocatalytic material for air purification, *R. Soc. Open Sci.* 6 (2) (2019), <https://doi.org/10.1098/rsos.181578>.
- [30] R. Parize, A. Katerski, I. Gromyko, L. Rapenne, H. Roussel, E. Kärber, E. Appert, M. Krunk, V. Consonni, ZnO/TiO₂/Sb₂S₃ core–shell nanowire heterostructure for extremely thin absorber solar cells, *J. Phys. Chem. C* 121 (18) (2017) 9672–9680, <https://doi.org/10.1021/acs.jpcc.7b00178>.
- [31] A.T. Oluwabi, A. Katerski, E. Carlos, R. Branquinho, A. Mere, M. Krunk, E. Fortunato, L. Pereira, I. Oja Acik, Application of ultrasonic sprayed zirconium oxide dielectric in zinc tin oxide-based thin film transistor, *J. Mater. Chem. C* 8 (11) (2020) 3730–3739, <https://doi.org/10.1039/C9TC05127A>.
- [32] X.H. Chan, J.R. Jennings, M.A. Hossain, K.K.Z. Yu, Q. Wang, Characteristics of p-NiO thin films prepared by spray pyrolysis and their application in CdS-sensitized photocathodes, *J. Electrochem. Soc.* 158 (7) (2011) H733–H740, <https://doi.org/10.1149/1.3590742>.
- [33] T. Dedova, I.O. Acik, Z. Chen, A. Katerski, K. Balmassov, I. Gromyko, T. Nagyné-Kovács, I.M. Szilágyi, M. Krunk, Enhanced photocatalytic activity of ZnO nanorods by surface treatment with H₂SO₄: Synergic effects through an electron scavenging, plasmon resonance and surface hydroxylation, *Mater. Chem. Phys.* 245 (2020), 122767, <https://doi.org/10.1016/j.matchemphys.2020.122767>.
- [34] N. Maticic, T. Kodalle, J. Lauche, R. Wenisch, T. Bertram, C.A. Kaufmann, I. Lauermann, In vacuo XPS investigation of Cu(In,Ga)Se₂ surface after RbF post-deposition treatment, *Thin Solid Films* 665 (2018) 143–147, <https://doi.org/10.1016/j.tsf.2018.09.026>.
- [35] M. Rusu, T. Kodalle, L. Choubrac, N. Barreau, C.A. Kaufmann, R. Schlattmann, T. Unold, Electronic structure of the CdS/Cu(In,Ga)Se₂ interface of KF- and RbF-treated samples by Kelvin Probe and photoelectron yield spectroscopy, *ACS Appl. Mater. Interfaces* 13 (6) (2021) 7745–7755, <https://doi.org/10.1021/acsami.0c20976>.
- [36] X. Chen, Z. Wu, D. Liu, Z. Gao, Preparation of ZnO photocatalyst for the efficient and rapid photocatalytic degradation of Azo Dyes, 143–143, *Nanoscale Res. Lett.* 12 (1) (2017), <https://doi.org/10.1186/s11671-017-1904-4>.
- [37] I. Oja, A. Mere, M. Krunk, R. Nisumaa, C.H. Solterbeck, M. Es-Souni, Structural and electrical characterization of TiO₂ films grown by spray pyrolysis, *Thin Solid Films* 515 (2) (2006) 674–677, <https://doi.org/10.1016/j.tsf.2005.12.243>.
- [38] D. Ao, Z. Li, Y. Fu, Y. Tang, S. Yan, X. Zu, Heterostructured NiO/ZnO nanorod arrays with significantly enhanced H₂S sensing performance, *Nanomaterials* 9 (6) (2019) 900, <https://doi.org/10.3390/nano9069000>.
- [39] I. Gromyko, M. Krunk, T. Dedova, A. Katerski, D. Klauson, I. Oja Acik, Surface properties of sprayed and electrodeposited ZnO rod layers, *Appl. Surf. Sci.* 405 (2017) 521–528, <https://doi.org/10.1016/j.apsusc.2017.02.065>.
- [40] A. Pal, T.K. Dey, A. Singhal, R.C. Bindal, P.K. Tewari, Nano-ZnO impregnated inorganic–polymer hybrid thinfilm nanocomposite nanofiltration membranes: an investigation of variation in structure, morphology and transport properties, *RSC Adv.* 5 (43) (2015) 34134–34151, <https://doi.org/10.1039/c4ra14854a>.
- [41] M. Wang, L. Jiang, E.J. Kim, S.H. Hahn, Electronic structure and optical properties of Zn(OH)₂: LDA+U calculations and intense yellow luminescence, *RSC Adv.* 5 (106) (2015) 87496–87503, <https://doi.org/10.1039/C5RA17024A>.
- [42] R. Al-Gaashani, S. Radiman, A.R. Daud, N. Tabet, Y. Al-Douri, XPS and optical studies of different morphologies of ZnO nanostructures prepared by microwave methods, *Ceram. Int.* 39 (3) (2013) 2283–2292, <https://doi.org/10.1016/j.ceramint.2012.08.075>.
- [43] K. Sakamoto, F. Hayashi, K. Sato, M. Hirano, N. Ohtsu, XPS spectral analysis for a multiple oxide comprising NiO, TiO₂, and NiTiO₃, *Appl. Surf. Sci.* 526 (2020), 146729, <https://doi.org/10.1016/j.apsusc.2020.146729>.
- [44] H. Tian, H. Fan, G. Dong, L. Ma, J. Ma, NiO/ZnO p–n heterostructures and their gas sensing properties for reduced operating temperature, *RSC Adv.* 6 (110) (2016) 109091–109098, <https://doi.org/10.1039/C6RA19520B>.
- [45] N. Spalatu, R. Krautmann, A. Katerski, E. Karber, R. Josepsson, J. Hiie, I.O. Acik, M. Krunk, Screening and optimization of processing temperature for Sb₂Se₃ thin film growth protocol: Interrelation between grain structure, interface intermixing and solar cell performance, *Sol. Energy Mater. Sol. Cells* 225 (2021), 111045, <https://doi.org/10.1016/j.solmat.2021.111045>.

Appendix 2

Table 1.1. Photocatalytic activity of ZnO nanoparticles, ZnO films and ZnO nanorods on substrates.

Catalyst	Substrate	Precursor	Synthesis method	Synthesis temp. (°C)	Annealing temp. (°C)	Catalyst amount (mg/L)	Pollutant	C ₀ (ppm)	V (mL)	Light	t (min)	η (%)	Ref.	
ZnO NPs	-	Zn(ac) ₂	Sol-gel	80	400	800	MO	30	50	UV	100	99	[45]	
		Zn(ac) ₂	Thermal decomposition	600	-	1250	MO	10	40	UV	120	98	[46]	
		Zn(NO ₃) ₂	Precipitation in solution	RT	200	300	MO	20	NA	UV	80	99	[47]	
		Zn(ac) ₂	Hydrothermal	120	-	NA	MO	12	NA	UV	180	89	[48]	
		Zn(ac) ₂		200	-	1000	RhB	6	60	UV	500	88	[49]	
		Plate-like	ZnCl ₂	Precipitation in solution	60	80	1000	MB	16	5	Sunlight	14	90	[50]
		Flower-like	ZnCl ₂	Precipitation in solution	50	-	200	MO	15	100	UV	50	99	[51]
Sponge-like	Zn(NO ₃) ₂	Solution combustion	400	NA	500	MG	5	100	UV	150	95	[52]		
ZnO film	SiO ₂	Zn(ac) ₂	Sol-gel	RT	400	NA	MO	6	5	Sunlight	150	18	[53]	
	Glass	Zn	DC sputtering	RT	-		MO	10	100	Sunlight	NA	53	[54]	
	Quartz	Zn(ac) ₂	Sol-gel	60	400		MO	5	10	UV-Vis	180	73	[55]	
	Si	Zn(C ₂ H ₅) ₂	Atomic layer deposition	80	-		MB	5	2	UV	240	40	[56]	
	Glass	Zn(ac) ₂	Ultrasonic spray pyrolysis	450	-		MB	-	-	UV	240	88	[57]	

Catalyst	Substrate	Precursor	Synthesis method	Synthesis temp. (°C)	Annealing temp. (°C)	Catalyst amount (mg/L)	Pollutant	C ₀ (ppm)	V (mL)	Light	t (min)	η (%)	Ref.
ZnO nanorods	Si	Zn(NO ₃) ₂	Hydrothermal	90	300		MO	5	NA	UV	60	87	[58]
	SiO ₂	Zn(NO ₃) ₂		100	-		MO	6	500	UV	160	95	[59]
	Glass	Zn(NO ₃) ₂		90	-		RhB	5	NA	UV-Vis	120	70	[60]
	ITO/glass	ZnCl ₂	Pneumatic spray pyrolysis	550	-		Doxycycline	25	20	UV	240	50	[8]
			Electrodeposition	80	85								
		Glass	Zn(ac) ₂	Hydrothermal	90	-		MB	10	20	UV	45	83
	Si	Zn(ac) ₂	Chemical bath deposition	95	-		RhB	10	5	UV	720	98	[62]

Table 1.2. Photocatalytic activity of ZnO/noble metal composites.

Catalyst	Substrate	Precursor	Synthesis method	Synthesis temp. (°C)	Annealing temp. (°C)	Catal. Amount (mg/L)	Pollutant	C ₀ (ppm)	V (mL)	Light	t (min)	η (%)	Ref.
ZnO/Au NPs		Zn(NO ₃) ₂ HAuCl ₄	Combustion	500	-	1500	MB	6	100	UV	160	ZnO NPs: 10 ZnO/Au NPs: 25	[63]
		Zn(NO ₃) ₂ HAuCl ₄	Ultrasonic spray pyrolysis	1000	-	50	RhB	5	100	UV	180	ZnO NPs: 33 ZnO/Au NPs: 80	[64]
		ZnCl ₂ HAuCl ₄	Hydrothermal	240	-	700	MB	4	75	UV	140	ZnO NPs: 15 ZnO/Au NPs: 96	[65]
		Zn(ac) ₂ HAuCl ₄	Precipitation in solution	90	-	100	MO	20	50	Vis	200	ZnO NPs: 15 ZnO/Au NPs: 75	[66]
		Zn(ac) ₂ , HAuCl ₄	Precipitation in solution	ZnO: 60 Au: 80	-	100	MO	10	100	UV	160	ZnO NPs: 76 ZnO/Au NPs: 96	[67]
ZnO/Ag NPs	-	Zn(ac) ₂ AgNO ₃	Precipitation in solution	70	550	1000	MB	10	100	UV-Vis	15	ZnO NPs: 65 ZnO/Ag NPs: 97	[68]
		Zn(ac) ₂ Ag(ac) ₂	Solvothermal	160	60	333	MO	16	90	UV	40	ZnO NPs: 81 ZnO/Ag NPs: 99	[69]
ZnO/Pt NPs ZnO/Au NPs		C ₂₂ H ₁₄ O ₄ Zn Pt(acac) ₂ AuCl ₃	Flame spray pyrolysis	NA	-	20	MB	10	200	UV	60	ZnO NPs: 54 ZnO/Pt NPs: 55 ZnO/Au NPs: 70	[70]
ZnO/Pd NPs		Zn(NO ₃) ₂ K ₂ PdCl ₄	ZnO: hydrothermal Pd: stirring in solution	ZnO: 150 Pd: RT	300	1500	Phenol	50	50	UV	60	ZnO NPs: 40 ZnO/Pd NPs: 98	[71]
		Zn(ac) ₂ PdCl ₂	Solvothermal	120	-	200	RhB	5	50	UV	15	ZnO NPs: 49 ZnO/Pd NPs: 82	[72]

Catalyst	Substrate	Precursor	Synthesis method	Synthesis temp. (°C)	Annealing temp. (°C)	Catal. Amount (mg/L)	Pollutant	C ₀ (ppm)	V (mL)	Light	t (min)	η (%)	Ref.
ZnO NPs ZnO/Ag NPs ZnO/Pd NPs ZnO/Pt NPs		Zn(NO ₃) ₂ AgNO ₃ Pd(NO ₃) ₂ H ₂ PtCl ₆	ZnO: hydrothermal Metal: photodeposition	180		50	AO II	20	100	UV	300	ZnO NPs: 70 ZnO/Ag NPs: 92 ZnO/Pd NPs: 96 ZnO/Pt NPs: 78	[73]
ZnO/Au thin film composite	Glass	Zn(ac) ₂ HAuCl ₄	Sol-gel spin coating	RT	500		MO	10	5	Sunlight	150	ZnO film: 63 ZnO film/Au: 94	[74]
ZnO/Ag thin film composite	Glass	Zn(ac) ₂ Ag NPs	Sol-gel spin coating	RT	500		IC	6	NA	UV-Vis	300	ZnO film: 18 ZnO film/Ag: 30	[75]
ZnO _{NR} /Au	Si	Zn(NO ₃) ₂ HAuCl ₄	ZnO: hydrothermal Au: precipitation in solution	90	-		RhB	10	-	UV	90	ZnO _{NR} : 27 ZnO _{NR} /Au: 91	[76]
	Glass	Zn(ac) ₂ HAuCl ₄	ZnO: hydrothermal Au: precipitation in solution	ZnO: 60 Au: 70	400		MO	5	20	UV-Vis	180	ZnO _{NR} : 66 ZnO _{NR} /Au: 100	[77]
	Fe-Co-Ni alloy	Zn(NO ₃) ₂ HAuCl ₄	ZnO: hydrothermal Au: precipitation in solution	ZnO: 70 Au: 50	-		MO	20	40	UV	210	ZnO _{NR} : 58 ZnO _{NR} /Au: 95	[78]
	TCO glass	Zn(NO ₃) ₂ Au	ZnO: Au: magnetron sputtering	ZnO: 80 Au: NA	200		MO	2.5	8	UV	240	ZnO _{NR} : 15 ZnO _{NR} /Au: 90	[79]
	Si	Zn(acac) ₂ HAuCl ₄	ZnO: chemical vapor deposition Au: photodeposition	525	-		MO	15	-	UV	180	ZnO _{NR} : 70 ZnO _{NR} /Au: 90	[80]

Catalyst	Substrate	Precursor	Synthesis method	Synthesis temp. (°C)	Annealing temp. (°C)	Catal. Amount (mg/L)	Pollutant	C ₀ (ppm)	V (mL)	Light	t (min)	η (%)	Ref.
ZnO _{NR} /Ag	Glass	Zn(ac) ₂ AgNO ₃	ZnO: chemical bath deposition Ag: photodeposition	ZnO: 80 Ag: RT	-		MB	2	15	UV	100	ZnO _{NR} : 36 ZnO _{NR} /Ag: 49	[81]
	Glass	Zn(NO ₃) ₂ AgNO ₃	ZnO: hydrothermal Ag: precipitation in solution	ZnO: 95 Ag: 80	400		MB	32	20	Vis	43	ZnO _{NR} : 60 ZnO _{NR} /Ag: 65	[82]
ZnO _{NR} /Pt	Zn foil	Zn foil H ₂ PtCl ₆	Hydrothermal	ZnO: 180 Pt: 180	-		RhB	24	5	UV	12	ZnO _{NR} : 37 ZnO _{NR} /Pt: 62	[83]
	Glass	Zn(NO ₃) ₂ H ₂ PtCl ₆	ZnO: Hydrothermal Pt: precipitation in solution	ZnO: 95 Pt: 100	400		MB	3	20	Vis	120	ZnO _{NR} : 26 ZnO _{NR} /Pt :32	[84]

Table 1.3. Photocatalytic activity of ZnO heterostructures (p-n heterojunctions) by coupling with other p-type semiconductors.

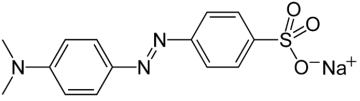
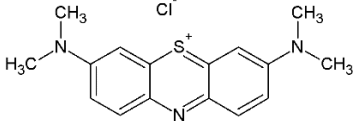
Catalyst	Substrate	Precursor	Synthesis method	Synthesis temp. (°C)	Annealing temp. (°C)	Catal. amount (mg/L)	Pollutant	C ₀ (ppm)	V (mL)	Light	t (min)	η (%)	Ref.
ZnO/Cu ₂ O NPs		ZnCl ₂ CuCl ₂	Hydrothermal	Cu ₂ O: 80 ZnO: 140	-	500	MO	10	100	Vis	120	Cu ₂ O: 30 ZnO/Cu ₂ O: 99	[92]
ZnO/CuO NPs		Zn(ac) ₂ Cu(ac) ₂	ZnO: hydrothermal CuO: precipitation in solution	ZnO: 150 CuO: 90	-	500	Phenol	10	100	Vis	180	CuO: 20 ZnO: 40 ZnO/CuO: 78	[93]
		Ni(ac) ₂ Zn(ac) ₂	Sonochemical route	60	250	500	MB	16	100	Sunlight	60	NiO: 20 ZnO: 50 ZnO/NiO: 90	[94]
ZnO/NiO NPs		Ni(NO ₃) ₂ Zn(NO ₃) ₂	Coprecipitation in solution	RT	400	500	RhB	10	100	UV	200	NiO: 20 ZnO: 80 ZnO/NiO: 90	[95]
		Ni(NO ₃) ₂ Zn(SO ₄) ₂		RT	400	500	MO	10	200	UV	NA	NiO: 10 ZnO: 40 ZnO/NiO: 100	[96]
		Ni(NO) ₃ Zn(NO) ₃		RT	60	1000	MB	10	50	UV	80	ZnO: 54 ZnO/NiO: 72	[97]
		Ni(ac) ₂ Zn(ac) ₂	Electrospinning	RT	500	1000	MB	3	50	UV	180	NiO:58 ZnO:50 ZnO/NiO:80	[98]
ZnO/NiO nanofibers		Ni(ac) ₂ Zn(ac) ₂		80	600	500	MB	10	100	Vis	180	NiO: 40 ZnO: 50 ZnO/NiO: 100	[99]
		Zn(ac) ₂ Ni(ac) ₂		RT	550	100	RhB	10	100	UV	50	NiO: 40 ZnO: 80 ZnO/NiO: 100	[100]

Catalyst	Substrate	Precursor	Synthesis method	Synthesis temp. (°C)	Annealing temp. (°C)	Catal. amount (mg/L)	Pollutant	C ₀ (ppm)	V (mL)	Light	t (min)	η (%)	Ref.
ZnO _{NR} /Cu ₂ O	ITO/glass	Zn(NO ₃) ₂ Cu(NO ₃) ₂	ZnO: hydrothermal Cu ₂ O: electrodeposition	Cu ₂ O: 60 ZnO: 148	-	-	MO	5	10	Vis	300	Cu ₂ O: 46 ZnO _{NR} : 4 ZnO _{NR} /Cu ₂ O: 90	[102]
	Glass	Zn(NO ₃) ₂ Cu	ZnO: hydrothermal Cu ₂ O: gas deposition	ZnO: 95 Cu ₂ O: NA	-	-	Orange II	18	1	UV	180	ZnO _{NR} : 56 ZnO _{NR} /Cu ₂ O: 64	[103]
ZnO _{NR} /CuO	Glass	ZnCl ₂ Cu(NO ₃) ₂	ZnO: precipitation in solution CuO: photodeposition	ZnO: 95 CuO: RT	400	-	MO	3	30	Vis	150	ZnO _{NR} : 20 ZnO _{NR} /CuO: 90	[104]
	Quartz	Zn(NO ₃) ₂ Cu(NO ₃) ₂	ZnO: hydrothermal CuO: hydrothermal	ZnO: 95 CuO: 60	-	-	MB	3	3	UV-Vis	180	ZnO _{NR} : 50 ZnO _{NR} /CuO: 78	[105]
ZnO _{NR} /CuO core-shell structure	Quartz	Zn(ac) ₂ Cu(NO ₃) ₂	ZnO: hydrothermal CuO: precipitation in solution	ZnO: 95 CuO: 60	-	-	MB	3	3	Vis	180	ZnO _{NR} : 35 ZnO _{NR} /CuO: 72	[106]
ZnO _{NR} /NiO core-shell structure	FTO/ glass	Zn(NO) ₃ Ni	ZnO: hydrothermal NiO: sputtering	ZnO: 92 NiO: RT	250	-	RhB	10	20	UV	180	ZnO _{NR} : 65 ZnO _{NR} /NiO: 67	[107]

Table 1.4. Photocatalytic activity of NiO nanoparticles and thin films.

Catalysts	Substrates	Precursor	Synthesis method	Synthesis temp. (°C)	Annealing temp. (°C)	Catalyst amount (mg/L)	Pollutant	C ₀ (ppm)	V (mL)	Light	t (min)	η (%)	Ref.			
NiO NPs		NiCl ₂	Sphere-like	Hydrothermal	130	-	1	MB	0.3	100	UV-Vis	180	64	[162]		
			Rod-like	Sol-gel	RT	500	1000	Phenol	100	100	UV	60	97	[167]		
		Plate-like		Ni(NO ₃) ₂	Combustion	RT	400	100	MO	3	100	Vis	50	80	[158]	
					Precipitation in solution	RT	250	200	MO	25	50	Vis	110	38	[159]	
				Ni(ac) ₂			185	400	400	MO	40	50	UV	120	53	[160]
					Hydrothermal		180	700	1000	RhB	10	100	UV	60	70	[164]
		Flower-like		Ni(ac) ₂			160	400	50	MB	15	20	Vis	20	99	[163]
					Precipitation in solution	RT	350	1000	MO	16	100	UV	120	49	[161]	
NiO film	Al film	NiCl ₂	Thermal decomposition	RT	400		MO	50	NA	UV	120	90	[169]			
	Glass	Ni	DC magnetron sputtering	NA	-		MG	10	NA	UV	120	70	[166]			
	LaAlO ₃	NiO	Pulsed laser deposition	NA	-	NA	RhB	10	1	UV-Vis	60	30	[165]			
	ITO glass	NiCl ₂	Electrodeposition	RT	400		Phenol	100	100	UV	60	45	[168]			
	Glass	NiCl ₂	Pneumatic spray pyrolysis	460	-		MB	NA	NA	UV	180	90	[170]			

Table 2.4. Description of pollutants used in this thesis.

Type of pollutant	Molecular structure
<p>Methyl orange (MO) is an anionic dye commonly used in textile and printing industries. MO is also a pH indicator frequently used in titration. It can cause vomiting and diarrhea if swallowed and respiratory tract irritation if inhaled. It may be carcinogenic as well.</p>	 <chem>CN(C)c1ccc(cc1)/N=N/c2ccc(cc2)S(=O)(=O)[O-].[Na+]</chem>
<p>Methylene blue (MB) is a cationic dye commonly used in textile and coloring industries. As a medication, MB injection is used in the treatment of methemoglobinemia and urinary tract infections. However, accumulation of MB in human body can cause kidney, brain, liver, and central nervous system deterioration.</p>	 <chem>CN(C)c1ccc2c(c1)nc3ccccc3s2[N+](=O)[Cl-]CN(C)C</chem>

Curriculum vitae

Personal data

Name: Zengjun Chen
Date of birth: 19.03.1993
Place of birth: Qingdao city, Shandong province, China
Citizenship: People's Republic of China

Contact data

E-mail: Zengjun.Chen@taltech.ee

Education

2018–2022 Tallinn University of Technology, Chemical and Materials Technology – PhD
2016–2018 Tallinn University of Technology, Materials and Processes for Sustainable Energetics – MSC
2011–2015 Qingdao University of Science and Technology, Chemical engineering and technology – BSC

Language competence

Chinese native
English intermediate

Participation in conference

2018–2021 Graduate school “Functional materials and technologies FMTDK”, Tallinn University of Technology and Tartu University, Estonia
15.09.2019–20.09.2019 E-MRS Fall Meeting, Warsaw – Poland
23.05.2018–25.05.2018 15th CYSENI international conference, Kaunas, Lithuania

Research Project

01.01.2014–31.12.2019 IUT19-4 “Thin films and nanomaterials by wet chemical methods for next-generation photovoltaics”.
01.01.2015–01.03.2023 TAR16016EK (TK141) “Advanced materials and high-technology devices for energy recuperation systems”.
01.01.2020–12.31.2024 PRG627 “Antimony-chalcogenide thin films for next-generation semi-transparent solar cells applicable in electricity producing windows”.

List of publications

1. T. Dedova, I. Oja Acik, **Z. Chen**, A. Katerski, K. Balmassov, I. Gromyko, T. Nagyné-Kovács, I.M. Szilágyi, and M. Krunks. Enhanced photocatalytic activity of ZnO nanorods by surface treatment with HAuCl₄: Synergic effects through an electron scavenging, plasmon resonance and surface hydroxylation. *Materials Chemistry and Physics*, 245, 122767, 2020, <https://doi.org/10.1016/j.matchemphys.2020.122767>.
2. **Z. Chen**, T. Dedova, I. Oja Acik, M. Danilson, and M. Krunks. Nickel oxide films by chemical spray: Effect of deposition temperature and solvent type on structural, optical, and surface properties. *Applied Surface Science*, 548, 149118, 2021, <https://doi.org/10.1016/j.apsusc.2021.149118>.

3. **Z. Chen**, T. Dedova, N. Spalatu, N. Maticiuc, M. Rusu, A. Katerski, I. Oja Acik, T. Unold, and M. Krunk. ZnO/NiO heterostructure with enhanced photocatalytic activity obtained by ultrasonic spray of a NiO shell onto ZnO nanorods. *Colloids and Surfaces A: Physicochemical and Engineering Aspects*, 648, 129366, 2022, <https://doi.org/10.1016/j.colsurfa.2022.129366>.
4. **Z. Chen**, I. Dündar, I. Oja Acik, and A. Mere. TiO₂ thin films by ultrasonic spray pyrolysis. *IOP Conference Series: Materials Science and Engineering*, 503, 012006, 2019, <http://doi.org/10.1088/1757-899X/503/1/012006>.

Elulookirjeldus

Isikuandmed

Nimi: Zengjun Chen
Sünniaeg: 19.03.1993
Sünnikoht: Qingdao linn, Shandongi provints, Hiina
Kodakondsus: Hiina Rahvavabariik

Kontaktandmed

E-post: Zengjun.Chen@taltech.ee

Hariduskäik

2018–2022 Tallinna Tehnikaülikool, keemia- ja materjalitehnoloogia – PhD
2016–2018 Tallinna Tehnikaülikool, Materjalid ja protsessid säästva energeetika jaoks – MSC
2011–2015 Qingdao teaduse ja tehnoloogia ülikool, keemiatehnika ja tehnoloogia – BSC

Keelteoskus

Hiina keel emakeel
Inglise keel kesktase

Konverentsil osalemine

2018–2021 Graduate school “Functional materials and technologies FMTDK”, Tallinn University of Technology and Tartu University, Estonia
15.09.2019–20.09.2019 E-MRS Fall Meeting, Warsaw – Poland
23.05.2018–25.05.2018 15th CYSENI international conference, Kaunas, Lithuania

Uuringuprojekt

01.01.2014–31.12.2019 IUT 19-4 “Thin films and nanomaterials by wet-chemical methods for next-generation photovoltaics”.
01.01.2015–01.03.2023 TAR16016EK (TK141) “Advanced materials and high-technology devices for energy recuperation systems”.
01.01.2020–12.31.2024 PRG627 “Antimony-chalcogenide thin films for the next generation of semi-transparent solar cells for use in power-producing windows”.

Publikatsioonid

1. T. Dedova, I. Oja Acik, **Z. Chen**, A. Katerski, K. Balmassov, I. Gromyko, T. Nagyné-Kovács, I.M. Szilágyi, and M. Krunk. Enhanced photocatalytic activity of ZnO nanorods by surface treatment with HAuCl₄: Synergic effects through an electron scavenging, plasmon resonance and surface hydroxylation. *Materials Chemistry and Physics*, 245, 122767, 2020, <https://doi.org/10.1016/j.matchemphys.2020.122767>.

2. **Z. Chen**, T. Dedova, I. Oja Acik, M. Danilson, and M. Krunks. Nickel oxide films by chemical spray: Effect of deposition temperature and solvent type on structural, optical, and surface properties. *Applied Surface Science*, 548, 149118, 2021, <https://doi.org/10.1016/j.apsusc.2021.149118>.
3. **Z. Chen**, T. Dedova, N. Spalatu, N. Maticiuc, M. Rusu, A. Katerski, I. Oja Acik, T. Unold, and M. Krunks. ZnO/NiO heterostructure with enhanced photocatalytic activity obtained by ultrasonic spray of a NiO shell onto ZnO nanorods. *Colloids and Surfaces A: Physicochemical and Engineering Aspects*, 648, 129366, 2022, <https://doi.org/10.1016/j.colsurfa.2022.129366>.
4. **Z. Chen**, I. Dündar, I. Oja Acik, and A. Mere. TiO₂ thin films by ultrasonic spray pyrolysis. *IOP Conference Series: Materials Science and Engineering*, 503, 012006, 2019, <http://doi.org/10.1088/1757-899X/503/1/012006>.

ISSN 2585-6901 (PDF)
ISBN 978-9949-83-926-1 (PDF)